UNIVERSIDAD COMPLUTENSE DE MADRID

FACULTAD DE CIENCIAS QUÍMICAS

TESIS DOCTORAL

Redes metal-orgánicas complejas con secuencias de metales para Catálisis Heterogénea

Complex metal-organic Frameworks with metal sequences for Heterogeneous Catalysis

MEMORIA PARA OPTAR AL GRADO DE DOCTOR

PRESENTADA POR

Raluca Loredana Vasile

DIRIGIDA POR

Felipe Gándara Barragá

UNIVERSIDAD COMPLUTENSE DE MADRID

FACULTAD DE CIENCIAS QUÍMICAS

INSTITUTO DE CIENCIA DE MATERIALES DE MADRID
(ICMM-CSIC)

TESIS DOCTORAL

Redes Metal-Orgánicas Complejas Con Secuencias de Metales Para Catálisis Heterogénea

Complex Metal-Organic Frameworks With Metal Sequences For Heterogeneous Catalysis

MEMORIA PARA OPTAR AL GRADO DE DOCTORA EN EL PROGRAMA DE QUÍMICA AVANZADA

PRESENTADA POR

Raluca Loredana Vasile

DIRECTOR

Felipe Gándara Barragán

TESIS DOCTORAL

Redes Metal-Orgánicas Complejas Con Secuencias De Metales Para Catálisis Heterogénea

Complex Metal-Organic Frameworks With Metal Sequences For Heterogeneous Catalysis

PRESENTADA POR

Raluca Loredana Vasile

DIRECTOR

Felipe Gándara Barragán

A mis padres, Daniela y Mihai, y a Samuel ♡

AGRADECIMIENTOS

Aquí me hallo, escribiendo los agradecimientos de mi tesis doctoral, sin poder creerme que este capítulo de mi vida esté a punto de cerrarse. Menuda aventura ha sido…comenzó hace 4 años, estando yo muy verde en esto de "la ciencia", y nada más empezar a cacharrear en el laboratorio llegó **la pandemia**. Aunque los comienzos fuesen algo agitados, y todo el proceso haya sido bastante caótico, ha sido un largo camino que jamás olvidaré. He sido muy feliz trabajando en el laboratorio, sintetizando cristalitos de mis MOFs, y guardaré todos los recuerdos de esta etapa de mi vida con mucho cariño en mi corazón.

Estaré eternamente agradecida a todas las personas que me han ayudado y apoyado, permitiéndome así crecer tanto a nivel profesional como personal.

En primer lugar, quiero dar las gracias a las personas a las cuales les dedico esta tesis, que son mi pilar fundamental y a quienes se lo debo todo: mis padres y Sam.

Soy consciente de que he tenido mucha suerte de contar con unos padres así, que me han dado todo lo que han podido y más, y siempre me han apoyado incondicionalmente en todo lo que he hecho. Si hoy estoy aquí finalizando mi tesis doctoral, es gracias a todos los sacrificios que han hecho a lo largo de todos estos años. Les doy las gracias por criarme, educarme y convertirme en la persona que soy hoy en día. ♡ *Dragii mei părinți, cuvintele nu pot exprima recunoștința pe care o simt pentru toți anii de dedicare necondiționată. M-ați adus pe lume, lângă voi am avut o copilărie minunată, și mi-ați arătat drumul cel bun. Vă port o iubire nemărginită* ♡

No sólo he tenido suerte con la familia que me ha tocado, sino también con la persona que ha estado a mi lado estos últimos 13 años de mi vida: Samuel (Sam ♡). Gracias Sam, por todo. Qué suerte tuve cuando nuestros caminos se cruzaron aquel día en el instituto. Gracias por ayudarme a ser mi mejor versión posible. Por acompañarme en absolutamente todos los momentos de mi vida. Por tu generosidad, por todo lo que has hecho (y haces)

y lo que has sacrificado siempre a favor de nuestra relación. Por tu paciencia y por tu amor incondicional. Por todo lo que te has esforzado para que formemos un presente y un futuro juntos. No concibo una vida sin ti. Te quiero.

Me gustaría agradecer a mi director de tesis, el doctor Felipe Gándara, por darme esta oportunidad y por confiar en que pudiese realizar la tesis; por encauzarme siempre que estaba perdida; por tener paciencia infinita conmigo y aguantar mi mundo caótico y poco organizado. Gracias Felipe, por ayudarme siempre que te ha sido posible, y por invertir tiempo en enseñarme sobre el maravilloso campo de la cristalografía y de los MOFs.

También me gustaría agradecer al grupo en el cual he trabajado estos años, el grupo de "Química Reticular y Cristalografía". Gracias a la profesora Ángeles Monge (Nines) y al profesor Enrique Gutiérrez-Puebla por tratarme siempre con cariño, por sentarse conmigo siempre que tenía dudas de cristalografía y no conseguía dar con la estructura correcta de mis cristales, y por compartir su amplio conocimiento sobre el mundo de la cristalografía. Gracias a la doctora Lina María Aguirre Diaz, por guiarme a la hora de dar mis primeros pasos en el laboratorio.

A la doctora Fátima Esteban Betegón. Fátima, me siento muy afortunada de haberte conocido, qué suerte tuvimos de que fueras parte del grupo. Además de ser una gran profesional que siempre trabaja duro y se deja la piel, eres un amor de persona que siempre se preocupa por los demás y está dispuesta a ayudar a cualquiera. Gracias por sacrificar tu valioso tiempo para sentarte a escuchar mis penas, comprenderme, aconsejarme y animarme. Por compartir tu vida (tu familia es encantadora) y tus vivencias/anécdotas con nosotras. Siempre seremos tus "niñas".

A Eloy, que empezó en el ICMM a la vez que yo, y que en poco tiempo pasó de ser un estudiante de prácticas a ser parte del grupo, y estoy segura de que en el futuro será un

gran investigador. Gracias Eloy, por tratarme siempre con cariño, por aconsejarme, y por animarme cuando tenía días malos.

A las personas que componen el despacho 032: Clara y Pilar, mis *science sisters*. Estoy muy contenta de haber podido compartir tanto tiempo con vosotras en nuestro despacho y en los laboratorios, ya que eso permitió forjar nuestra amistad. Ojalá en un futuro pueda trabajar en un ambiente tan bueno como en el que teníamos en nuestro laboratorio, ya que nos ayudábamos mutuamente (no dudábamos en plantear en la pizarra cualquier duda sobre química, aunque fuesen cosas super básicas), y siempre velábamos por el bien de las otras. Vosotras dos habéis sido fundamentales para mí en estos años de doctorado ya que hemos trabajado codo con codo todos los días, y habéis sido testigos directos de mi aventura al completo. Jamás olvidaré los cofis, las charlas, las risas, los momentos musicales, las partidas de rummikub, las consultas (cómo redactar un correo, cómo hacer un powerpoint, si este color queda bien o si estaba mejor el otro tono…), nuestras paredes llenas de prints, los viajes que hemos hecho juntas, los millones de sustos que me habéis pegado a lo largo de estos años (qué le voy a hacer, soy un gato). Ojalá nuestras pegatinas se queden en la puerta del 032 para siempre. Confío en que nos reencontraremos en la catcafelería. Rula os quiere mucho.

A Clara, Celegé, la Cñora. Jamás imaginé que conectaría tan rápido con una persona. Aún recuerdo cuando apareció "la chica nueva pero no tan nueva del grupo", y tenía tanto miedo de no llegar a llevarme bien con ella, pero cuatro años después se ha convertido en una de mis mejores amigas (de cuyo sitio en la mesa el lab me adueñé) que tanto me ha apoyado estos años. Celegé, hacemos muy buen equipo porque nos complementamos y nos apoyamos la una a la otra constantemente, y por supuesto no me refiero a solo en lo profesional. Gracias por estar siempre al pie del cañón. Por ser tan transparente y mostrarte tal y como eres siempre. Por preocuparte por mi y ayudarme en todo lo que has

podido. Por hacerme salir de “mi zona de confort”. Por enseñarme que la vida nunca te golpea con la suficiente fuerza como para no poder volver a levantarte. Por dejarme conocerte (más bien, en esforzarte para que yo me fiara de ti) y por aceptarme tal y como soy (desconfiada, sobre todo). Por cada minuto que hemos pasado juntas. Espero poder estar a tu lado siempre, tanto en los momentos malos como en las celebraciones de tus mayores logros. Confía en ti misma, te espera un futuro brillante.

A Pilar, Pylar, Popsi (I’m so sorry). Fuiste para mí un descubrimiento, al principio no pensé que te abrirías tanto con nosotras y que llegaríamos a forjar una amistad. Eres una caja de sorpresas. Echaré mucho de menos la rutina que teníamos de llegar por las mañanas y contarnos lo que habíamos hecho la tarde anterior (y hasta detallar lo que habíamos desayunado); no nos cansábamos nunca y eso que nos veíamos todos los días. Eres la culpable de que se nos hayan pegado tantas expresiones, pero gracias a ello ahora recordaremos con mucho cariño muchos momentos graciosos. Gracias por no dudar nunca en ayudarme con cualquier cosa, por permitirme ser tu compi de paseos, por hacerme descubrir tantas cosas nuevas y por compartir conmigo tu manera de pensar y de ver la vida, he aprendido mucho de ti. Lo que Fresquito y Mango, el amor por la sopa y por los animales, y dos bocaos en la pierna han unido, que nadie nunca lo separe.

Además del grupo, también quiero agradecer a todas las personas que constituyen el departamento de Materiales Multifuncionales y Supramoleculares, en especial a la doctora Marta Iglesias, que me acogió en su despacho cuando me quedaba atascada con los experimentos y tenía dudas. Gracias Marta, por aconsejarme, por estar dispuesta a ayudarme siempre, y por compartir conmigo tus valiosos conocimientos sobre campo de la catálisis.

A los “potsdocs”. Gracias Raúl, por ese buen rollo contagioso. Gracias Ángela, Marcelo y Antonio por la calidez con la que me acogisteis en vuestro “Friday Gourmet Club”

cuando yo era una recién llegada al ICMM, y por compartir vuestros consejos y experiencias.

A “las chicas de arriba”: Ángela, Bea, Mari Carmen y Pilar. Aunque he compartido poco tiempo con vosotras, quería daros las gracias por aguantar que yo fuese tan pesada con el croma (ayyy, el croma) y por ayudarme siempre que subía a preguntaros dudas o a pediros cosas. Os deseo mucha suerte en el futuro.

No me puedo olvidar de la labor de los técnicos del ICMM, ya que ha sido vital para mi tesis, y quería agradecer en especial a Ismael Ballesteros Jiménez. Gracias Ismael, por aguantarme tantas horas (espero haber sido una de las usuarias VIP del SEM), por tu amabilidad (aunque yo te llevase para analizar los mismos cristales cincuenta millones de veces) y por tener siempre una actitud positiva.

Tampoco me puedo olvidar de los estudiantes de prácticas (los “michis”, como los llamábamos cariñosamente): Alba, Laura, Manuel y Agustín. Cuando llegaron al laboratorio, me sentía muy insegura porque era muy nueva en el mundo del doctorado y pensé “cómo iba a encargarse de un estudiante una recién graduada que no tiene ni idea de cómo va la vida ni la ciencia???”, pero han tenido paciencia conmigo y me han ayudado a aprender a guiar a otra persona, a afrontar las responsabilidades que conlleva, a solventar problemas y a organizarme mejor. Michis, gracias por hacerme crecer en el ámbito profesional, os deseo mucha suerte en el futuro.

Quiero agradecer también al grupo del profesor Shuhei Furukawa, en Kyoto, Japón, que me recibió en su laboratorio durante mi estancia predoctoral. *Shuhei, I am deeply grateful to have had the opportunity to work in your lab. I have learnt a lot about the amazing chemistry you do in your lab, thank you for your patience and for sharing all your knowledge with me. It was truly an enriching experience, and your city (and country!) is absolutely beautiful. I would also like to thank Makiko-san for being so kind*

and nice, and for helping me organize the trip. Thank you to all the members of the group for being so warm and welcoming. Thank you, Javi, for guiding me in the lab, for always being so nice to me even though my work wasn't amazing, and for all the advice you've given me. Thank you, Yu-Shan and Xiangmei, for all the time we spent together having fun and eating delicious food.I hope to meet you again in the future. どうもありがとうございました.

Quiero dar las gracias también a las personas de la Universidad Complutense, la universidad que me vio crecer en lo profesional. Al profesor David Ávila Brande, por acogerme en el TFM y despertar mi interés por los MOFs, materiales a los cuales les he dedicado 4 años de trabajo, por enseñarme la oferta de doctorado que se acabó convirtiendo en mi tesis, y por "tutorizarme" en la misma. A mis compañeras de carrera, Cris y Hachi, por todos los momentos vividos.

En los duros años de carrera tuve la suerte de conocer a mi *best friend*, mi TiTa, mi mitocondria azul, la doctora Andrea Canal Martín. Gracias Andrea, por todos estos años en los que hemos crecido juntas, y por todo lo que me has enseñado por el camino. Gracias por saltar a defenderme siempre, por ayudarme siempre que te ha sido posible (y cuando no, también) y por compartir conmigo todo el conocimiento que has adquirido sola (gracias a tu esfuerzo y trabajo constante). Por absolutamente todas las batatitas de estos años: los fresones, las clases de ingeniería química a las que solo asistíamos las dos pero solo atendía (y me mantenía despierta) yo, las peripecias de la Bienal (para empezar ni siquiera aterrizamos en la ciudad correcta, cómo no), cuando fuimos a hablar al profe de redacción (aquel día que temí por mi nota), el tito Seve, las visitas a tu lab, el caos que fue la carrera (y que en vez de separarnos, nos unió mucho más). Por confiar en mí, por escucharme, y por ayudarme siempre en mis momentos malos. Qué suerte tengo de poder tener en mi vida a una persona como tú, genuina, trabajadora, tenaz y leal, que le da el

verdadero significado a la palabra amistad. Por enseñarme que una siempre puede resurgir de sus propias cenizas cual ave Fénix. Disfruta de tu nueva libertad, tengo muchas ganas de ver qué aventuras te depara el futuro, y quiero estar siempre a tu lado para poder vivirlas contigo. Tú y tu familia sois encantadores. ¡Ah! No me puedo olvidar de mencionar a Peque, los tones, y a Pompón (la nueva incorporación a la familia). Todos ellos han sido piezas fundamentales que nos han acompañado durante todos estos años, y nos han hecho reír cuando más lo necesitábamos.

Me gustaría agradecer a los colaboradores que han participado en los estudios realizados para esta tesis, en especial a la doctora Inés Puente-Orench, por su valioso análisis de difracción de neutrones y por haberme acogido en mi visita al ILL, y a la doctora Consuelo Álvarez Galván por su ayuda con la catálisis de los MOFs calcinados. Consuelo, gracias por tu amabilidad y por dedicarme tu tiempo. A lo mejor a ti te parecerá poca cosa el detalle que tuviste conmigo, igual ni te acuerdas, pero yo lo recordaré siempre con mucho cariño.

A la confabulación de cuervas (Pilar, Cris, Celegé y Sam), por las infinitas risas, y esos viajes tan intensos. *Oh là là, les chevaliers.*

A mis amigos de toda la vida, los Pistachos: Sergio, Tamara, Javi y Andrea. Gracias por tantas aventuras juntos, por aguantarme, y por vuestro cariño. Esta dura etapa de mi vida ha sido más llevadera gracias a los ratos que he pasado con vosotros. *"Son, mis amigos, en la calle pasábamos las horas. Son, mis amigos, por encima de todas las cosas".*

Por último, una mención especial a mi familia no humana: Gravity, Newton y Nami. Cómo no iba a agradecer a mis gatos, su labor a la hora de analizar y validar el trabajo que he realizado para la comunidad científica ha sido crucial (cotillear y mirar

fijamente absolutamente todas las pantallas/papeles). Su criterio ha sido muy valioso a la hora de tomar decisiones y de publicar trabajos (las cosas que acababan tiradas al suelo sencillamente no estaban a la altura).

A los que hayáis llegado hasta el final de este extenso apartado, y a los que se hayan leído esta tesis doctoral completa, solo me queda deciros que…

Os estoy infinitamente agradecida a todos

∞

Table of Contents

Resumen

Las redes metal-orgánicas (en inglés, *Metal-Organic Frameworks*, MOFs) constituyen un campo relativamente nuevo de la química de materiales. El desarrollo de estos materiales ha sufrido un crecimiento exponencial desde su creación en la década de los 90, y en gran parte se debe a estrechan la brecha existente entre dos campos de la química que siempre se han mantenido independientes: la química inorgánica y la orgánica. Los MOFs son materiales que presentan una estructura cristalina que surge de sinergia entre la combinación de moléculas orgánicas (en inglés, *linkers*) y de unidades inorgánicas que pueden ser centros metálicos o un clúster de estos (en inglés*, Secondary Building Units, SBU*). Por tanto, las características intrínsecas de los dos tipos de unidades de construcción (composición, geometría, conectividad, reactividad) brindan a estos materiales de una gran riqueza estructural y química. Esta versatilidad será una de sus características clave ya que permite extender sus aplicaciones a un amplio abanico de posibilidades: catálisis, adsorción y separación de gases, almacenamiento de energía, aplicaciones biomédicas.

Los MOFs son responsables del auge de la química reticular, ya que permitieron desarrollar la química más allá de la molécula (0-1 dimensiones) y así explorar y ampliar la diversidad estructural de estructuras extendidas en dos y tres dimensiones. Las propiedades químicas, físicas y estructurales de un MOF dependen de la composición de su SBU, por lo tanto, mediante la modulación de estas SBUs es posible dotar al MOF de las características deseadas, y "diseñarlo a medida" para una aplicación concreta. Con el afán de ir más allá de una red sencilla y optimizar las propiedades de estos materiales multifuncionales, en los últimos años se ha ido introduciendo el concepto de heterogeneidad. Mediante la combinación de varias SBUs con la misma geometría y

conectividad, pero diferente composición en posiciones topológicamente equivalentes, es posible introducir cierto grado de heterogeneidad dentro del "orden" o periodicidad de la red. El material multimetálico resultante contará con las ventajas de la combinación de los cationes metálicos que lo componen, y generalmente estos materiales presentan una mejora de algunas propiedades respecto a sus versiones monometálicas. Aunque existen diferentes estrategias para insertar dos o más cationes metálicos en una misma red (síntesis en un paso o "*one-pot*" en inglés; intercambio de metales post-sintético; uso de metaloligandos; uso de unidades preformadas), no es un asunto trivial dado que es difícil predecir la distribución de estos metales a nivel atómico y mesoscópico. Resulta fundamental comprender los mecanismos de síntesis y cristalización de un MOF para poder controlar y dirigir la distribución de los cationes y así generar materiales con una composición concreta.

Por tanto, el trabajo de investigación de esta Tesis Doctoral, que lleva por título "Redes metal-orgánicas complejas con secuencias de metales para catálisis heterogénea" está enfocado en estudiar qué metales se pueden combinar en un mismo MOF, si se puede conseguir cualquier combinación y composición deseada, y cuáles son los factores determinantes que dictan la distribución de dichos metales. Igualmente, siguiendo esta línea, se buscó demostrar si mediante la combinación de distintos metales en una misma estructura es posible sintetizar materiales que incluyan elementos con gran potencial que hasta ahora permanecían escasamente explorados en la química de los MOFs. También, como objetivo secundario, se ha estudiado la posibilidad de transferir determinadas secuencias de metales a otros sólidos, como los óxidos derivados a partir de MOFs.

Se escogió una familia de MOFs con una SBU lineal basada en elementos de tierras raras, *Rare-Earth Polymeric Framework-4* (**RPF-4**), como plataforma para llevar a cabo el estudio de la inserción de combinaciones binarias de metales. Se consideró la relevancia

de estudiar primero las muestras monometálicas dado que, aunque la estructura cristalina sea compatible con toda la serie de los lantánidos, se desconoce el efecto del mecanismo de cristalización sobre la morfología de los cristales. En esta primera etapa del estudio se comprobó que, una vez formados, los cristales de RPF-4 basado en lantano sufren una redisolución de la parte central y una posterior cristalización en las caras externas, lo cual les lleva a presentar canales en el plano basal. Al pasar a las combinaciones binarias, se observó que, aunque el análisis del bulk de las muestras indica una composición homogénea y con la proporción deseada, un estudio exhaustivo de cristales individuales señala que las combinaciones de otros metales con lantano dan lugar a una segregación de fase, y esto se debe a la compleja interacción entre factores cinéticos y termodinámicos de los mecanismos de cristalización. Este estudio pone en evidencia la importancia que tiene comprender cómo cristaliza una determinada estructura para poder controlar la distribución de metales de diferente naturaleza en las SBUs. Tras haber adquirido conocimientos sobre cómo funciona el sistema multimetálico RPF-4, se ha evaluado el efecto de las secuencias de metales sobre el comportamiento magnético de las muestras, y también se han tratado térmicamente estos materiales con el fin transferir sus secuencias de metales a otros materiales, en este caso óxidos que han sido utilizados como catalizadores heterogéneos.

Por otra parte, con el fin de insertar iridio en MOFs, se han llevado a cabo varios experimentos de combinaciones de iridio con metales de diferentes grupos de la tabla periódica. Se ha comprobado que, en las condiciones probadas, el iridio no era compatible con los sistemas escogidos. Finalmente, mediante una estrategia multimetálica en un solo paso, usando indio o escandio y un ligando con dos grupos funcionales distintos, se ha conseguido dirigir la coordinación de cada metal y reticular el iridio, obteniendo así la familia de MOFs multimetálicos basados en iridio, llamada **MIrPF-13** (*Iridium*

Polymeric Framework-13, con M = Sc, In). La relevancia de esta nueva familia de MOFs radica en que se ha conseguido incorporar nuevos centros metálicos activos y expandir el rango de reactividad que se puede conseguir con los MOFs.

Summary

Metal-organic frameworks (MOFs) are a fairly new field of materials chemistry. The development of these materials has undergone an exponential growth since their creation in the 1990s, mainly because they bridge the gap between two fields of chemistry that have always been independent: inorganic and organic chemistry.

MOFs are materials that display a crystalline structure arising from the synergy between the combination of organic molecules (linkers) and inorganic units that can be metal centers or a cluster (secondary building units, SBUs). Therefore, the intrinsic characteristics of the two types of SBUs (composition, geometry, connectivity, reactivity) provide these materials with a great structural and chemical diversity. This versatility is one of its hallmarks, as it allows extending its applications to a wide range of possibilities: catalysis, gas adsorption and separation, energy storage, biomedical applications.

MOFs are responsible for the rise of reticular chemistry, as they allowed the development of chemistry beyond the molecule (0-1 dimensions) and thus explore and expand the structural diversity of extended structures in two and three dimensions. The chemical, physical and structural properties of a MOF depend on the composition of its SBU, therefore, the modulation of these SBUs provides the MOF with the desired characteristics, and allows to "tailor" its characteristics for a specific application. In the quest of going beyond a simple framework and optimizing the properties of these multifunctional materials, the concept of heterogeneity has been implemented over the last few years.

When combining several SBUs with the same geometry and connectivity, but different composition in topologically equivalent positions, a certain degree of heterogeneity within the "order" or periodicity of the lattice can be induced. The resulting multi-metal material will benefit from the advantages of the different metal cations of the

combination, and generally these materials present an enhancement of some of their properties when compared to their single-metal counterparts. Although there are different strategies to insert two or more metal cations into the same framework (one-pot synthesis; post-synthetic metal exchange; use of metalloligands; use of preformed units), it is not a trivial matter since it is difficult to predict the distribution of these metals at both atomic and mesoscopic levels. It is crucial to understand the synthesis and crystallization mechanisms of a MOF in order to control and direct the distribution of the cations and generate materials with a specific composition.

Thus, the research work carried out in this Doctoral Thesis, titled "Complex metal-organic frameworks with sequences for heterogeneous catalysis" is focused on studying which metals can be combined in the same MOF, whether any desired combination and composition can be achieved, and what are the determining factors that dictate the distribution of these metals. Following this line, this work also seeks to demonstrate whether it is possible to synthesize materials based on metal atoms with significant potential that until now have remained unexploited in the chemistry of MOFs by using combinations of different metal elements. Also, as a secondary objective, the possibility of transferring certain metal sequences to other solids, such as MOF-derived oxides, has been evaluated.

A family of MOFs with a rare-earth rod-shaped SBU, Rare-Earth Polymeric Framework-4 (**RPF-4**), was chosen as a platform to carry out the study of the insertion of binary metal combinations. Although the crystal structure is compatible with the whole lanthanide series, it is relevant to first study the monometallic samples, as the effect of the crystallization mechanism on the morphology of the crystals is unknown. This first stage of the study revealed that, once formed, the lanthanum-based RPF-4 crystals undergo a redissolution of the central part and a subsequent crystallization on the external faces,

which leads them to present channels along the basal planes. When moving to binary combinations, although the bulk analysis of the samples point to a homogeneous composition with the desired ratio, a thorough study of single-crystals indicates that combinations of other metals with lanthanum result in a phase segregation, and this is due to the complex interplay between kinetic and thermodynamic factors of the crystallization mechanisms. This study highlights the importance of understanding the crystallization mechanism of a structure in order to control the distribution of metals of different nature within the SBUs. After having acquired knowledge on how the RPF-4 multi-metal system works, the effect of the metal sequences on the magnetic behavior of the MOFs was evaluated, and these materials have also been thermally treated in order to transfer their metal sequences to other materials, in this case MOF-derived oxides that have been used as heterogeneous catalysts.

On the other hand, in order to insert iridium atoms into MOFs, several experiments have been carried out with combinations of iridium with metals from different groups of the periodic table.

In the conditions tested, the experiments demonstrated that iridium was not compatible with the chosen systems. Finally, through of a one-pot multi-metal strategy, by using indium or scandium and a ligand with two different functional groups, it has been possible to direct the coordination of each metal and reticulate the iridium atoms, thus obtaining the family of iridium-based multi-metal MOFs **MIrPF-13** (Iridium Polymeric Framework-13, with M = Sc, In). The relevance of this new family of MOFs lies in the fact that new active metal centers have been incorporated into frameworks and the range of reactivity that can be achieved with MOFs has been expanded.

List of abbreviations and acronyms

BET	Brunauer-Emmett-Teller
bipy	2,2'-bipyridine
BTB	1,3,5-Tris(4-carboxyphenyl)benzene
DFT	Density function theory
DMA	Dimethylacetamide
DMF	Dimethylformamide
EA	Elemental Analysis
EDX	Energy dispersive X-Ray Spectroscopy
EtOH	Ethanol
Hfipbb	4,4′-(Hexafluoroisopropylidene)bis(benzoic acid)
IRMOF	Isoreticular Metal-organic framework
IUPAC	International Union of Pure and Applied Chemistry
MOF	Metal-Organic Framework
MTV-MOF	Multivariate Metal-Organic Framework
NPD	Neutron powder diffraction
PXRD	Powder X-Ray Diffraction
RPF-4	Rare-Earth Polymeric Framework-4
RWGS	Reverse Water Gas Shift
SBU	Secondary Building Unit
SCXRD	Single-Crystal X-Ray Diffraction
SEM	Scanning Electron Microscopy
TGA	Thermogravimetric analysis
TXRF	Total X-Ray Fluorescence Spectroscopy
ZIF	Zeolitic imidazolate Framework

─ CHAPTER 1 ─

Introduction

1.1. Metal-Organic Frameworks (MOFs): the best of both worlds

Over the last decades, we have witnessed the exponential development of a new class of materials: Metal-Organic Frameworks (MOFs). In 2013, the IUPAC (International Union of Pure and Applied Chemistry) determined that the term Metal-Organic Framework or MOF comes very close to a self-definition, however, according to the IUPAC a MOF is "a coordination network with organic ligands containing potential voids", and a coordination network is "a coordination compound extending through repeating coordination entities in 2 or 3 dimensions".[1,2] So, a MOF is a potentially porous material that displays a crystalline structure arising from the combination of an organic building unit (organic linker) and an inorganic building unit called secondary building unit (SBU).[3] The inorganic SBU can either be a single metal or a cluster (dimers, trimers, polynuclear clusters, chains, rings). This term, defined and used for the first time by Yaghi *et al.* in 1995,[4] was the turning point in the development of MOF chemistry as it contributed to the design of robust crystalline materials with predetermined structures and properties through the control of the geometry and connectivity of the SBUs.

Versatility is the hallmark of MOFs, and it is the result of their wide structural and chemical diversity, and also of their applicability in a variety of fields, such as catalysis,[5,6] gas sorption and separation,[7] water decontamination,[8,9] water harvesting,[10] energy storage,[11] optics,[12] biomedicine[13,14] and magnetism.[15,16]

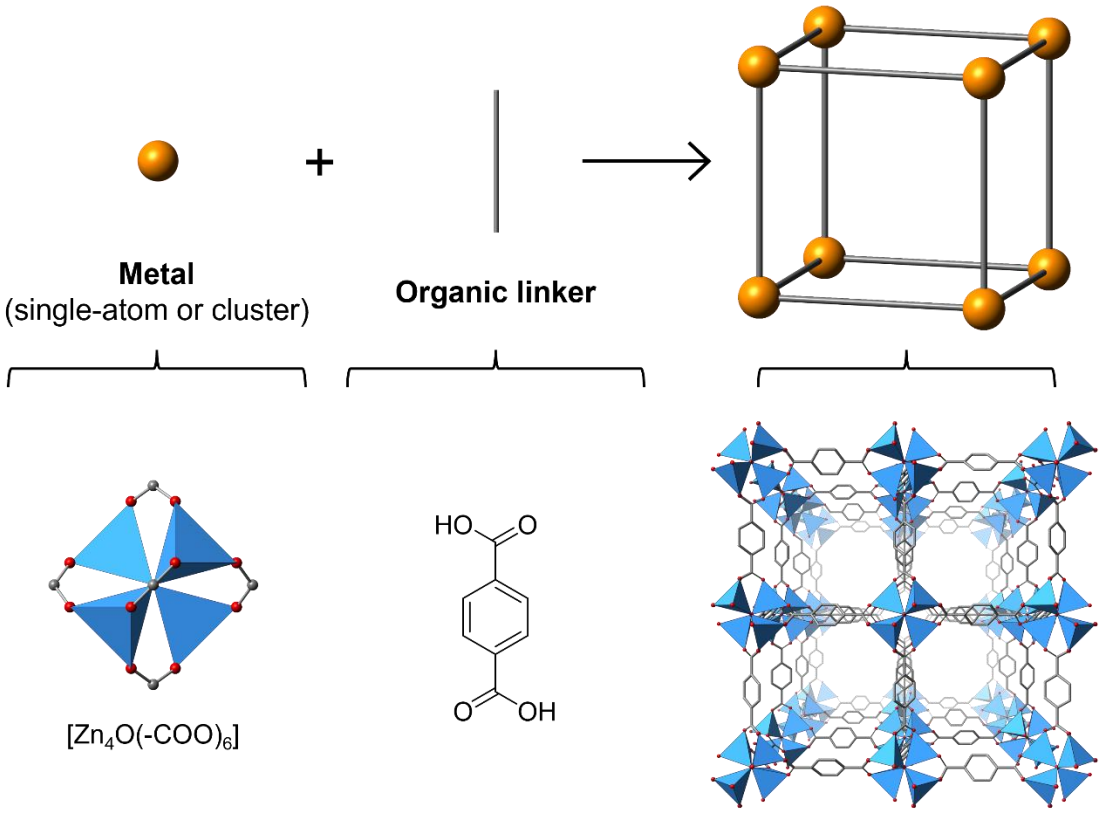

Figure 1.1. Schematic representation of the building units of a MOF. From left to right, inorganic and organic building units are combined to generate extended structures.

1.1.1. Historical context: How MOFs emerged

In order to elaborate more on these materials, we must first understand their origins and even reach back to the earliest reported coordination compounds. During the XX century, coordination chemistry underwent a breakthrough as many theories such as Werner's coordination theory[17] or Lewis' concept of acids and bases[18] emerged, and the behavior and the structure of already existing complexes began to be comprehended. This laid the foundations of modern coordination chemistry and sparked the beginning of its development. Classic coordination compounds such as Prussian blues, $Fe_4^{3+}[Fe^{2+}(CN)_6]_3 \times H_2O$,[19] or Hofmann clathrates, $[Ni(CN)_2(NH_3)](C_6H_6)$,[20] are considered forerunners to MOFs. When they first were discovered, not much was known

about their structure as they were thought to be molecular compounds and conclusions about their behavior were exclusively based on phenomenological observations. Later on, crystallographic techniques revealed that these compounds actually displayed a crystalline extended coordination structure.

In 1959, Saito and coworkers designed an array of crystalline materials based on tetrahedral Cu^{+} ions coordinated to nitrile linkers.[21] In their study, the authors presented 1D, 2D, and 3D structures generated with linkers of different lengths. The structures that Saito *et al*. reported are supported by rather weak non-covalent interactions (in this case, metal-N donor interactions), which implies that the loss of the guest molecules causes the structures to collapse.

In the late 1980s, Iwamoto *et al.*[22] and Hoskins and Robson[23,24] described the formation of coordination networks with diamond topology, directed by the coordination geometry of the selected metal cations (Cd^{2+} and Cu^{+}, respectively). These are among the first reports where coordination networks are described based on their topology, in a manner equivalent to how Wells described the crystal structures of inorganic solids,[25] in terms of nets based on nodes and links. These reports already illustrated the possibility of increasing the chemical versatility through the variations in the inorganic and organic moieties.

It was not until a few years later, in 1995, when the term metal-organic framework, MOF, was first coined by Yaghi *et al.*,[4] when describing the overall composition (metal ions and organic linkers) and character of the structure (framework) of $[Cu(bipy)_{1.5}](NO_3)$, constituted by trigonal planar Cu^{+} ions and linear 4,4'-bipyridine linkers. In the subsequent years, the term MOF also started alluding to additional structural features and properties, such as structural rigidity and stability and permanent porosity.

A few years later, in 1997, Kitagawa *et al*. reported a material based on the same linker, 4,4'-bipyridine, but with Co, Ni and Zn as metal ions.[26] In this case, the 3D structure displays a complex distribution of channels and cavities, and was able to absorb gases in a reversible fashion with no structural deformation in a pressure range of 1-36 atm and at a temperature of 298 K, displaying a type I adsorption isotherm. This report was the first coordination polymer that displayed a porous behavior, although microporosity was not evidenced as it can only be determined with low pressure sorption measurements.

A year later, in 1998, Yaghi *et al*. reported the synthesis of MOF-2, with formula $[Zn(BDC)](H_2O)(DMF)$, a structure constituted by benzenedicarboxilic acid (H_2BDC) and Zn^{2+} ions.[27] The special feature of this structure is that the zinc ions generate a polynuclear cluster node, specifically dimeric $[Zn_2(\text{-}COO)_4]$ paddlewheel units that are bridged by BDC linkers creating a square lattice. The polynuclear nodes provide the structure with architectural stability as the metal ions are forced in a particular position and direction within the network, and the charge of the linker molecules increased the strength of the bonds and lead to an overall charge neutrality of the framework. Owing to this structural robustness, it was possible to extract all the solvent molecules without any framework deformation, leading to the first record of a type I N_2 isotherm at 77K in the P/P_0 range of 0 to 1 for a coordination compound.

A turning point for the field of porous coordination materials happened shortly after, in 1999, when two MOFs that displayed unprecedentedly high values of accessible surface area were presented. Firstly, Williams *et al*. reported a material named HKUST-1 (Hong Kong University of Science and Technology-1), with formula $[Cu_3(BTC)_2(H_2O)_3]_n$, constituted by 1,3,5-benzenetricarboxylic acid (H_2BTC) and Cu^{2+} paddlewheel units.[28] This 3D MOF displays a pore size of 1 nanometer and an accessible permanent porosity corresponding to about 40% of the solid, with a Brunauer–Emmett–Teller (BET) surface

area of 692 m^2g^{-1}, and the framework is stable up to 240 ºC. Another interesting feature of this material is that the pores can be chemically functionalized as the authors demonstrated that the water molecules connected to the Cu paddlewheels can be replaced by pyridines. A few months later, Yaghi and coworkers presented MOF-5, $[Zn_4O(BDC)_3](DMF)_x$, constituted by Zn-based clusters and 1,4-benzenedicarboxylic acid (BDC) as a linker. In this case, the inorganic octahedral $[Zn_4O(-COO)_6]$ clusters consist of four tetrahedral ZnO_4 units sharing a common vertex, bridged by ditopic BDC linkers, generating a 3D framework. The combination of the size and high connectivity of the clusters and the organic linker leads to an open porous structure (61% of the unit cell volume is accessible porosity) that facilitates diffusion of guest molecules. MOF-5 displays a high thermal stability (up to 300 ºC), and a very high N_2 uptake (BET area = 2500 m^2g^{-1}) that exceeded the values displayed by other traditional microporous materials such as zeolites. It was in this report where the authors implemented the SBU strategy: using polynuclear clusters to lock in place the metal ions via the binding groups of the organic linkers, and thus target a particular structure topology.

This approach based on linking molecular building blocks by strong bonds to generate extended crystalline structures is now widely known as reticular chemistry,[29] and it is the cornerstone in the expansion of both coordination and organic chemistry from zero and one-dimension (molecules and polymers), to infinite 2D and 3D with a diversity and tunability that until that moment was not known in traditional chemistry. From this point on, and given the success of reticular chemistry, the field of MOFs has undergone exponential growth, and is now being studied in laboratories in all over the world.[30]

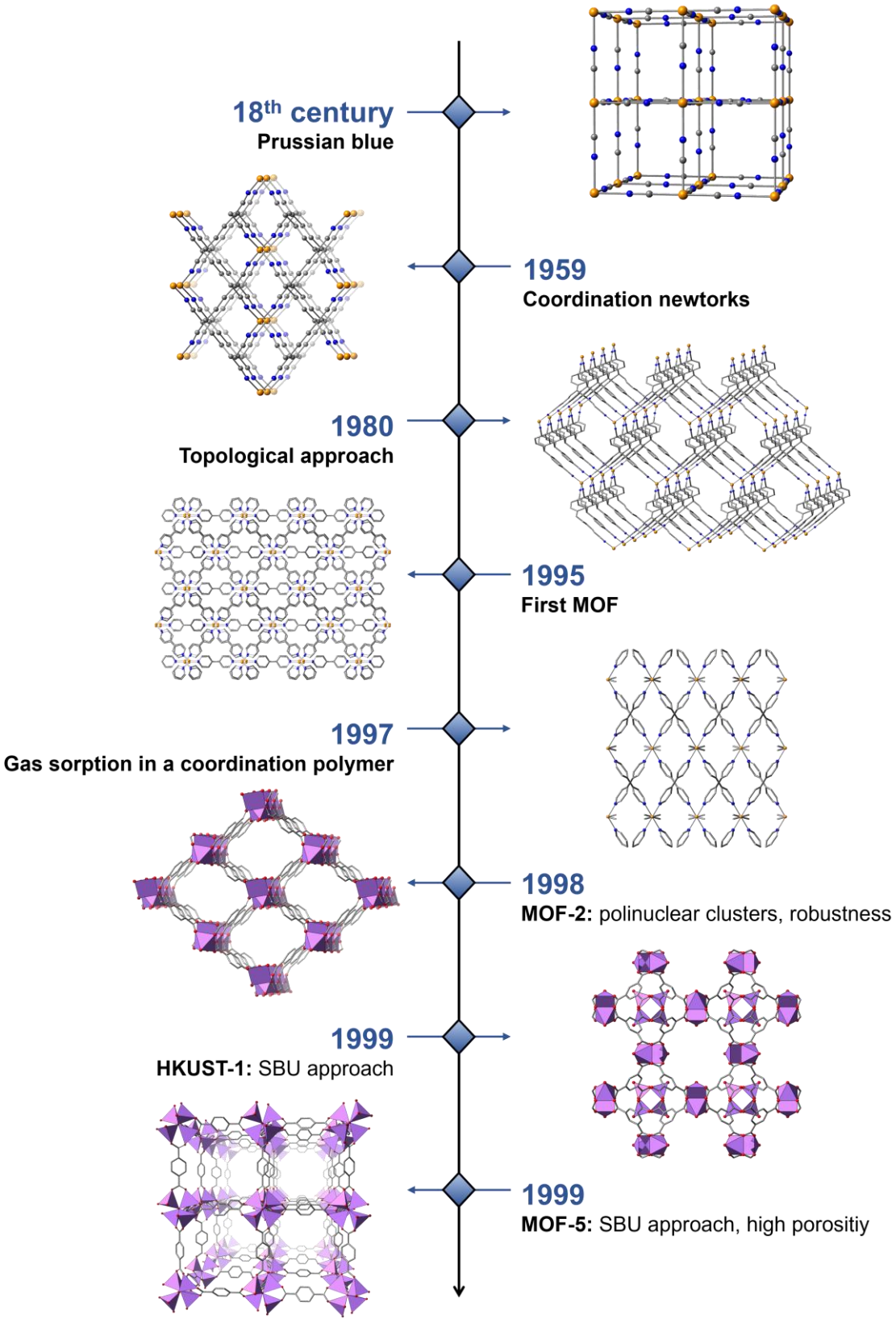

Figure 1.2. Chronological scheme of the major events that contributed to the early development of MOFs.

1.1.2. Reticular synthesis of MOFs

As mentioned in the previous section, the first reports of coordination networks described them based on their topology, following the principles of crystal chemistry established by Wells.[25] The system that Wells defined consists in describing crystals structures in terms of nets constructed form nodes or vertices and links or edges (topology), considering only the connectivity and not the chemical information, thus simplifying them. The nomenclature used to define net topologies consists in using a three-letter code, generally corresponding to naturally occurring minerals of that specific topology (for example diamond, **dia**), but newly reported topologies can have arbitrarily assigned letters.

The concept of underlying topology is crucial in MOF chemistry as it helps design and access new structures based on almost infinite combinations of different of linkers and SBU types.[31] The isoreticularity principle stemmed from the fact that the structure and properties of a MOF can be altered without changing their underlying topology. This principle has been applied to expand the pore size of a MOF and unlock ultrahigh porosity. The most straightforward way of enlarging the pores of a framework is to use linkers of a greater length, but with the same functional groups and connectivity, thus maintaining the same geometry as the initial parent MOF. This is the strategy that Yaghi *et al*. followed to enlarge the pore of the archetypal parent MOF-5 and generate a series of up to 16 isoreticular MOFs (IRMOF) with the same topology (**pcu** in this case).[32] Not only does this strategy work for systematically enlarging the pore size of a MOF, but also for tuning the pore environment, as the authors demonstrated in the same study by using functionalized versions (–Br, $–OC_3H_7$, $–OC_5H_{11}$, $–C_2H_4$, $–C_4H_4$) of the same 1,4-benzenedicarboxylate (BDC) linker.

The isoreticular expansion principle can also be applied to finely tune the pore aperture of a MOF in order to selectively include specific large molecules (vitamin B12) or proteins without them unfolding.[33]

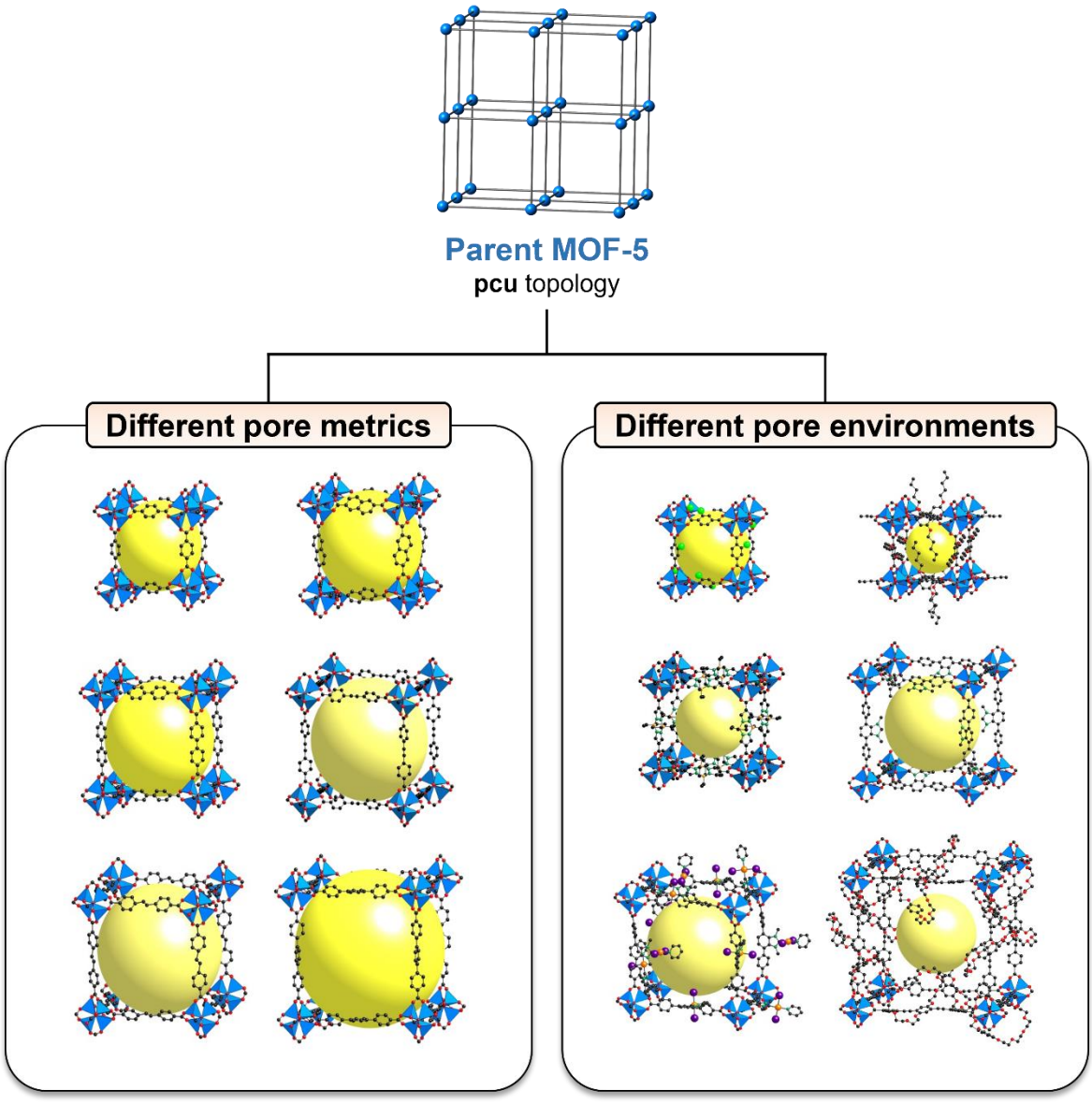

Figure 1.3. Schematic representation of the isoreticularity principle applied to MOF-5 (**pcu** topology) as a parent structure.

1.2. Complexity within the frameworks: multicomponent MOFs

In the early years of MOFs, the field of reticular chemistry was mainly concerned with making the frameworks more thermally, architecturally, and chemically stable. As years went by and progress was made, reticular chemists went beyond the typical "one metal and one linker" synthetic strategy. As already mentioned in this chapter, a high chemical and structural tunability is the main advantage of MOFs. With this in mind and also striving to expand the range of properties, reticular chemists are shifting towards exploring more sophisticated concepts such as MOFs that embrace higher chemical and structural complexity. Thus, complexity within frameworks is achieved by combining more than two types of different building units with specific crystallographic positions, therefore the components are arranged and repeated throughout the lattice with strict periodicity.[34] These building units can be either different organic linkers, different types of SBUs, or a combination of both.[35]

An early example of a mixed-linker MOF is UMCM-1, $[Zn_4O(BDC)(BTB)_{4/3}]$.[36] This MOF is a ternary system comprised by Zn^{2+} ions, the linear ditopic linker H_2BDC and the trigonal tritopic linker H_3BTB (H_3BTB = 1,3,5-tris(4-carboxyphenyl)benzene), with a **muo** topology. The outcome of the synthetic pathway of this MOF directly depends on the ratio between the linkers. An excess of H_3BTB generates MOF-177 ($[Zn_4O(BTB)_2]$, **qom** topology),[37] and an excess of H_2BDC generates MOF-5 ($[Zn_4O(BDC)_3](DMF)_x$, **pcu** topology). The multicomponent MOF UMCM-1 can only be obtained with ratios ranging from 6:4 to 4:6, therefore this illustrates the significance of finding a perfect balance between the elements that will generate the system, especially because of the degree of unpredictability that a mixture of several building units can induce.

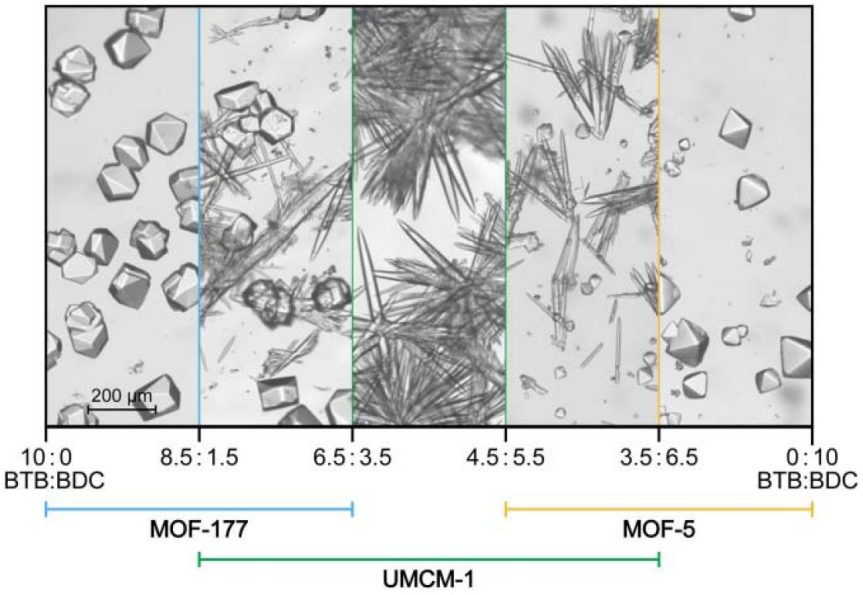

Figure 1.4. Schematic representation of the correlation between the $H_3BTB:H_2BDC$ ratio and the formation of different MOF phases. The SEM images of the crystals of each sample showcase the scenarios of phase coexistence or phase purity. Reprinted with permission from reference [34].

An effective strategy to obtain complex heterometallic MOFs is a cluster cooperative approach, as evidenced by Sun *et al.* [38] The authors used isonicotinic acid (INA) to generate a multi-metal MOF, MTM-1, through the cooperative assembly of hexameric Ti clusters $[Ti_6O_6][iPrO]_6^{6+}$ and Cu_2I_2 dimers. The most striking feature of this MOF is that the resulting hexagon-shaped $\{[Ti_6O_6][iPrO]_6[INA]_6\}$ units are connected together by 24 Cu clusters, generating a octahedral sodalite supercage.

Reaching a high degree of complexity does not necessarily entail having to use a lot of building units. Li *et al*. combined only the ditopic linker 4-pyrazolecarboxylic acid (H_2PyC) with Zn and Cu nitrates in a simple solvothermal reaction to afford single crystals of $[(Zn_4O)_5(Cu_3OH)_6(PyC)_{22.5}(OH)_{18}(H_2O)_6][Zn(OH)(H_2O)_3]$, FDM-3 (Fudan Materials-3).[39] This structure displays three geometrically and compositionally different

types of SBUs: a triangular [$Cu_3(OH)(PyC)_3$] cluster; octahedral [$Zn_4O(COO)_3R_3$] nodes where R = –COO or –NN in PyC, distributed in four possible combinations; square-pyramidal [$Zn_4O(COO)_4R$] nodes with R = –COO or –NN in PyC, distributed in two possible combinations. Also, the framework of FDM-3 is composed of four types of cages (two microporous and two mesoporous), and contains a total of 28 microporous and 11 mesoporous cages per unit cell. So, this example illustrates that both high complexity and high porosity (surface area of 2585 m^2g^{-1}) can be combined in the same MOF structure without the need of using a high number of building elements.

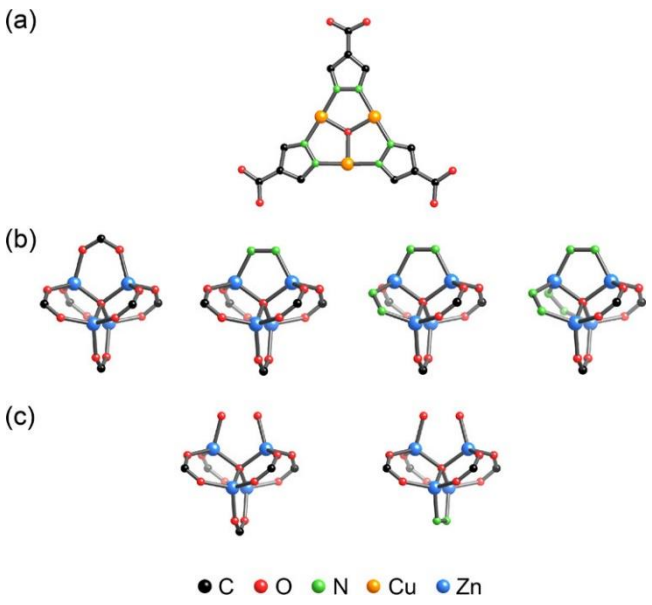

Figure 1.5. Schematic representation of the SBUs of FDM-3. **a)** triangular clusters [$Cu_3(OH)(PyC)_3$], **b)** octahedral [$Zn_4O(COO)_3R_3$] (R = –COO or –NN), **c)** square pyramidal [$Zn_4O(COO)_4R$] (R = –COO or –NN). Reprinted with permission from reference [39].

1.3. Introducing heterogeneity: Multivariate MOFs

In the quest of going beyond a simple MOF structure and with the aim of turning these materials into multifunctional platforms with optimized properties, reticular chemists have gravitated towards the concept of heterogeneity. Heterogeneity within frameworks is achieved by combining multiple linkers with the same connectivity and length and bearing different chemical functionalities, or metal ions that form the same SBU into the backbone of a MOF. As the new elements are introduced in topologically equivalent positions, the overall topology and network connectivity is not altered, therefore the parent structure is transformed into a multivariate MOF (MTV-MOF).[34]

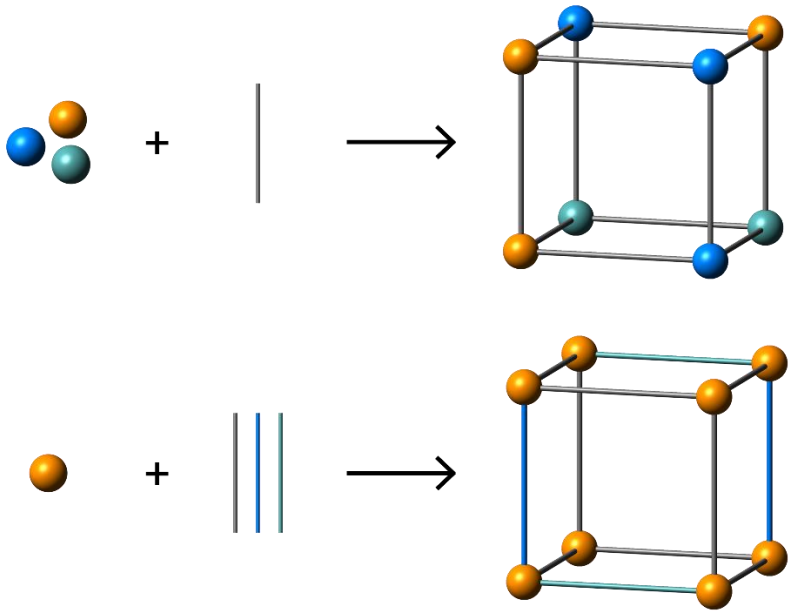

Figure 1.6. Schematic representation of **(up)** a multi-metal MTV-MOF and **(down)** a multi-linker MTV-MOF. Metal nodes are represented as blue, orange and green spheres; organic linkers are displayed as black, blue and green sticks.

However, this heterogeneity comes with a challenge, and that is determining the outcome of the distribution of the building blocks at both atomic and mesoscopic levels. When combining two different building blocks in the same framework, different distribution scenarios can occur, which are strongly directed by the compatibility between the building elements and the target framework. If the building blocks display a similar chemical behavior, the result will likely be a MTV-MOF with an even composition. However, if there is a preferential incorporation of one building block over the others, different distribution scenarios can occur (Figure 1.7): complete segregation (the elements do not coexist in the same framework), partial segregation (coexistence of frameworks with compositions rich in one building block), formation of domains within the structure, core-shell architecture, or sequencing.

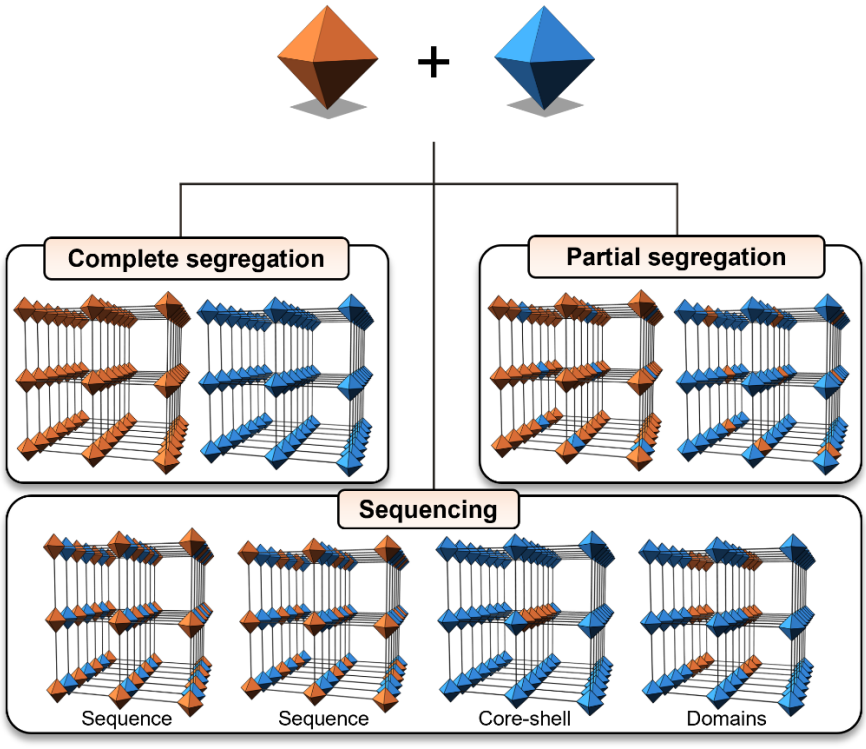

Figure 1.7. Representation of the different distribution scenarios that can occur when mixing two building blocks (represented in orange and blue).

Elucidating the distribution of the building units within a framework is not a trivial matter. In many cases, X-ray diffraction techniques cannot distinguish between metal atoms with similar atomic numbers, or even between organic linkers with different functional groups, which are present with partial occupancies. So, many scientists resort to using a combination of techniques, like in the case of the study presented by Reimer, Yaghi *et al*. in which a 3D mapping of the distribution of the organic linkers in MTV-MOF-5 was carried out by using a combination of molecular simulations and multidimensional solid-state nuclear magnetic resonance.[40] In a more recent report, Li, Yaghi *et al*. determined the sequencing of metals within the SBUs of MTV-MOF-74 by using a more sophisticated technique, in this case atom probe tomography.[41]

1.3.1. Multi-linker MTV-MOFs

MOF-5, which was already mentioned in this chapter, was the object of study of the first report of a MTV-MOF. In this report, Yaghi *et al*. synthesized an array of isostructural MTV-MOF-5 samples by using combinations of up to eight differently substituted versions of the linker H_2BDC.[42] An issue here was that the distribution of the different linkers within the framework could not be determined by diffraction techniques, and this is the reason why the authors turned to a combination of solid-state MAS NMR and molecular dynamic simulations. They found that the distribution of the different functionalized linkers within the framework highly depends on their chemical nature. Additionally, these particular distributions generate a complex pore environment that leads to a nonlinear enhancement of the properties. The authors found an 84% increase in the H_2 uptake for the MTV-MOF-5 containing the combination of NO_2-BDC, $(OC_3H_5)_2$-BDC, and $(OC_7H_7)_2$-BDC. Additionally, the same sample displayed an enhancement of 400% in the selective adsorption of CO_2 compared to the parent MOF-5.

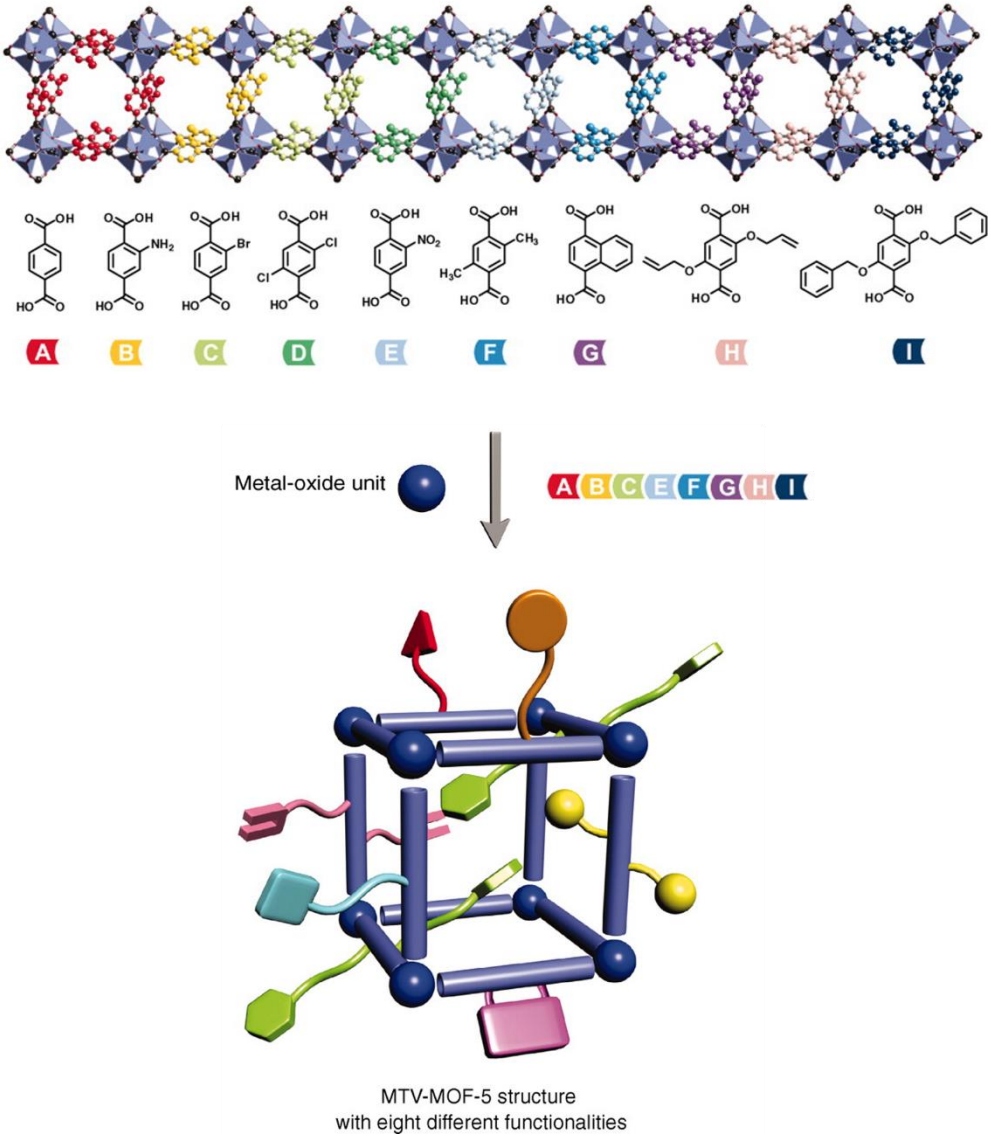

Figure 1.8. From A to I, linkers used to generate combinations of multi-linker MTV-MOF-5. Up to 8 linkers (A-B-C-E-F-G-H-I) were combined in the same multivariate framework. Adapted from reference [42].

If the one-pot combination of different linkers is not viable, it is still possible to obtain MTV-MOFs by means of other synthetic approaches. For instance, Martí-Gastaldo, Padial *et al.* synthesized a multivariate version of UiO-68 (Universitetet i Oslo-68) containing both its original linker, H_2TPDC ([1,1′:4′,1″-terphenyl]-4,4″-dicarboxylic

acid) and a tetrazine derivative, H_2TZDC (4,4′-(1,2,4,5-tetrazine-3,6-diyl)dibenzoic acid).[43] In this case, since the MTV-MOF could not be obtained through a one-pot synthesis, the authors carried out a linker exchange reaction by using single crystals of the parent UiO-68 as a template. The reaction time was a particularly crucial factor that directed the overall distribution of the tetrazine linker in the MOF. While a thermodynamically controlled diffusion led to a homogeneous distribution, a more kinetically controlled linker diffusion generated core-shell architectures which proved to improve the overall photocatalytic performance of the material.

1.3.2. Multi-metal MTV-MOFs

The combination of multiple cations within the same framework is fairly unexplored when compared to the multi-linker MTV-MOFs. One reason behind this is that the synthesis of multi-metal MTV-MOFs is not as straightforward, as mixing different chemical elements inevitably brings about different reactivities, and it also comes with a few shortcomings. Firstly, some metals display intrinsic difficulties, like the case of titanium salts, which tend to generate amorphous phases due to their high reactivity in solution.[44] As the metal elements of the periodic table display different ionic radii, acidity, polarizing power, lability and coordination geometries, it is challenging to find a combination of metals with a perfect balance and compatibility with the connectivity of the target MOF. The computational study of Coudert *et al.* shines light on the cation distribution of heterometallic MOF-5 with different metal combinations.[45] The authors found that if cations with similar iconic radii (Zn-Mg) coexist in the same SBU, intra-cluster charge transfer occurs between them which seems to stabilize the system. A size mismatch (Zn-Cd, Ca-Mg, Be-Mg) induces local strains which are alleviated by the organic linkers; however this might result in a positive mixing energy meaning that the

system is energetically unfavorable. When faced with combinations of metals in which both effects have comparable importance, the MOF system can either benefit from them if they interact in a cooperative manner (Zn-Ca), or undergo detrimental structural hinders if the interaction is competitive (Cd-Mg).

Despite these challenges, a series of approaches are widely used to generate multi-metal MTV-MOFs (Figure 1.9.), and they will be explained in the following sections.

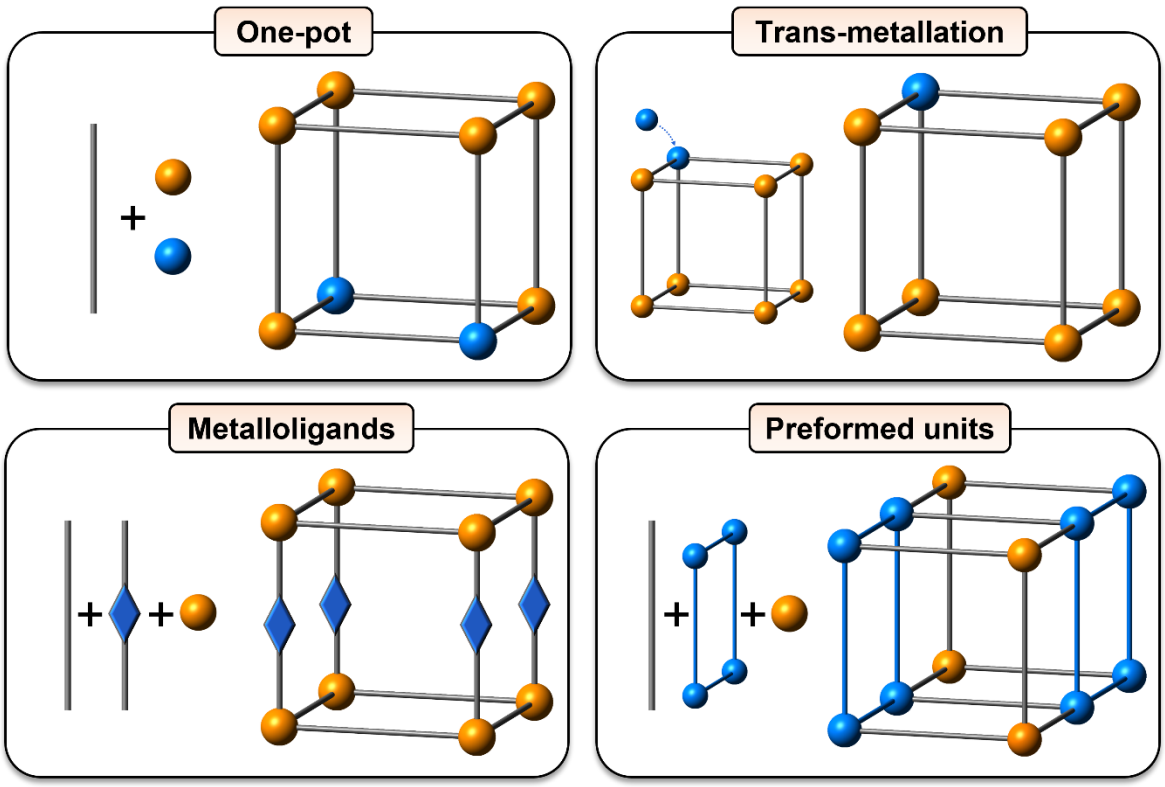

Figure 1.9. Representation of the different strategies to obtain multi-metal MTV-MOFs. Metal ions are represented as blue and orange spheres, linkers as black sticks, metalloligands as black sticks with a blue rhombus.

1.3.2.1. One-pot synthesis

A one-pot synthetic approach is the most direct strategy to obtain a multi-metal MTV-MOF, as it consists of combining several metal precursors during the synthesis of the MOF. One of the advantages of this strategy is that many metal ions can be incorporated into a target MOF if there is compatibility between the metals, the synthetic procedure and the framework. The case of MTV-MOF-74 is an illustration of this, as combinations of 2, 4, 6, 8 and up to 10 metals (Mg, Ca, Sr, Ba, Mn, Fe, Co, Ni, Zn, and Cd) were straightforwardly inserted into the framework through one-pot solvothermal reactions.[46] Additionally, one striking fact is that this strategy also facilitated the incorporation of particular metals (Ba, Sr and Ca) that were not able to generate the single-metal parent MOF. However, ICP and EDX analysis of individual crystals of this material indicate the presence of all the metals initially combined, but distributed in a heterogeneous fashion. In a recent report, Yaghi *et al.* used atom probe tomography to determine the precise sequence of metals in the same MTV-MOF-74 system, and learnt that the outcome of the reactions was significantly influenced by the combination of metals and the temperatures of the synthesis.[41] For example, the combination of Co and Cd at a reaction temperature of 85 ºC lead to short duplicates of the same type aligned between neighboring rods of the framework, while at 120 ºC the distribution was random. Li and coworkers introduced Cu^{+} nodes into heterometallic CuM-MOF-74 (M = Co, Ni, Zn) by partially reducing the Cu^{2+} centers during the one-pot solvothermal reaction.[47] The ratio between Cu^{+} and M^{2+} sites can be finely tuned, and the EDX analysis reveals that the metals are evenly dispersed throughout the framework. This new dual site Cu^{+}–Co^{2+} MOF-74 displays a significantly increased selectivity (up to 87.6%) for styrene oxide in the aerobic epoxidation of styrene.

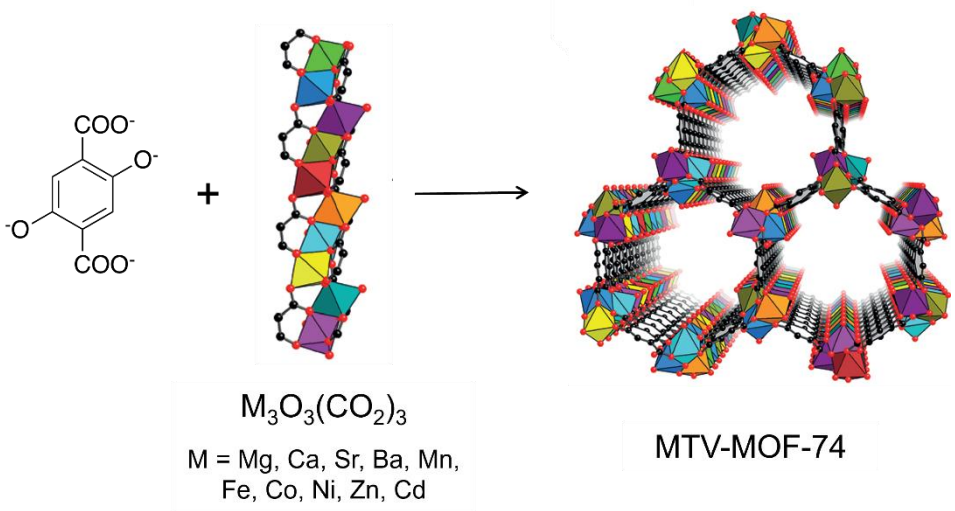

Figure 1.10. One-pot approach to synthesize a heterogeneous distribution of up to 10 metals in MTV-MOF-74. Reprinted with permission from reference [46].

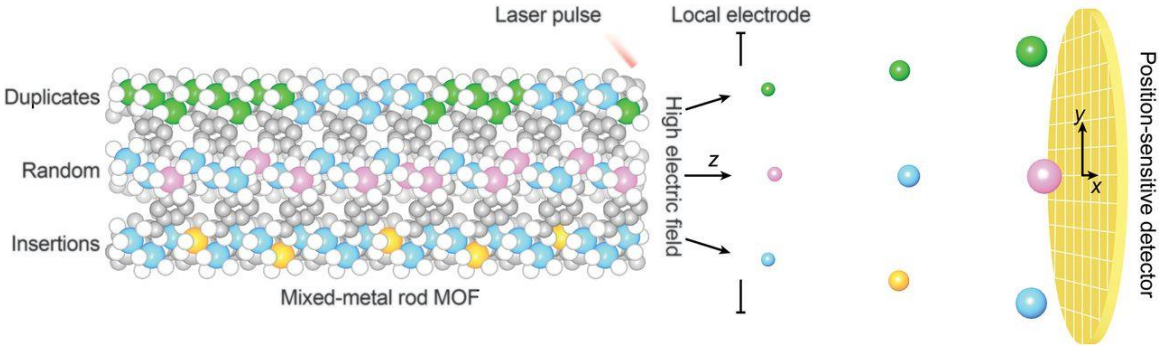

Figure 1.11. Schematic representation of how the atom probe tomography helped determine the precise sequence of metals in the MTV-MOF-74 system. Reprinted with permission from reference [41].

MTV-MOFs are not only limited to combinations with transition metals. These materials can also be obtained with rare-earth cations as their similar high coordination numbers enables their coexistence in the same framework. In a recent study, a MOF constituted by the linker 1,7-di(4-carboxyphenyl)-1,7-dicarba-closo-dodecaborane (mCB-L) was able to withstand the insertion of up to 8 rare-earth ions (La, Ce, Eu, Gd, Tb, Dy, Y, and Yb).[48] This report stands out as it is not a trivial matter to create materials with a high (>3) number of metals. The authors highlight that the bulky and weakly basic nature of the linker provides flexibility to the SBUs of the MOF, and this makes them more adaptable to slight changes in the radii of the metal ions. The features of the linker were the reason behind the successful results of the experiments. ICP and EDX analyses confirmed that, when combined, all the metals distribute uniformly through the crystals of the samples in an equimolar ratio.

Trimeric clusters, $[M_3(O/OH)](RCOO)_6$, are among the most important SBUs, and it is also possible to achieve heterogeneity in MOFs based on these building units. The tetrakis(4-carboxyphenyl)porphyrin-based (TCPP) MOF with formula $[M_3O]_2$(TCPP-M)$_3$ (M = Mg, Mn, Co, Ni, Fe) was obtained as a multi-metal MTV family by inserting combinations of transition metals.[49] In this case, both the M_3O trimer SBUs and the porphyrin units can include metal centers, which can further increase the heterogeneity of the system. The authors deciphered the spatial arrangement by combining the results from EDX, X-ray photoelectron spectroscopy (XPS) and UV−Vis diffuse reflectance spectra (DRS), and their MTV-MOF system displayed two distribution scenarios within the SBUs. While the combination of metals with size and electronegativity mismatch (Mn^{2+} and Fe^{3+}) results in the formation of domains of SBUs comprised of only one type of metal, other combinations of metals, such as Ni^{2+} and Fe^{3+} generate mixed-metal SBUs with formula $[(Ni_2Fe)O]$ distributed in a homogeneous fashion in the MOF. The

distribution of these metals had a direct impact on the catalytic properties of the material, as the well-mixed MTV-MOF clearly displayed a better performance in the photooxidation of 1,5-dihydroxynapthalene.

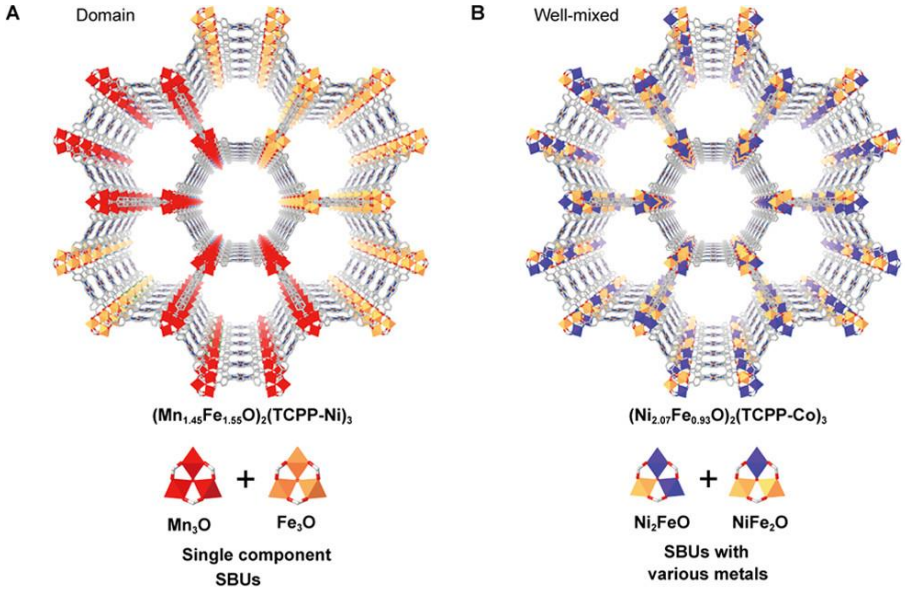

Figure 1.12. The two special arrangement scenarios in the SBUs of $[M_3O]_2(TCPP\text{-}M)_3$. **a)** Representation of the formation of domains when mixing Mn with Fe and **b)** representation of a homogeneous distribution when mixing Ni with Fe. Reprinted with permission from reference [49].

A similar well-mixed distribution scenario was also observed for MIL-100, a MOF that also displays the trimeric M_3O SBU.[50] The combination of Ni^{2+} and Fe^{3+} generated SBUs with formula $(NiFe_2)O$, evenly distributed throughout the framework. The incorporation of Ni in the MOF enhanced its Lewis acidity, and lead to a better performance in the acid-catalyzed Prins reaction. However, when Al and Fe are combined in the same framework, both ions randomly occupy the metal sites in the SBU trimers, as revealed by a combination of spectroscopy techniques (^{27}Al nuclear magnetic resonance, X-band

electron spin resonance, Mössbauer). Therefore, in this case, the framework is comprised by randomly distributed Al_3O, Fe_3O, $(Fe_2Al)O$ and $(FeAl_2)O$ SBU units.[51]

Another type of significant building units for MOF structures are hexameric clusters, which are present in the archetypal MOF UiO-66 as $[Zr_6O_4(OH)_4]$ units.[52] Lamberti *et al.* presented a study of the exact stoichiometry of the SBUs of a mixed-metal MTV-UiO-66.[53] By performing a multiple-edge extended X-ray absorption fine structure analysis (EXAFS), they demonstrated that when Zr and Ce are combined in the hexanuclear SBU of the structure, there is a coexistence of $CeZr_5$ clusters with monometallic Zr_6 (for a Ce content lower than 17%) and with Ce_6 clusters (with excess of Ce).

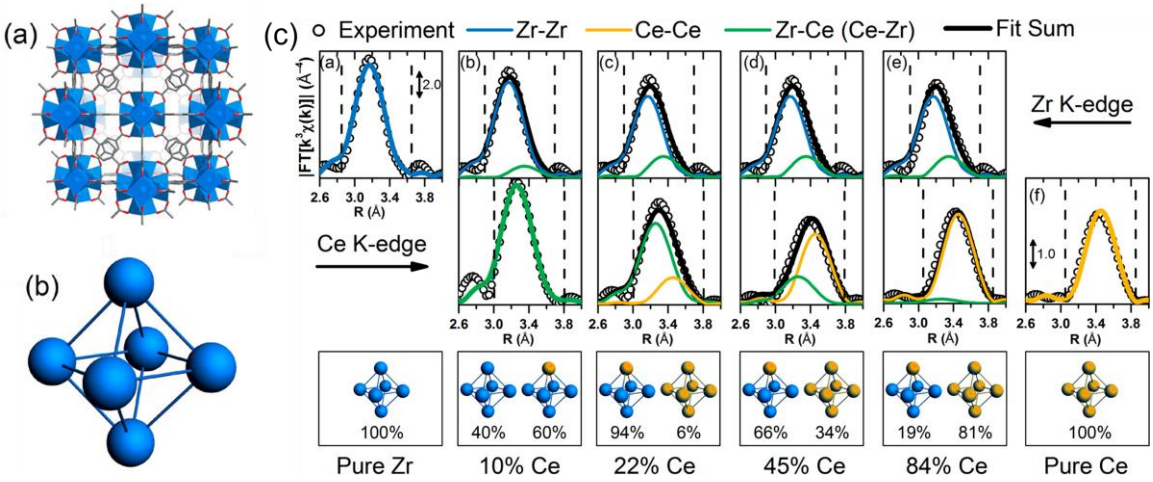

Figure 1.13. a) Representation of the crystal structure of UiO-66. Zr atoms are displayed in blue, O in red, C in gray. H atoms are omitted for clarity. **b)** The hexameric Zr_6 cluster of UiO-66. **c)** Results of the EXAFS fitting and the composition of the clusters used for fitting each spectrum. Experimental data is presented as white circles, and the fitted curves as full lines. The Zr–Zr contribution is displayed in blue, the Ce–Ce contribution in yellow and the Zr–Ce and Ce–Zr contributions in green. For the multi-metal MTV-MOFs, the sum of the two contributions is shown in black. The best fitting is obtained for 10% of Ce. Adapted from reference [53].

The concept of heterogeneity is not exclusive to carboxylate-based MOFs. ZIFs (Zeolitic Imidazolate Frameworks)[54] are a class of MOFs based on imidazolate linkers, and display structures based on 4-connected nets of tetrahedral units, analogous to zeolites. Goodwin and coworkers conducted a study of the structural and mechanical consequences of Zn/Cd substitution in the compositional family of ZIF-8, $Zn_{1-x}Cd_x(mIm)_2$ (HmIm = 2-methylimidazole).[55] Cd-substitution conveys flexibility to the framework as Cd-mIm interactions display weaker bonding, and it also generates a threefold reduction in the magnitude of thermal expansion behavior of the MOF. The authors used a computational reverse Monte Carlo (RMC) approach to determine compositional correlations in the MTV-ZIF-8, and they found that Zn and Cd monometallic clustering is significantly more predominant that a random distribution of the metals in all compositions.

Group 13 is one of the least studied metal groups as MOF inorganic building units, yet there are examples of multi-metal group 13 MOFs in the literature. A series of MTV-MOFs with formula $[In_xGa_{1-x}(O_2C_2H_4)_{0.5}(hfipbb)]$ ($H_2hfipbb$ = 4,4′-(hexafluoroisopropylidene)bis(benzoic acid)), based on combinations of In and Ga, was synthesized by my group.[56] This report is particularly noteworthy as it is the first example of how the catalytic activity of a MOF can be tuned by modulating the ratio between the metals. Thus, while the single-metal counterparts only yielded reaction intermediates or by-products when used at catalysts for the one-pot multicomponent Strecker reaction, the synergy between the multiple cations of the MTV-MOFs lead to the desired α-aminonitrile Strecker product.

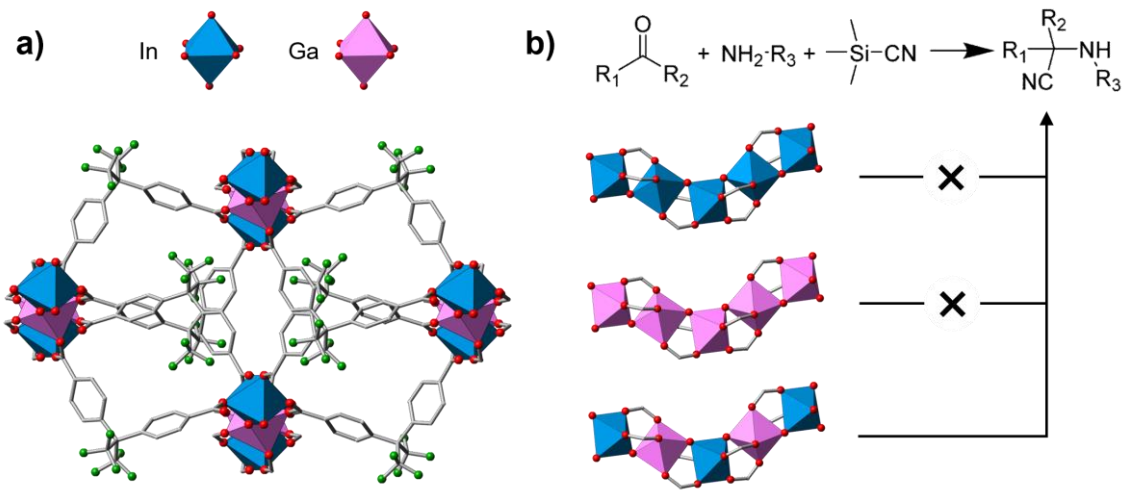

Figure 1.14. a) Representation of the crystal structure of $[In_xGa_{1-x}(O_2C_2H_4)_{0.5}(hfipbb)]$. In atoms are displayed in blue, Ga in pink, O in red, F in green, C in gray. H atoms are omitted for clarity. **b)** When using this MOF as a heterogeneous catalyst for the multicomponent Strecker reaction, the chemical composition of its SBUs directly influences the outcome of the reaction. Adapted from reference [56].

More recent reports of my group illustrated how to control the distribution of multiple metal ions at both atomic and mesoscopic scales.[57] The sequencing scenarios in the multi-metal MOFs derived from ZnPF-1, [Zn(hfipbb)], were unraveled by using diffraction techniques supported by density functional theory calculations. The rod-shaped SBUs of ZnPF-1 consist of tetrahedral coordinated Zn atoms. When Co atoms are inserted, they might appear in tetrahedral or octahedral environments, depending on the initial metal ratios and on the temperature. When they are in an octahedral environment, a crystal symmetry change occurs (the *c* parameter of the unit cell is doubled) as the SBUs accommodate the new ions, which is revealed by a combination of X-ray and neutron diffraction techniques. Conversely, when combined with zinc, Mn ions are exclusively found in an octahedral coordination, resulting in an ordered atomic distribution. On the other hand, SEM and EDX studies revealed that the combinations with Co were the only

ones that displayed an uneven distribution within the framework, with a larger amount of Co in the external sections of the crystals and hollow morphologies. The authors attributed these concentration gradients and hollow core-shell morphologies to a crystallization mechanism based on an initial formation of Zn-rich crystals, and a subsequent redissolution of the inner parts of the crystals followed by a growth stage of Co-rich layers on the surface of the crystals. These differences in the incorporation kinetics of different metal elements were used to address specific atomic arrangements and sequences in the SBUs. They also evidenced that the arrangement of the atoms of the SBUs can be directly translated to metal oxides by calcining the MOFs with selected combinations and metal ratios.[58]

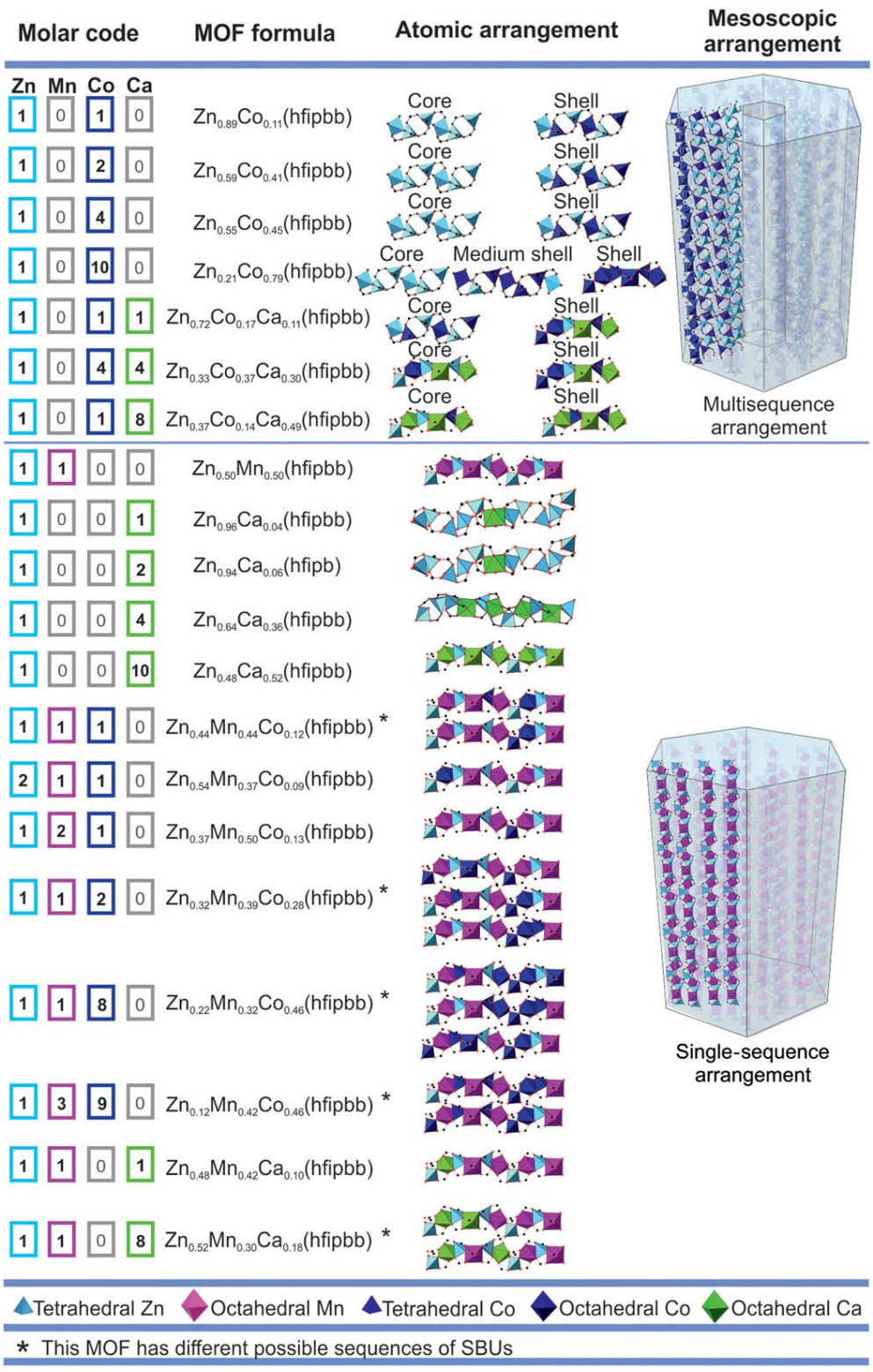

Figure 1.15. Different atomic sequencing scenarios in the SBUs of multi-metal MTV-ZnPF-1. Reprinted with permission from reference [57].

1.3.2.2. Post-synthetic metal exchange: trans-metalation

In cases when the one-pot strategy is not feasible, (either because of problems in the compatibility of the strategy with the framework or the desired metal combinations, or because the desired compositions are not achievable through this approach), alternative methods can be used. The post-synthetic metal exchange is an emerging route for accessing multi-metal SBUs. This strategy is milder than a conventional high-temperature synthesis, and it consists of carrying out a metal exchange at the metal nodes of the framework by submerging preformed crystals of single-metal MOFs into a solution of the metal that will be incorporated in the parent framework. The thermodynamic and kinetic rates of the exchange reactions tend to be easily influenced by a series of factors such as the solvent (polarity, viscosity, solubility of the metal salts), the lability of the metals, the structure of the MOF, temperature, or time.[59,60]

The archetypal MOF-5 was used to illustrate this strategy. Dincă *et al*. obtained MTV-MOF-5 crystals by soaking Zn-MOF-5 single crystals into a saturated solution of Ni nitrate.[61] The authors observed that the insertion of Ni^{2+} into the framework was thermodynamically driven, and the resulting Ni to Zn ratio was 1:3. As there is a color change in the crystals after the soaking stage (from colorless to yellow), the authors hypothesized that the Ni^{2+} ions must be in a octahedral coordination which implies that both the Zn SBUs of the MOF and the overall lattice are being distorted to accommodate the Ni ions. In a following report, Dincă and coworkers used the same approach to access the insertion of other transition metal ions into MOF-5, specifically reduced early metal ions like V^{2+} and Ti^{3+} (which are typically incompatible with standard MOF synthetic conditions), $Cr^{2+/3+}$, Fe^{2+} and Mn^{2+}.[62] The degree of ion exchange was estimated by elemental microanalysis (EA), and inductively coupled plasma atomic emission

spectroscopy (ICP-AES), and the MTV-MOF samples show drastically different Zn exchange levels, and overall under 20%. The authors attribute this to the nature of each metal, specifically to their stability constants which lead to a kinetic control over the exchange reaction. The stability constants of nearly all complexes of bivalent atoms (regardless of the number of chemical nature of the ligand molecules) has been found to follow the order Mn < Fe < Co < Ni < Cu > Zn,[63] and this fits well with the mismatch observed in the substitution degree of the Zn cations observed by the authors.

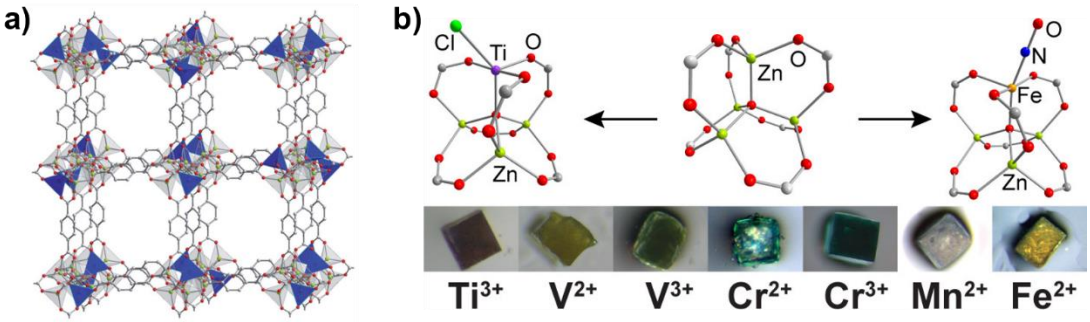

Figure 1.16. a) Representation of the crystal structure of $Ni_xZn_{4-x}O(BDC)_3$ (x = 1). The positions of the Ni^{2+} atoms cannot be clearly identified within the $NiZn_3$ clusters, so they are distributed randomly. Ni atoms are displayed as blue tetrahedrons, Zn as gray tetrahedrons, O as red spheres, and C as gray sticks. H atoms are omitted for clarity. **b)** The SBUs of MOF-5 display different geometries depending on the additional metal incorporated in the framework: pseudotetrahedral for V^{2+}, Cr^{2+}, Mn^{2+}, Fe^{2+}, Co^{2+}, and Ni^{2+} and pseudotrigonal bipyramidal Ti^{3+}, V^{3+}, and Cr^{3+} with terminal chloride moieties. Adapted from references [61-62].

For Zn-HKUST-1, $[Zn_3(BTC)_2(H_2O)_3]$, and Zn-PMOF-2, $[Zn_{24}L_8(H_2O)_{12}]$, where L = 1,3,5-tris(3,5-dicarboxylphenylethynyl)benzene)) which share a $[Zn_2(COO)_4]$ paddlewheel SBU, Lah *et al.* reported an exchange of the Zn centers with Cu.[64] This example was selected to showcase how the degree of the overall framework flexibility (for MOFs that share the same SBU type) has a direct impact on the accessibility of the metal centers and influences the outcome of the cation exchange process. In the case of Zn-HKUST-1, a more rigid framework, the conversion of the Zn metal centers to Cu reached 56%, as demonstrated by ICP-AES analysis. For Zn-PMOF-2, a more flexible system, the metal exchange displays site selectivity in single-crystals, and the complete trans-metalation was only achieved on the surface of the crystals. As the metal centers located on the surface of the crystals are in a more flexible environment, they showed a higher reactivity than the ones located in the core (also, the trans-metalation starts at the surface of a crystalline particle), and this led to a core-shell distribution. The authors highlighted that the reverse trans-metalation was not possible in neither case.

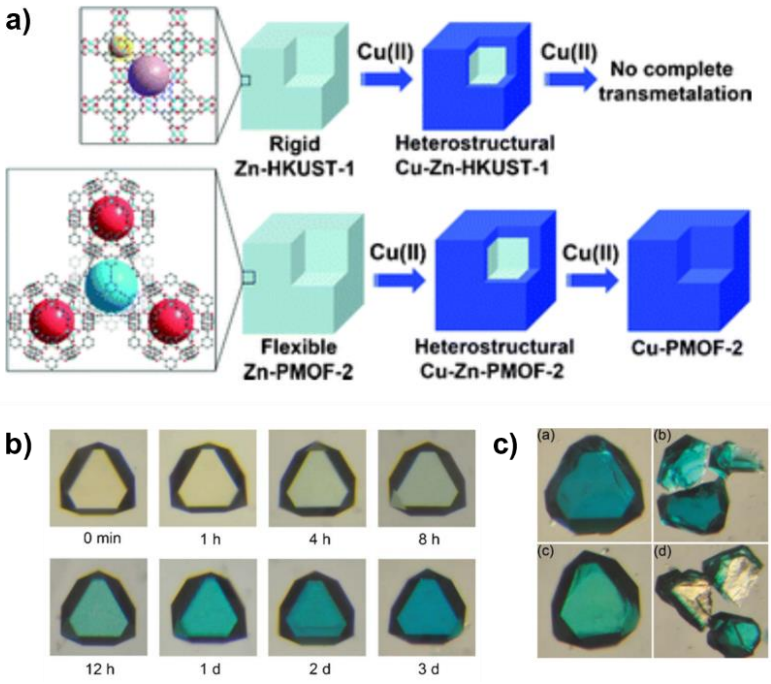

Figure 1.17. a) Schematic representation of the result of the cation exchange in both HKUST-1 and Zn-PMOF-2. **b)** Optical microscopic photographs of a single crystal of Zn-PMOF-2 submerged into a copper nitrate methanol solution, and the evolution of the cation exchange process over time. **c)** Optical microscopic photographs of **(up)** a single crystal of Zn-PMOF-2 submerged into a copper nitrate methanol solution for 3 days and its core-shell architecture **(down)** and the same crystal submerged in the solution for 12 hours. These images evidence that the total trans-metalation occurs after 3 days. Adapted from reference [64].

The last two examples of this section are included to showcase that alterations in the SBUs following the trans-metalation strategy lead to the development of new functions or the enhancement of particular features of the MOF. Firstly, the post-synthetic metal exchange of Zn-MFU-4l(arge), $[Zn_5Cl_4(BTDD)_3]$ with BTDD = bis(1H-1,2,3-triazolo-[4,5-b],[40,50-i])dibenzo-[1,4]-dioxin, with Co^{2+} lead to a redox-active version of the parent MOF with one Co center per pentanuclear MOF which displayed reversible gas-

phase oxidation properties.[65] Martí-Gastaldo *et al.* reported that MUV-10 (MUV, Materials of Universidad de Valencia) displays metal-induced topological transformations.[66] In this case, the starting MUV-10 crystals comprised heterometallic Ti^{4+}–Ca^{2+} SBUs with formula $[Ti_2Ca_2(O)_2(H_2O)_4(RCO_2)_8]$, since the combination of soft (M^{2+}) and hard (M^{4+}) metals in the nodes would facilitate the controlled metal exchange only in the soft positions. The newly formed heterometallic SBUs are in a thermodynamically metastable state, and they evolve towards clusters with lower nuclearity, thus inducing a MOF-to-MOF transformation that leads to new topologies. The insertion of M^{2+} (M = Fe, Co, Ni, Zn) induces a phase transformation of the parent MOF to MUV-101, isostructural with the prototypical MIL-100 family, and displays trinuclear SBUs with formula $[TiM_2(\mu_3\text{-}O)(H_2O)_3(RCO_2)_6]$. For Cu^{2+}, DFT calculations show that the formation of $TiCu_2$ clusters is not favorable, and the initial SBUs transform into paddlewheel clusters with formula $[TiCu(RCO_2)_2(O)(H_2O)]$, leading to heterometallic MUV-102, isostructural with HKUST-1. In a recent study, a series of single- and multi-metal MTV-MUV-101 were subjected to a catalytic activity test.[67] From the five samples (containing Fe_3, Ti_3, $TiFe_2$, $TiCo_2$, or $TiNi_2$ clusters) tested for the aminolysis of epoxides, only the sample containing $TiFe_2$ trimers displayed results comparable to benchmark catalysts, and this enhancement of the catalytic activity results from the combination of Lewis Ti^{4+} and Brønsted Fe^{3+}–OH acid sites.

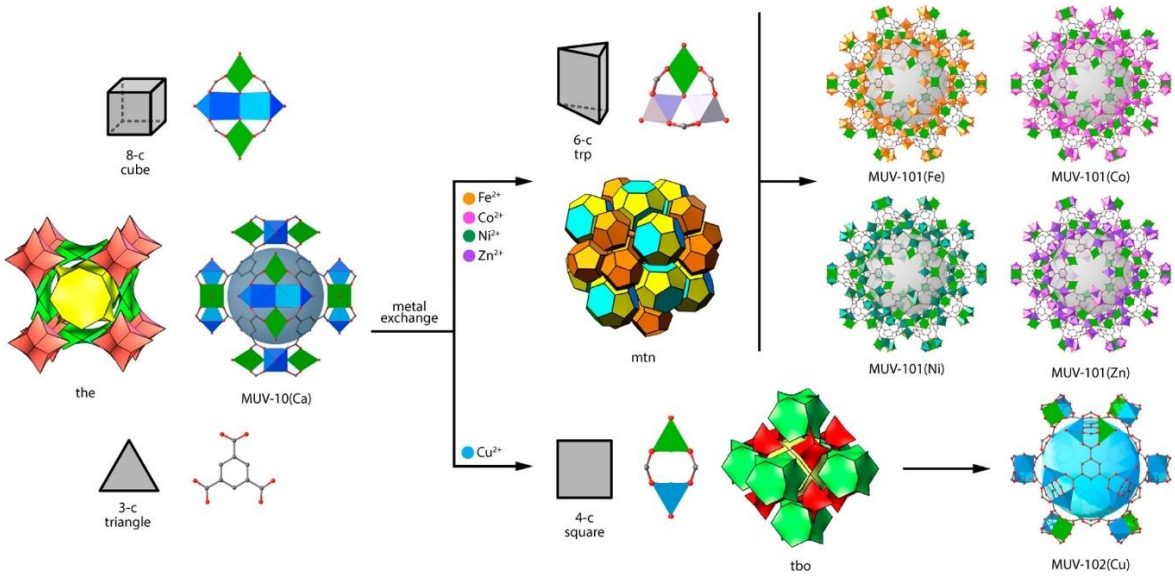

Figure 1.18. Graphical overview of how cation exchange in MUV-10(Ca) induces a MOT-to-MOF topological transformation, and the resulting structures and their building units. Reprinted with permission from reference [66].

1.3.2.3. Linkers containing metal-binding sites (metalloligands)

When the two previously described strategies fail to generate an MTV-MOF, reticular chemists can resort to using organic linkers that bear additional metal binding sites (metalloligands) which do not play any structural role or interfere in the formation of the structure.[68] One benefit of this approach is that the metal centers are "locked" in a pre-defined position, and this enables a higher control over the distribution of the metal nodes in the framework.

Linkers that contain bipyridine chelating groups are widely used.[69,70] The structure of MOF-253, [Al(OH)(bpydc)] with H_2bpydc = 2,2′-bipyridine-5,5′-dicarboxylic acid displays open metal sites in the bipyridine groups which can coordinate to Pd in a post-synthetic metalation process.[71] The Pd centers convey the structure a significantly higher sorption selectivity factor for CO_2. A similar strategy was followed to coordinate Ir

complexes to two Zr-based MOFs, and the new multi-metal MTV-MOFs displayed activity in the water oxidation reaction.[72]

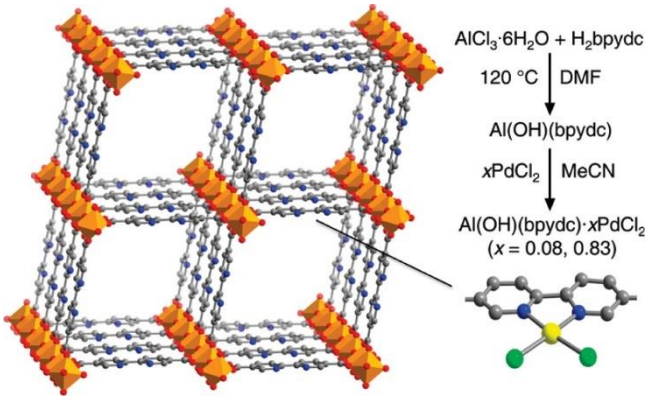

Figure 1.19. Representation of the crystal structure of MOF-253 and is synthesis pathway (including the insertion of $PdCl_2$ into the open bipy sites). Al atoms are displayed in orange, N in blue, C in gray, O in red, Pd in yellow, Cl in green. H atoms are omitted for clarity. Reprinted with permission from reference [71].

Porphyrins are also another type of widely used metalloligands. Based on a previous report of MOF-545,[73] a Zr-based structure that combines the highly stable $[Zr_6O_8(H_2O)_8]$ clusters linked by the porhpirinic linker M-TCPP (TCPP = tetrakis(4-carboxyphenyl)porphyrin), Zhou *et al*. designed the stable, redox-active MOF PCN-222(M) with M = Mn, Co, Ni, Cu, and Zn.[74] This structure displayed an enzyme-mimicking catalytic activity in aqueous solution, showing highly effective biomimetic oxidation on a number of substrates. The Zn-based version of the hexatopic linker [(5,15-bis(4-carboxyphenyl)-10,20-bis(3,5-dicarboxyphenyl)]porphyrin (H_6HCPP) was used in combination with typical transition metal elements like Mn or Co, p-block metals such as In and Pb, and lanthanide elements such as Gd, Pr and Yb to yield a series of open frameworks.[75]

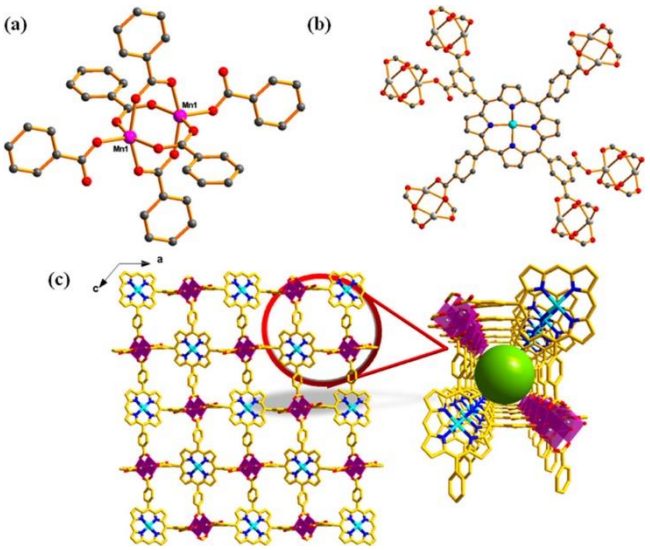

Figure 1.20. Representation of the crystal structure of {Mn_2[Zn(H_2O)-H_2HCPP]}·13DMF·3H_2O, obtained through the combination of Zn-H_6HCPP and Mg. **a)** Six-connected Mn_2-centered paddlewheel SBUs **b)** Connectivity of every Zn-H_2HCPP with six Mn_2 paddlewheel clusters **c)** The framework viewed parallel to the *ac* plane, displaying the open 1D intralattice channels that propagate parallel to the *b* axis. Zn atoms are displayed in cyan, Mn in magenta, N in blue, C in gray, O in red. H atoms are omitted for clarity. Reprinted with permission from reference [75].

Other chelating groups such as 1′-bi-2-naphthol allowed the insertion of Ti clusters in a series of isoreticular chiral Cu-based MOFs, and this enhanced the activity of the frameworks in asymmetric catalysis reactions.[76]

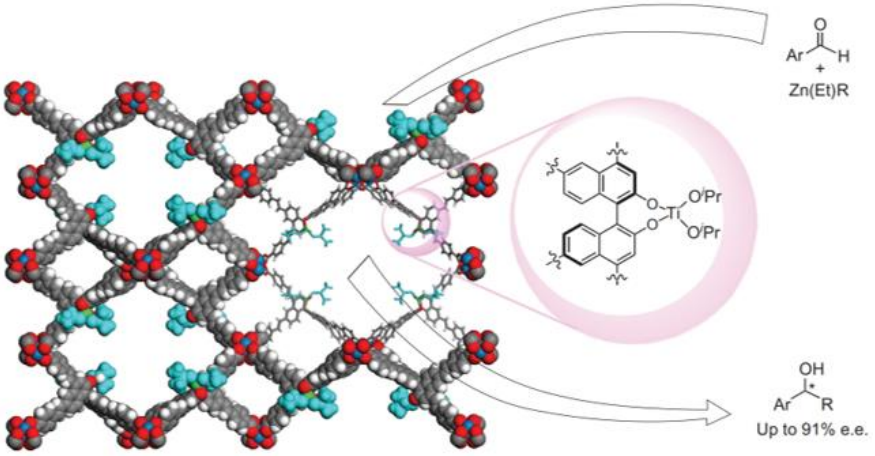

Figure 1.21. Representation of $Ti(O^iPr)_4$ clusters anchored to the 1′-bi-2-naphthol-derived linker of a Cu-based MOF (CMOF-3b), and the asymmetric catalysis product generated when using the MOF as a heterogeneous catalyst. Reprinted with permission from reference [76].

1.3.2.4. Preformed units

One way to prevent the inhomogeneous distribution of the metals and avoid the preferential incorporation of specific ions is to start from preformed metal clusters and thus direct the synthesis toward the desired structure.

This strategy was applied by Zhou *et al*. to obtain a series of robust multivariate iron-containing MOFs.[77] Since $[M_3(\mu^3\text{-}O)(COO)_6]$ (M = Al, Cr, Fe, In, Sc, V) is a typical trivalent metal-based building unit in MOFs, their starting building unit of choice was a $[Fe_2M(\mu^3\text{-}O)]$ cluster (M = Co, Fe, Mn, Ni, Zn). These particular clusters were feasible candidates to generate frameworks due to their very high solubility which facilitates their chemistry in solution. Additionally, they benefit from an inherent robustness due to the strong electrostatic interactions between the Fe^{3+} and the $\mu^3\text{-}O^{2-}$ sections, which would help preserve the integrity of the core during the synthesis reaction.

Another example of this trimeric cluster being used as a starting material was reported by Serre *et al*. to obtain multivariate Fe_2/M MIL-127, MIL-100 and MIL-88b (M = Co, Ni, Mg).[78] In this case, they prepared the oxo-centered trimeric $Fe^{3+/}M^{2+}$ acetate clusters by mixing the corresponding monometallic acetate salts. The authors highlight that bearing in mind the different characteristics of each metal, with their approach it is feasible to synthesize MOFs with a 2:1 $Fe^{3+/}M^{2+}$ ratio, and a direct synthesis using monometallic metal salts is not viable as it only leads to amorphous products or recrystallized linker.

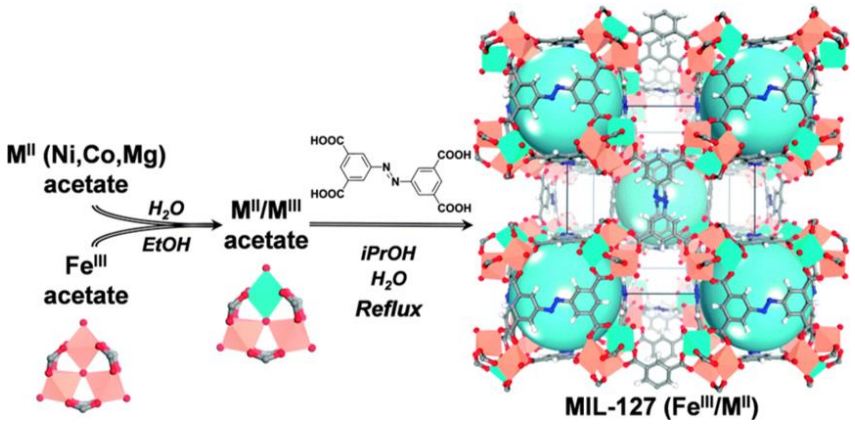

Figure 1.22. Schematic representation of the synthetic pathway that generates multi-metal MTV-MIL-127. Reprinted with permission from reference [78].

A more sophisticated approach was used in a recent study to obtain MTV-MOFs with specific sequences of metal elements.[79] The main idea was to use a specific heterometallic cluster to carry the desired combination of metals and to let them transform during the synthesis and become part of the structure of the framework while preserving the sequence of metals. A well-known family of heterometallic ring-shaped clusters with formula $[Ga_7NiF_8(PivO)_{16}]$ (PivOH = pivalic acid) was used as the preformed unit, which the authors refer to as *m*BU (messenger building unit). During the synthesis reaction, the *m*BU rings open and generate rods which eventually become the SBU of the MOF. In this

case, the mixture of the rod-type SBUs and 2,6-napthalenedicarboxylic acid generate a framework isostructural to MIL-69, but with Ga and Ni in the selected 7:1 ratio, as confirmed through EDX, total reflection X-ray fluorescence, and X-ray absorption spectroscopy analysis.

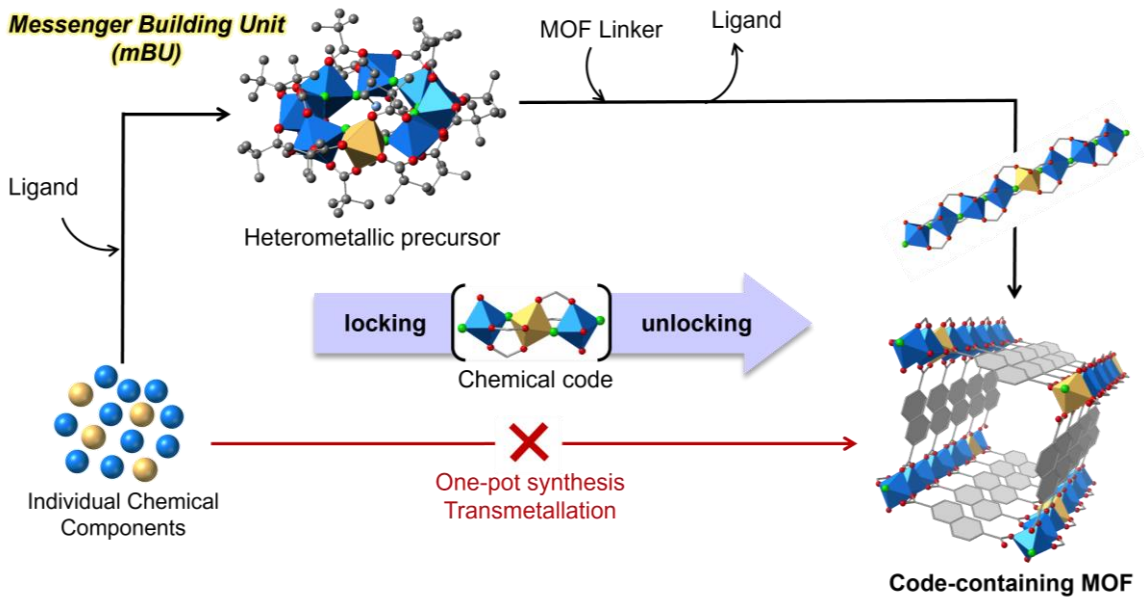

Figure 1.23. Schematic representation of the strategy used to obtain GaNi-MIL-69 with a 7:1 Ga-Ni ratio and sequence. Ga atoms are displayed in blue, Ni in yellow, O in red, C in gray. H atoms are omitted for clarity. Adapted from reference [79].

1.4. Perspectives and challenges

In essence, as Yaghi, Canossa *et al*. stated in a recent paper, the concept of multivariety "changes reticular chemistry at a fundamental level by making framework properties no longer discrete and periodic, but a spectrum of spatially varying states encoding chemical and physical functions".[80] The properties that multivariate systems display stem not from just the simple sum, but the synergy between theses spatial arrangements.

Throughout this introductory chapter, we have seen through many examples that obtaining multi-metal MTV-MOFs is attainable, albeit not trivial. Many questions remain unanswered:

- Can any combinations of metals result in a multi-metal MTV-MOF with a target composition?
- Is it possible to create any desired sequence or distribution of metals within the SBU of a MOF? Is this distribution or composition maintained at both atomic and mesoscopic levels?
- How and to what precision can we achieve synthetic reproducibility of specific sequences?
- Do the sequences interact with each other to encode specific properties? How?
- Is it possible to access any sequence-dependent properties?
- Can theses sequences be translated to other solids?

1.5. References

(1) Batten, S. R.; Champness, N. R.; Chen, X. M.; Garcia-Martinez, J.; Kitagawa, S.; Öhrström, L.; O'Keeffe, M.; Suh, M. P.; Reedijk, J. Coordination Polymers, Metal-Organic Frameworks and the Need for Terminology Guidelines. *CrystEngComm* **2012**, *14* (9), 3001–3004. https://doi.org/10.1039/c2ce06488j.

(2) Batten, S. R.; Champness, N. R.; Xiao-ming, C.; García-martínez, J.; Kitagawa, S.; Ohrström, L.; O'Keeffe, M.; Suh, M. P.; Reedijk, J. Terminology of Metal–Organic Frameworks and Coordination Polymers (IUPAC Recommendations 2013)* Stuart. *Pure and Applied Chemistry* **2013**, *85* (8), 1715–1724. https://doi.org/http://dx.doi.org/10.1351/PAC-REC-12-11-20.

(3) Kalmutzki, M. J.; Hanikel, N.; Yaghi, O. M. Secondary Building Units as the Turning Point in the Development of the Reticular Chemistry of MOFs. *Sci Adv* **2018**, *4* (10). https://doi.org/10.1126/sciadv.aat9180.

(4) Yaghi, O.; Li, H. Hydrothermal Synthesis of a Metal-Organic Framework Containing Large Rectangular Channels. *J Am Chem Soc* **1995**, *117* (41), 10401–10402.

(5) Baek, J.; Rungtaweevoranit, B.; Pei, X.; Park, M.; Fakra, S. C.; Liu, Y. S.; Matheu, R.; Alshmimri, S. A.; Alshehri, S.; Trickett, C. A.; Somorjai, G. A.; Yaghi, O. M. Bioinspired Metal-Organic Framework Catalysts for Selective Methane Oxidation to Methanol. *J Am Chem Soc* **2018**, *140* (51), 18208–18216. https://doi.org/10.1021/jacs.8b11525.

(6) López-Maya, E.; Padial, N. M.; Castells-Gil, J.; Ganivet, C. R.; Rubio-Gaspar, A.; Cirujano, F. G.; Almora-Barrios, N.; Tatay, S.; Navalón, S.; Martí-Gastaldo, C. Selective Implantation of Diamines for Cooperative Catalysis in Isoreticular Heterometallic

Titanium–Organic Frameworks. *Angewandte Chemie - International Edition* **2021**, *60* (21), 11868–11873. https://doi.org/10.1002/anie.202100176.

(7) Zhao, X.; Wang, Y.; Li, D. S.; Bu, X.; Feng, P. Metal–Organic Frameworks for Separation. *Advanced Materials* **2018**, *30* (37), 1–34. https://doi.org/10.1002/adma.201705189.

(8) Yang, S.; Peng, L.; Syzgantseva, O. A.; Trukhina, O.; Kochetygov, I.; Justin, A.; Sun, D. T.; Abedini, H.; Syzgantseva, M. A.; Oveisi, E.; Lu, G.; Queen, W. L. Preparation of Highly Porous Metal-Organic Framework Beads for Metal Extraction from Liquid Streams. *J Am Chem Soc* **2020**, *142* (31), 13415–13425. https://doi.org/10.1021/jacs.0c02371.

(9) Xue, T.; He, T.; Peng, L.; Syzgantseva, O. A.; Li, R.; Liu, C.; Sun, D. T.; Xu, G.; Qiu, R.; Wang, Y.; Yang, S.; Li, J.; Li, J. R.; Queen, W. L. A Customized MOF-Polymer Composite for Rapid Gold Extraction from Water Matrices. *Sci Adv* **2023**, *9* (13). https://doi.org/10.1126/sciadv.adg4923.

(10) Song, W.; Zheng, Z.; Alawadhi, A. H.; Yaghi, O. M. MOF Water Harvester Produces Water from Death Valley Desert Air in Ambient Sunlight. **2023**. https://doi.org/10.1038/s44221-023-00103-7.

(11) Sheberla, D.; Bachman, J. C.; Elias, J. S.; Sun, C. J.; Shao-Horn, Y.; Dincă, M. Conductive MOF Electrodes for Stable Supercapacitors with High Areal Capacitance. *Nat Mater* **2017**, *16* (2), 220–224. https://doi.org/10.1038/nmat4766.

(12) Zeng, M.; Ji, S. Y.; Wu, X. R.; Zhang, Y. Q.; Liu, C. M.; Kou, H. Z. Magnetooptical Properties of Lanthanide(III) Metal-Organic Frameworks Based on an Iridium(III) Metalloligand. *Inorg Chem* **2022**, *61* (7), 3097–3102. https://doi.org/10.1021/acs.inorgchem.1c03322.

(13) Giménez-Marqués, M.; Hidalgo, T.; Serre, C.; Horcajada, P. Nanostructured Metal-Organic Frameworks and Their Bio-Related Applications. *Coord Chem Rev* **2016**, *307*, 342–360. https://doi.org/10.1016/j.ccr.2015.08.008.

(14) Imaz, I.; Rubio-Martínez, M.; An, J.; Solé-Font, I.; Rosi, N. L.; Maspoch, D. Metal-Biomolecule Frameworks (MBioFs). *Chemical Communications* **2011**, *47* (26), 7287–7302. https://doi.org/10.1039/c1cc11202c.

(15) Shi, P. F.; Zheng, Y. Z.; Zhao, X. Q.; Xiong, G.; Zhao, B.; Wan, F. F.; Cheng, P. 3 D MOFs Containing Trigonal Bipyramidal Ln 5 Clusters as Nodes: Large Magnetocaloric Effect and Slow Magnetic Relaxation Behavior. *Chemistry - A European Journal* **2012**, *18* (47), 15086–15091. https://doi.org/10.1002/chem.201202412.

(16) Yin, J. J.; Lu, T. Q.; Chen, C.; Zhuang, G. L.; Zheng, J.; Zheng, X. Y.; Zheng, X. Y.; Shao, F. Magnetocaloric Effect and Slow Magnetic Relaxation on Two-Dimensional Layered 3d-4f Cluster-Based Metal-Organic Frameworks. *Cryst Growth Des* **2020**, *20* (6), 4005–4012. https://doi.org/10.1021/acs.cgd.0c00294.

(17) Constable, E. C.; Housecroft, C. E. Coordination Chemistry: The Scientific Legacy of Alfred Werner. *Chem Soc Rev* **2013**, *42* (4), 1429–1439. https://doi.org/10.1039/c2cs35428d.

(18) Jensen, W. B. The Lewis Acid-Base Definitions: A Status Report. *Chem Rev* **1978**, *78*.

(19) Buser, H. J.; Ludi, A.; Schwarzenbach, D.; Petter, W. The Crystal Structure of Prussian Blue: Fe4[Fe(CN)6]3·xH2O. *Inorg Chem* **1977**, *16* (11), 2704–2710. https://doi.org/10.1021/ic50177a008.

(20) H. M. Powell; J. H. Rayner. Clathrate Compound Forrmed by Benzene with an Ammonia-Nickel Cyanide Complex. *Nature* **1949**, *163*, 566–567.

(21) Kinoshita, Y.; Matsubara, I.; SaitoY. The Crystal Structure of Bis(Succinonitrilo)Copper(I) Nitrate. *Bulletin of the Chemical Society of Japan 32* **1959**, *7*, 741–747.

(22) Kitazawa, T.; Nishikori, S.; Kuroda, R.; Iwamoto, T. Novel Clathrate Compound of Cadmium Cyanide HOst with an Adamantane-like Cavity. *Chem Lett* **1988**, 1729–1732.

(23) Wells, A. The Geometrical Basis of Crystal Chemistry. Part 1. *Acta Crystallogr* **1954**, *7*, 535–544.

(24) Hoskins, B. F.; Robson, R. Infinite Polymeric Frameworks Consisting of Three Dimensionally Linked Rod-like Segments. *J Am Chem Soc* **1989**, *111* (15), 5962–5964. https://doi.org/10.1021/ja00197a079.

(25) Wells, A. F. *Structural Inorganic Chemistry*, 4th ed.; Oxford University Press: London, **1975**.

(26) Kondo, M.; Yoshitomi, T.; Matsuzaka, H.; Kitagawa, S.; Seki, K. Three-Dimensional Framework with Channeling Cavities for Small Molecules: {[M2(4, 4′-Bpy)3(NO3)4]·xH2O}n (M = Co, Ni, Zn). *Angewandte Chemie International Edition* **1997**, *36* (16), 1725–1727.

(27) Li, H.; Eddaoudi, M.; Groy, T. L.; Yaghi, O. Establishing Microporosity in Open Metal−Organic Frameworks: Gas Sorption Isotherms for Zn(BDC) (BDC = 1,4-Benzenedicarboxylate). *J Am Chem Soc* **1998**, *120* (33), 8571–8572.

(28) S.S.Y. Chui; S.M.F. Lo; J.P.H. Charmant; A.G. Orpen; I.D. Williams. A Chemically Functionalizable Nanoporous Material [Cu3(TMA)2(H2O)3]n. *Science* **1999**, *283* (February), 1148.

(29) Yaghi, O. M. Reticular Chemistry in All Dimensions. *ACS Cent Sci* **2019**, *5* (8), 1295–1300. https://doi.org/10.1021/acscentsci.9b00750.

(30) Gropp, C.; Canossa, S.; Wuttke, S.; Gándara, F.; Li, Q.; Gagliardi, L.; Yaghi, O. M. Standard Practices of Reticular Chemistry. *ACS Cent Sci* **2020**, *6* (8), 1255–1273. https://doi.org/10.1021/acscentsci.0c00592.

(31) Yaghi, O. M.; O'Keeffe, M.; Ockwig, N. W.; Chae, H. K.; Eddaoudi, M.; Kim, J. Reticular Synthesis and the Design of New Materials. *Nature* **2003**, *423* (6941), 705–714. https://doi.org/10.1038/nature01650.

(32) Eddaoudi, M.; Kim, J.; Rosi, N.; Vodak, D.; Wachter, J.; O'Keeffe, M.; Yaghi, O. M. Systematic Design of Pore Size and Functionality in Isoreticular MOFs and Their Application in Methane Storage. *Science* **2002**, *295* (5554), 469–472. https://doi.org/10.1126/science.1067208.

(33) Furukawa, H.; Cordova, K. E.; O'Keeffe, M.; Yaghi, O. M. The Chemistry and Applications of Metal-Organic Frameworks. *Scienc*e **2013**, *341* (6149). https://doi.org/10.1126/science.1230444.

(34) Yaghi, O. M.; Kalmutzki, M. J.; Diercks, C. S. Complexity and Heterogeneity in MOFs . *Introduction to Reticular Chemistry* **2019**, No. ii, 121–144. https://doi.org/10.1002/9783527821099.ch5.

(35) Lee, S. J.; Telfer, S. G. Multicomponent Metal-Organic Frameworks. *Angewandte Chemie International Edition* **2023**, *202306341*. https://doi.org/10.1002/anie.202306341.

(36) Koh, K.; Wong-Foy, A. G.; Matzger, A. J. A Crystalline Mesoporous Coordination Copolymer with High Microporosity. *Angewandte Chemie - International Edition* **2008**, *47* (4), 677–680. https://doi.org/10.1002/anie.200705020.

(37) Chae, H. K.; Siberio-Pérez, D.; Kiim, J.; Go, Y.; Eddaoudi, M.; Matzger, A. J.; O'Keeffe, M.; Yaghi, O. M.; Group, M. design and discovery. A Route to High Surface Area, Porosity and Inclusion of Large Molecules in Crystals. *Nature* **2004**, *427*, 523–527. https://doi.org/doi:10.1038/nature02311.

(38) Wang, C.; Liu, C.; He, X.; Sun, Z. M. A Cluster-Based Mesoporous Ti-MOF with Sodalite Supercages. *Chemical Communications* **2017**, *53* (85), 11670–11673. https://doi.org/10.1039/c7cc06652j.

(39) Tu, B.; Pang, Q.; Ning, E.; Yan, W.; Qi, Y.; Wu, D.; Li, Q. Heterogeneity within a Mesoporous Metal-Organic Framework with Three Distinct Metal-Containing Building Units. *J Am Chem Soc* **2015**, *137* (42), 13456–13459. https://doi.org/10.1021/jacs.5b07687.

(40) Kong, X.; Deng, H.; Yan, F.; Kim, J.; Swisher, J. A.; Smit, B.; Yaghi, O. M.; Reimer, J. A. Mapping of Functional Groups in Metal-Organic Frameworks. *Science* **2013**, *341* (6148), 882–885. https://doi.org/10.1126/science.1238339.

(41) Ji, Z.; Li, T.; Yaghi, O. M. Sequencing of Metals in Multivariate Metal-Organic Frameworks. *Science* **2020**, *369* (6504), 674–680. https://doi.org/10.1126/science.aaz4304.

(42) Deng, H.; Doonan, C. J.; Furukawa, H.; Ferreira, R. B.; Towne, J.; Knobler, C. B.; Wang, B.; Yaghi, O. M. Multiple Functional Groups of Varying Ratios in Metal-Organic Frameworks. *Science* **2010**, *327* (5967), 846–850. https://doi.org/10.1126/science.1181761.

(43) Lerma-Berlanga, B.; R. Ganivet, C.; Almora-Barrios, N.; Tatay, S.; Peng, Y.; Albero, J.; Fabelo, O.; González-Platas, J.; García, H.; M. Padial, N.; Martí-Gastaldo, C. Effect of

Linker Distribution in the Photocatalytic Activity of Multivariate Mesoporous Crystals. *J Am Chem Soc* **2021**, *143* (4), 1798–1806. https://doi.org/10.1021/jacs.0c09015.

(44) Castells-Gil, J.; Almora-Barrios, N.; Lerma-Berlanga, B.; Padial, N. M.; Martí-Gastaldo, C. Chemical Complexity for Targeted Function in Heterometallic Titanium-Organic Frameworks. *Chem Sci* **2023**, *14* (25). https://doi.org/10.1039/d3sc01550e.

(45) Trousselet, F.; Archereau, A.; Boutin, A.; Coudert, F. X. Heterometallic Metal-Organic Frameworks of MOF-5 and UiO-66 Families: Insight from Computational Chemistry. *Journal of Physical Chemistry C* **2016**, *120* (43), 24885–24894. https://doi.org/10.1021/acs.jpcc.6b08594.

(46) Wang, L. J.; Deng, H.; Furukawa, H.; Gándara, F.; Cordova, K. E.; Peri, D.; Yaghi, O. M. Synthesis and Characterization of Metal-Organic Framework-74 Containing 2, 4, 6, 8, and 10 Different Metals. *Inorg Chem* **2014**, *53* (12), 5881–5883. https://doi.org/10.1021/ic500434a.

(47) Liu, H.; Liu, W.; Xue, G.; Tan, T.; Yang, C.; An, P.; Chen, W.; Zhao, W.; Fan, T.; Cui, C.; Tang, Z.; Li, G. Modulating Charges of Dual Sites in Multivariate Metal-Organic Frameworks for Boosting Selective Aerobic Epoxidation of Alkenes. *J Am Chem Soc* **2023**, *145* (20), 11085–11096. https://doi.org/10.1021/jacs.3c00460.

(48) Li, Z.; Li, X.-B.; Light, M. E.; Carrillo, A. E.; Arauzo, A.; Valvidares, M.; Roscini, C.; Teixidor, F.; Viñas, C.; Gándara, F.; Bartolomé, E.; Planas, J. G. A Metal-Organic Framework Incorporating Eight Different Size Rare-Earth Metal Elements: Toward Multifunctionality À La Carte. *Adv Funct Mater* **2023**, 2307369. https://doi.org/https://doi.org/10.1002/adfm.202307369.

(49) Liu, Q.; Cong, H.; Deng, H. Deciphering the Spatial Arrangement of Metals and Correlation to Reactivity in Multivariate Metal-Organic Frameworks. *J Am Chem Soc* **2016**, *138* (42), 13822–13825. https://doi.org/10.1021/jacs.6b08724.

(50) Giménez-Marqués, M.; Santiago-Portillo, A.; Navalón, S.; Álvaro, M.; Briois, V.; Nouar, F.; Garcia, H.; Serre, C. Exploring the Catalytic Performance of a Series of Bimetallic MIL-100(Fe, Ni) MOFs. *J Mater Chem A Mater* **2019**, *7* (35), 20285–20292. https://doi.org/10.1039/c9ta01948k.

(51) Mali, G.; Mazaj, M.; Arčon, I.; Hanžel, D.; Arčon, D.; Jagličić, Z. Unraveling the Arrangement of Al and Fe within the Framework Explains the Magnetism of Mixed-Metal MIL-100(Al,Fe). *Journal of Physical Chemistry Letters* **2019**, *10* (7), 1464–1470. https://doi.org/10.1021/acs.jpclett.9b00341.

(52) Winarta, J.; Shan, B.; McIntyre, S. M.; Ye, L.; Wang, C.; Liu, J.; Mu, B. A Decade of UiO-66 Research: A Historic Review of Dynamic Structure, Synthesis Mechanisms, and Characterization Techniques of an Archetypal Metal-Organic Framework. *Cryst Growth Des* **2020**, *20* (2), 1347–1362. https://doi.org/10.1021/acs.cgd.9b00955.

(53) Lomachenko, K. A.; Jacobsen, J.; Bugaev, A. L.; Atzori, C.; Bonino, F.; Bordiga, S.; Stock, N.; Lamberti, C. Exact Stoichiometry of Ce x Zr 6-x Cornerstones in Mixed-Metal UiO-66 Metal-Organic Frameworks Revealed by Extended X-Ray Absorption Fine Structure Spectroscopy. *J Am Chem Soc* **2018**, *140* (50), 17379–17383. https://doi.org/10.1021/jacs.8b10343.

(54) Park, K. S.; Ni, Z.; Côté, A. P.; Choi, J. Y.; Huang, R.; Uribe-Romo, F. J.; Chae, H. K.; O'Keeffe, M.; Yaghi, O. M. Exceptional Chemical and Thermal Stability of Zeolitic Imidazolate Frameworks. *Proc Natl Acad Sci U S A* **2006**, *103* (27), 10186–10191. https://doi.org/10.1073/pnas.0602439103.

(55) Sapnik, A. F.; Geddes, H. S.; Reynolds, E. M.; Yeung, H. H. M.; Goodwin, A. L. Compositional Inhomogeneity and Tuneable Thermal Expansion in Mixed-Metal ZIF-8 Analogues. *Chemical Communications* **2018**, *54* (69), 9651–9654. https://doi.org/10.1039/c8cc04172e.

(56) Aguirre-Díaz, L. M.; Gándara, F.; Iglesias, M.; Snejko, N.; Gutiérrez-Puebla, E.; Monge, M. Á. Tunable Catalytic Activity of Solid Solution Metal-Organic Frameworks in One-Pot Multicomponent Reactions. *J Am Chem Soc* **2015**, *137* (19), 6132–6135. https://doi.org/10.1021/jacs.5b02313.

(57) Castillo-Blas, C.; De La Peña-O'Shea, V. A.; Puente-Orench, I.; De Paz, J. R.; Sáez-Puche, R.; Gutiérrez-Puebla, E.; Gándara, F.; Monge, Á. Addressed Realization of Multication Complex Arrangements in Metal-Organic Frameworks. *Sci Adv* **2017**, *3* (7), 1–11. https://doi.org/10.1126/sciadv.1700773.

(58) Castillo-Blas, C.; López-Salas, N.; Gutiérrez, M. C.; Puente-Orench, I.; Gutiérrez-Puebla, E.; Ferrer, M. L.; Monge, M. Á.; Gándara, F. Encoding Metal-Cation Arrangements in Metal-Organic Frameworks for Programming the Composition of Electrocatalytically Active Multimetal Oxides. *J Am Chem Soc* **2019**, *141* (4), 1766–1774. https://doi.org/10.1021/jacs.8b12860.

(59) Brozek, C. K.; Dincă, M. Cation Exchange at the Secondary Building Units of Metal-Organic Frameworks. *Chem Soc Rev* **2014**, *43* (16), 5456–5467. https://doi.org/10.1039/c4cs00002a.

(60) Rieth, A. J.; Wright, A. M.; Dincă, M. Kinetic Stability of Metal–Organic Frameworks for Corrosive and Coordinating Gas Capture. *Nat Rev Mater* **2019**, *4* (11), 708–725. https://doi.org/10.1038/s41578-019-0140-1.

(61) Brozek, C. K.; Dinca, M. Lattice-Imposed Geometry in Metal-Organic Frameworks: Lacunary Zn 4O Clusters in MOF-5 Serve as Tripodal Chelating Ligands for Ni 2+. *Chem Sci* **2012**, *3* (6), 2110–2113. https://doi.org/10.1039/c2sc20306e.

(62) Brozek, C. K.; Dincă, M. Ti3+-, V2+/3+-, Cr2+/3+-, Mn2+-, and Fe2+-Substituted MOF-5 and Redox Reactivity in Cr- and Fe-MOF-5. *J Am Chem Soc* **2013**, *135*, 12886–12891.

(63) Irving, B. H.; Williams, R. J. P. The Stability of Transition-Metal Complexes. *J Chem Soc* **1953**, No. 637, 3192.

(64) Song, X.; Jeong, S.; Kim, D.; Lah, M. S. Transmetalations in Two Metal-Organic Frameworks with Different Framework Flexibilities: Kinetics and Core-Shell Heterostructure. *CrystEngComm* **2012**, *14* (18), 5753–5756. https://doi.org/10.1039/c2ce26115d.

(65) Denysenko, D.; Werner, T.; Grzywa, M.; Puls, A.; Hagen, V.; Eickerling, G.; Jelic, J.; Reuter, K.; Volkmer, D. Reversible Gas-Phase Redox Processes Catalyzed by Co-Exchanged MFU-4l(Arge). *Chemical Communications* **2012**, *48* (9), 1236–1238. https://doi.org/10.1039/c2cc16235k.

(66) Padial, N. M.; Lerma-Berlanga, B.; Almora-Barrios, N.; Castells-Gil, J.; Da Silva, I.; De La Mata, M.; Molina, S. I.; Hernández-Saz, J.; Platero-Prats, A. E.; Tatay, S.; MartÍ-Gastaldo, C. Heterometallic Titanium-Organic Frameworks by Metal-Induced Dynamic Topological Transformations. *J Am Chem Soc* **2020**, *142* (14), 6638–6648. https://doi.org/10.1021/jacs.0c00117.

(67) Rubio-Gaspar, A.; Navalón, S.; Tatay, S.; Cirujano, F. G.; Fernández-Conde, C.; Padial, N. M.; Martí-Gastaldo, C. Metal Node Control of Brønsted Acidity in Heterobimetallic

Titanium-Organic Frameworks. *J Am Chem Soc* **2022**. https://doi.org/10.1021/jacs.2c12718.

(68) Das, M. C.; Xiang, S.; Zhang, Z.; Chen, B. Functional Mixed Metal-Organic Frameworks with Metalloligands. *Angewandte Chemie - International Edition* **2011**, *50* (45), 10510–10520. https://doi.org/10.1002/anie.201101534.

(69) Manna, K.; Zhang, T.; Greene, F. X.; Lin, W. Bipyridine- and Phenanthroline-Based Metal-Organic Frameworks for Highly Efficient and Tandem Catalytic Organic Transformations via Directed C-H Activation. *J Am Chem Soc* **2015**, *137* (7), 2665–2673. https://doi.org/10.1021/ja512478y.

(70) Tu, T. N.; Nguyen, M. V.; Nguyen, H. L.; Yuliarto, B.; Cordova, K. E.; Demir, S. Designing Bipyridine-Functionalized Zirconium Metal–Organic Frameworks as a Platform for Clean Energy and Other Emerging Applications. *Coord Chem Rev* **2018**, *364*, 33–50. https://doi.org/10.1016/j.ccr.2018.03.014.

(71) Bloch, E. D.; Britt, D.; Lee, C.; Doonan, C. J.; Uribe-Romo, F. J.; Furukawa, H.; Long, J. R.; Yaghi, O. M. Metal Insertion in a Microporous Metal-Organic Framework Lined with 2,2′-Bipyridine. *J Am Chem Soc* **2010**, *132* (41), 14382–14384. https://doi.org/10.1021/ja106935d.

(72) Wang, C.; Wang, J. L.; Lin, W. Elucidating Molecular Iridium Water Oxidation Catalysts Using Metal-Organic Frameworks: A Comprehensive Structural, Catalytic, Spectroscopic, and Kinetic Study. *J Am Chem Soc* **2012**, *134* (48), 19895–19908. https://doi.org/10.1021/ja310074j.

(73) Morris, W.; Volosskiy, B.; Demir, S.; Gándara, F.; McGrier, P. L.; Furukawa, H.; Cascio, D.; Stoddart, J. F.; Yaghi, O. M. Synthesis, Structure, and Metalation of Two New Highly

Porous Zirconium Metal-Organic Frameworks. *Inorg Chem* **2012**, *51* (12), 6443–6445. https://doi.org/10.1021/ic300825s.

(74) Feng, D.; Gu, Z. Y.; Li, J. R.; Jiang, H. L.; Wei, Z.; Zhou, H. C. Zirconium-Metalloporphyrin PCN-222: Mesoporous Metal-Organic Frameworks with Ultrahigh Stability as Biomimetic Catalysts. *Angewandte Chemie - International Edition* **2012**, *51* (41), 10307–10310. https://doi.org/10.1002/anie.201204475.

(75) Tripuramallu, B. K.; Goswami, S.; Goldberg, I. Open MOFs with Unique Hexatopic Zinc-5,15-Bis(4′-Carboxyphenyl)-10,20-Bis(3′,5′-Dicarboxyphenyl)Porphyrin Linker. *Cryst Growth Des* **2018**, *18* (1), 230–241. https://doi.org/10.1021/acs.cgd.7b01171.

(76) Ma, L.; Falkowski, J. M.; Abney, C.; Lin, W. A Series of Isoreticular Chiral Metal-Organic Frameworks as a Tunable Platform for Asymmetric Catalysis. *Nat Chem* **2010**, *2* (10), 838–846. https://doi.org/10.1038/nchem.738.

(77) Feng, D.; Wang, K.; Wei, Z.; Chen, Y. P.; Simon, C. M.; Arvapally, R. K.; Martin, R. L.; Bosch, M.; Liu, T. F.; Fordham, S.; Yuan, D.; Omary, M. A.; Haranczyk, M.; Smit, B.; Zhou, H. C. Kinetically Tuned Dimensional Augmentation as a Versatile Synthetic Route towards Robust Metal-Organic Frameworks. *Nat Commun* **2014**, *5*. https://doi.org/10.1038/ncomms6723.

(78) Wongsakulphasatch, S.; Nouar, F.; Rodriguez, J.; Scott, L.; Guillouzer, C. Le; Devic, T.; Horcajada, P.; Llewellyn, P. L.; Vimont, A.; Clet, G.; Daturi, M.; Serre, C. Direct Accessibility of Mixed-Metal (III/II) Acid Sites through the Rational Synthesis of Porous Metal Carboxylates. **2015**, *51*, 10194–10197. https://doi.org/10.1039/Mo.

(79) López-García, C.; Canossa, S.; Hadermann, J.; Gorni, G.; Oropeza, F. E.; De La Peña O'Shea, V. A.; Iglesias, M.; Angeles Monge, M.; Gutiérrez-Puebla, E.; Gándara, F. Heterometallic Molecular Complexes Act as Messenger Building Units to Encode

Desired Metal-Atom Combinations to Multivariate Metal-Organic Frameworks. *J Am Chem Soc* **2022**, *144* (36), 16262–16266. https://doi.org/10.1021/jacs.2c06142.

(80) Canossa, S.; Ji, Z.; Gropp, C.; Rong, Z.; Ploetz, E.; Wuttke, S.; Yaghi, O. M. System of Sequences in Multivariate Reticular Structures. *Nat Rev Mater* **2022**, *3*. https://doi.org/10.1038/s41578-022-00482-5.

─ CHAPTER 2 ─

Objectives

In the introductory chapter, some of the major challenges associated to obtaining MTV-MOFs have been discussed, leaving several open questions that need to be addressed in order to gain further knowledge on how to design and control the composition of multi-metal materials. Not only is it not clear which parameters dictate the outcome of the reactions and the atomic distribution (atomic radius, reactivity of the metals, coordination environments of the metals, ratios between the metals, reaction kinetics), but also not much is known about the compatibility between metals and parent structures, which makes predicting and designing a MOF with a target composition quite challenging.

To shed some light on the challenges posed, the research work carried out in this Doctoral Thesis was oriented towards the study of combinations of metals of different nature or different groups. With this in mind, the focal point of this Doctoral Thesis is to investigate the feasibility of certain metal atom combinations, including rare-earths and noble metals, of generating multi-metal MOFs with a target composition from a synthetic and crystallization point of view.

To accomplish this main goal, the work carried out in this Doctoral Thesis has been structured as follows.

- Firstly, the key point of Chapter 4 is to elucidate the impact of different combinations of rare-earth ions on the atomic sequencing, and investigate the kinetic and thermodynamic synthesis and crystallization parameters in order to determine which binary metal combinations can result in a MTV-MOF with a controllable composition. For this, the rare-earth MOF family RPF-4 was selected as ideal platform due to its unique features. Also, the investigation work carried out in this Doctoral Thesis aimed to study the effect of the selected metal combinations on the properties of the resulting MTV-MOFs, and to demonstrate that oxides with a specific rare-earth ratio can be obtained by calcining these MTV-MOFs.

- Chapters 6 and 7 are centered around exploring other cation combinations from the periodic table and evaluating the viability of inserting cations that have never been reported as nodes of a MOF, in particular iridium (III). Therefore, one of the specific goals of this Doctoral Thesis was to study the role of the second metal involved in the binary combination, and to develop a multi-metal synthetic strategy that would reticulate iridium (III) atoms and thus generate a multi-metal MOF based on this noble metal, and to demonstrate its activity as a heterogeneous catalyst.

─ CHAPTER 3 ─

Experimental Section

3.1. General techniques: Chemical analysis

3.1.1. Elemental Analysis (EA)

The carbon, nitrogen, and hydrogen content of some specific samples were determined by elemental analysis. The samples were vacuum-dried and sent to the EA department at the Chemical Analysis facility at the Instituto de Ciencia de Materiales de Madrid (ICMM), where they operate a CNHS Perkin Elmer 2400 elemental analyzer.

3.1.2. Thermogravimetric analysis (TGA)

The thermal stability of some specific samples was determined by thermogravimetric analysis. The samples sent to the TGA department at the Chemical Analysis facility at the Instituto de Ciencia de Materiales de Madrid (ICMM), where they operate a simultaneous TGA/ATD STD-Q600 equipment from TA Instruments. The samples were placed in platinum crucibles, and were heated in air (100 mL/min flow), in a temperature range between 25 °C and 800 °C with a rate of 10 °C/min.

3.1.3. Infrared Spectroscopy (IR)

The infrared spectrum of some specific samples was recorded at the IR Spectroscopy and Ellipsometry facility at the Instituto de Ciencia de Materiales de Madrid (ICMM), where they operate a Bruker Vertex 70V. The IR spectra of the samples were recorded from KBr pellets in a range from 300 to 4000 cm^{-1}.

3.1.4. Total X-Ray Fluorescence Spectroscopy (TXRF)

Some of the samples could not be broken down, even after acid digestion, and therefore the ratio between metals could not be estimated. For this reason, Total-reflection X-Ray fluorescence spectrometry (TXRF) was selected as a quantification technique to determine the metal content of the samples. With this technique, solid samples can be suspended in an adequate liquid media, and analyzed without the need of an acid digestion.[1] TXRF analysis of the selected samples was performed at the Servicio

Interdepartamental de Investigación (SIdI) at the Universidad Autónoma de Madrid (Spain), where they operate a Bruker S2 PicoFox spectrometer equipped with a Peltier-cooled XFlash Silicon Drift detector that operates at a voltage of 50 kV and a current of 600 μA.

3.2. Diffraction techniques

3.2.1. Powder X-Ray Diffraction (PXRD)

Powder X-ray Diffraction (PXRD) patterns were collected with a Bruker D8 DaVinci diffractometer equipped with a Ni-filtered CuKα radiation tube (Kα1 = 1.5406 Å, Kα2 = 1.5444 Å, and Kα1/Kα2 = 0.5) operated at a voltage of 40 kV and at a current of 40 mA. Each rutinary experiment was recorded with an exposure time of 0.1 s per step and a step size of 0.02° (the exposure time and step size were adjusted if the experiments required a longer collection time for higher intensity). The samples were prepared by placing a small amount of a suspension of crystals in acetone on a glass sample carrier, forming a thin layer in the center.

3.2.2. Single-Crystal X-Ray Diffraction (SCXRD)

Single-Crystal X-ray Diffraction (SCXRD) experiments were performed at the Instituto de Ciencia de Materiales de Madrid (ICMM). The samples were placed on a glass slide and submerged in mineral oil. Suitable crystals were selected with a Kapton loop from MiTeGen, using a polarized optical microscope to check their size and quality.

Single crystal X-ray data was collected with four-circle kappa diffractometers. The first one was a Bruker D8 diffractometer equipped with a Cu INCOATED microsource, a Bruker VANTEC 500 area detector (microgap technology) and operated at 30W power (45kV, 0.60mA) to generate Cu Kα radiation (λ = 1.54178 Å). The second one was a Bruker D8 Venture, equipped with three microsources,a Photon III detector, and operated at 30W power (45kV, 0.60mA) to generate Cu, Mo and Ag radiation. The diffraction data was collected with a resolution of 0.85 Å and a completeness > 95%.

3.2.3. Neutron Powder Diffraction (NPD)

Neutron Powder Diffraction (NPD) data was acquired at the D1B instrument of the Institut Laue-Langevin in Grenoble (France). For the room temperature measurements, samples were placed in 5 mm cylindrical vanadium cans (that display a broad peak at 70–74°), while for the sub-kelvin experiments, a 6 mm cylindrical copper container was used. All data sets were recorded with a monochromatic neutron wavelength of 2.5260 Å. The peak broadening contribution of the instrument was determined for the refinement of the standard $Na_2Ca_3Al_2F_{14}$. The main contribution of parasitic diffraction peaks arising from the environment of the sample was removed by a radial oscillating collimator.

The Rietveld refinements were performed using the Reflex module of the software Materials Studio 2019, and the starting atomic coordinates were provided by the single-metal reported structures.

3.3. Scanning Electron Microscopy-Energy Dispersive X-Ray Spectroscopy (SEM-EDX)

Details about the morphology of the samples were determined through Scanning Electron Microscopy (SEM). The samples were studied at the SEM facility at the Instituto de Ciencia de Materiales de Madrid (ICMM), where they operate a FE-SEM FEI Nova NANOSEM 230 microscope equipped with an Everhard-Thornley ETD detector and an operating voltage between 5 and 15 kV. Some of the studies were occasionally performed at the Servicio Interdepartamental de Investigación (SIdI) at the Universidad Autónoma de Madrid (Spain), with a Hitachi S-3000 N microscope equipped with a Bruker Quantax EDS XFlash 6I30 analyzer.

The samples were prepared by placing the crystals on a double-sided adhesive conductive carbon tape that was attached to a flat aluminum sample holder, which was metallized with a gold layer of 127.5 Å with a Leica EM ACE200 sputter.

A semi-quantitative analysis of the composition of the samples, and therefore of the ratio between metal ions were determined by Energy Dispersive X-Ray Spectroscopy (EDX). The EDX microanalyses were performed with an EDAX Apollo 10–300 mm detector. Several points of the crystals were recorded, generally from the basal planes and the body of the crystal. The ratio between the metals was calculated following the formula:

$$\text{ratio M1} = \frac{\text{Atomic \% M1}}{\text{Atomic \% M1} + \text{Atomic \% M2}} \times 10$$

3.4. Magnetic characterization

3.4.1. Magnetometry

Magnetometry experiments were performed at the Magnetometry and low temperatures facility at the Instituto de Ciencia de Materiales de Madrid (ICMM). For the DC magnetization measurements, a MPMS-5 S SQUID magnetometer from Quantum Design (San Diego, USA) was operated in a temperature range from 1.8 to 400 K and a range of magnetic fields up to 5 T. The AC magnetic susceptibility measurements were performed on a multipurpose platform (physical property measurement system, PPMS) from Quantum Design (San Diego, USA) in a temperature range from 1.8 to 400 K, with an excitation modulate field of 1–10 Oe in amplitude and the frequency range from 10 Hz to 10 kHz. Additionally, the AC susceptibility was measured under a superimposed DC field in the range from 0 to 9 T.

3.4.2. Thermal measurements

Heat capacity experiments were performed at the Magnetometry and low temperatures facility at the Instituto de Ciencia de Materiales de Madrid (ICMM), where they operate a PPMS platform (physical property measurement system, PPMS) with the heat pulse method. The sample was attached with Apiezon N-grease to a small sapphire plate, which has a calibrated heater and a Cernox thermometer in the bottom part. By a heat pulse and the measurement of the temperature relaxation, the heat capacity is calculated under the approach of one or two relaxation times. A previous measurement of the heat capacity produced by the grease addenda was made before each measurement. The temperature range covered in these measurements ranged from 1.8 to 300 K, and the applied external magnetic field extended ranged from 0 to 9 T.

3.5. Computational details

Theoretical calculations by periodic density functional theory (DFT) were performed at Instituto Madrileño de Estudios Avanzados-Energía (iMDEA-Energía). As a starting point, crystallographic data of each structure were used. Geometry and electronic structure were performed using Plane-wave density functional (PW-DF) calculations with the VASP package.[2,3] The total energies corresponding to the optimized geometries of all samples were calculated using the spin polarized version of the Perdew-Burke-Ernzerhof (PBE).[4] The effect of the core electrons on the valence electron density was described by the projector augmented wave (PAW) method.[5,6] The cutoff for the kinetic energy of the plane waves was set to 450 eV throughout, which after extensive tests proved to ensure a total energy convergence better than 10−5 eV.

3.6. Catalysis experiments

3.6.1. Reverse-water gas shift reaction (RWGS)

The reaction is carried out in a continuous mode at three different temperatures (700, 600 and 500 ºC) with a 2.5 hour hold stage at each temperature. The higher temperature was selected as a starting point to avoid the Sabatier reaction (transformation of CO_2 into CH_4)[7] which generates undesired byproducts like methane, and the Boudouard reaction (conversion of CO into CO_2)[8] which results in carbon deposition which deactivates the catalyst.

The reactions are carried out in a fixed-bed tubular reactor with an external diameter of 6 mm, an internal diameter of 4 mm and a length of 280 mm, with its corresponding hinged tubular furnace. Both reactor and furnace are connected to a HP 6890 gas chromatograph, which is equipped with a SUPELCO® Carboxen 1010 PLOT column and a thermal conductivity detector (TCD), which operate simultaneously.

3.6.2. Photooxidation of sulfides

All reagents and solvents employed were commercially available and used as received without further purification. Prior to the reaction, the catalyst was activated by heating it at 100 ºC overnight. In a SUPELCO glass microreactor, 0.135 mmol of the corresponding sulfide, 2 mol% of the catalyst, ScIrPF-13 (based on Ir), and 0.5 mL of acetonitrile were mixed. The resulting suspension was stirred in an O_2 atmosphere (balloon) and irradiated with 2 blue LED light 30 W lamps. The reactions were monitored by gas chromatography.

Flame Ionization Detector-Gas Chromatography (FID-GC) measurements were conducted at the Institute of Materials Sciences of Madrid (ICMM), with a Konik 5000C chromatography system, equipped with a flame ionization detector. Mesitylene was used as a standard in a 1:1 ratio with the substrates.

3.7. References

(1) Fernández-Ruiz, R. TXRF Spectrometry in the Bioanalytical Sciences: A Brief Review. *X-Ray Spectrometry* **2022**, *51* (3), 279–293. https://doi.org/10.1002/xrs.3243.

(2) Kresse, G.; Furthmuller, J. Efficiency of Ab-Initio Total Energy Calculations for Metals and Semiconductors Using a Plane-Wave Basis Set. *Comput Mater Sci* **1996**, *6*, 15–50.

(3) Kresse, G.; Hafner, J. Ab Initio Molecular Dynamics for Liquid Metals. *Phys Rev B* **1993**, *47*, 558–561.

(4) P., P. JJ.; Burke, K.; Ernzerhof, M. Generalized Gradient Approximation Made Simple. *Phys Rev Lett* **1996**, *77*, 3865.

(5) Kresse, G.; Joubert, D. From Ultrasoft Pseudopotentials to the Projector Augmented-Wave Method. *Phys Rev B* **1999**, *56*, 1758–1775.

(6) Blöchl, P. E. Projector Augmented-Wave Method. *Phys Rev B* **1994**, *50*, 17943–17979.

(7) Roiaz, M.; Monachino, E.; Dri, C.; Greiner, M.; Knop-Gericke, A.; Schlögl, R.; Comelli, G.; Vesselli, E. Reverse Water-Gas Shift or Sabatier Methanation on Ni(110)? Stable Surface Species at Near-Ambient Pressure. *J Am Chem Soc* **2016**, *138* (12), 4146–4154. https://doi.org/10.1021/jacs.5b13366.

(8) Lim, J. Y.; McGregor, J.; Sederman, A. J.; Dennis, J. S. The Role of the Boudouard and Water–Gas Shift Reactions in the Methanation of CO or CO2 over Ni/γ-Al2O3 Catalyst. *Chem Eng Sci* **2016**, *152*, 754–766. https://doi.org/10.1016/j.ces.2016.06.042.

─ CHAPTER 4 ─

Influence of the Synthesis and Crystallization Processes on the Cation Distribution in a Series of Multivariate Rare-Earth Metal–Organic Frameworks and Their Magnetic Characterization

4.1. Introduction

Controlling the distribution of multiple cations within the same framework remains a challenge as it is difficult to direct the insertion of such cations into specific positions. Bearing in mind that the characteristics of a material are determined by its chemical composition and its overall structure, it is crucial to be able to tune how the metal cations are arranged within the framework. The ongoing investigation of my group on multi-metal MOFs has been focused on frameworks that display rod-shaped SBUs because they can lead to different atomic sequencing scenarios, as detailed in Chapter 1. In a previously reported work of our group, the MOF family ZnPF-1 (Zinc Polymeric Framework-1), constituted by the organic linker 4,4'-(hexafluoroisopropylidene)bis(benzoic acid) (H_2hfipbb) and zinc cations, was the subject of a study of the influence of the initial metal combination on the final sequence within the structure.[1,2] For this rod-shaped SBU MOF, selecting the appropriate initial ratio and metal combination was key to control the introduction of the second metal cation, the coordination environment of the atoms and the arrangement within the SBU.

Understanding the synthesis and crystallization process of a MOF is crucial in order to control and direct the distribution of the cations, and thus generate materials with controllable metal combinations. To further explore this topic, we gravitated towards another highly related MOF family reported by our group, RPF-4 (Rare-Earth Polymeric Framework-4), based on the same organic linker, H_2hfipbb, and rare-earth cations (Figure 4.1).[3] Contrary to the previous example with transition metals, this topology can be obtained in single-metal form with an array of lanthanide ions and single-metal RPF-4, with formula $Ln_2(hfipbb)_3$ can be obtained for Ln = La, Ce, Pr, Nd, Sm, Eu, Gd, Tb, Dy, Ho, Er, Yb. This MOF family displays polymorphism, and up to three different polymorphs can be obtained during the synthesis,[4] and for this study we will focus on the

α polymorph. α-RPF-4 crystallizes in the orthorhombic *Pnan* space group, and it consists of rod-shaped SBUs with nine-coordinated Ln^{3+} cations, connected through the organic linkers generating channels that run parallel to the SBUs along the crystallographic *a* axis.

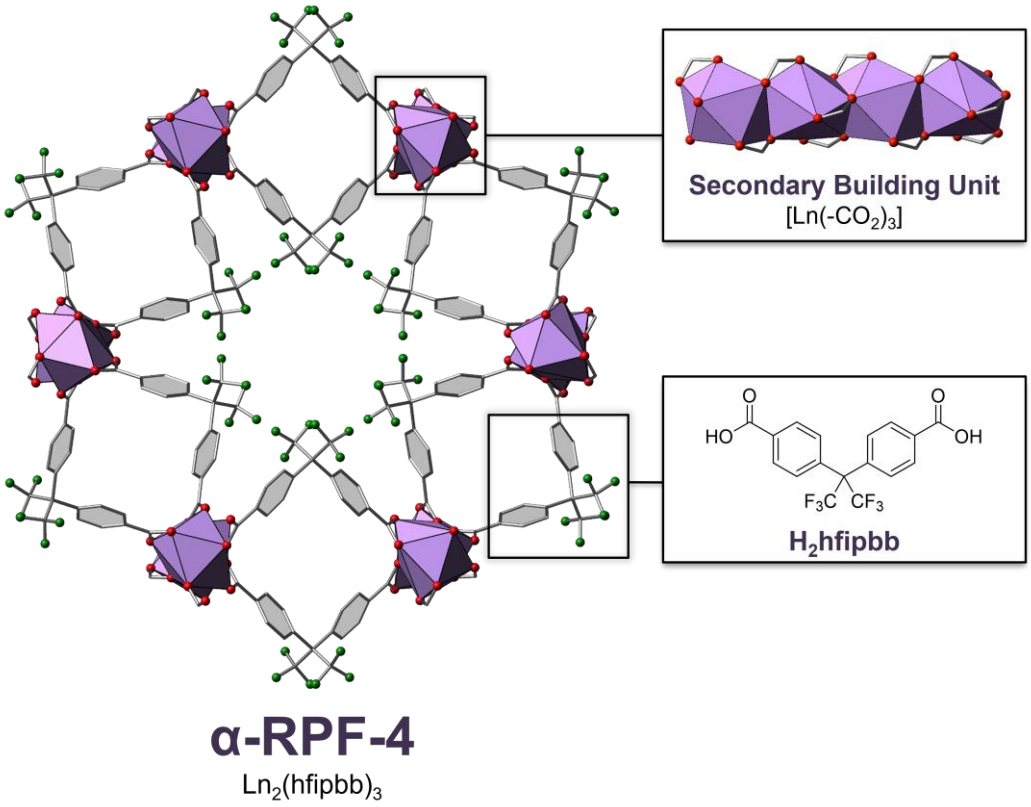

Figure 4.1. Representation of the crystal structure of α-RPF-4 viewed along the *a* axis. O atoms are displayed in red, C in grey, F in green, Ln in purple polyhedra. H atoms are omitted for clarity.

We aimed to study an array of lanthanide binary combinations of RPF-4, and investigate the role of the initial metal ratio on the crystallization process of the framework. Our first step was to synthesize and characterize the corresponding single-metal samples, as it is essential to understand their behavior before moving on to the more complex binary

samples, and this preliminary study helped to shed light on how the multi-metal samples behave.

Powder X-ray diffraction patterns of all the samples confirmed that in all cases α-RPF-4 (from now on referred to as RPF-4) was formed as a pure crystalline phase. In order to determine the atomic and mesoscopic arrangement of the cations within the SBU of the framework, we used a combination of diffraction and microscopy techniques. We studied the morphology of the crystals by SEM, and regarding the local composition of the multi-metal systems, we carried out EDX microanalyses throughout both the basal planes and the body of several individual crystals. As for the average bulk composition of the samples, we carried out TXRF measurements. The combination of the data obtained through these techniques, and the results from neutron powder diffraction experiments and DFT calculations led to understanding the crystallization mechanism of this MTV-MOF system. Our findings illustrate that it is crucial to understand the crystallization mechanism of a multi-metal MTV-MOF in order to gain control over the atomic sequencing within a complex material and to be able to tune its composition for any application.

4.2. Synthesis of RPF-4: single- and multi-metal binary combinations

All reagents and solvents employed were commercially available and used as received without further purification: 4,4′-(hexafluoroisopropylidene)bis(benzoic acid), H_2hfipbb (>98%, TCI); lanthanum nitrate hexahydrate, $La(NO_3)_3 \times 6H_2O$ (99.9%, Alfa Aesar); cerium nitrate hexahydrate, $Ce(NO_3)_3 \times 6H_2O$ (99%, Aldrich); gadolinium nitrate hexahydrate, $Gd(NO_3)_3 \times 6H_2O$ (99.9%, Strem Chemicals); dysprosium nitrate hexahydrate, $Dy(NO_3)_3 \times 6H_2O$ (99.9%, Strem Chemicals); holmium nitrate hydrate, $Ho(NO_3)_3 \times nH_2O$ (99.9%, Strem Chemicals); erbium nitrate pentahydrate (99.99%, Alfa Aesar); ytterbium nitrate pentahydrate, $Yb(NO_3)_3 \times 5H_2O$ (99.9%, Strem Chemicals); ethanol absolute (Scharlau); acetone (99.6%, Labkem).

4.2.1. Synthesis of single-metal RPF-4

0.115 mmol of $Ln(NO_3)_3 \times nH_2O$ (Ln = La, Ce, Nd, Eu, Gd, Tb, Dy, Ho, Er, Yb) and 0.176 mmol of H_2hfipbb were dissolved in a solvent mixture of 7.5 mL of absolute ethanol and 5 mL of water. The mixture was placed in a 50 mL Teflon-lined steel autoclave and heated overnight in an oven at 160 °C. After cooling to room temperature, the crystals were filtered and washed with water (3x10 mL) and acetone (3x10 mL).

4.2.2. Synthesis of multi-metal RPF-4

All the multi-metal samples were obtained following the same synthetic strategy as the single-metal MOFs. The amount of metal salt was adjusted according to every combination. All the quantities of metal salts used in all the synthesis are listed in Table 4.1. To illustrate how each combination was obtained, an example is given as follows: for the synthesis of the La-Yb 1:9 combination, $La(NO_3)_3 \times 6H_2O$ (0.0115 mmol, 4.98 mg), $Yb(NO_3)_3 \times 5H_2O$ (0.1035 mmol, 46.53 mg) and H_2hfipbb (0.176 mmol, 70.45 mg) were dissolved in 7.5 mL of absolute ethanol and 5 mL of water. The mixture was placed in a

Teflon-lined steel autoclave and heated overnight in an oven at 160 °C. After cooling to room temperature, the crystals were filtered and washed with water and acetone.

Table 4.1. Synthesis ratios for the multi-metal RPF-4 binary combinations.

	Molar code	$La(NO_3)_3 \times 6H_2O$		$Yb(NO_3)_3 \times 5H_2O$	
		mg	mmol	mg	mmol
La-Yb	1:9	4.98	0.01	46.53	0.1
	2:8	9.97	0.02	41.36	0.09
	3:7	14.95	0.03	36.19	0.08
	4:6	19.94	0.05	31.02	0.07
	1:1	24.92	0.06	25.85	0.06
	6:4	29.91	0.07	20.68	0.05
	7:3	34.89	0.08	15.51	0.03
	8:2	39.88	0.09	10.34	0.02
	9:1	44.86	0.1	5.17	0.01
La-Ce	**Molar code**	**$La(NO_3)_3 \times 6H_2O$**		**$Ce(NO_3)_3 \times 6H_2O$**	
		mg	mmol	mg	mmol
	1:9	4.98	0.01	45.39	0.1
	3:7	14.95	0.03	35.30	0.08
	1:1	24.92	0.06	25.22	0.06
	7:3	34.89	0.08	15.13	0.03
	9:1	44.86	0.1	5.04	0.01
La-Gd	**Molar code**	**$La(NO_3)_3 \times 6H_2O$**		**$Gd(NO_3)_3 \times 6H_2O$**	
		mg	mmol	mg	mmol
	1:9	4.98	0.01	46.77	0.1
	1:1	24.92	0.06	25.98	0.06
	9:1	44.86	0.1	5.20	0.01
La-Dy	**Molar code**	**$La(NO_3)_3 \times 6H_2O$**		**$Dy(NO_3)_3 \times 6H_2O$**	
		mg	mmol	mg	mmol
	1:9	4.98	0.01	47.31	0.1
	1:1	24.92	0.06	26.28	0.06
	9:1	44.86	0.1	5.26	0.01
Yb-Gd	**Molar code**	**$Yb(NO_3)_3 \times 5H_2O$**		**$Gd(NO_3)_3 \times 6H_2O$**	
		mg	mmol	mg	mmol
	1:9	5.17	0.1	46.77	0.01
	1:1	25.85	0.06	25.98	0.06
	9:1	46.53	0.01	5.20	0.1
Yb-Dy	**Molar code**	**$Yb(NO_3)_3 \times 5H_2O$**		**$Dy(NO_3)_3 \times 6H_2O$**	
		mg	mmol	mg	mmol
	1:9	5.17	0.1	47.31	0.1
	1:1	25.85	0.06	26.28	0.06
	9:1	46.53	0.01	5.26	0.01
Yb-Er	**Molar code**	**$Yb(NO_3)_3 \times 5H_2O$**		**$Er(NO_3)_3 \times 5H_2O$**	
		mg	mmol	mg	mmol
	1:1	25.85	0.06	25.49	0.06

4.3. Single-metal RPF-4: characterization and discussion

We synthesized single-metal RPF-4 with lanthanide ions of different atomic radii: La^{3+}, Ce^{3+}, Gd^{3+}, Dy^{3+}, Er^{3+} and Yb^{3+}. In Figure 4.2, the experimental powder X-ray diffraction (PXRD) patterns of all the synthesized single-metal RPF-4 samples are compared to the pattern calculated from the data of La-RPF-4 taken from reference 3, displayed in black. The patterns match perfectly, so it is evident that all the MOFs display the same structure type, and no other crystalline phase is present.

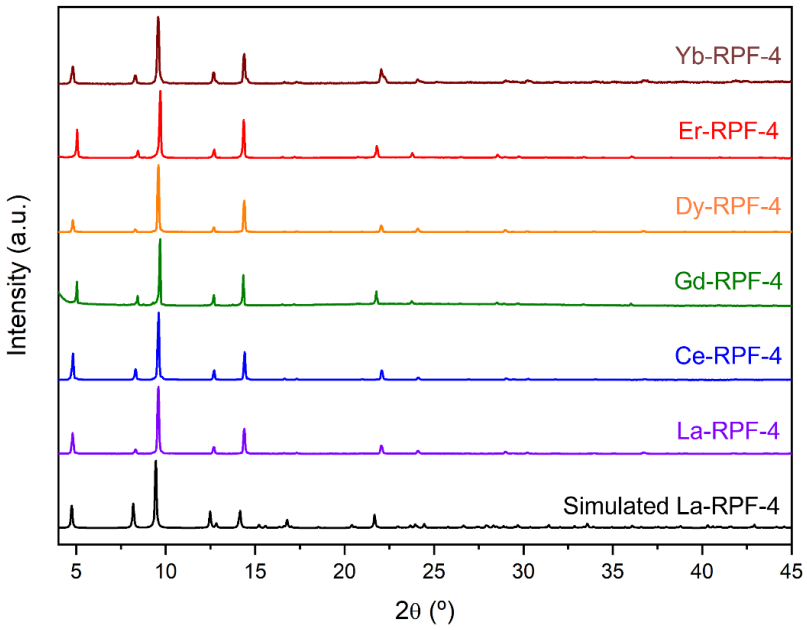

Figure 4.2. PXRD patterns of the single-metal RPF-4 samples compared to the calculated pattern of La-RPF-4 (black).[3]

As mentioned in the introduction, my group carried out an extensive study of multi-metal combinations of the MOF family ZnPF-1, and depending on the metals involved in the combinations and their arrangement within the rod-shaped SBUs of the MOF, the SEM-EDX study of the crystals of the samples showed that they displayed either mesoscopic

gradients (core-shell distribution) or a homogeneous appearance. In the case of RPF-4, even if the crystal structure is compatible with any metal from the lanthanide series, we do not have knowledge on how each metal and its chemical behavior impacts the overall morphology of the crystals. To determine if the synthesis of each MOF follows the same crystallization mechanism, we carried out a detailed examination of the crystals of each MOF via SEM, and we discovered differences in the morphological features of the crystals depending on the metal cation of each MOF. Figure 4.3 showcases the SEM images of the single-metal samples, and La-RPF-4 stands out as it is the only sample that displays crystals with uneven textures and presence of holes, in contrast to the rest of the samples that display smooth crystals with well-defined faces, and no obvious defects.

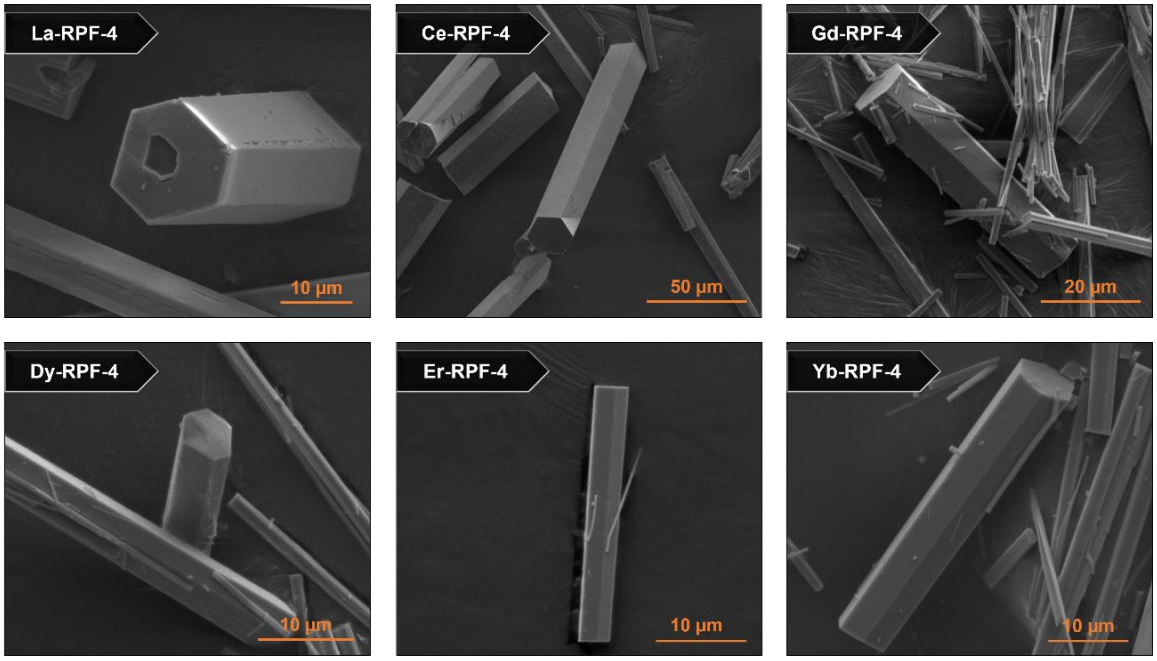

Figure 4.3. SEM images of the single-metal RPF-4 samples.

The presence of hollow crystals, with holes in their inner part, suggests that the crystallization of La-RPF-4 follows an Ostwald ripening mechanism (Figure 4.4), based on initial nucleation events, and subsequent dissolution of the inner part of the crystal, followed by the growth of the external faces.[5,6] This particular crystallization pathway generates crystals with visible indents, cracks and holes, and we observed a similar hollow morphology in a previous study of multi-metal combinations of the MOF family ZnPF-1.[1]

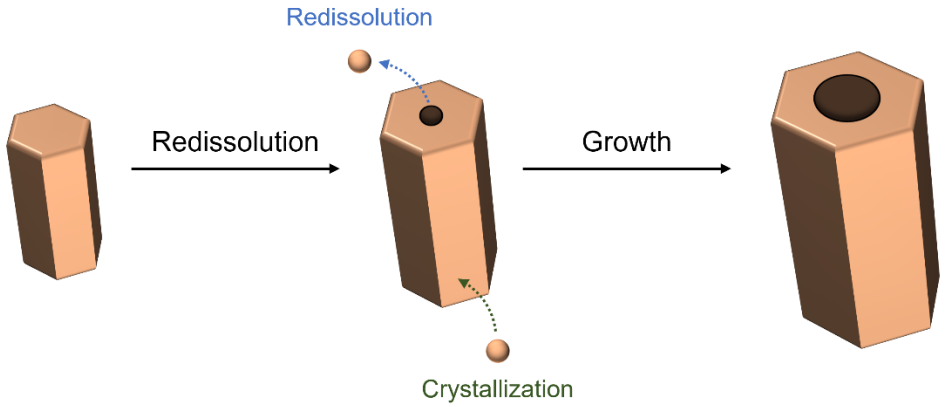

Figure 4.4. Schematic representation of the Ostwald ripening mechanism.

4.4. Multi-metal RPF-4: characterization and discussion

Given the different crystallization paths of the single-metal RPF-4 samples, in order to analyze the impact they have on the formation of a multi-metal MTV-MOF and on the incorporation of the different metals into the frameworks, we continued our study with binary combinations of rare-earths. When pondering what metal ratios to choose for these combinations, we considered three scenarios: in two of them, one metal element is in a significantly higher concentration than the other one, so it could potentially direct the formation of the framework (1:9 and 9:1); in the third scenario, both metals are in the same concentration, which can potentially lead to either the formation of an equimolar MTV system, or to a competition during the crystallization (1:1). Although these three are the main ratios we studied for most of the combinations, we did analyze additional ones when necessary, as detailed below.

As there is clear evidence that La-RPF-4 behaves in a different way than the rest of the rare-earth systems, we opted to explore and compare binary combinations with and without lanthanum.

4.4.1. Binary combinations with Lanthanum

La-Yb: Firstly, studying the combination of La with Yb would provide insight into the ability of the structure to withstand the incorporation of metals with different enough atomic radii (La = 1.95 Å; Yb = 1.75 Å). The PXRD patterns of all the samples are displayed in Figure 4.5, and they confirm that RPF-4 was obtained as a pure crystalline phase in all cases.

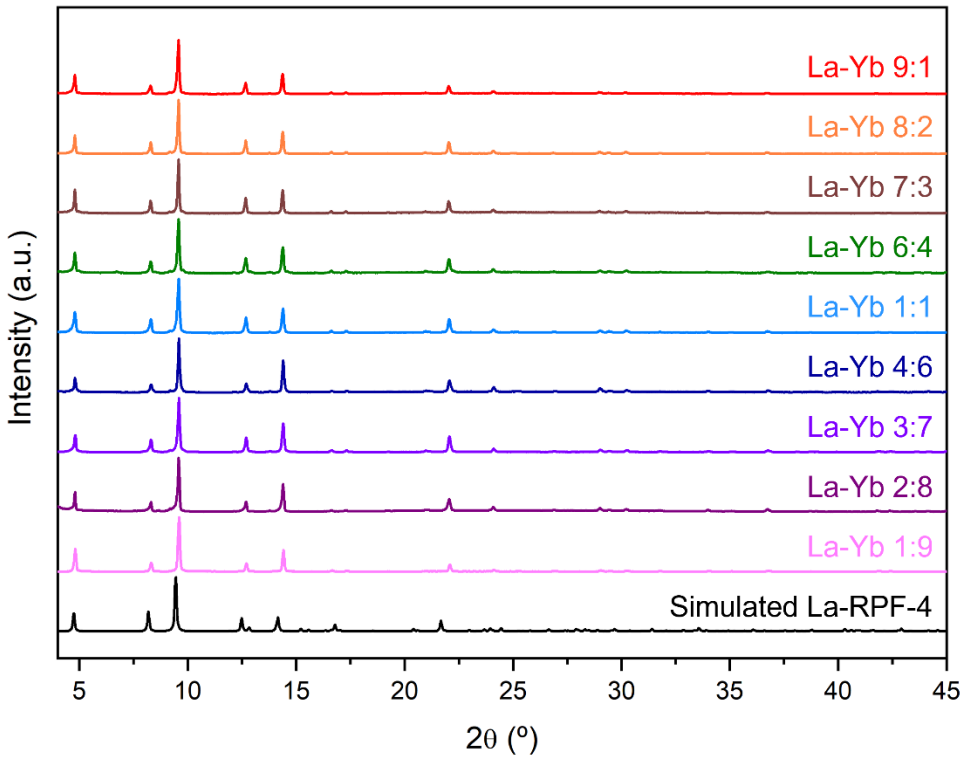

Figure 4.5. PXRD patterns of the La-Yb combination.

For the La-Yb 9:1 initial ratio, the SEM images show that the crystals display defective features such as inner holes and rough surfaces, analogous to the ones observed for La-RPF-4. Likewise, for the La-Yb 1:9 ratio, the morphology of the crystals is similar to that of Yb-RPF-4, with well-defined and smooth faces. In both cases, the EDX analysis confirms that the output ratios match the initial ones, which implies that a MTV-MOF is obtained and this metal combination can generate an atomic sequencing with insertion of ytterbium atoms in the lanthanum SBUs, and vice versa. In both cases, the crystallization mechanism seems to be driven by the element present in a higher proportion, as evidenced by the SEM images.

For synthesis reaction carried out with an 1:1 La-Yb initial ratio, despite the TXRF bulk analysis indicates a 4:6 average output ratio, the SEM study clearly revealed a co-existence of two types of crystals with different features and compositions, as determined by EDX: on one hand, crystals rich in lanthanum are found displaying morphologies similar to single-metal La-RPF-4; on the other hand, crystals rich in ytterbium with no presence of defects are also present, similar to those of single-metal Yb-RPF-4. These observations indicate that in the studied conditions, a MTV-MOF with equivalent amount of both elements cannot be obtained from an equimolar combination of lanthanum and ytterbium. Instead, there is a competition between both single-metal phases, which results in a product with compositionally segregated crystals. Considering that previous experiments with 9:1 and 1:9 initial ratios resulted in the formation of crystals with homogenous composition, the question arises of whether crystals with different metal combinations can be obtained by further modifying the initial ratios. Therefore, we studied additional initial La-Yb ratios. Interestingly, when gradually increasing the amount of lanthanum (La-Yb initial ratios 2:8, 3:7, 4:6), the EDX analyses showed that the output ratios were close to 1:9 in every case, and the morphological features of the crystals were equivalent to the ones displayed by Yb-RPF-4. We observed the same compositional bias for a gradually higher amount of ytterbium (La-Yb initial ratios 8:2, 7:3, 6:4), as the EDX results did not follow the growing concentration trend, and displayed a 9:1 ratio with morphological features similar to those of La-RPF-4. This clearly indicates that there is no gradual shift towards the phase coexistence. Instead, the MOF formation is governed by the metal element present in higher concentration, only allowing the insertion of a limited amount of the second metal element. Consequently, this combination of metals does not allow obtaining a MTV-MOF with the desired metal ratio nor adjustable metal sequences.

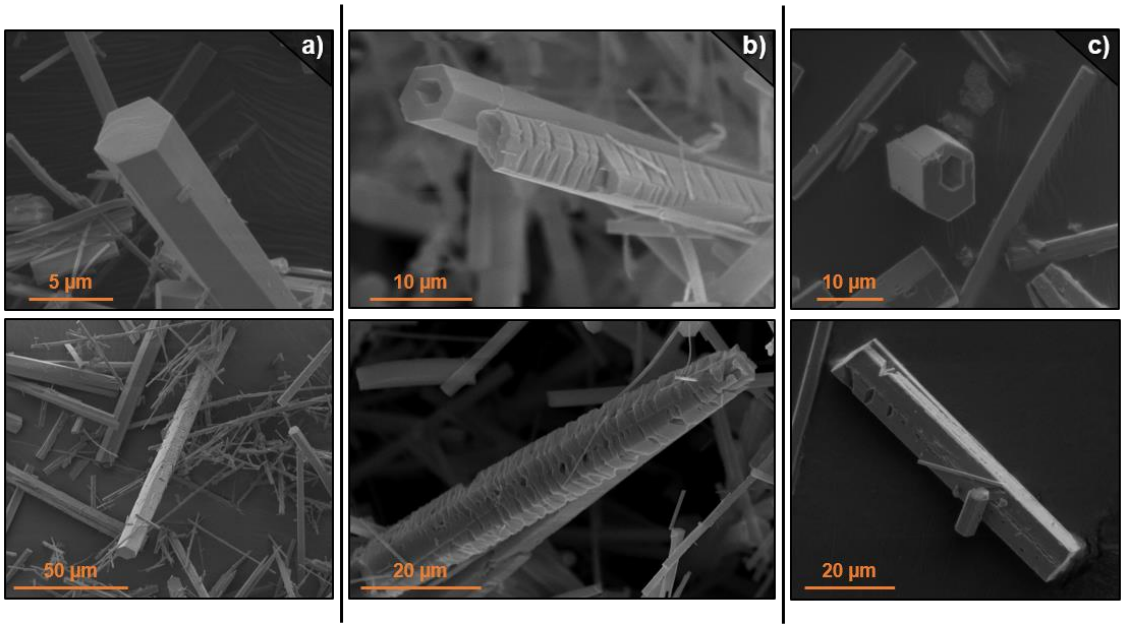

Figure 4.6. SEM images of crystals corresponding to LaYb-RPF-4 combinations

a) La-Yb 1:9; **b)** La-Yb 1:1; **c)** La-Yb 9:1.

La-Ce: Given the results obtained for La-Yb, we wondered what would happen if we combined elements with similar atomic radii, and for that reason we studied the La-Ce combination (atomic radius La = 1.95 Å; atomic radius Ce = 1.85 Å), with initial ratios of 1:9, 1:1 and 9:1. For the 1:9 and 9:1 ratios, the results are similar to the previous case as the outputs of the synthesis match the initial ones. However, for the equimolar ratio, it seems to be feasible to obtain a MTV-MOF as the EDX microanalysis results point to a homogeneous 1:1 ratio (within experimental error) for the whole sample.

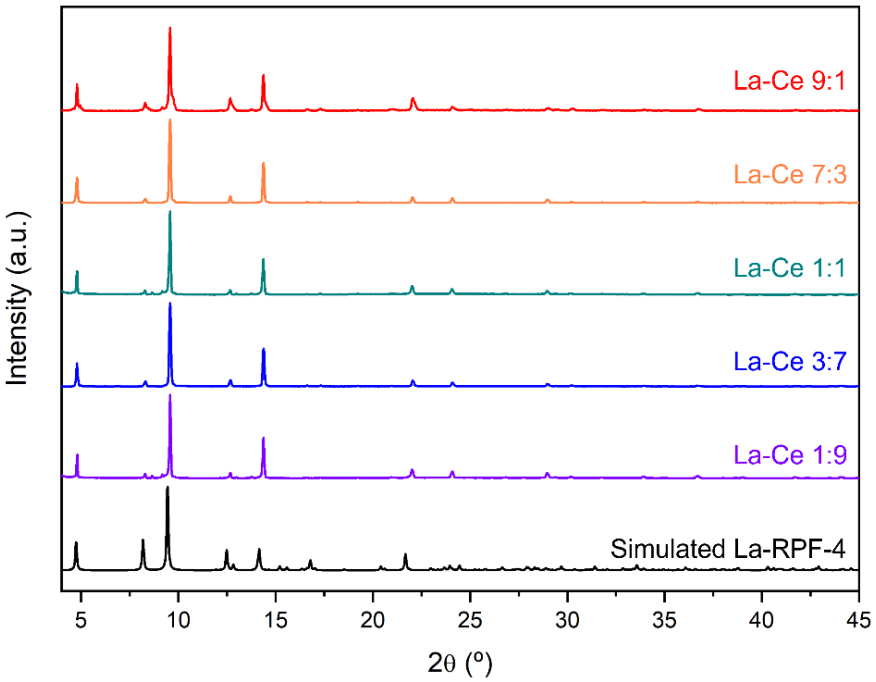

Figure 4.7. PXRD patterns of the La-Ce combination.

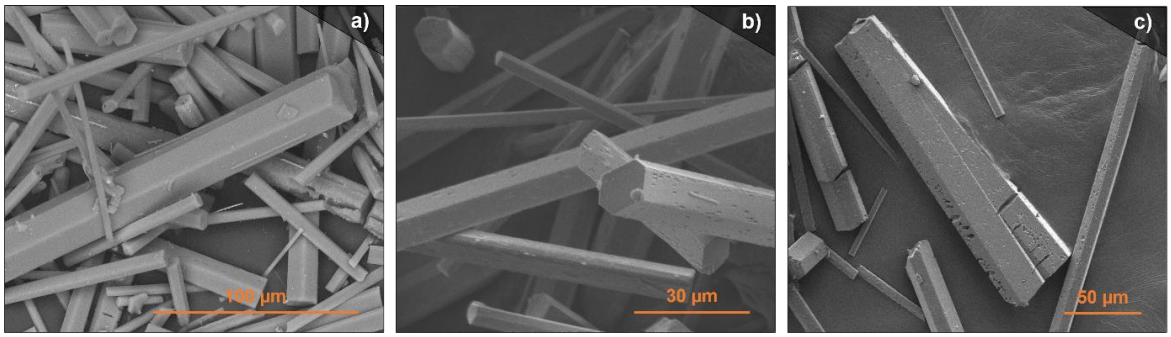

Figure 4.8. SEM images of crystals corresponding to LaCe-RPF-4 combinations.

a) La-Ce 1:9; **b)** La-Ce 1:1; **c)** La-Ce 9:1.

La-Gd: As in the previous examples we studied combinations of elements with similar (La-Ce) and different (La-Yb) atomic radii and observed very different behaviors, we wondered if there was a critical radii value that would induce a segregation scenario in the arrangement of the atoms within the SBU of the MOF. So, we carried out the synthesis

of combinations of lanthanum with metals further apart than cerium in the lanthanide series, in this case we chose gadolinium (atomic radius La = 1.95 Å; atomic radius Gd = 1.80 Å), and the initial metal ratios 1:9, 1:1 and 9:1. On one hand, for the non-equimolar initial ratios the results are consistent with our previous observations. On the other hand, the TXRF analysis of the sample with a 1:1 La-Gd ratio displayed a ratio of 3:7, and through SEM-EDX we found a coexistence of two types of crystals with different compositions. EDX analysis confirmed an uneven distribution of the metal ratios among the crystals, finding a 4:6 distribution in some of the measurements. Therefore, the combination of La with Gd does not seem to generate a MTV-MOF with an equimolar metal ratio. However, we did notice some values closer to the 1:1 ratio which were not observed for the La-Yb combination, which points to a higher compatibility between the metals of this combination.

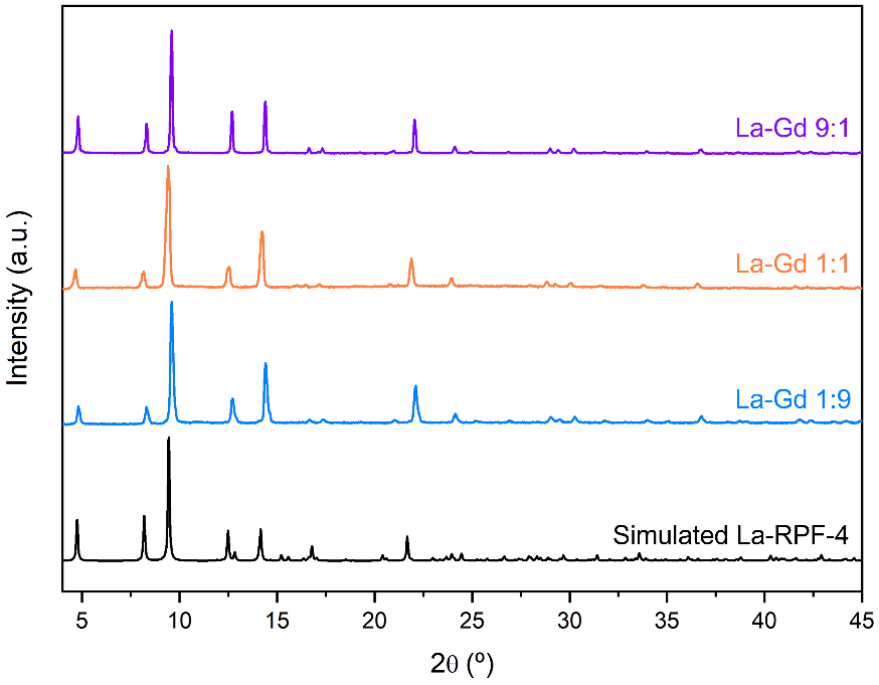

Figure 4.9. PXRD patterns of the La-Gd combination.

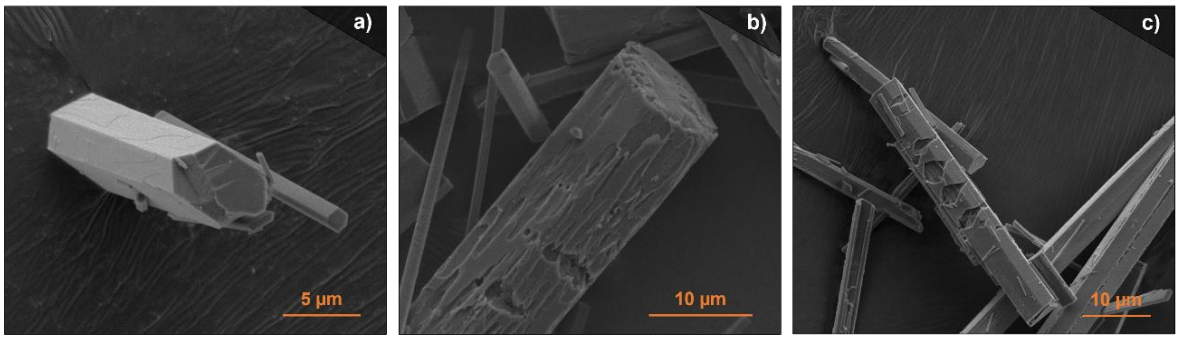

Figure 4.10. SEM images of crystals corresponding to LaGd-RPF-4 combinations

a) La-Gd 1:9; **b)** La-Gd 1:1; **c)** La-Gd 9:1.

La-Dy: We moved a bit further in the lanthanide series in order to find out which is the critical atomic radius that would result in a compositional segregation of the metals similar to that of La-Yb, so we synthesized 1:9, 1:1 and 9:1 combinations of La and Dy (atomic radius La = 1.95 Å; atomic radius Dy = 1.75 Å). Once again, the results for the 1:9 and 9:1 ratios are in line with the previous results of this chapter. Regarding the equimolar combination, the SEM analysis illustrated a coexistence of two types of crystals, with ratios ranging from 8:2, 1:1 and 4:6, and the average ratio of the bulk of the sample was confirmed to be 6:4 through TXRF. In this case of the combination of La with Dy, it is also not possible to obtain a MTV-MOF with an equimolar metal ratio. Yet, in the same fashion as the La-Gd combinations, we did notice the presence of some values closer to the 1:1 ratio which were not observed for the La-Yb combination.

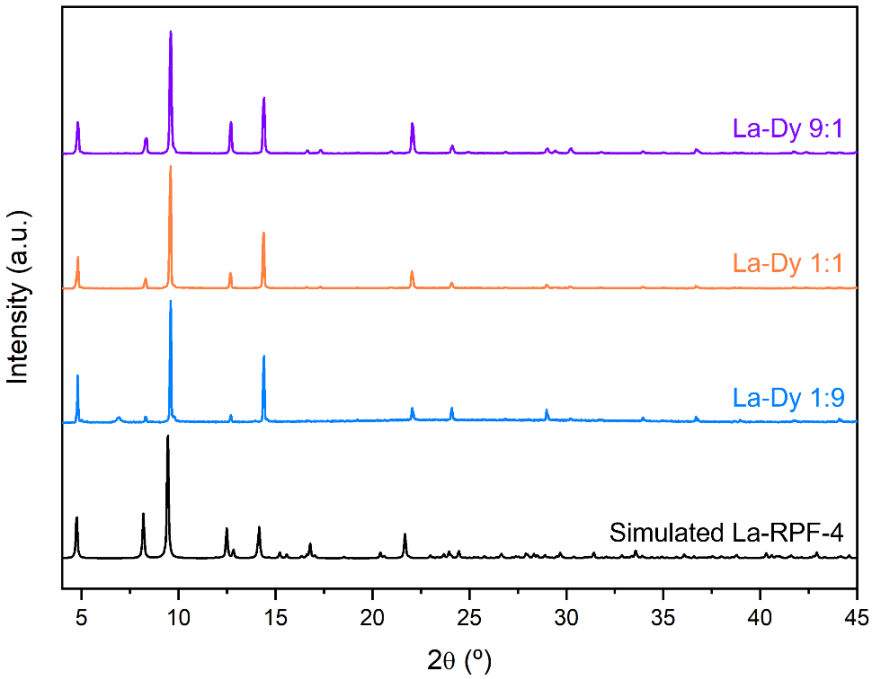

Figure 4.11. PXRD patterns of the La-Dy combination.

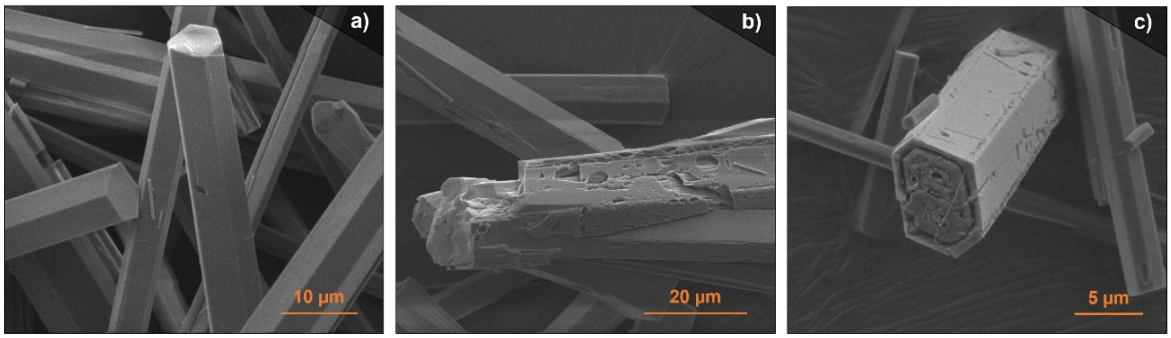

Figure 4.12. SEM images of crystals corresponding to LaDy-RPF-4 combinations

a) La-Dy 1:9; **b)** La-Dy 1:1; **c)** La-Dy 9:1.

In light of these results, it seems that there is a correlation between the metals involved in the binary combination and the possibility to generate a multi-metal MTV-MOF with an even distribution of homogeneous crystals. It seems that, although MTV-MOFs are formed in all cases, a compositional segregation is clearly generated for certain combinations, which are related to differences in the crystallization process, as suggested by the clear changes in the features of the crystals, and these differences are more evident for combinations with higher differences in the atomic radii.

4.4.2. Binary combinations not involving Lanthanum

As pointed out previously in this chapter, La-RPF-4 follows a particular crystallization mechanism which has a clear impact on the formation of MTV-MOFs. We wanted to find out if other binary combinations of metals with different atomic radii but not involving La, and therefore following the same crystallization pathway, would also display a compositional segregation, and thus not allowing the formation of a MTV-MOF with the desired atomic sequence. Thus, we prepared samples of Yb-Dy and Yb-Gd with the initial ratios 1:9, 1:1, 9:1. When one of the metals is in excess (1:9 and 9:1 initial ratios), both EDX and TXRF results show that the output ratio coincides with the initial one, and the morphology of the crystals matches the corresponding single-metal samples. However, for the 1:1 ratio, while all the crystals of both combinations displayed a smooth and defect-free surface, we noticed a compositional bias for Yb-Gd. EDX microanalysis showed that the average output for Yb-Gd was 3:7, and considering that the sample does not display compositional segregation, we ascribed this bias to kinetic effects, which implies that the incorporation rate of Gd seems to be faster than that of Yb.

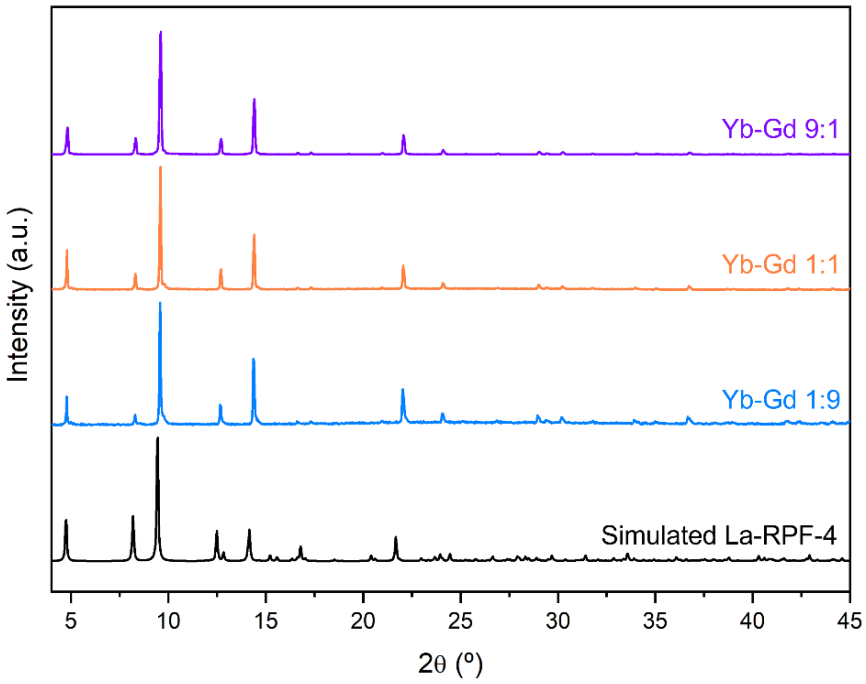

Figure 4.13. PXRD patterns of the YbGd-RPF-4 combination.

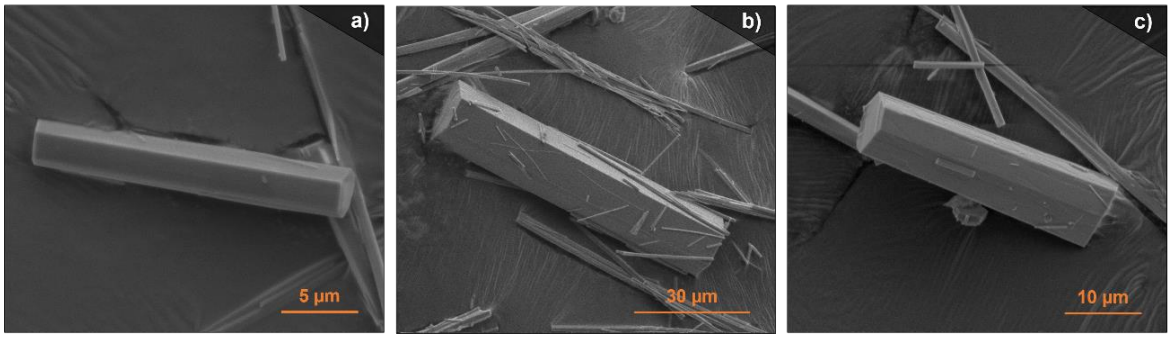

Figure 4.14. SEM images of crystals corresponding to YbGd-RPF-4 combinations

a) Yb-Gd 1:9; **b)** Yb-Gd 1:1; **c)** Yb-Gd 9:1.

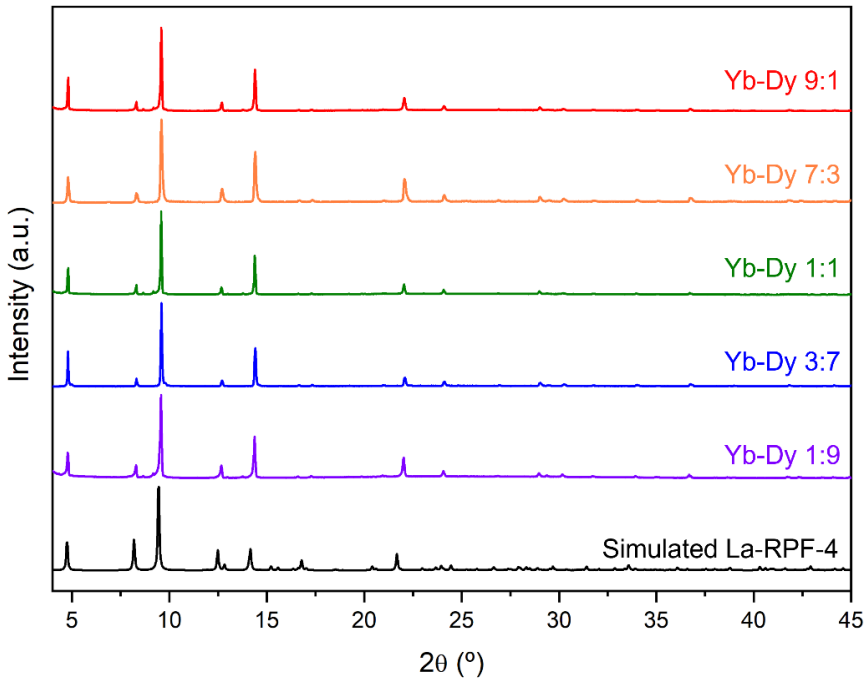

Figure 4.15. PXRD patterns of the YbDy-RPF-4 combination.

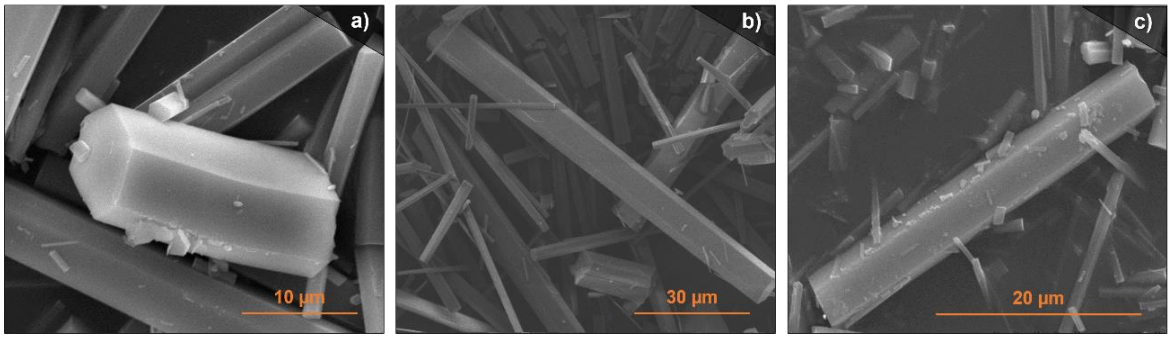

Figure 4.16. SEM images of crystals corresponding to YbDy-RPF-4 combinations

a) Yb-Dy 1:9; **b)** Yb-Dy 1:1; **c)** Yb-Dy 9:1.

As the selected metals from the lanthanide series have similar atomic number and X-ray scattering factors, it is difficult to identify the possible sequencing scenarios (complete or partial segregation, random distribution, formation of domains, or sequencing) happening in the SBUs using X-ray diffraction techniques. For a deeper insight into the atomic distribution, we carried out neutron powder diffraction (NPD) experiments for which we selected the combination of Yb and Er since there is enough difference between their coherent scattering lengths (12.43 and 7.79 fm, respectively) so that each element can be easily discerned. We prepared samples of the 1:9, 1:1 and 9:1 initial ratios, and the PXRD patterns of the samples are displayed in Figure 4.17. The results are similar to our previous observations for binary combinations of RPF-4 without lanthanum. The SEM analysis revealed that all the samples are homogeneous and display defect-free crystals (Figure 4.18) Regarding the composition, EDX and TXRF bulk analysis results show that the initial metal ratios match the output. For the 1:9 and 9:1 combinations, the NPD refinements (Figure 4.21 and Figure 4.22) converge for a chemical occupancy of the metal atoms of 0.1 and 0.9, and 0.9 and 0.1, respectively. For the 1:1 ratio, the NPD measurements did not evidence any additional symmetry nor phase change, and the refinement successfully converged for a 50% occupancy of each rare-earth atom at the same crystallographic site (Figure 4.23) Thus, we were able to rule out other possible sequencing scenarios such as the formation of monometallic domains or cations alternated in the same rod.

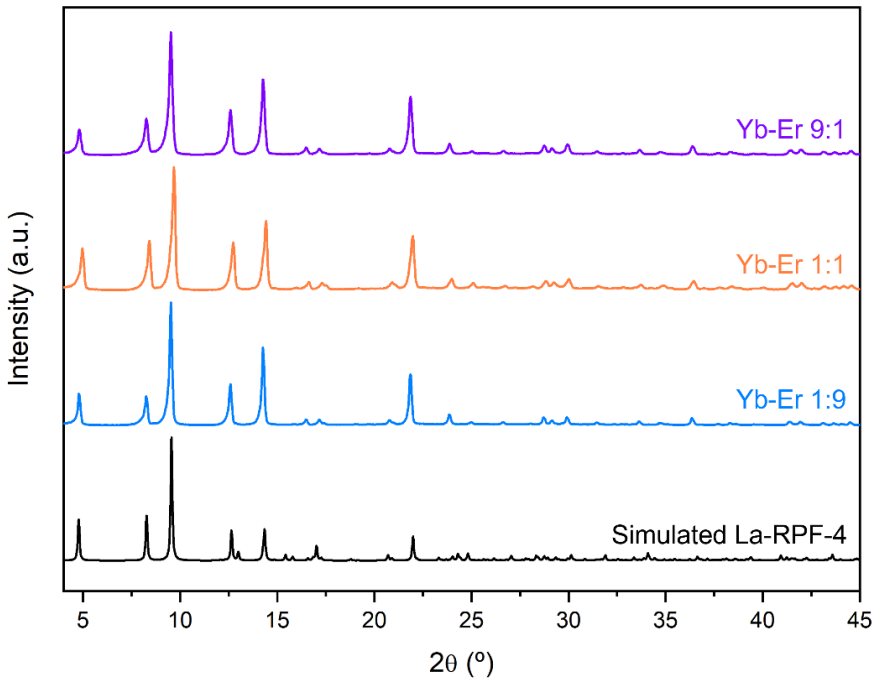

Figure 4.17. PXRD patterns of the YbEr-RPF-4 combination.

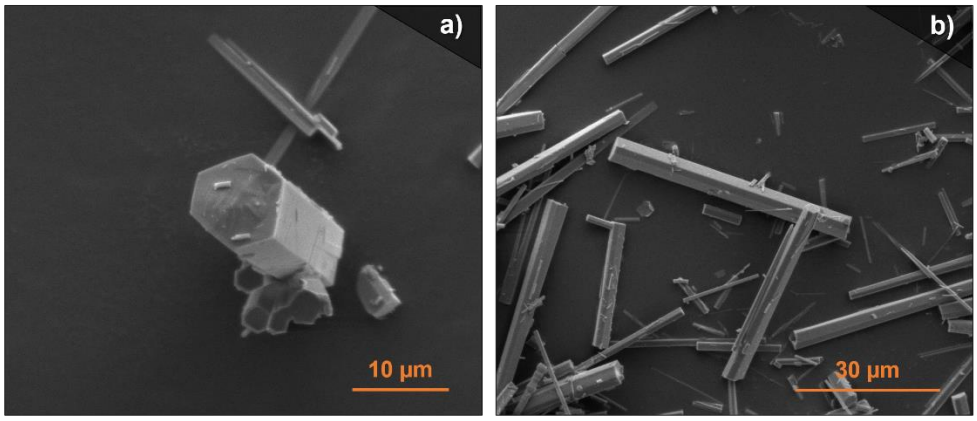

Figure 4.18. SEM images of crystals corresponding to the 1:1 Yb-Er combination.

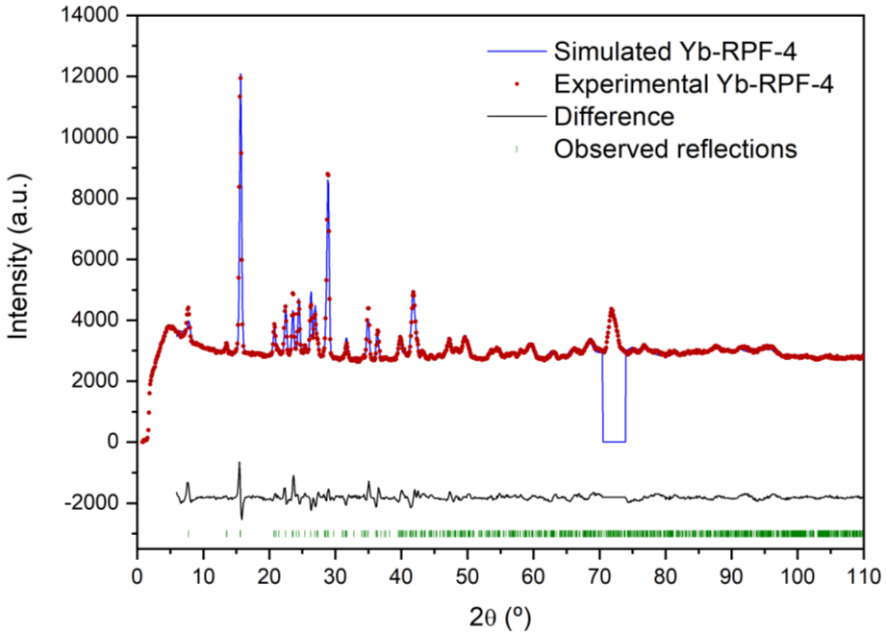

Figure 4.19. NPD pattern and Rietveld refinement of Yb-RPF-4. Rwp = 3.10%; Rp = 2.10%. The broad peak broad peak at 70–74° corresponds to the vanadium sample holder.

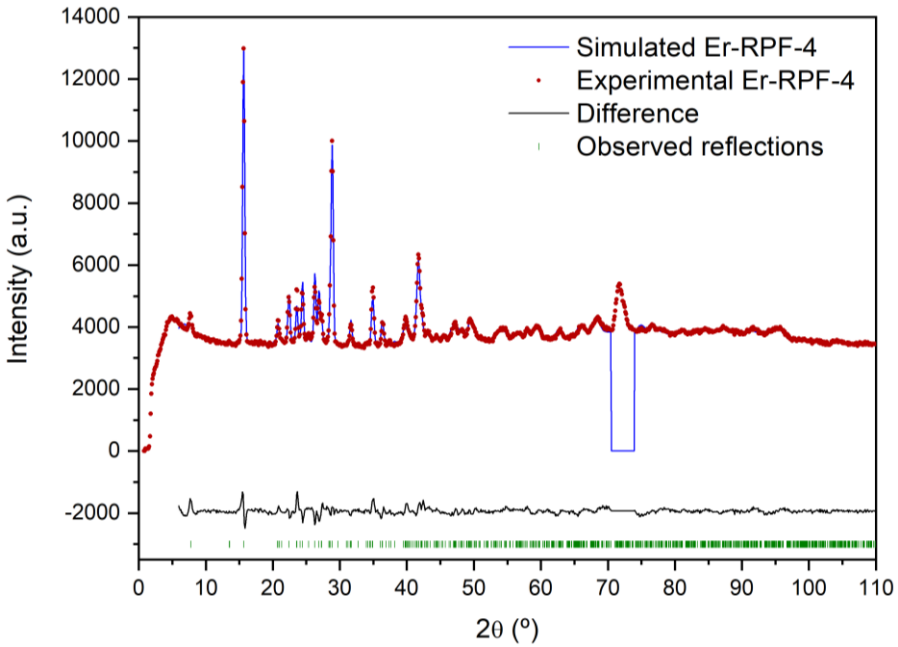

Figure 4.20. NPD pattern and Rietveld refinement of Er-RPF-4. Rwp = 2.23%; Rp = 1.57%. The broad peak broad peak at 70–74° corresponds to the vanadium sample holder.

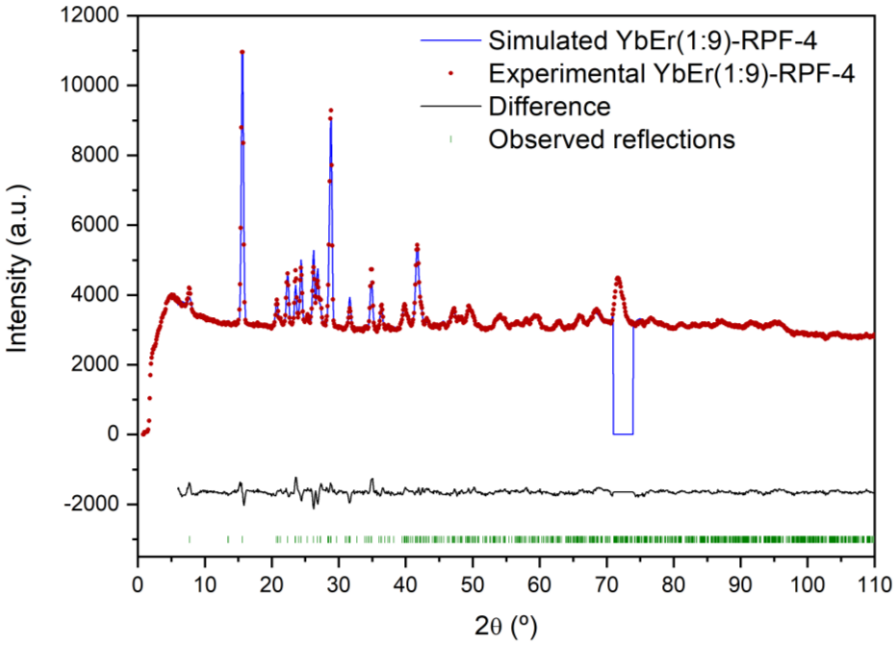

Figure 4.21. NPD pattern and Rietveld refinement of YbEr(1:9)-RPF-4. Rwp = 2.06%; Rp = 1.46%. The broad peak broad peak at 70–74° corresponds to the vanadium sample holder.

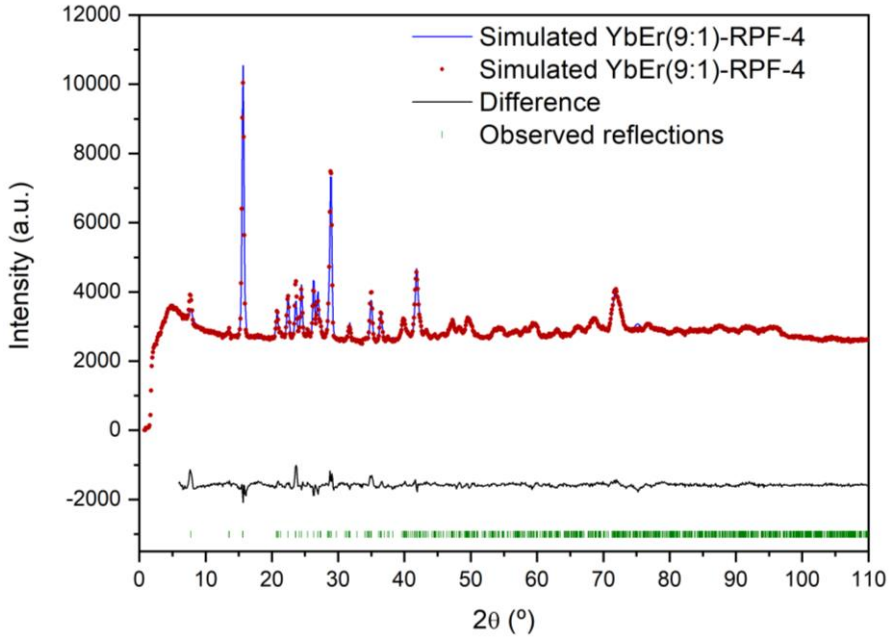

Figure 4.22. NPD pattern and Rietveld refinement of YbEr(9:1)-RPF-4. Rwp = 2.13%; Rp = 1.44%. The broad peak broad peak at 70–74° corresponds to the vanadium sample holder.

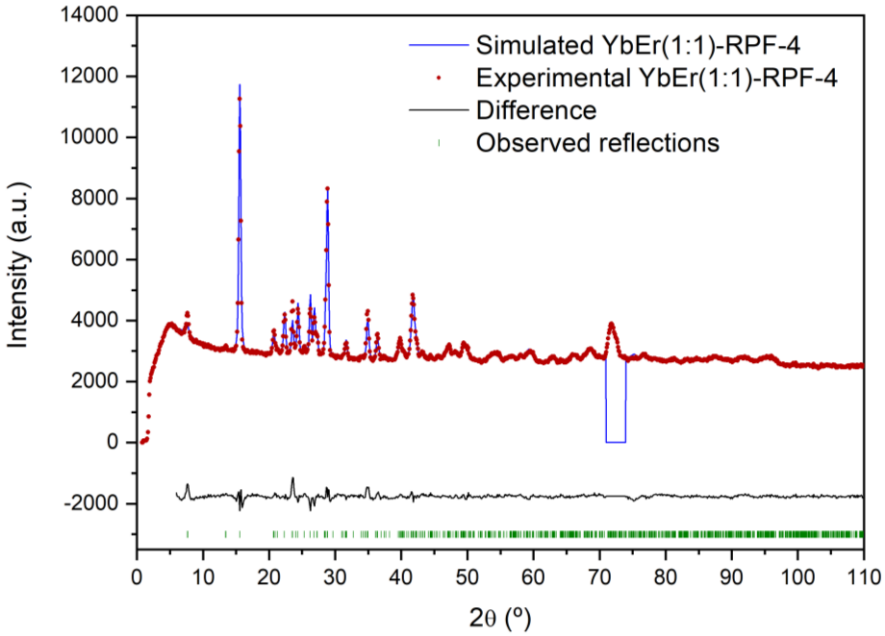

Figure 4.23. NPD pattern and Rietveld refinement of YbEr(1:1)-RPF-4. Rwp = 2.15%; Rp = 1.45%. The broad peak broad peak at 70–74° corresponds to the vanadium sample holder.

4.4.3. Effects of kinetics: extending the reaction time

Upon observing compositional segregation between crystals of the same sample, and kinetic incorporation rate biases, we wondered whether an extended reaction time would mitigate the inconsistencies between the input and the output metal ratios, especially in the case of La-based combinations in which a redissolution of the samples occurs. Moreover, we know from previous studies of this structure that α-RPF-4 is a kinetically controlled polymorph.[4] Thus, we carried out synthesis experiments with the same initial metal ratios and combinations, but extending the reaction time from 1 day to 3 days. The PXRD patterns of all the combinations can be found in Figure 4.24, and the average EDX and TXRF bulk results are displayed in Table 4.2.

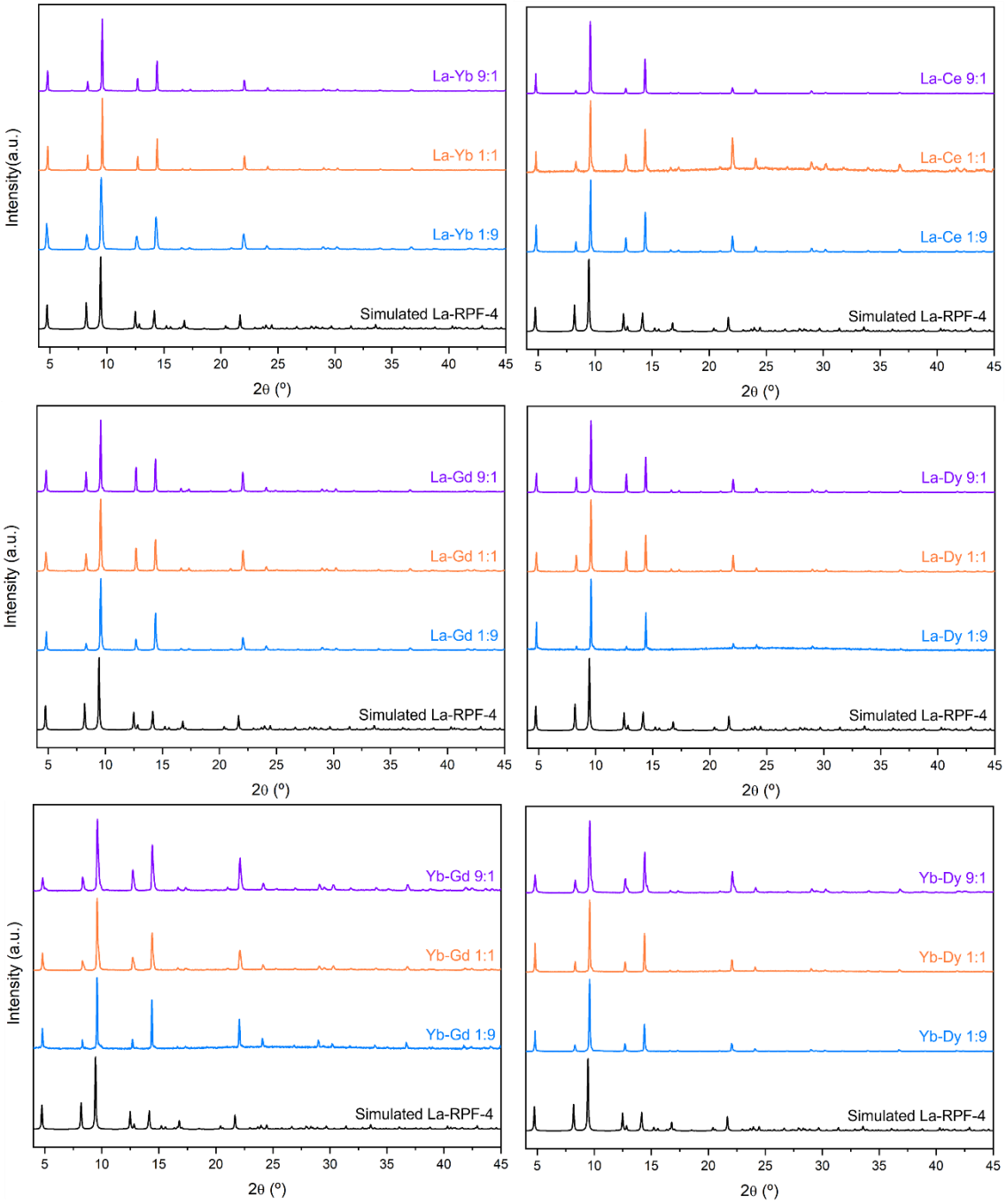

Figure 4.24. PXRD patterns of the RPF-4 binary combinations synthesized in a reaction time of 3 days.

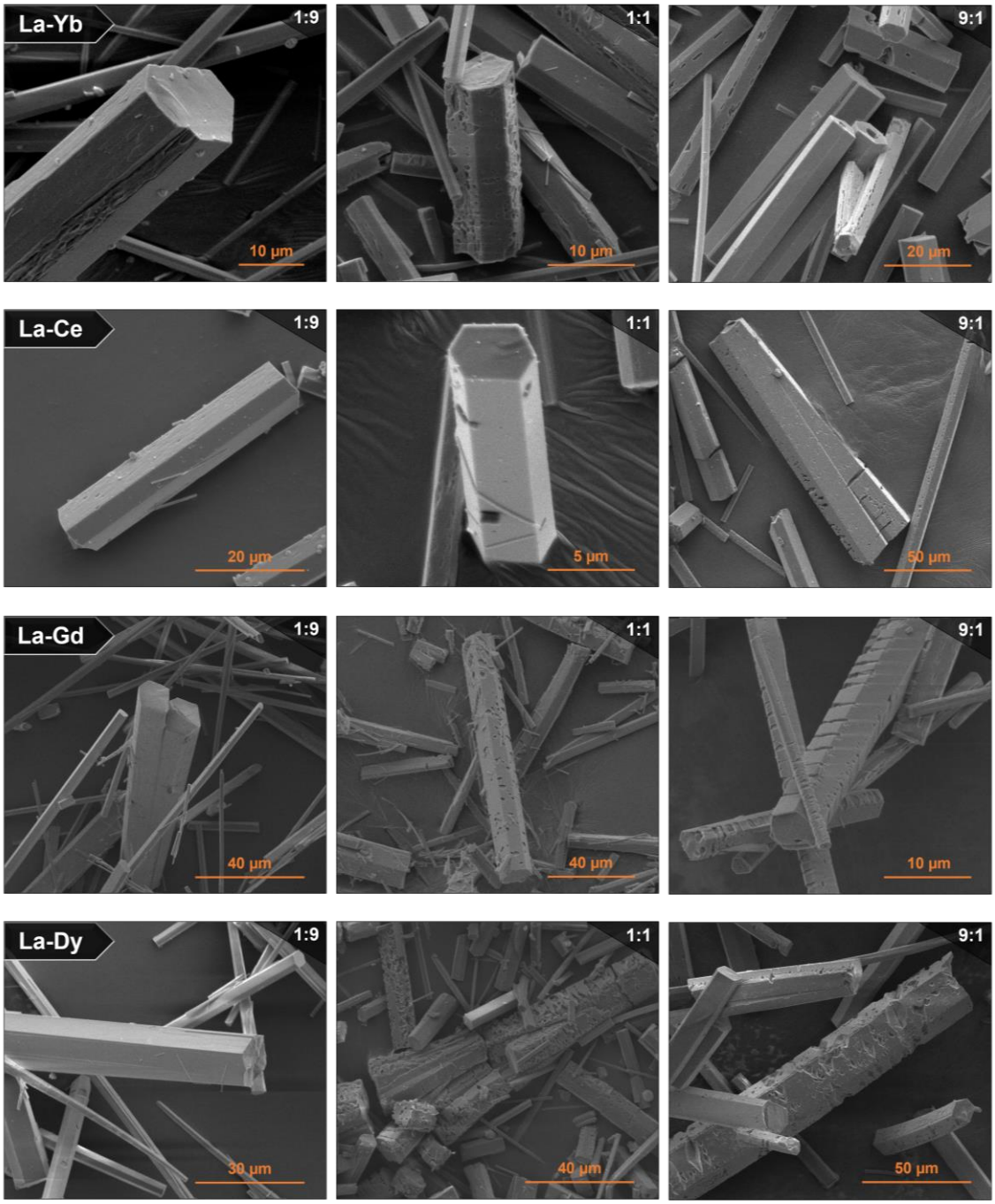

Figure 4.25. SEM images of the La-based RPF-4 binary combinations synthesized in a reaction time of 3 days.

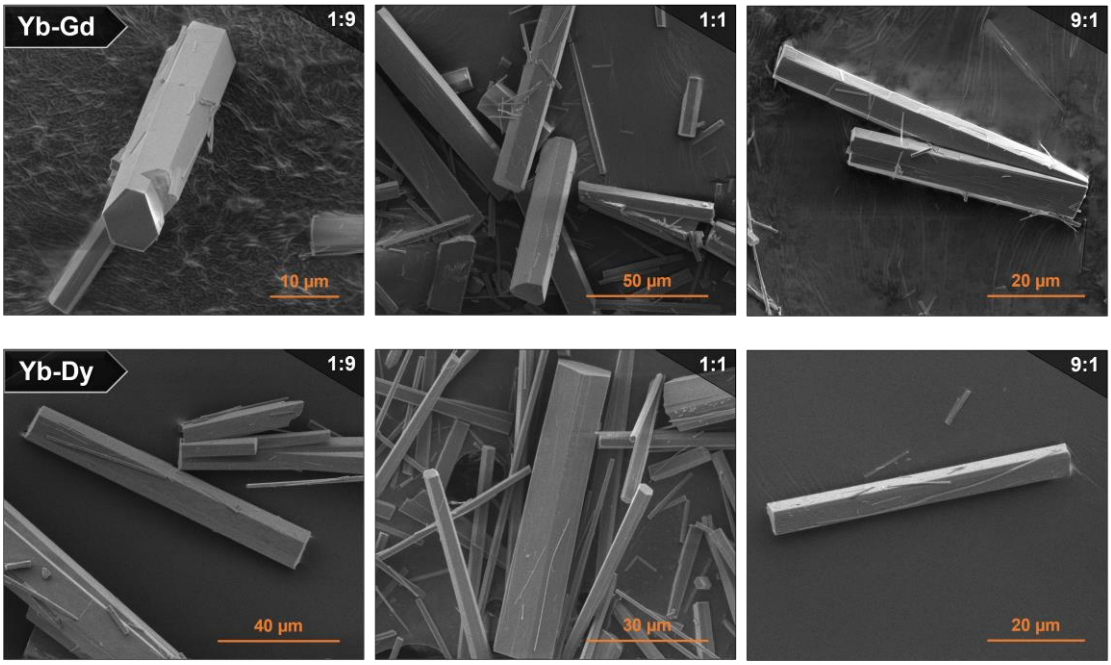

Figure 4.26. SEM images of the Yb-based RPF-4 binary combinations synthesized in a reaction time of 3 days.

For the combination of La and Yb, we noticed that while a compositional segregation was still evident for the equimolar ratio, crystals with a metal ratio closer to the input such as 6:4 and 1:1 are now observed. As it is unclear if these crystals are the result of new nucleation events, or of a partial redissolution and subsequent growing of already existing crystals (comparable to an in situ trans-metalation process), we carried out the following seeding experiments that would help rule out scenarios or identify the cause.

The first scenario consists of using single-metal La-RPF-4 crystals and ytterbium nitrate as starting materials to obtain LaYb-RPF-4 in a 9:1 ratio. SEM and EDX results show that defective crystals with the expected composition are formed, thus indicating that a trans-metallation process actually occurs, most likely facilitated by the redissolution of the La-RPF-4 crystals trough the Ostwald ripening mechanism.

The second scenario consists of using single-metal Yb-RPF-4 crystals and lanthanum nitrate as starting materials to obtain LaYb-RPF-4 in a 9:1 ratio. In this case, we observed the presence of lanthanum-containing particles distributed unevenly over the surface of the crystals of the sample. We ruled out the possibility of them being lanthanum nitrate particles deposited onto the crystals by washing the samples with distilled water and ethanol, and confirming the purity of the sample through a PXRD analysis (Figure 4.27). From this experiment we can conclude that for this scenario a trans-metalation process does not occur as the insertion of La atoms is occurring only on the surface of the crystals. These newly formed particles are the result of a partial surface redissolution and growth of the already existing crystals, similar to one described by our group.[7]

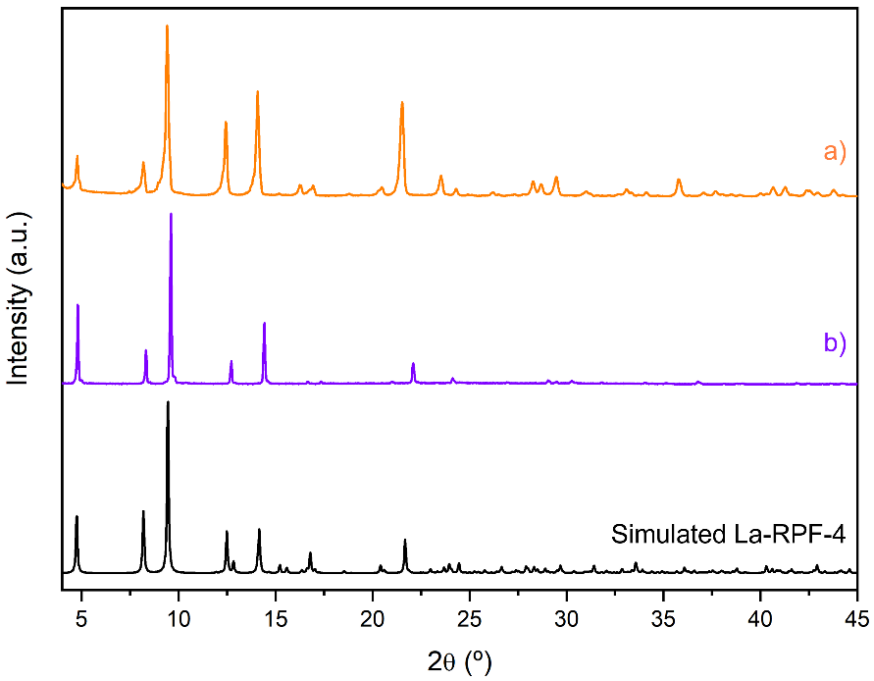

Figure 4.27. PXRD pattern of **a)** the first seeding experiment, La-RPF-4 + $Yb(NO_3)_3$, and **b)** the second seeding experiment, Yb-RPF-4 + $La(NO_3)_3$.

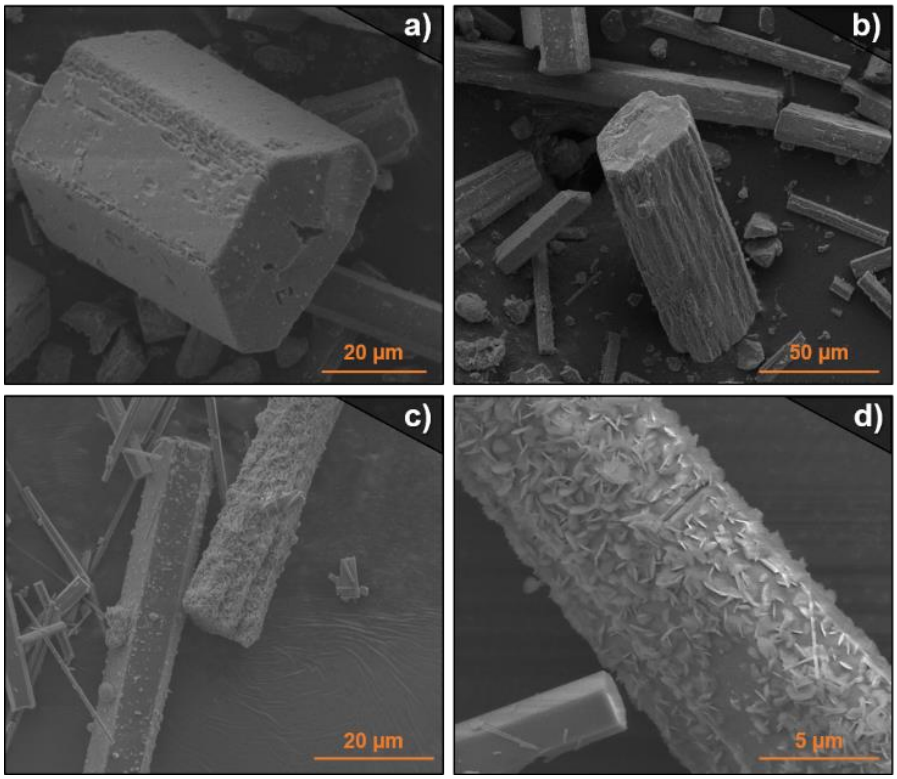

Figure 4.28. SEM images of the crystals obtained by combining single-metal La-RPF-4 and $Yb(NO_3)_3$ **(a, b)**, or Yb-RPF-4 and $La(NO_3)_3$ **(c, d)**.

Contrary to the La-Yb combination, increasing the reaction time did not seem to have an evident effect on the overall composition of La-Ce, La-Dy and Yb-Dy. However, it is noted that for the 1:1 La-Gd combination, while the compositional segregation is still present, the average output ratio contains a higher lanthanum content. Also, an increase in the reaction time did eliminate the compositional bias observed for the 1:1 Yb-Gd combination, as the sample displays crystals with compositions that match the initial ratio, which did not occur in the sample prepared in one day.

These results seem to point to some sort of limitation that hinders the formation of certain binary combinations of RPF-4. We associated the compositional segregation observed for some of the equimolar La-based systems with differences in the crystallization mechanisms, leading to partial redissolution of the crystals during the synthesis reaction. Nevertheless, we did consider the possibility of an energy constraint for some of the combinations, or even a barrier in the formation of certain types of atomic arrangements within the SBU. To address this issue more thoroughly, we carried out DFT calculations to compute the relative formation energy of the RPF-4 systems, and the results are displayed in Figure 4.29.a. For the single-metal RPF-4 samples, Yb-RPF-4 displayed the largest formation energy, and the rest of the samples showed values up to 1.8 eV. To study the formation mechanism of the binary systems, we focused on the La-Yb combination, and we computed the formation energy of RPF-4 structures in two scenarios: substitution of an increasing number (from 1 to 4) of La metal centers in La-RPF-4 by Yb atoms; substitution of an increasing number (from 1 to 4) of Yb metal centers in Yb-RPF-4 by La atoms. Both scenarios follow a linear trend, but while the insertion of La in Yb-RPF-4 leads to a stabilization of the framework, the insertion of Yb atoms in La-RPF-4 destabilizes the system (Figure 4.29.b). So, it seems that during the formation of a MTV-MOF, different crystallization mechanisms coexist and compete

with each other. Also, the MOF formation processes seem to be thermodynamically controlled in the case of reaction with excess of La, and kinetically controlled in the case of excess of Yb.

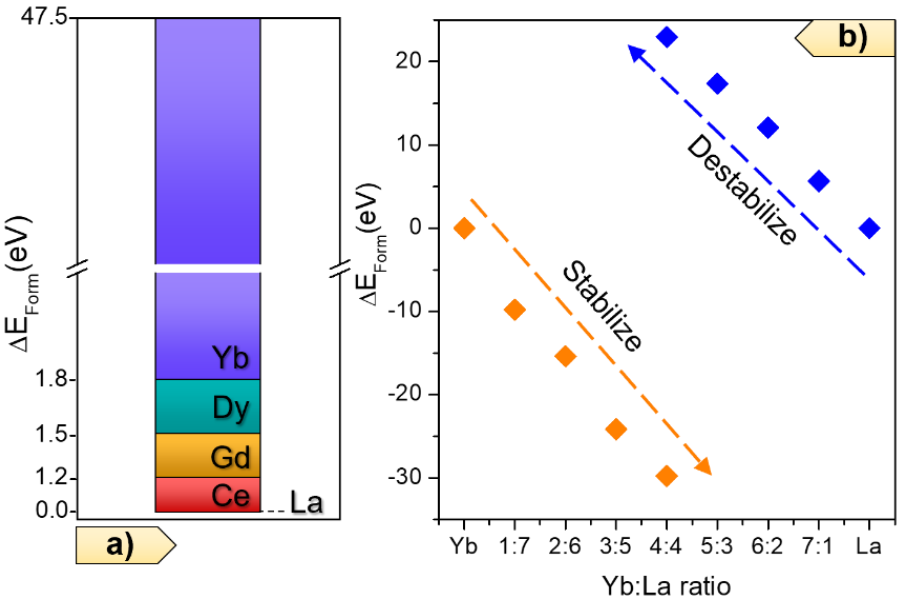

Figure 4.29. Relative values of formation energy for **a)** various single-metal RPF-4 structures, with La-RPF-4 as the reference, and **b)** for binary La-Yb samples with different metal substitution ratios.

Table 4.2. Starting molar ratio of each RPF-4 combination, EDX and TXRF data for the output.

Combination	Initial molar ratio		Metal ratio for 1-day synthesis $Ln_2(hfipbb)_3$		Metal ratio for 3-day synthesis $Ln_2(hfipbb)_3$	
			EDX average	TXRF bulk	EDX average	TXRF bulk
La-Yb	1	9	$La_{0.2}Yb_{1.8}$	$La_{0.2}Yb_{1.8}$	$La_{0.1}Yb_{1.9}$ $La_{0.6}Yb_{1.4}$	-
	1	1	$La_{0.4}Yb_{1.6}$ $La_{1.8}Yb_{0.2}$	$La_{0.8}Yb_{1.2}$	$La_{0.4}Yb_{1.6}$ $La_{1.2}Yb_{0.8}$	$La_{1.0}Yb_{1.0}$
	9	1	$La_{1.8}Yb_{0.2}$	$La_{1.8}Yb_{0.2}$	$La_{1.8}Yb_{0.2}$	-
La-Ce	1	9	$La_{0.2}Ce_{1.8}$	$La_{0.2}Ce_{1.8}$	$La_{0.2}Ce_{1.8}$	-
	1	1	$La_{0.8}Ce_{1.2}$	$La_{1.0}Ce_{1.0}$	$La_{1.0}Ce_{1.0}$	$La_{1.0}Ce_{1.0}$
	9	1	$La_{0.2}Ce_{1.8}$	$La_{0.2}Ce_{1.8}$	$La_{1.6}Ce_{0.4}$	-
La-Gd	1	9	$La_{0.2}Gd_{1.8}$	$La_{0.2}Gd_{1.8}$	$La_{0.2}Gd_{1.8}$	-
	1	1	$La_{0.6}Gd_{1.4}$ $La_{0.8}Gd_{1.2}$	$La_{0.6}Gd_{1.4}$	$La_{0.8}Gd_{1.2}$ $La_{1.4}Gd_{0.6}$	$La_{1.0}Gd_{1.0}$
	9	1	$La_{1.8}Gd_{0.2}$	$La_{1.8}Gd_{0.2}$	$La_{1.8}Gd_{0.2}$	-
La-Dy	1	9	$La_{0.2}Dy_{1.8}$	$La_{0.1}Dy_{1.9}$	$La_{0.2}Dy_{1.8}$	-
	1	1	$La_{0.8}Dy_{1.2}$ $La_{1.6}Dy_{0.4}$	$La_{0.6}Dy_{1.4}$	$La_{0.6}Dy_{1.4}$ $La_{1.6}Dy_{0.4}$	$La_{0.8}Dy_{1.2}$
	9	1	$La_{1.8}Dy_{0.2}$	$La_{1.8}Dy_{0.2}$	$La_{1.8}Dy_{0.2}$	-
Yb-Gd	1	9	$Yb_{0.2}Gd_{1.8}$	$Yb_{0.2}Gd_{1.8}$	$Yb_{0.2}Gd_{1.8}$	-
	1	1	$Yb_{0.6}Gd_{1.4}$	$Yb_{1.0}Gd_{1.0}$	$Yb_{0.6}Gd_{1.4}$ $Yb_{1.2}Gd_{0.8}$	$Yb_{1.0}Gd_{1.0}$
	9	1	$Yb_{1.8}Gd_{0.2}$	$Yb_{1.8}Gd_{0.2}$	$Yb_{1.8}Gd_{0.2}$	-
Yb-Dy	1	9	$Yb_{0.2}Dy_{1.8}$	$Yb_{0.2}Dy_{1.8}$	$Yb_{0.2}Dy_{1.8}$	-
	1	1	$Yb_{1.0}Dy_{1.0}$	$Yb_{1.0}Dy_{1.0}$	$Yb_{1.0}Dy_{1.0}$	$Yb_{1.0}Dy_{1.0}$
	9	1	$Yb_{1.8}Dy_{0.2}$	$Yb_{1.8}Dy_{0.2}$	$Yb_{1.8}Dy_{0.2}$	-
Yb-Er	1	1	-	-	$Yb_{1.0}Er_{1.0}$	$Yb_{1.0}Er_{1.0}$

4.4.4. Modifying the synthetic medium

Modifying the parameters of the reaction could potentially lead to a different outcome in the metal arrangement within the SBUs. We chose to modify the synthetic medium as it is a way of altering the kinetics of the formation of the MOF. For these experiments we chose to substitute the ethanol with acetone as it is compatible with the synthetic path of RPF-4, and we carried out the synthesis of the combinations of La with Yb, and La with Gd (1:9, 1:1 and 9:1 initial ratios) as they showed the most distinct features in the previous experiments.

It seems that a slightly different synthetic medium did not affect the output of the 1:9 and 9:1 ratios, as the results are congruent with the previous observations for a water/ethanol mixture. An excess of Yb or Gd generates defect-free crystals with an average metal ratio of 1:9. Conversely, an excess of La determines the distribution of the metals and the morphology of the crystals, as they display rough surfaces with defects and holes, and EDX analysis confirmed that the average ratio is 9:1.

For the 1:1 ratio, for both combinations we found crystals with a particular core-shell morphology in which the exterior layer is rich in La and display different types of defects that match the La-rich composition, and the inner core contains a higher concentration of either Yb or Gd. For this type of morphology to have formed, the nuclei generated in the initial crystallization phase must have been contained an excess of Gd or Yb, and in the later growth phase these nuclei must have been coated with a lanthanum-rich layer. EDX analysis indicate that the average output for both combinations was 7:3, and this excess of lanthanum in the bulk seems to suggest that the lanthanum-rich layers that coat the initial nuclei hinder any possible trans-metalation processes that could facilitate the insertion of other cations in the exterior layers.

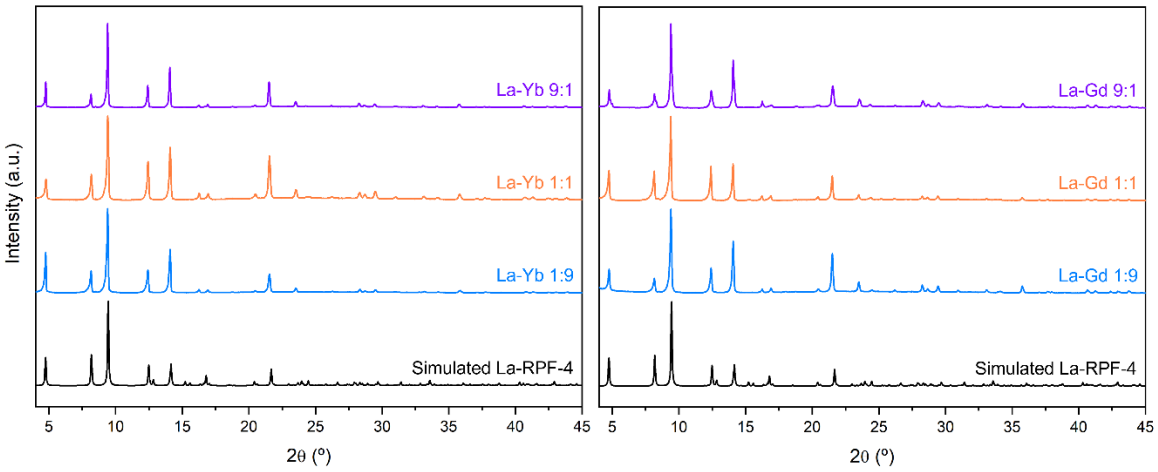

Figure 4.30. PXRD patterns of **(left)** LaYb-RPF-4 and **(right)** LaGd-RPF-4 combinations synthesized in acetone/water.

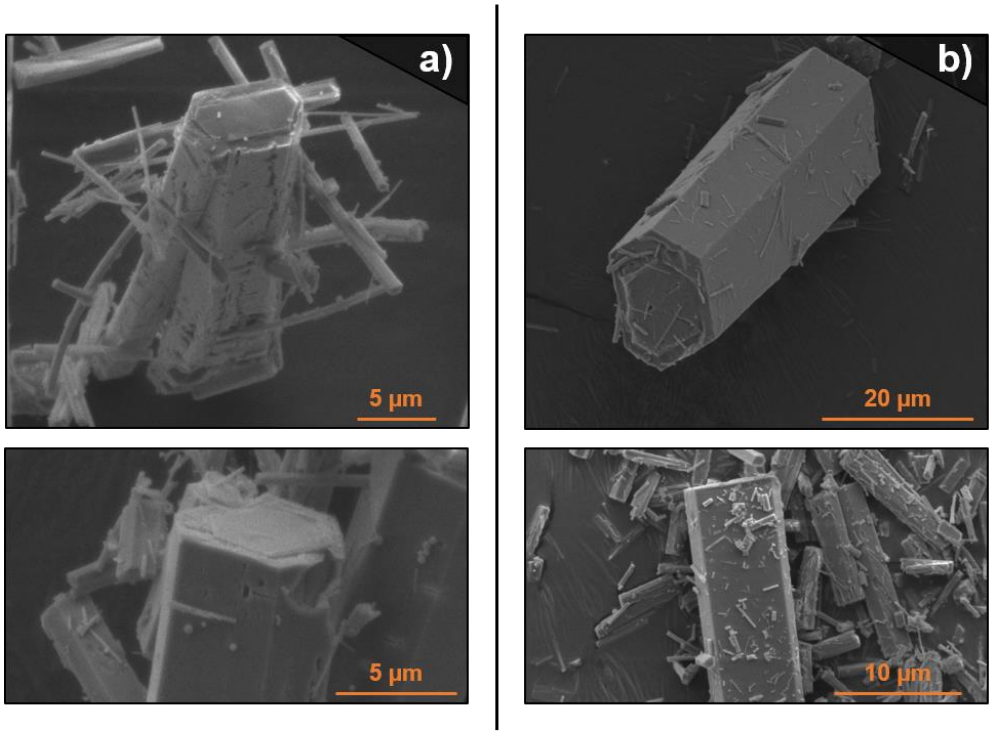

Figure 4.31. SEM images of **a)** equimolar LaYb-RPF-4 and **b)** equimolar LaGd-RPF-4 synthesized in acetone/water.

4.5. Magnetic characterization of the samples

One hallmark of the RPF-4 family is the rod-shaped SBU, which places the lanthanide atoms at short distances from one another (3.6-3.9 Å), comparable to the ones between 3d cations in traditional inorganic oxides. This structural feature could generate long-range magnetic interactions between the metal ions, and this would be of interest from the point of view of the magnetic properties. With this in mind, we conducted a magnetic characterization of the behavior of both single and multi-metal versions of this system.

Firstly, we measured the magnetic susceptibility with a moderate applied field of 100Oe, and we observed that it displays a paramagnetic behavior from 1.8 to 300K. The inverse of the magnetic susceptibility was fitted to a Cuire-Weiss linear law behavior, which allowed us to calculate the paramagnetic moment of each rare-earth atom as well as the Curie constants, and the results are presented in Table 4.3. Only Eu-RPF-4 displayed a considerable shift between the experimental and theoretical values, and this is likely because of the well-known different magnetic states of europium. The plots of the temperature dependence of the inverse magnetic susceptibility of the different members of the RPF-4 series is presented in Figure 4.32.

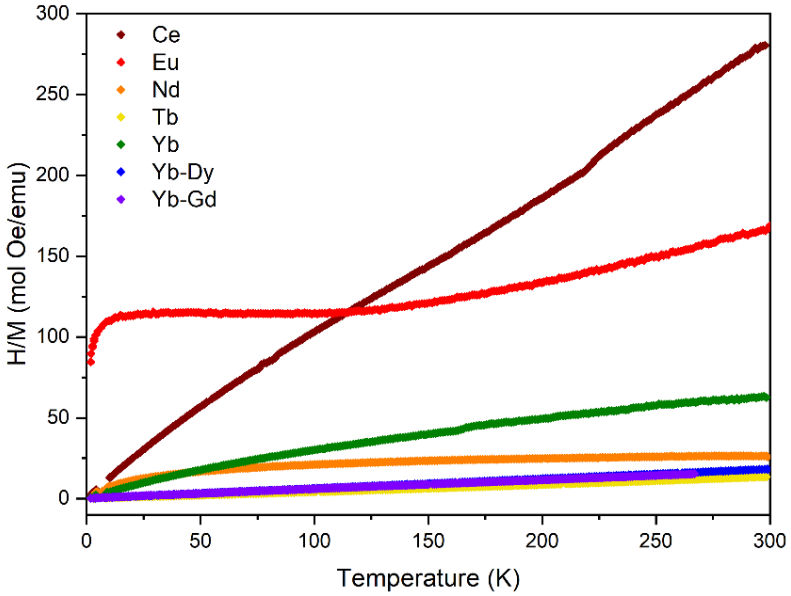

Figure 4.32. Temperature dependence on the inverse magnetic susceptibility for different members of the RPF-4 series.

Table 4.3. The Curie Constant (Θ, K), the paramagnetic moment per formula unit (PM, μ_B/f.u.) or per rare-earth atom (PM, μ_B/atom), the saturation magnetization at 1.8K per atom (Ms, μ_B/atom) and the expected or theoretical effective paramagnetic moment per rare earth atom (PM, $(\mu_B)_{Effective}$) for the different single- and multi-metal RPF-4. *M_S (μ_B/f.u.).

	Θ (K)	**PM (μ_B/f.u.)**	**PM (μ_B/atom)**	**M_S (μ_B/atom) @1.8K**	**PM $(\mu_B)_{Efective}$**
Ce	-5.0	2.8	2.0	0.9	2.5
Nd	-58.0	5.3	3.7	1.2	3.6
Eu	-192.0	4.8	3.4	0	0
Gd	-9.0	15.8	11.0	7.0	7.9
Tb	+15.0	13.0	9.2	6.0	9.8
Dy	+0.5	11.3	8.0	8.0	10.5
Ho	-22.4	16.7	11.8	6.0	10.6
Er	-21.0	14.8	10.4	8.0	9.6
Yb	-191.0	7.4	5.2	1.9	4.5
Yb-Gd	-9.4	9.8	-	10.0*	9.1
Yb-Dy	-4.9	11.5	-	8.0*	11.4

The magnetization versus applied field plot (Figure 4.33) shows that none of the samples presents a coercive field, and we also observed a saturation phase dependent on the rare earth ion for the magnetic field dependence of the magnetization at a fixed temperature (1.8 K). This behavior might be related to the polarization effect on the paramagnetic rare earth atom, which is subjected to the intense external applied magnetic field.

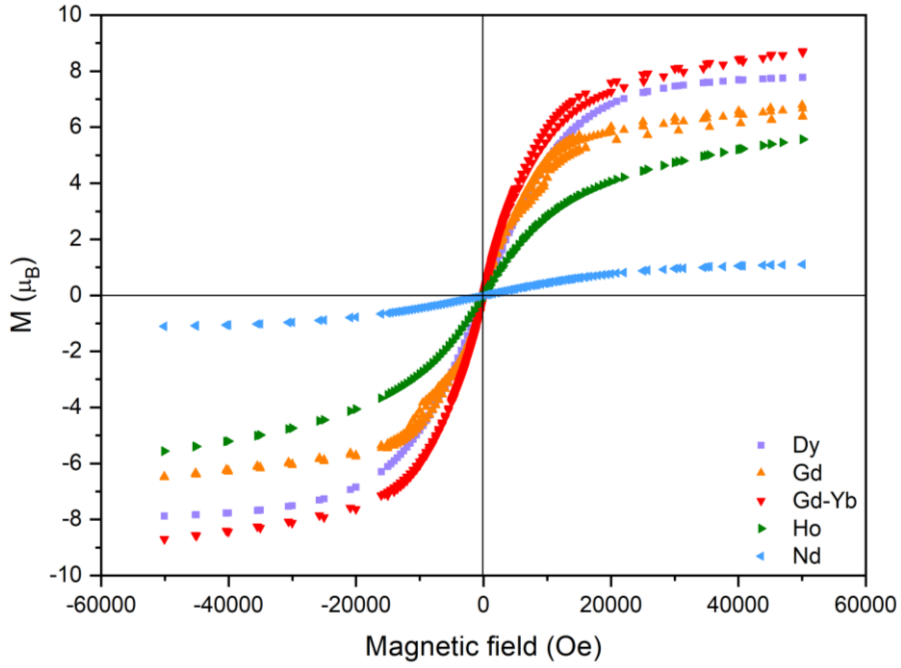

Figure 4.33. Magnetic Field dependence of the magnetization at 1.8K of different members of the RPF-4 family.

We recorded the DC magnetic susceptibility of Gd-RPF-4 under applied magnetic fields ranging from 0 to 5T, in the temperature range from 2 to 25K, and the results are plotted in Figure 4.34.a. For lower magnetic fields, a maximum is achieved at around 2K. When increasing the applied magnetic field, the maximum shifts towards higher temperatures, and this behavior could be related to a certain type of magnetic interaction between the low-lying energy levels of the lanthanides, which could be split by crystal and magnetic field.

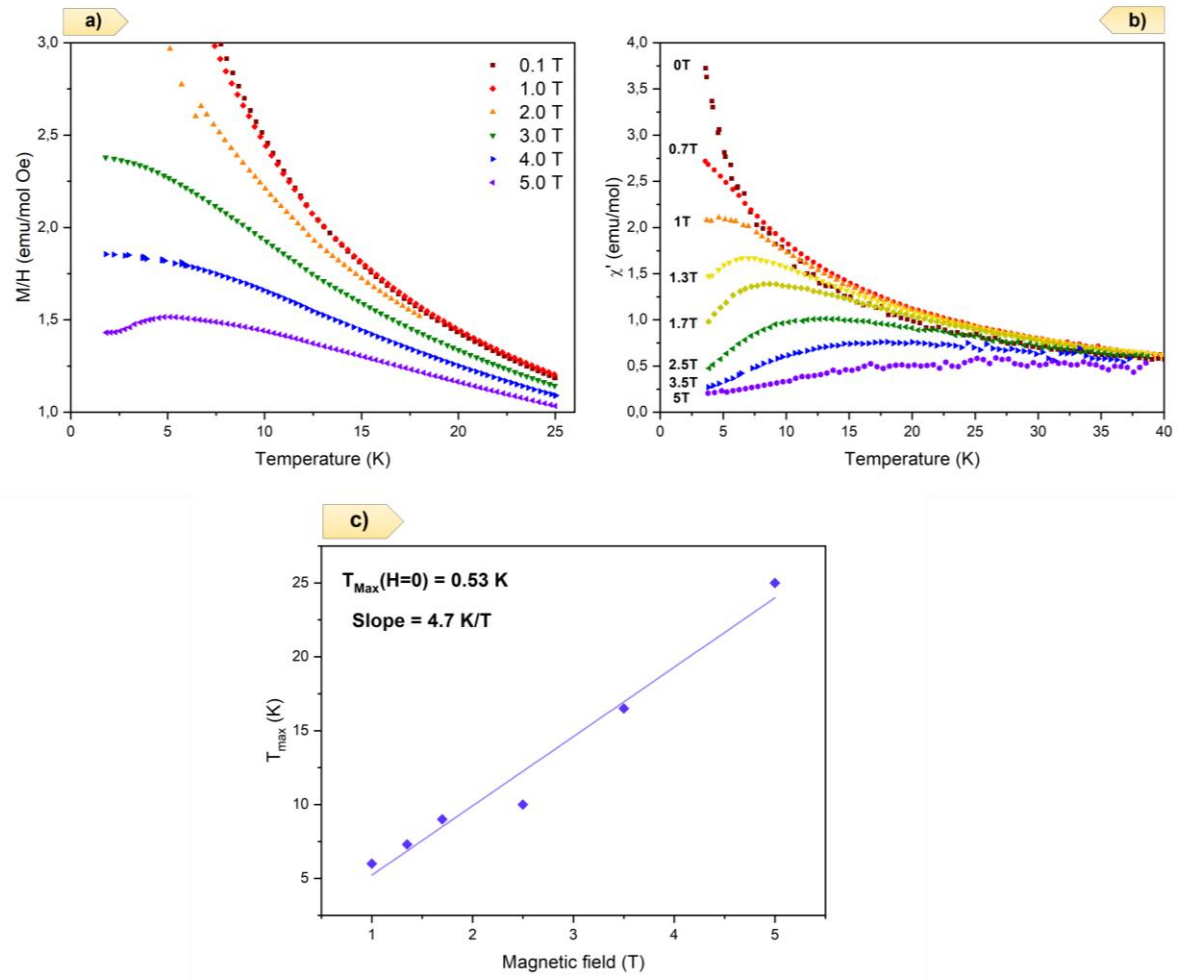

Figure 4.34. a) Temperature dependence of the magnetic susceptibility at different applied magnetic fields, in the range of 0.1T to 5T for Gd-RPF-4. **b)** Temperature dependence of the AC magnetic susceptibility at a fixed frequency of 10KHz and amplitude of 1Oe, for different external magnetic fields for Gd-RPF-4. **c)** Linear fitting of the magnetic field dependence of the T_{Max} in the AC magnetic susceptibility for Gd-RPF-4.

To have a deeper understanding of the intrinsic magnetic behavior, we measured the AC magnetic susceptibility with a magnetic field amplitude of 1Oe in a wide range of frequencies (10 Hz-10 KHz), and these measurements could be subjected to an external DC magnetic field (Figure 4.34.b). The results of these measurements point to a clear paramagnetic behavior, however a maximum appears at a given temperature, T_{Max}, and it can be seen more clearly for external DC magnetic fields from 0.7 up to 3.5T. This maximum shifts towards higher values when a significant external magnetic field is applied, and it follows a linear behavior (Figure 4.34.c) from which we can extrapolate a T_{Max} for zero magnetic field of 0.53 K, as well as a slope of 4.7 K/Tesla in the case of Gd-RPF-4. The values of T_{max} at zero magnetic field for all the samples are listed in Table 4.4, and these values were always found to be below our experimental accessible temperature range (above 2K) except for Tb-RPF-4 and YbGd-RPF-4.

Table 4.4. Values of T_{Max} (K) extracted from the AC magnetic susceptibility data.

RPF-4	T_{Max} (K) extracted from AC data
Ce	0.4
Nd	0.2
Eu	1.2
Gd	0.5
Tb	3.7
Dy	0.6
Ho	0.6
Er	1.6
Yb	0.4
Yb-Gd	2.7
Yb-Dy	1.6

In summary, the magnetic susceptibility (both AC and DC) under different external magnetic fields seems to indicate a complex magnetic behavior that stems from the interaction between the lower energy crystal field levels associated to the lanthanide ions. To shed some light on this, we thoroughly analyzed the specific heat (C_p) of all the samples as the low-temperature specific heat is very sensitive to the transitions between the low energy crystal field levels in lanthanides (Schottky anomalies). The low-temperature specific heat consists of three components: lattice vibrations (phonons), electronic component (extremely weak in insulators) and the magnetic contribution. To extract the magnetic component of the specific heat, we subtracted the heat capacity obtained from La-RPF-4, which only displays the phonon contribution, but not the magnetic component related to the magnetic moment and the crystal field level transition related to the magnetic rare earth ions. Due to the insulating character of the compounds, we assume that the electronic component of the specific heat is extremely weak. The plot of the magnetic component of the specific heat versus the temperature under 20K is displayed in Figure 4.35. The magnetic component of this plot strongly increases at around 3K, and displays a broad maximum at 2.3K in the case of Ho-RPF-4.

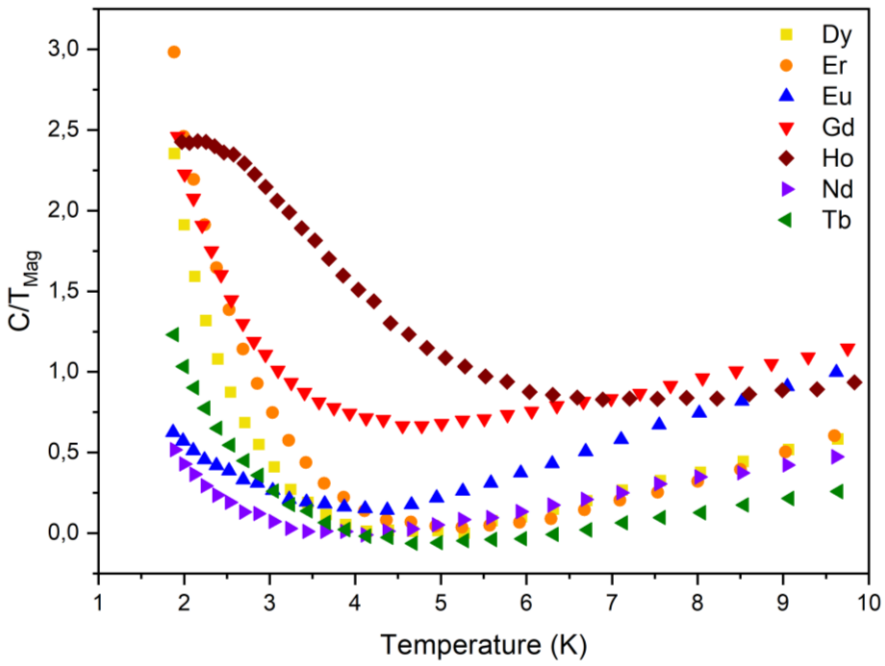

Figure 4.35. Temperature dependence, in logarithmic scale, of the magnetic component of the specific heat for different members of the RPF-4 family.

To have a deeper understanding of this complex behavior, we carried out a study of the magnetic field dependance of the specific heat in the same temperature range. For the equimolar combination of Yb and Gd, we recorded the specific heat subjected to an external magnetic field ranging from 0 to 8T. The results are displayed in Figure 4.36.a, and the magnetic specific heat presents a broad maximum at magnetic fields higher than 3T. To emphasize the real effect of the applied external magnetic field, we subtracted the C/T data at H=0T from every C/T value. The data is plotted in Figure 4.36.b, and it displays a more pronounced broad maximum than in the previous case, but it does not provide new information.

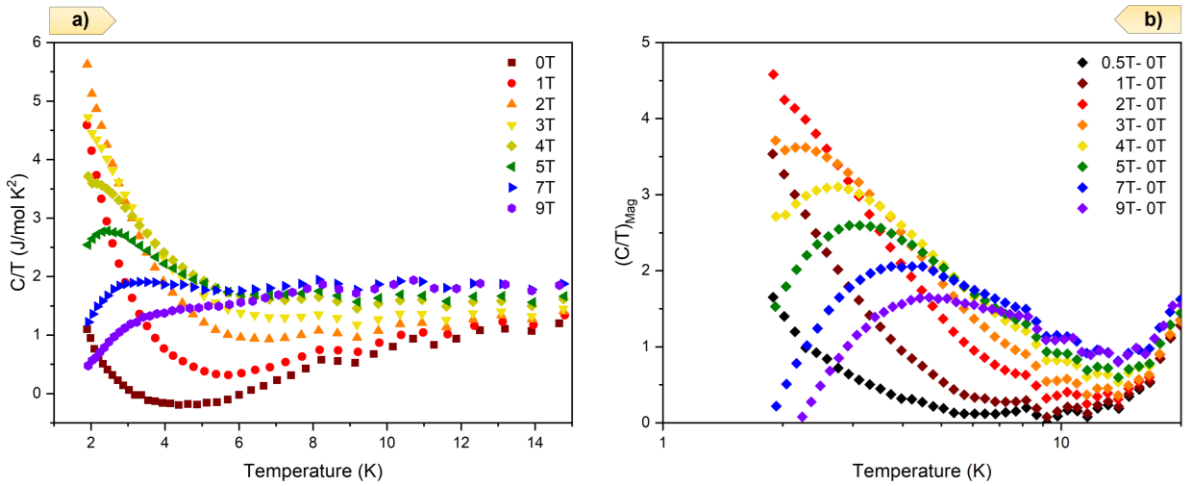

Figure 4.36. a) Temperature dependence of the magnetic specific heat of YbGd-RPF-4, under different magnetic fields. **b)** Temperature dependence of the magnetic component of C/T, after the subtraction of the $(C/T)_{0T}$, for YbGd-RPF-4.

As a complementary approach, we recorded the isothermal magnetic field dependence of the magnetic specific heat (Figure 4.37.a). The data displays a maximum below 4T for temperatures under 5K, and the H_{Max} shifts towards higher fields as the temperature increases from 1.9K to 5K. From the previous results we extracted the magnetic field dependence of the T_{Max}, and the data follows a linear behavior from which we extracted a value of T_{Max} of 0.4K at zero magnetic field (Figure 4.37.b). This is consistent with the magnetic susceptibility data, but at slightly different temperatures, again pointing to transitions between low crystal field energy levels of the rare earth ions.

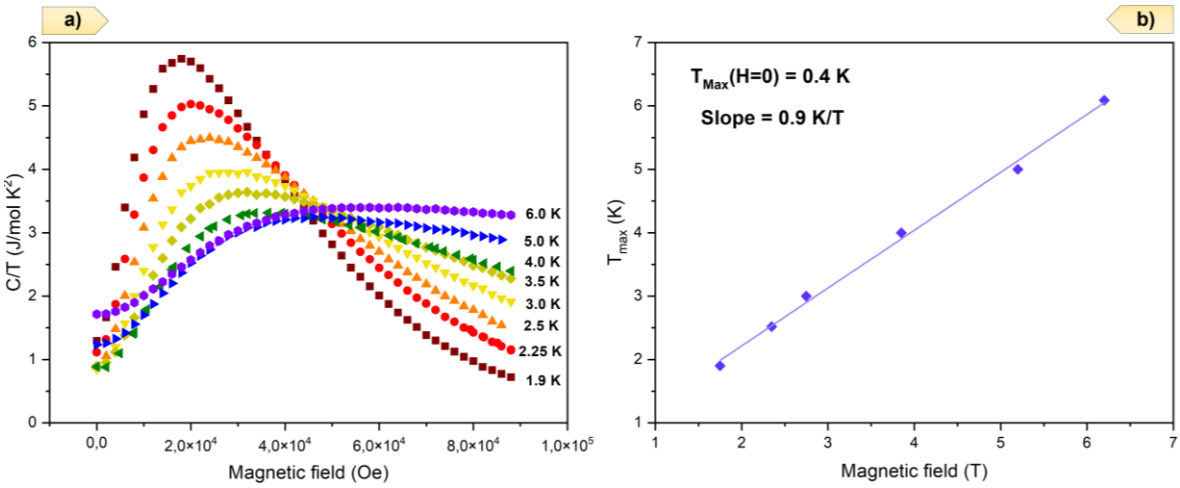

Figure 4.37. a) Magnetic field dependence of the magnetic component of the specific heat, at different temperatures (isothermal) for YbGd-RPF-4. **b)** Linear fitting of the magnetic Field dependence of the T_{Max}, for YbGd-RPF4, obtained from the isothermal specific heat.

The integration of the magnetic field dependence of the T_{Max} is related to the magnetic entropy, and it depends on the rare earth ion, as displayed in Figure 4.38. The magnetic component of the specific heat under applied external magnetic fields shows very broad maximum, which should have no relation to a long-range magnetic order.

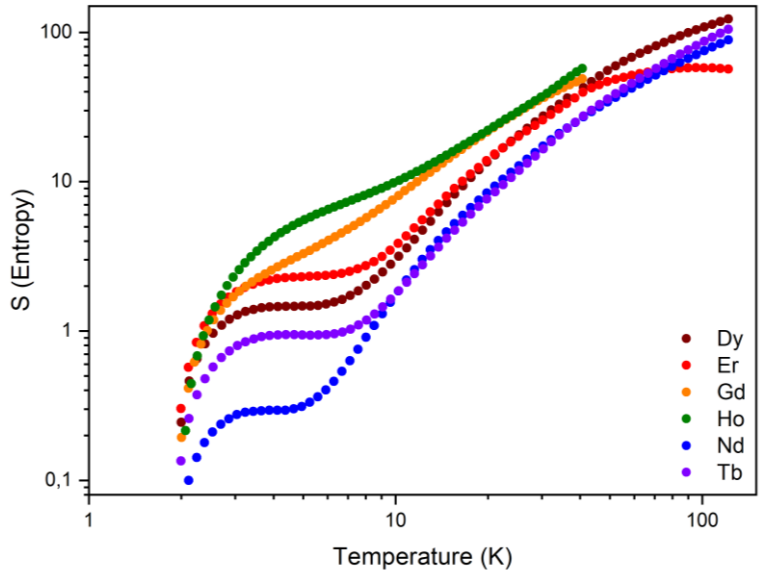

Figure 4.38. Magnetic entropy as a function of temperature, in logarithmic scale, for the different members of the RPF-4 family.

However, to rule out this possibility, we performed a neutron powder diffraction experiment at a very low temperature (below 1.5K). We recorded the NPD pattern of Er-RPF-4 at 84 mK, and it did not display extra peaks, or an intensity increase of the already existing peaks. Therefore, the broad maximum of the magnetic field dependent specific heat could not be associated to a magnetic phase transition, so it could maybe stem from a very complex temperature dependence of the rare earth crystal field level transitions. This low temperature peak in the specific heat is commonly seen in rare earth-based compounds, and it can be attributed to the few-level electronic system of the partially split ground-state manifold of the rare-earth 4f-electrons.[8] These levels can be altered by both the applied magnetic field and the crystal field of the host. In our case, the low temperature, magnetic field dependent specific heat was analyzed in terms of the Schottky model of a 2-level system.[9] The first step was to remove the effect of the host. The heat capacity of the matrix (phonons) is typically accounted for by measuring a non-magnetic

rare-earth filled variant, typically with La or Lu.[10] In our case, we measured La-RPF-4 as a background for the mass normalized specific heat. As expected, this sample did not display any low-temperature anomaly or magnetic field dependence of the heat capacity.[11] After removing the host effect, we fitted the extracted magnetic heat capacity to a cubic background that accounted for the remnants up to higher temperatures, and the gap energy was estimated by using 2-level Schottky heat capacity.

The Schottky model allows different degeneracies for the ground and excited levels, and this is not a straightforward issue in our case. We analyzed several options for each sample in each field, and many of the samples could be analyzed with the simplest model: two non-degenerate levels for Ce-, Gd-, Ho-, Nd- and Tb-RPF-4, as displayed in Figure 4.39.a. The resulting Schottky Gap (H) dependence is similar for all the samples except Tb-RPF-4, as the estimated gap displayed dependance on the field at 0.5-1T, and it was analyzed with a double degenerate excited level model, however this does not work at all in zero or higher fields.

Eu-RPF-4 could only be analyzed using double degenerate ground level as it does not display much Gap vs. H dependence, in a similar fashion to Tb-RPF-4. Although Er-RPF-4 must be analyzed using double degenerate ground level in intermediate fields, non-degenerate ground level gives similar gap energies in both low and high fields (Figure 4.39.b).

Both Yb-RPF-4 and Dy-RPF-4 gave the best results for double degenerate excited levels, and we also compared YbDy-RPF-4 and YbGd-RPF-4 to their single-metal counterparts. While YbDy-RPF-4 could be analyzed with only non-degenerate levels, it was not the case for both Yb-RPF-4 and Dy-RPF-4 (Figure 4.39.c). On one hand, the model works well for Dy-RPF-4, except at 8.8T where a non-degenerate model fits better, which is expected for higher fields. It displays a Gap (H) dependence similar to both Ce- and Gd-

RPF-4, but with a bit less slope. On the other hand, Yb-RPF-4 required non-degenerate excited level in the lowest field. Its Gap (H) dependence is stronger than for Dy-RPF-4, YbGd-RPF-4 could be mostly analyzed with non-degenerate excited state except in low fields where double-degenerate excited levels are needed, similar to Yb-RPF-4, although it was not necessary in the case of Gd-RPF-4, as it can be analyzed in any magnetic field using non-degenerate levels (Figure 4.39.d).

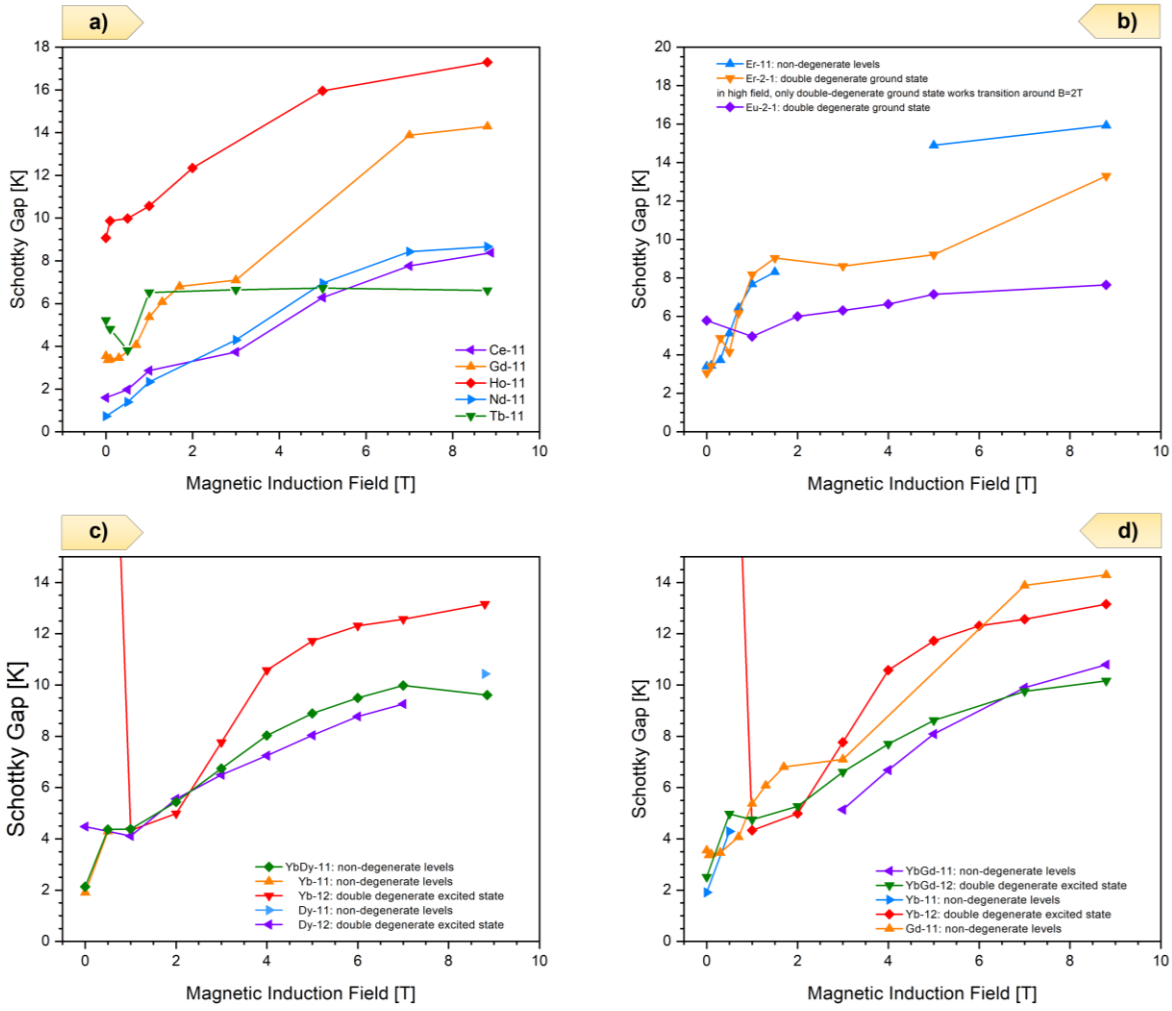

Figure 4.39. Magnetic field dependence of the estimated gap from a Schottky analysis. **a)** Ce-RPF-4 (purple), Gd-RPF-4 (orange), Ho-RPF-4 (red), Nd-RPF-4 (blue) and Tb-RPF-4 (green); **b)** Eu-RPF-4 (purple) and Er-RPF-4 (orange for a double degenerate ground state analysis, and blue for non-degenerate levels); **c)** YbDy-RPF-4 (green) compared to Yb- (orange and red) and Dy-RPF-4 (blue and purple). The "vertical" red line of the plot indicates that absurd Gap values are obtained at low fields for a double-degenerate level analysis for Yb-RPF-4; **d)** YbGd-RPF-4 (purple and green), Gd-RPF-4 (orange) and Yb-RPF-4 (blue triangles and red). The "vertical" red line of the plot indicates that absurd Gap values are obtained at low fields for a double-degenerate level analysis for Yb-RPF-4.

We used Er-RPF-4 as an example to illustrate the Schottky analysis, as it can be analyzed using either non-degenerate or double-degenerate ground levels. Figure 4.40 displays the Schottky fit to the extracted ΔCp(T) excess or magnetic heat capacity data at different magnetic fields. The Schottky model is based on the statistical physics of a few level system with thermal occupation:[10]

$$C_{Sch}(T)=\frac{R}{T^2}\left[\frac{\sum \nu_i \Delta_i^2 e^{-\Delta_i/T}}{\sum \nu_i e^{-\Delta_i/T}}-\left(\frac{\sum \nu_i \Delta_i e^{-\Delta_i/T}}{\sum \nu_i e^{-\Delta_i/T}}\right)^2\right]$$

where Δ_i is the energy gap (in K units) and $\Delta_0=0$ corresponds to the ground level. The model features the energy gaps, Δ_i, as free parameters. Therefore, once the number and degeneracy of levels, ν_i, is specified, only one fitting parameter for 2-level systems is left. For low-temperature 4f-electron systems it is often sufficient to consider only the first excited level together with the ground level. Such a two-level Schottky system has a characteristic peak in the heat capacity. In our data, a free cubic background must also be included to account for the higher temperature evolution of the specific heat.

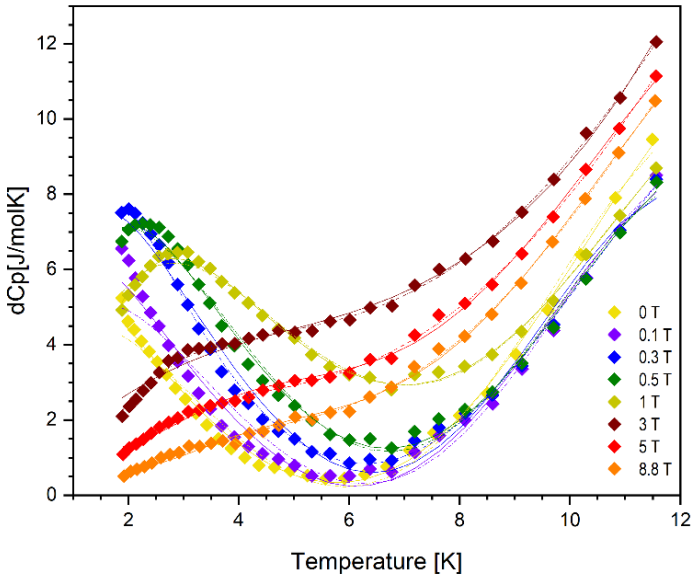

Figure 4.40. Temperature dependent excess or magnetic heat capacity of Er-RPF-4 at different magnetic fields. The fits use non-degenerate (solid lines) and double-degenerate (dashed lines) ground levels.

The results of the Schottky analysis of the single- and multi-metal RPF-4 samples are displayed in Table 4.5. Since the estimated gap does not always vary linearly with the magnetic field, Table 4.5 also includes the $E_gB[K/T]=(\Delta E_g(B)-\Delta E_g)/B$ values obtained by using the heat capacity measured in the highest measured field (usually 8.5 T). Additionally, the data is ordered according to the zero-field gap, and can be compared to the 4f configuration. Interestingly, the multi-metal RPF-4 samples display similar gap values to Yb-RPF-4, even though both Gd- and Dy-RPF-4 have considerably larger gaps.

Table 4.5. Estimated 2-level Schottky-model energy gap without magnetic field (ΔE_g) in temperature units, and its magnetic field dependence (E_gB) for the different members of the RPF-4 family.

RPF-4	ΔE_g[K]	E_gB[K/T]
La	0	0
Nd	0.73	0.9
Ce	1.6	0.8
Yb	1.9	1.3
Yb-Dy	2.1	0.8
Yb-Gd	2.5	0.9
Er	3.4	1.1
Gd	3.6	1.2
Dy	4.9	0.7
Tb	5.2	0.16
Eu	5.9	0.21
Ho	9.1	0.9

4.6. Conclusions

To summarize, equimolar La-containing combinations of the RPF-4 MOF family result in a phase segregation generated by a competitive formation of isoreticular crystals with different composition in the same sample, even if the chemical analysis of the composition of the bulk seems to point to an overall homogeneous output. This does not occur for equimolar binary combinations of RPF-4 not containing lanthanum, as they easily generate the MTV-MOF with the desired metal sequence in the SBU. Therefore, even if the MOFs can be obtained in single-metal form with any of the lanthanides we studied, the formation of a binary MTV-MOF seems to be driven by the complex interplay between thermodynamic and kinetic crystallization factors.

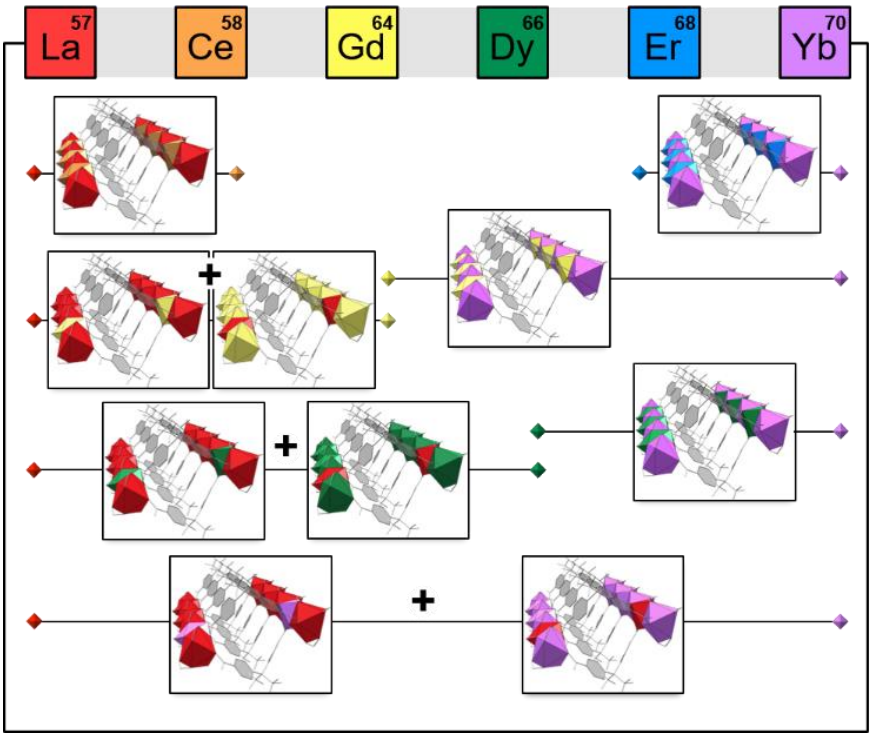

Figure 4.41. Summary scheme of the possibility to obtain MTV-MOFs for the 1:1 binary metal RPF-4 combinations studied in this chapter.

Our results illustrate the relevance of understanding the crystallization process of multi-metal MTV-MOFs in order to control the atomic sequencing scenario within the SBUs. Also, they underline the significance of a careful analysis of a sample, because while the compositional analysis of the bulk might indicate a homogeneous distribution of the metal atoms, the analysis of individual single-crystals might reveal a different scenario.

Regarding the magnetic behavior of the RPF-4 family, the samples we studied stay in the paramagnetic regime until the lowest temperature. However, the interaction between the low-lying levels of the f-electrons strongly depends on the variations induced by the crystal field and the external applied magnetic field, giving rise to a rich phenomenology in the magnetic susceptibility (AC and DC) and also in the specific heat.

The results of this chapter have been published in Chemistry of Materials in 2022, volume 34 (15), pages 7029-7041, with the title "*Influence of the Synthesis and Crystallization Processes on the Cation Distribution in a Series of Multivariate Rare-Earth Metal–Organic Frameworks and Their Magnetic Characterization*".

Additionally, based on the magnetic experiments detailed in this chapter, another study has derived in order to understand the correlation of the magnetocaloric effect of the framework with the metal centers, in this case, gadolinium. The influence of the dimensionality of the SBU (rods, hexameric clusters, layers), and the associated density of Gd atoms per formula unit were also investigated in detail. The results of this study have been published in Inorganic Chemistry in 2023, volume 62 (48), pages 19741–19748, with the title "*Magnetocaloric Properties in Rare-Earth Based Metal-Organic Frameworks: Influence of Magnetic Density and Hydrostatic Pressure*".

4.7. References

(1) Castillo-Blas, C.; De La Peña-O'Shea, V. A.; Puente-Orench, I.; De Paz, J. R.; Sáez-Puche, R.; Gutiérrez-Puebla, E.; Gándara, F.; Monge, Á. Addressed Realization of Multication Complex Arrangements in Metal-Organic Frameworks. *Sci Adv* **2017**, *3* (7), 1–11. https://doi.org/10.1126/sciadv.1700773.

(2) Castillo-Blas, C.; López-Salas, N.; Gutiérrez, M. C.; Puente-Orench, I.; Gutiérrez-Puebla, E.; Ferrer, M. L.; Monge, M. Á.; Gándara, F. Encoding Metal-Cation Arrangements in Metal-Organic Frameworks for Programming the Composition of Electrocatalytically Active Multimetal Oxides. *J Am Chem Soc* **2019**, *141* (4), 1766–1774. https://doi.org/10.1021/jacs.8b12860.

(3) Gándara, F.; De Andrés, A.; Gómez-Lor, B.; Gutiérrez-Puebla, E.; Iglesias, M.; Monge, M. A.; Proserpio, D. M.; Snejko, N. A Rare-Earth MOF Series: Fascinating Structure, Efficient Light Emitters, and Promising Catalysts. *Cryst Growth Des* **2008**, *8* (2), 378–380. https://doi.org/10.1021/cg700796m.

(4) Gándara, F.; De La Peña-O'Shea, V. A.; IIIas, F.; Snejko, N.; Proserpio, D. M.; Gutiérrez-Puebla, E.; Monge, M. A. Three Lanthanum MOF Polymorphs: Insights into Kinetically and Thermodynamically Controlled Phases. *Inorg Chem* **2009**, *48* (11), 4707–4713. https://doi.org/10.1021/ic801779j.

(5) Chun Zeng, H. Ostwald Ripening: A Synthetic Approach for Hollow Nanomaterials. *Curr Nanosci* **2007**, *3* (2), 177–181. https://doi.org/10.2174/157341307780619279.

(6) di Gregorio, M. C.; Elsousou, M.; Wen, Q.; Shimon, L. J. W.; Brumfeld, V.; Houben, L.; Lahav, M.; van der Boom, M. E. Molecular Cannibalism: Sacrificial Materials as

Precursors for Hollow and Multidomain Single Crystals. *Nat Commun* **2021**, *12* (1), 1–9. https://doi.org/10.1038/s41467-021-21076-9.

(7) Chiodini, S.; Reinares-Fisac, D.; Espinosa, F. M.; Gutiérrez-Puebla, E.; Monge, A.; Gándara, F.; Garcia, R. Angstrom-Resolved Metal-Organic Framework-Liquid Interfaces. *Sci Rep* **2017**, *7* (1), 1–6. https://doi.org/10.1038/s41598-017-11479-4.

(8) Xie, L.; Su, T. S.; Li, X. G. Magnetic Field Dependence of Schottky Anomaly in the Specific Heats of Stripe-Ordered Superconductors La1.6−xNd0.4SrxCuO4. *Physical Superconductors* **2012**, *480*, 14–18.

(9) Burriel, R.; Castro, M.; Saez-Puche, R. Calorimetric Study of the Structural and Magnetic Ordering in R2NiO4 (R = La, Pr and Nd). *Pure and Applied Chemistry* **1995**, *67*, 1825–1830.

(10) Taira, N.; Wakeshima, M.; Hinatsu, Y. Magnetic Susceptibility and Specific Heat Studies on Heavy Rare Earth Ruthenate Pyrochlores R2Ru2O7 (R = Gd–Yb). *J Mater Chem* **2002**, *12*, 1475–1479.

(11) He, C.; Zheng, H.; Mitchell, J. F.; Foo, M. L.; Cava, R. J.; Leighton, C. Low Temperature Schottky Anomalies in the Specific Heat of LaCoO3: Defect-Stabilized Finite Spin States. *Appl Phys Lett* **2009**, *94*, 102514.

─ CHAPTER 5 ─

Multi-Metal Oxides Derived from MTV-MOFs and Their Use as Catalysts for The Reverse Water-Gas Shift Reaction

5.1. Introduction

Not only has the field of MOFs undergone an exponential growth in the past decades, but also their use to obtain MOF-derived materials (oxides, carbons, nanoparticles) have recently emerged as an alternative of generating different classes of functional materials. The reason behind this is that some applications are carried out in conditions that are not compatible with the chemical nature of MOFs. Reactions carried out at high temperatures (>300 ºC), high pressures (>8MPa), or in hash conditions (highly acidic or alkaline media) generally cause the frameworks to collapse; however, they can be still used as precursors or sacrificial templates to generate other derived compounds. While MOF-derived carbon-based materials are especially relevant in the field of electrocatalysis,[1] energy storage and conversion,[2,3] nanomaterials derived from MOFs show great potential for applications such as sensing, catalysis, and energy or gas storage.[4–6]

The key point here is that the composition, tuned in the initial MOFs at the atomic level, can be translated to other classes of solids, while preserving the specific distribution of the active sites. One of the most straightforward routes of synthesizing MOF-derived materials consists of using MOFs as precursors and subjecting them to a thermal treatment.[7] Based on this strategy, my group recently conducted a study focused on obtaining MOF-derived catalysts for the reverse water gas shift (RWGS) reaction.[8] A family of multi-metal MOFs with combinations of up to four metal atoms (Zn, Co, Mn, Ca)[9,10] were calcined to obtain multi-metal spinels with a specific ratio and distribution of the metal cations, and these oxides were found to be highly efficient pre-catalysts for the RWGS reaction.

Chapter 4 of this thesis has the study of the multi-metal MTV-RPF-4 family as its main subject, so we know how different ratios or rare-earth combinations impact the

distribution of the metals within the SBUs and the overall output of the synthesis. So, the calcination of multi-metal combinations of this MTV-MOF family is expected to generate oxides with specific metal ratios, and the knowledge obtained in said chapter can be applied to obtain complex catalysts. Therefore, it would be interesting to evaluate and compare the catalytic activity of the calcined multi-metal RPF-4 combinations, as opposed to other traditional synthesis routes. When pondering about what catalysis reaction would fit our MOF-derived rare-earth oxides, we gravitated towards reactions involving carbon dioxide (CO_2), which is the primary greenhouse gas emitted through human activities. Although it is naturally present in the atmosphere, emissions stemming from human activities are increasing alarmingly, disrupting the natural balance. The current global energy crisis and the inexorable increase of the demand for fossil fuels seem to be intractable problems that bespeak the disquieting situation of the environment. Fossil fuel shortages and the contamination resulting from their combustion are taking a toll on the atmosphere, as the result is a continuously increasing amount of greenhouse gas emissions. To alleviate the strain that we are putting on our planet, these high-priority issues must be tackled.

One approach to reduce CO_2 emissions is to consider this gas as a resource rather than a waste, thus recycling it and turning it into a value-added product. The valorization of CO_2 can be carried out through its transformation into CO, a key C_1 and C_{2+} building block[11] in many industrial processes, such as organic synthesis,[12] formation of longer-chain hydrocarbons (Fisher-Tropsch reaction)[13], carbonylation,[14] synthesis of renewable high-calorific fuels such as CH_4,[15] and important compounds for the chemical industry such as methanol[16] or formic and acetic acid.[17] CO_2 can be reduced to CO and H_2O through a route called reverse water-gas shift (RWGS, eq. 1). This reaction is endothermic (ΔH^0 = +41,1 kJ/mol) and thermodynamically limited, being favoured at higher temperatures.[18]

(eq.1) $CO_2 + H_2 \rightarrow CO + H_2O$

Many catalysts have been studied for this reaction, mainly metal-based oxides,[19] being noble (Au, Pd, Pt, Ru) and transition metals (Cu, Ni, Fe) among the most widely studied. As a consequence of the high temperatures required for the RWGS reaction, the catalysts can suffer from deactivation by either metal sintering or carbon deposition (coking).[20] One way to circumvent these hinders is to use catalysts with a homogeneous and "physically" confined distribution of the metal ions (for example, physical encapsulation of metal particles),[21] or to synthesize multi-metal catalysts that include a metal with a higher melting point.[22,23] As already mentioned, traditional oxides have been the main catalysts used for the RWGS reaction; however, as this field has evolved over the years, more sophisticated versions of these oxides (mixed-metals, nanoparticles supported on an oxide matrix, metal combinations or proportions not achievable through traditional synthesis) could access unprecedented catalytic performances.

Generally, the catalytic activity of the RWGS reaction can be boosted by using a reducible metal oxide such as CeO_2, CrO_3 or TiO_2, which display oxygen vacancies that promote CO_2 adsorption and activation.[24] Among these oxides, ceria (CeO_2) displays the highest efficiency at high temperatures.[25] When doping ceria with La^{3+} ions, the number of oxygen vacancies increases as the lanthanum ions substitute part of the Ce^{4+} positions, and this further enhances the oxygen mobility which results in an improvement of the reducibility of the system. A recent study demonstrated that the optimal La doping value is 10%, which corresponds to a maximum surface proportion of Ce^{3+} and the highest CO yield.[26]

Thus, we selected the Ce-La RPF-4 combination with ratios 9.5:0.5, 9:1, 8:2 so that the La doping amount would be in the 5-20% range. Additionally, we also chose the

combinations of Ce-Pr and Ce-Nd, both in a 9:1 ratio. Generally, doping ceria with metals of lower ionic radius than Ce results in structural distortions that increases its reducibility, enhancing their reactivity in CO oxidation reactions.[27] On one hand, praseodymium doping promotes oxygen donation in ceria;[28] on the other hand, neodymium-doped ceria displays a higher ionic conductivity.[29]

Bearing all this in mind, this chapter is focused on obtaining RPF-4-derived multi-metal oxides with tuned compositions based on previous knowledge (chapter 4 of this thesis) of how to adjust the composition of this MOF family. The performance of these materials as catalysts for the RWGS reaction was evaluated in comparison to oxides synthesized via traditional routes, and these experiments were carried out in collaboration with Carlos Martínez Gómez and Consuelo Álvarez Galván (Instituto de Catálisis y Petroquímica-ICP, Madrid, Spain). These preliminary results prove that the MOF-based samples yield a higher catalytic activity which is directly related to the intrinsic characteristics of the samples, further demonstrating that MOF-derived materials offer advantages over other classes of compounds.

5.2. Synthesis and characterization of the initial MOFs

5.2.1. Synthesis of multi-metal MTV-RPF-4

All reagents and solvents employed were commercially available and used as received without further purification: 4,4′-(hexafluoroisopropylidene)bis(benzoic acid), H_2hfipbb (>98%, TCI); lanthanum nitrate hexahydrate, $La(NO_3)_3 \times 6H_2O$ (99.9%, Alfa Aesar); cerium nitrate hexahydrate, $Ce(NO_3)_3 \times 6H_2O$ (99%, Aldrich); neodymium nitrate hexahydrate, $Nd(NO_3)_3 \times 6H_2O$ (99.9%, Strem Chemicals); praseodymium nitrate hexahydrate, $Pr(NO_3)_3 \times 6H_2O$ (99.9%, Strem Chemicals); ethanol absolute (Scharlau); acetone (99.6%, Labkem).

The amount of metal salt was adjusted according to every combination. All the quantities of metal salts used in all the synthesis are listed in Table 5.1. To illustrate how each combination was obtained, an example is given as follows: for the synthesis of the Ce-La 8:2 combination, $Ce(NO_3)_3 \times 6H_2O$ (0.09 mmol, 40.3 mg), $La(NO_3)_3 \times 6H_2O$ (0.2 mmol, 10.4 mg) and H_2hfipbb (0.176 mmol, 70.45 mg) were dissolved in 7.5 mL of absolute ethanol and 5 mL of water. The mixture was placed in a Teflon-lined steel autoclave and heated during 72 hours in an oven at 160 °C. After cooling to room temperature, the crystals were filtered and washed with water and acetone.

Table 5.1. Synthesis ratios for the multi-metal MTV-RPF-4 binary combinations used to obtain the corresponding mixed-metal oxides.

Ce-La	**Molar code**	**$Ce(NO_3)_3$ x $6H_2O$**		**$La(NO_3)_3$ x $6H_2O$**	
		mg	**mmol**	**mg**	**mmol**
	8:2	40.3	0.09	10.4	0.02
	9:1	44.94	0.1	4.98	0.01
	9.5:0.5	47.44	0.105	2.7	0.005
Ce-Pr	**Molar code**	**$Ce(NO_3)_3$ x $6H_2O$**		**$Pr(NO_3)_3$ x $6H_2O$**	
		mg	**mmol**	**mg**	**mmol**
	9:1	44.94	0.1	5	0.01
Ce-Nd	**Molar code**	**$Ce(NO_3)_3$ x $6H_2O$**		**$Nd(NO_3)_3$ x $6H_2O$**	
		mg	**mmol**	**mg**	**mmol**
	9:1	44.94	0.1	5.04	0.01

5.2.2. Characterization of multi-metal MTV-RPF-4

The purity of the samples was confirmed by PXRD (Figure 5.1), and all the patterns match the simulated pattern of single-metal La-RPF-4.

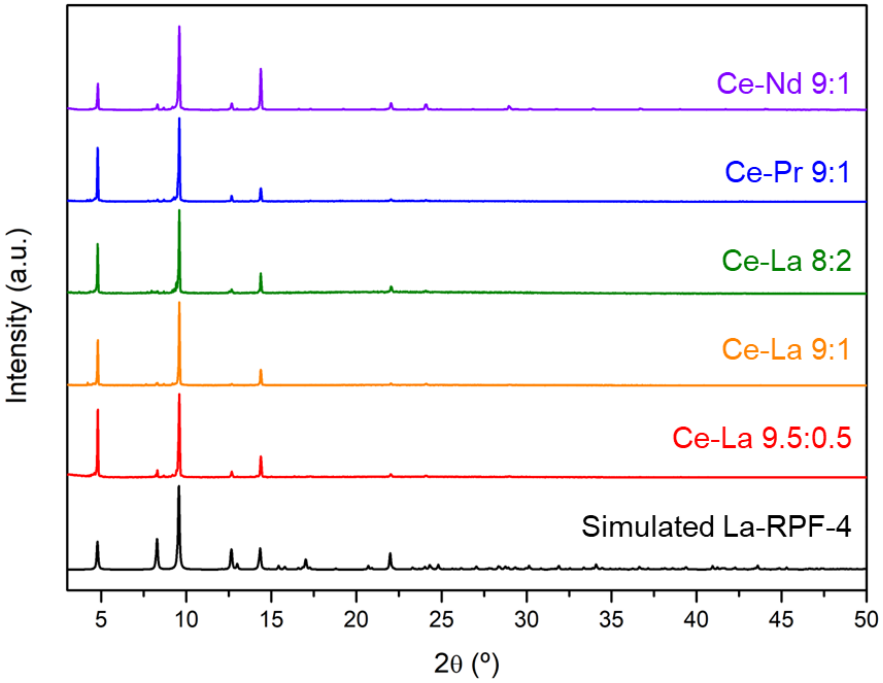

Figure 5.1. PXRD patterns of all the samples: as-synthesized RPF-4 MOFs.

Regarding the morphology and composition of the crystals, as already mentioned in chapter 4, the Ce-La combinations yield hexagonal prism-like crystals with generally smooth faces, and with presence of a higher number of defects for the higher La concentration. The Ce-Nd and Ce-Pr RPF-4 combinations were not studied in chapter 4, however these samples display a similar behavior to the Ce-La combination. Here, Ce, which is in a higher concentration, directs the crystallization mechanism of the structure and the morphology is analogous to that of single-metal Ce-RPF-4. EDX analysis confirmed that the composition of the crystals of all the samples matches the initial metal ratios (Figure 5.3).

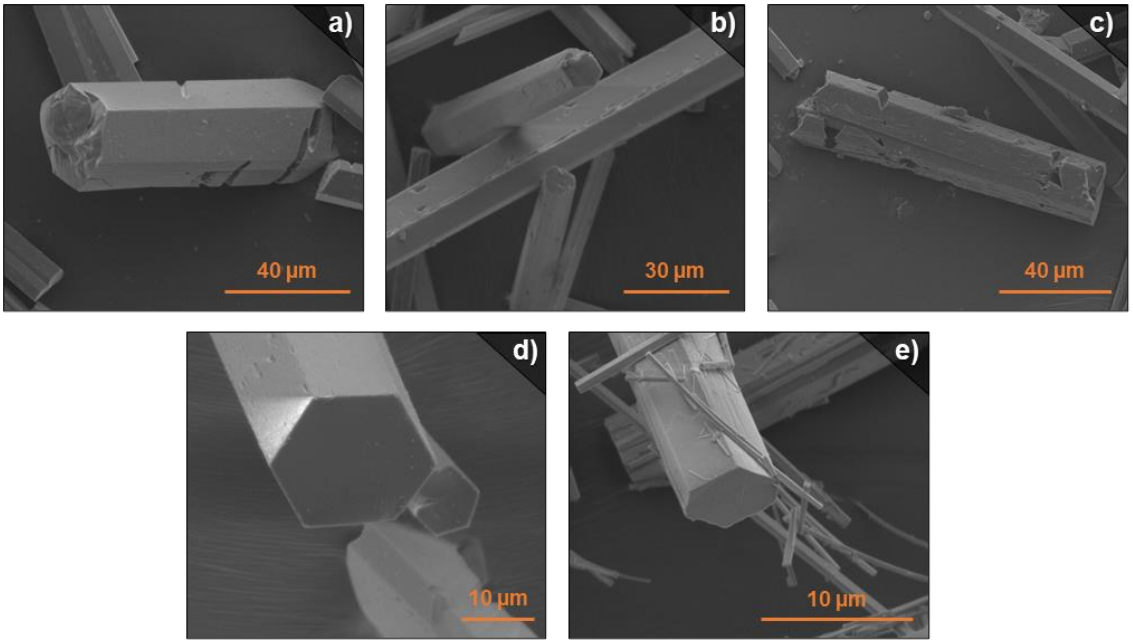

Figure 5.2. SEM images of the MTV-RPF-4 samples. **a)** Ce-La 9.5:0.5 **b)** Ce-La 9:1 **c)** Ce-La 8:2 **d)** Ce-Pr 9:1 and **e)** Ce-Nd 9:1.

5.3. Calcination of the MOFs and characterization of the products

5.3.1. Calcination of multi-metal MTV-RPF-4

The multi-metal MTV-RPF-4 samples were transferred to zirconia crucibles and were subjected to a thermal treatment in air. The first step consisted of a heating stage of 6 hours 20 minutes (2.5 ºC/min heating rate) from room temperature to 800 ºC; the temperature was maintained for 4 hours, and the sample was left to slowly cool down to room temperature. The RPF-4 structure totally decomposes at 550 ºC,[30] therefore this calcination strategy ensures the total transformation of the MOF and the elimination of any organic component.

5.3.2. Characterization of the calcined products

The purity check and phase identification of the calcined samples were carried out through PXRD (Figure 5.3). All the patterns match the formation of the cubic CeO_2 crystal phase (fluorite-type structure, PDF database code 04-018-4984), which implies that the Ce^{3+} atoms have been oxidized to Ce^{4+}, as expected bearing in mind that the thermal treatment was carried out in air. The absence of any other crystalline phase in the PXRD patterns suggests that the La atoms are effectively incorporated in the CeO_2 lattice, thus generating oxygen vacancies.

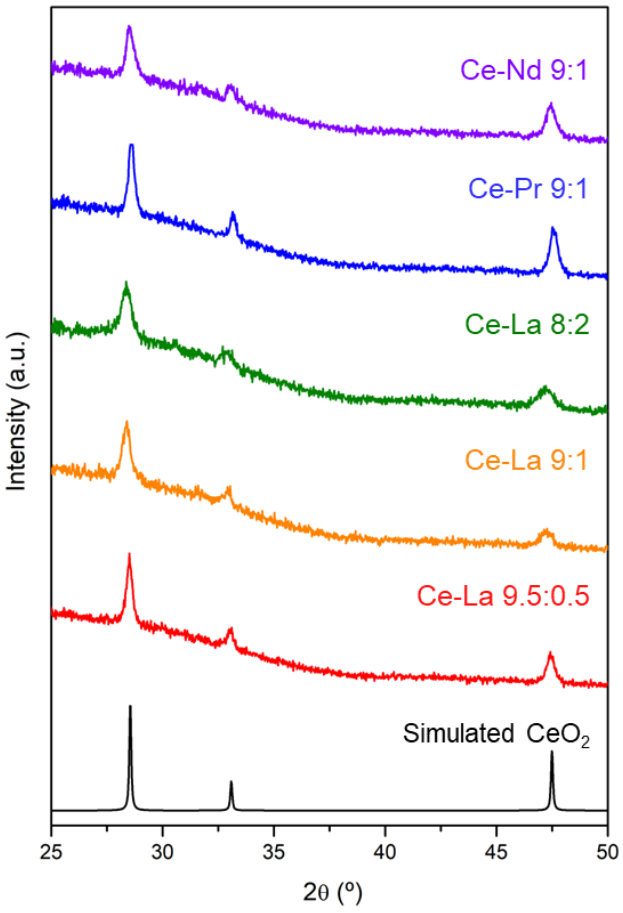

Figure 5.3. PXRD patterns of the calcinated MTV-RPF-4 samples.

To further characterize the calcination products and to rule out any changes in the composition or the ratio between the metals, a SEM-EDX study was conducted (Figure 5.4). The initial hexagonal prism-like morphology of the parent MOFs is partially retained, which is frequently observed in many thermally treated MOFs;[31,32] however, the crystals are clearly contracted and slightly deformed, as result of the calcination process and removal of the organic part. A closer look at the crystals shows that they are now formed by aggregated particles. The EDX analysis confirmed that the metal ratios of the initial MOFs were successfully transferred to the oxides (Figure 5.6).

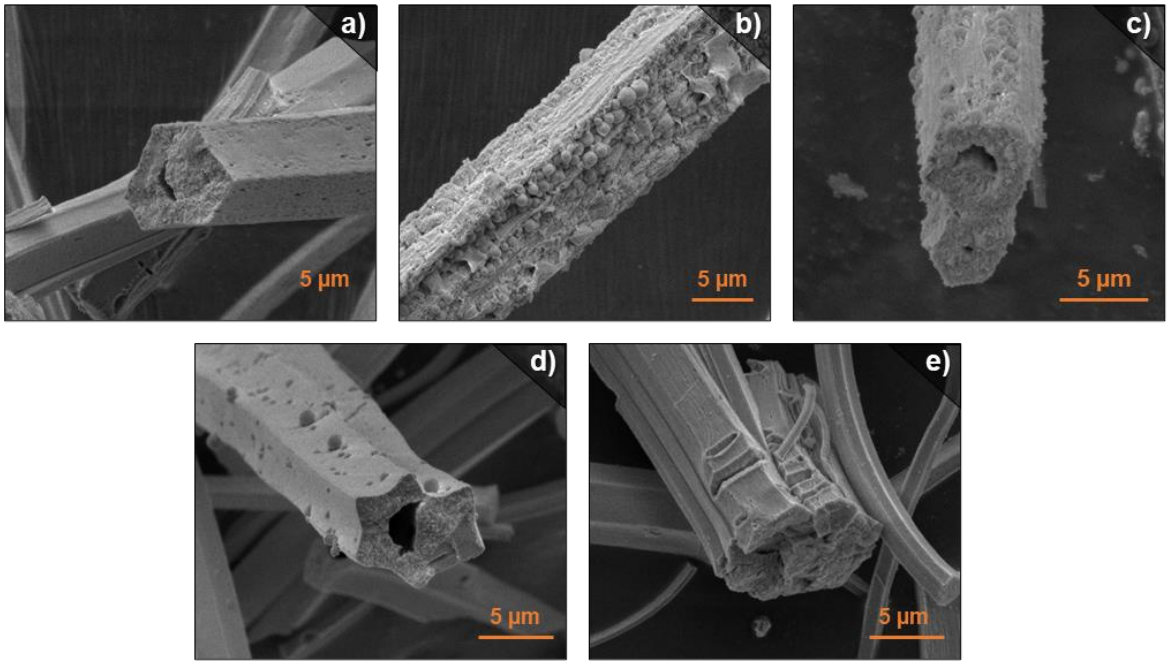

Figure 5.4. SEM images of the calcined MTV-RPF-4 samples. **a)** Ce-La 9.5:0.5 **b)** Ce-La 9:1 **c)** Ce-La 8:2 **d)** Ce-Pr 9:1 and **e)** Ce-Nd 9:1.

5.4. Catalytic performance evaluation: RWGS reaction

5.4.1. Catalysis procedure

The reaction is carried out in a continuous mode at three different temperatures (700, 600 and 500 ºC) with a 2.5 hour hold stage at each temperature. The higher temperature was selected as a starting point to avoid the Sabatier reaction (transformation of CO_2 into CH_4)[33] which generates undesired byproducts like methane, and the Boudouard reaction (conversion of CO into CO_2)[34] which results in carbon deposition which deactivates the catalyst.

5.4.2. Results and discussion

In addition to the aforementioned samples, CeO_2 doped with 10% La was synthesized following a reported sol-gel route[8] to be used as a benchmark (denoted CeLa 9:1 – SG).

Firstly, as displayed in Figure 5.5, an induction period is observed in the first reaction hour as conversion values quickly increase. In the first reaction stage at 700 ºC, the oxides derived from MTV-RPF-4 show higher conversion values than the sol-gel prepared sample. After 2.5 hours of reaction time, maximums of 41%, 43%, and 45% of conversion were reached for the MOF-derived oxides with Ce-La ratios of 9.5:0.5, 9:1, and 8:2, respectively, while the sol-gel prepared oxide displays a conversion value of 36%. For the Ce-Pr and Ce-Nd 9:1 samples, the conversion values are slightly lower than the lanthanum-containing samples (39.9% and 38.7%, respectively). This trend is maintained in the second reaction stage at 600 ºC. As expected, there is a general conversion decrease associated to the drop in temperature. Again, the sol-gel prepared oxide displays a low conversion value (16.6%), and the Ce-Nd 9:1 sample yielded slightly lower values. The lanthanum-containing MOF-derived oxides demonstrate the best activity, with

conversion values of 19.8%, 18,6% and 23.5% for Ce-La ratios of 9.5:0.5, 9:1 and 8:2, respectively. The most striking fact is that the selectivity towards CO is 100% in all cases, and this value is maintained even at 500 ºC (Figure 5.6). The CO yield is the most significant parameter to evaluate the catalytical performance as it includes both conversion and selectivity, CO yield = (selectivity × conversion) / 100; however, as the selectivity of all the samples displays a constant value of 100% during all the cycles, the CO yield plot matches the conversion plot.

After completing the catalysis cycles, the samples were recovered and were analyzed by PXRD to check for any structural or compositional changes. As displayed in Figure 5.7, the PXRD plots of the MOF-derived oxides match the structure of CeO_2, and do not display any change after being subjected to the conditions of the catalysis experiments.

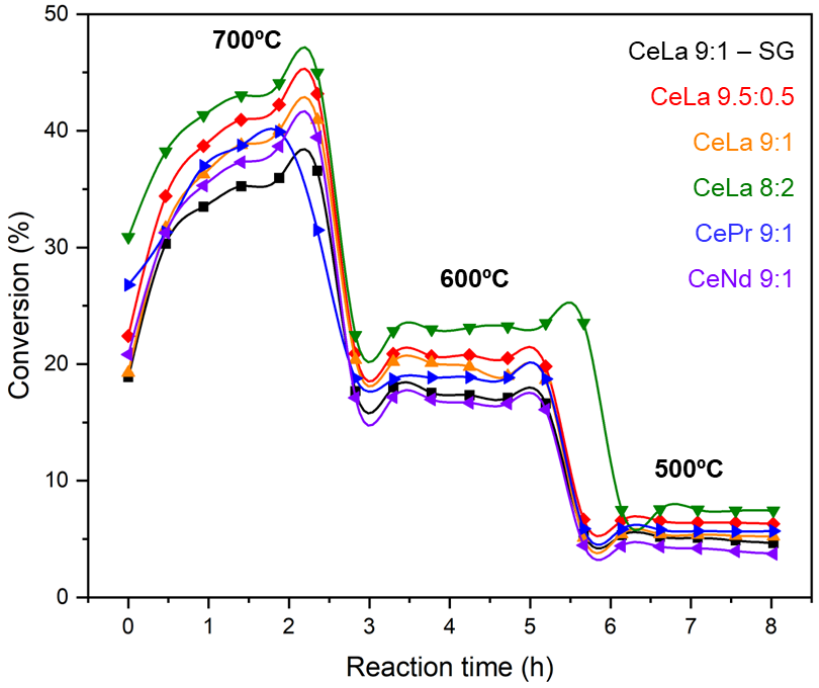

Figure 5.5. CO_2 conversion versus reaction time plot.

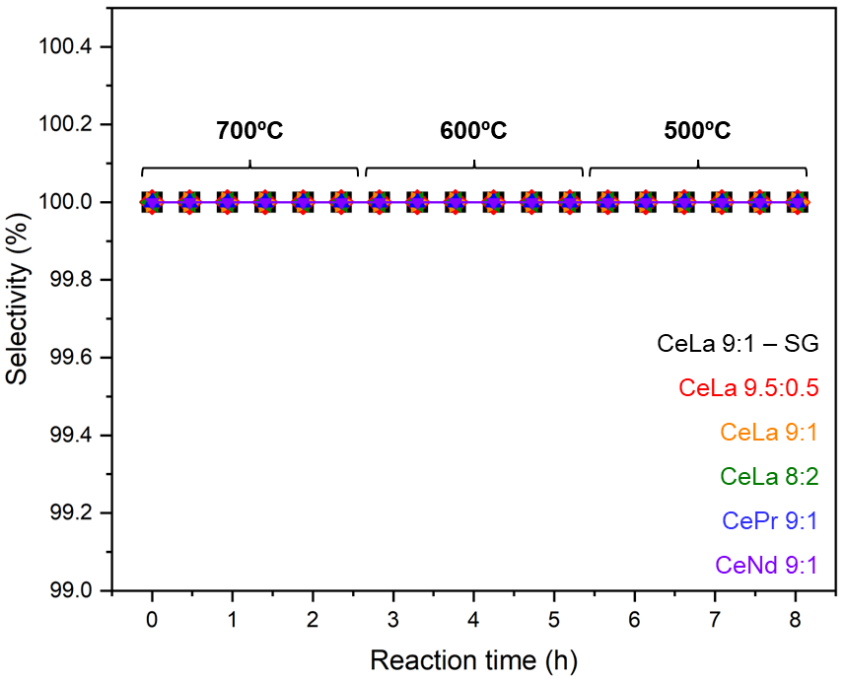

Figure 5.6. Selectivity towards CO versus reaction time plot.

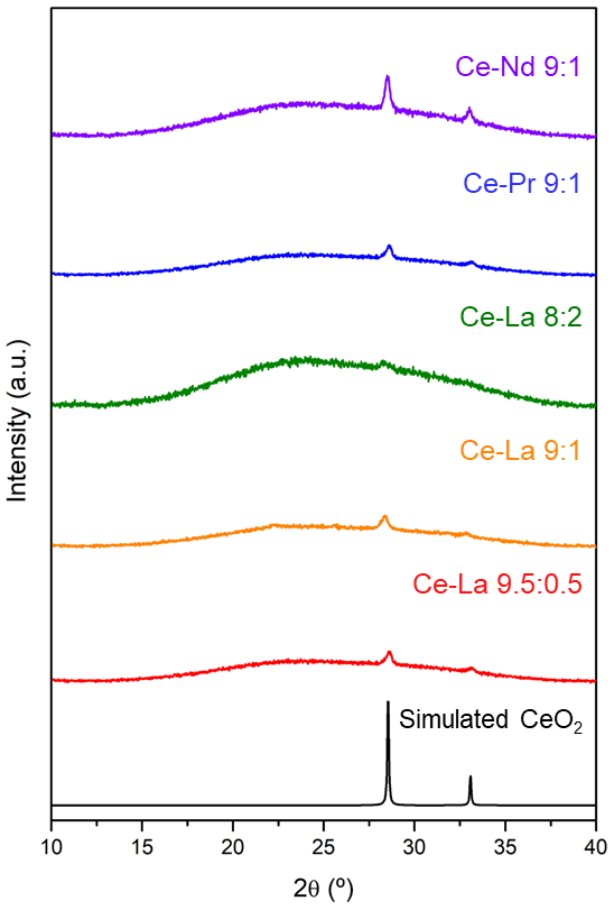

Figure 5.7. PXRD patterns of the calcined MTV-MOFs post-catalysis.

The chemical composition of the surface of the MOF-derived Ce-La 9:1 sample was analyzed through XPS. As displayed in Table 5.2, the La/Ce ratio is very close to the theoretical value, and both species are in the form of oxides.

Table 5.2. Atomic composition of the Ce – La (9:1) catalyst by XPS.

Atoms	C 1s	O 1s	Ce 3d	La 3d	La/Ce
Composition (%)	32.53	56.24	9.94	1.29	0.13

Additionally, the deconvolution of the spectrum of the 3d orbital of Ce was carried out to evaluate the proportion of Ce^{3+} and Ce^{4+} (in their corresponding forms, Ce_2O_3 and CeO_2) in the sample. As expected for the Ce 3d XPS spectrum of ceria,[35] up to ten maximum peaks are observed in the deconvolution of the spectrum displayed in Figure 5.8, of which three doublets correspond to Ce^{4+}, and two doublets to Ce^{3+}. Each peak was assigned an ion based on information found in different literature sources,[36,37] and the data is presented in Table 5.3.

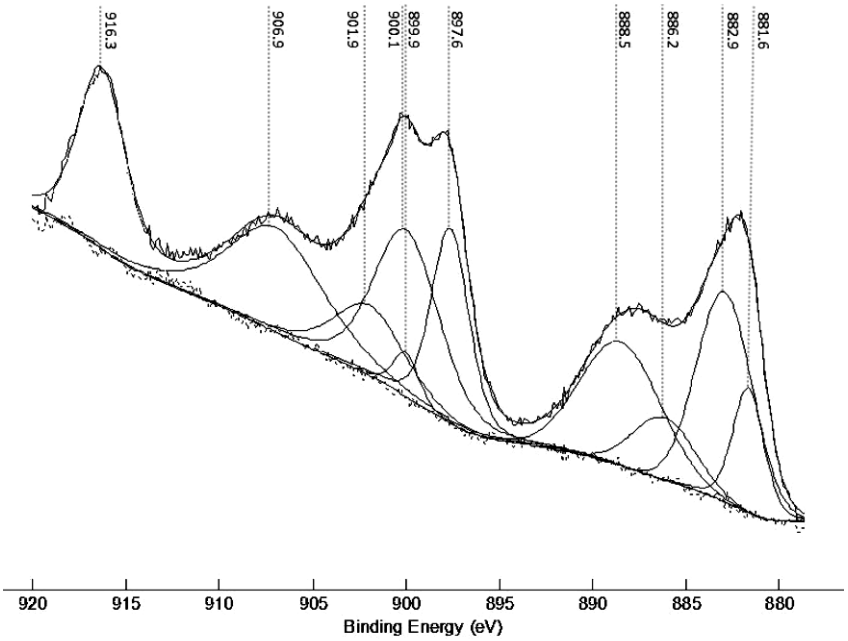

Figure 5.8. Deconvolution of the XPS spectrum corresponding to the Ce 3d orbital for the MOF-derived sample Ce-La 9:1.

Table 5.3. Ce 3d deconvolution spectrum peak assignation. v, u = integrated peak areas.

Ion	Binding energy (eV)	Assignation
Ce^{4+}	882.9	v
	888.5	v''
	897.6	v'''
	900.1	u
	906.9	u''
	916.3	u'''
Ce^{3+}	881.5	v^0
	886.2	v'
	899.9	u^0
	901.9	u'

Given these results and following the equations used by Chan *et al.* in their report (eq. 2-4),[35] the Ce^{3+} and Ce^{4+} percentages can be estimated by using the area under the curve of each peak, and the calculated value for Ce^{3+} of 33.4%, which points to a higher presence of Ce^{4+} (CeO_2) in the sample.

(eq.2) $$Ce^{3+} = v^0 + v' + u^0 + u'$$

(eq.3) $$Ce^{4+} = v + v'' + v''' + u + u'' + u'''$$

(eq.4) $$\%Ce^{3+} = Ce^{3+} / (Ce^{3+} + Ce^{4+})$$

Regarding lanthanum, the 3d peak was deconvoluted in two signals due to its asymmetry. The major signal (834.4 eV, 62%) corresponds to La^{3+} in oxide form, and the minor signal (838.41 eV, 38%) corresponds to carbonates or surface hydroxides of La^{3+}.

5.5. Conclusions

To sum up, in this chapter, five multi-metal oxide catalysts were prepared through the calcination of multi-metal MTV-MOFs. The initial metal ratios and sequences were successfully transferred from the initial MOFs to the oxides. Due to intrinsic features of their structure, these materials displayed a higher catalytic activity for the RWGS reaction compared to that of oxides prepared via a traditional synthesis route. This was clearly evidenced when comparing the CO conversion of the MOF-derived catalysts (45% at 700 ºC for the Ce-La 8:2 sample) with the sol-gel synthesized one (36% at 700 ºC). The MOF-derived catalyst that displayed the highest CO yield is Ce-La 8:2, and this performance can be attributed to the higher proportion of oxygen vacancies generated by the higher La doping proportion.

The results presented in this chapter are a great first step towards the optimization of a MOF-derived catalyst for the RWGS. The insertion of an additional metal, specifically Ni, would further enhance the catalytic activity, based on the fact that Ni/La-doped CeO_2 (with a determinate Ni-La proportion) has displayed an unprecedented performance.[8,38] Our MOF-derived catalysts already display a good catalytical performance, so the insertion of Ni would further improve the results. So, the future of this investigation topic will be focused towards obtaining Ni-containing catalysts (either by one-pot synthesis or post-synthetical Ni impregnation) and the evaluation of their catalytic activity.

The results of this chapter have not yet been published; however, a manuscript has been already prepared and will be submitted to a journal once a few pending experiments will be completed.

5.6. References

(1) Wang, H. F.; Chen, L.; Pang, H.; Kaskel, S.; Xu, Q. MOF-Derived Electrocatalysts for Oxygen Reduction, Oxygen Evolution and Hydrogen Evolution Reactions. *Chem Soc Rev* **2020**, *49* (5), 1414–1448. https://doi.org/10.1039/c9cs00906j.

(2) Wu, H. Bin; Lou, X. W. Metal-Organic Frameworks and Their Derived Materials for Electrochemical Energy Storage and Conversion: Promises and Challenges. *Sci Adv* **2017**, *3* (12), 1–17. https://doi.org/10.1126/sciadv.aap9252.

(3) Lu, X. F.; Fang, Y.; Luan, D.; Lou, X. W. D. Metal−organic Frameworks Derived Functional Materials for Electrochemical Energy Storage and Conversion: A Mini Review. *Nano Lett* **2021**, *21* (4), 1555–1565. https://doi.org/10.1021/acs.nanolett.0c04898.

(4) Dang, S.; Zhu, Q. L.; Xu, Q. Nanomaterials Derived from Metal-Organic Frameworks. *Nat Rev Mater* **2017**, *3*. https://doi.org/10.1038/natrevmats.2017.75.

(5) Shen, K.; Chen, X.; Chen, J.; Li, Y. Development of MOF-Derived Carbon-Based Nanomaterials for Efficient Catalysis. *ACS Catal* **2016**, *6* (9), 5887–5903. https://doi.org/10.1021/acscatal.6b01222.

(6) Wang, Q.; Astruc, D. State of the Art and Prospects in Metal-Organic Framework (MOF)-Based and MOF-Derived Nanocatalysis. *Chem Rev* **2020**, *120* (2), 1438–1511. https://doi.org/10.1021/acs.chemrev.9b00223.

(7) Castells-Gil, J.; Ould-Chikh, S.; Ramírez, A.; Ahmad, R.; Prieto, G.; Gómez, A. R.; Garzón-Tovar, L.; Telalovic, S.; Liu, L.; Genovese, A.; Padial, N. M.; Aguilar-Tapia, A.; Bordet, P.; Cavallo, L.; Martí-Gastaldo, C.; Gascon, J. Unlocking Mixed Oxides with Unprecedented Stoichiometries from Heterometallic Metal-Organic Frameworks for the

Catalytic Hydrogenation of CO2. *Chem Catalysis* **2021**, *1* (2), 364–382. https://doi.org/10.1016/j.checat.2021.03.010.

(8) Castillo-Blas, C.; Álvarez-Galván, C.; Puente-Orench, I.; García-Sánchez, A.; Oropeza, F. E.; Gutiérrez-Puebla, E.; Monge, Á.; de la Peña-O'Shea, V. A.; Gándara, F. Highly Efficient Multi-Metal Catalysts for Carbon Dioxide Reduction Prepared from Atomically Sequenced Metal Organic Frameworks. *Nano Res* **2021**, *14* (2), 493–500. https://doi.org/10.1007/s12274-020-2813-x.

(9) Castillo-Blas, C.; De La Peña-O'Shea, V. A.; Puente-Orench, I.; De Paz, J. R.; Sáez-Puche, R.; Gutiérrez-Puebla, E.; Gándara, F.; Monge, Á. Addressed Realization of Multication Complex Arrangements in Metal-Organic Frameworks. *Sci Adv* **2017**, *3* (7), 1–11. https://doi.org/10.1126/sciadv.1700773.

(10) Castillo-Blas, C.; López-Salas, N.; Gutiérrez, M. C.; Puente-Orench, I.; Gutiérrez-Puebla, E.; Ferrer, M. L.; Monge, M. Á.; Gándara, F. Encoding Metal-Cation Arrangements in Metal-Organic Frameworks for Programming the Composition of Electrocatalytically Active Multimetal Oxides. *J Am Chem Soc* **2019**, *141* (4), 1766–1774. https://doi.org/10.1021/jacs.8b12860.

(11) Zhou, W.; Cheng, K.; Kang, J.; Zhou, C.; Subramanian, V.; Zhang, Q.; Wang, Y. New Horizon in C1 Chemistry: Breaking the Selectivity Limitation in Transformation of Syngas and Hydrogenation of CO2 into Hydrocarbon Chemicals and Fuels. *Chem Soc Rev* **2019**, *48* (12), 3193–3228. https://doi.org/10.1039/c8cs00502h.

(12) Liu, Q.; Wu, L.; Jackstell, R.; Beller, M. Using Carbon Dioxide as a Building Block in Organic Synthesis. *Nat Commun* **2015**, *6*. https://doi.org/10.1038/ncomms6933.

(13) Dry, M. E. The Fischer-Tropsch Process: 1950-2000. *Catal Today* **2002**, *71* (3–4), 227–241. https://doi.org/10.1016/S0920-5861(01)00453-9.

(14) Peng, J. B.; Geng, H. Q.; Wu, X. F. The Chemistry of CO: Carbonylation. *Chem* **2019**, *5* (3), 526–552. https://doi.org/10.1016/j.chempr.2018.11.006.

(15) Li, K.; Peng, B.; Peng, T. Recent Advances in Heterogeneous Photocatalytic CO2 Conversion to Solar Fuels. *ACS Catal* **2016**, *6* (11), 7485–7527. https://doi.org/10.1021/acscatal.6b02089.

(16) Yang, H.; Wu, Y.; Li, G.; Lin, Q.; Hu, Q.; Zhang, Q.; Liu, J.; He, C. Scalable Production of Efficient Single-Atom Copper Decorated Carbon Membranes for CO2 Electroreduction to Methanol. *J Am Chem Soc* **2019**, *141* (32), 12717–12723. https://doi.org/10.1021/jacs.9b04907.

(17) Cui, W. G.; Zhang, G. Y.; Hu, T. L.; Bu, X. H. Metal-Organic Framework-Based Heterogeneous Catalysts for the Conversion of C1 Chemistry: CO, CO 2 and CH 4. *Coord Chem Rev* **2019**, *387*, 79–120. https://doi.org/10.1016/j.ccr.2019.02.001.

(18) Nielsen, D. U.; Hu, X. M.; Daasbjerg, K.; Skrydstrup, T. Chemically and Electrochemically Catalysed Conversion of CO2 to CO with Follow-up Utilization to Value-Added Chemicals. *Nat Catal* **2018**, *1* (4), 244–254. https://doi.org/10.1038/s41929-018-0051-3.

(19) Kattel, S.; Liu, P.; Chen, J. G. Tuning Selectivity of CO2 Hydrogenation Reactions at the Metal/Oxide Interface. *J Am Chem Soc* **2017**, *139* (29), 9739–9754. https://doi.org/10.1021/jacs.7b05362.

(20) González-Castaño, M.; Dorneanu, B.; Arellano-García, H. The Reverse Water Gas Shift Reaction: A Process Systems Engineering Perspective. *React Chem Eng* **2021**, *6* (6), 954–976. https://doi.org/10.1039/d0re00478b.

(21) Yang, X.; Su, X.; Chen, X.; Duan, H.; Liang, B.; Liu, Q.; Liu, X.; Ren, Y.; Huang, Y.; Zhang, T. Promotion Effects of Potassium on the Activity and Selectivity of Pt/Zeolite Catalysts for Reverse Water Gas Shift Reaction. *Appl Catal B* **2017**, *216*, 95–105. https://doi.org/10.1016/j.apcatb.2017.05.067.

(22) Kharaji, A. G.; Shariati, A.; Takassi, M. A. A Novel γ-Alumina Supported Fe-Mo Bimetallic Catalyst for Reverse Water Gas Shift Reaction. *Chin J Chem Eng* **2013**, *21* (9), 1007–1014. https://doi.org/10.1016/S1004-9541(13)60573-X.

(23) Santos, V. P.; Borges, L.; Sartipi, S.; van der Linden, B.; Dugulan, A. I.; Chojecki, A.; Davidian, T.; Ruitenbeek, M.; Meima, G. R.; Kapteijn, F.; Makkee, M.; Gascon, J. High-Temperature Fischer-Tropsch Synthesis over FeTi Mixed Oxide Model Catalysts: Tailoring Activity and Stability by Varying the Ti/Fe Ratio. *Appl Catal A Gen* **2017**, *533*, 38–48. https://doi.org/10.1016/j.apcata.2017.01.002.

(24) Puigdollers, A. R.; Schlexer, P.; Tosoni, S.; Pacchioni, G. Increasing Oxide Reducibility: The Role of Metal/Oxide Interfaces in the Formation of Oxygen Vacancies. *ACS Catal* **2017**, *7* (10), 6493–6513. https://doi.org/10.1021/acscatal.7b01913.

(25) Trovarelli, A.; de Leitenburg, C.; Dolcetti, G.; Lorca, J. L. CO2 Methanation under Transient and Steady-State Conditions over Rh/CeO2 and CeO2-Promoted Rh/SiO2: The Role of Surface and Bulk Ceria. *Journal of Catalysis*. 1995, pp 111–124. https://doi.org/10.1006/jcat.1995.1014.

(26) Alvarez-Galvan, C.; Lustemberg, P. G.; Oropeza, F. E.; Bachiller-Baeza, B.; Dapena Ospina, M.; Herranz, M.; Cebollada, J.; Collado, L.; Campos-Martin, J. M.; De La Peña-O'shea, V. A.; Alonso, J. A.; Ganduglia-Pirovano, M. V. Highly Active and Stable Ni/La-Doped Ceria Material for Catalytic CO2Reduction by Reverse Water-Gas Shift Reaction.

ACS Appl Mater Interfaces **2022**, *14* (45), 50739–50750. https://doi.org/10.1021/acsami.2c11248.

(27) Xiao, G.; Li, S.; Li, H.; Chen, L. Synthesis of Doped Ceria with Mesoporous Flowerlike Morphology and Its Catalytic Performance for CO Oxidation. *Microporous and Mesoporous Materials* **2009**, *120* (3), 426–431. https://doi.org/10.1016/j.micromeso.2008.12.015.

(28) Milberg, B.; Juan, A.; Irigoyen, B. Redox Behavior of a Low-Doped Pr-CeO 2 (111) Surface. A DFT+U Study. *Appl Surf Sci* **2017**, *401*, 206–217. https://doi.org/10.1016/j.apsusc.2016.12.245.

(29) Omar, S.; Wachsman, E. D.; Jones, J. L.; Nino, J. C. Crystal Structure-Ionic Conductivity Relationships in Doped Ceria Systems. *Journal of the American Ceramic Society* **2009**, *92* (11), 2674–2681. https://doi.org/10.1111/j.1551-2916.2009.03273.x.

(30) Gándara, F.; De Andrés, A.; Gómez-Lor, B.; Gutiérrez-Puebla, E.; Iglesias, M.; Monge, M. A.; Proserpio, D. M.; Snejko, N. A Rare-Earth MOF Series: Fascinating Structure, Efficient Light Emitters, and Promising Catalysts. *Cryst Growth Des* **2008**, *8* (2), 378–380. https://doi.org/10.1021/cg700796m.

(31) Tang, J.; Yamauchi, Y. Carbon Materials: MOF Morphologies in Control. *Nat Chem* **2016**, *8* (7), 638–639. https://doi.org/10.1038/nchem.2548.

(32) Yang, S. J.; Kim, T.; Im, J. H.; Kim, Y. S.; Lee, K.; Jung, H.; Park, C. R. MOF-Derived Hierarchically Porous Carbon with Exceptional Porosity and Hydrogen Storage Capacity. *Chemistry of Materials* **2012**, *24* (3), 464–470. https://doi.org/10.1021/cm202554j.

(33) Roiaz, M.; Monachino, E.; Dri, C.; Greiner, M.; Knop-Gericke, A.; Schlögl, R.; Comelli, G.; Vesselli, E. Reverse Water-Gas Shift or Sabatier Methanation on Ni(110)? Stable

Surface Species at Near-Ambient Pressure. *J Am Chem Soc* **2016**, *138* (12), 4146–4154. https://doi.org/10.1021/jacs.5b13366.

(34) Lim, J. Y.; McGregor, J.; Sederman, A. J.; Dennis, J. S. The Role of the Boudouard and Water–Gas Shift Reactions in the Methanation of CO or CO2 over Ni/γ-Al2O3 Catalyst. *Chem Eng Sci* **2016**, *152*, 754–766. https://doi.org/10.1016/j.ces.2016.06.042.

(35) Zhang, F.; Wang, P.; Koberstein, J.; Khalid, S.; Chan, S. W. Cerium Oxidation State in Ceria Nanoparticles Studied with X-Ray Photoelectron Spectroscopy and Absorption near Edge Spectroscopy. *Surf Sci* **2004**, *563* (1–3), 74–82. https://doi.org/10.1016/j.susc.2004.05.138.

(36) Shyu, J. z.; Otto, K. Characterization of Pt/γ-Alumina Catalysts Containing Ceria. *J Catal* **1989**, *115* (1), 16–23. https://doi.org/https://doi.org/10.1016/0021-9517(89)90003-1.

(37) González-Gil, R.; Herrera, C.; Larrubia, M. A.; Mariño, F.; Laborde, M.; Alemany, L. J. Hydrogen Production by Ethanol Steam Reforming over Multimetallic RhCeNi/Al2O3 Structured Catalyst. Pilot-Scale Study. *Int J Hydrogen Energy* **2016**, *41* (38), 16786–16796. https://doi.org/10.1016/j.ijhydene.2016.06.234.

(38) Alvarez-Galvan, C.; Martínez, J. L.; Capel-Sanchez, M.; Pascual, L.; Alonso, J. A. Magnetic Properties of Efficient Catalysts Based on La-Doped Ceria-Supported Nickel Nanoparticles for RWGS Reaction. Influence of Ni Loading. *Adv Sustain Syst* **2021**, *5* (11), 1–10. https://doi.org/10.1002/adsu.202100029.

─ CHAPTER 6 ─

New Bismuth- and Indium-based MOFs

6.1. Introduction

The prevailing elements in the reticular chemistry of MOFs are transition metals, followed by rare earth atoms, and other main group atoms (Mg, Ca, Sr). Elements from group 13 (Al, Ga, In) and bismuth remain in the small percentage of MOF reports. My group became aware of the potential of these metals, and focused on studying Bi- and In-based MOFs, finding interesting behaviors such as framework adaptability in response to the changes triggered by the binding of guest species in the case of Bi-MOFs,[1] and an exceptional catalytical performance of both single- and multi-metal In-MOFs.[2,3]

Bismuth is a non-toxic and environmental-friendly element, used for many years in pharmaceutical preparations, especially for gastric diseases or to inhibit bacterial growth,[4] and in combination with a bioinspired linker it can generate a MOF that can behave as a biocompatible platform.[5] It is cost-effective, and in combination with its Lewis acid character, it can render a good performance as a heterogeneous green catalyst for different relevant chemical reactions.[6] Bi^{3+} has a flexible coordination geometry which stems from the combination of the presence of a stereochemically active lone electron pair ($6s^2$ electrons),[7,8] a relatively large covalent radius (1.48 Å)[9] and a high affinity for multidentate linkers containing oxygen, nitrogen or sulfur atoms.[10] Despite it benefitting from an array of advantages, Bi^{3+} is a cation that still remains fairly unexplored as a coordination node in MOFs. The first few reports of Bi-based MOFs with limited porosity were published during 2007-2011, and in 2012, Stock *et al.* reported the first highly porous and crystalline Bi-based MOF, CAU-7.[11] Since then, other reports have emerged, focused on an array of applications, such as catalysis,[12] energy storage, biomedical imaging, biocompatible platform, drug delivery, antibacterial coating,[13] fluorescence sensing, adsorption and separation; however, the number is still low when compared to publications based on transition metals.

Indium is a group 13 element known for its strong Lewis acid character, and is widely used in the field of catalysis.[14,15] It displays a rich structural diversity, given its different coordination capabilities.[16] The first indium-based MOF, InPF-1 was reported in 2002 by my group,[17] and since then the field has undergone a slow and steady growth, especially due to the high robustness and stability of the frameworks that this metal generates.[18]

The goal envisioned of this chapter was to further explore the chemistry of Bi and In in MOFs, and also evaluate the compatibility of this metals with Ir, a metal relevant in the catalysis field (a more detailed discussion about the insertion of Ir in MOFs is provided in chapter 7), and the possibility of obtaining a multi-metal MOF.

Thus, the first experiments were performed with the aim of combining iridium and bismuth or indium in a same framework, and for this we focused on three MOFs already obtained in my group: BiPF-1 ([Bi(BTB)$(DMF)_2$]),[19] BiPF-3 ([Bi_2(hfipbb)$_3$], with H_2hfipbb = 4,4′-hexafluoroisopropylidenebisbenzoic acid),[19] and InPF-18 ([$In_3(OH)_3(popha)_2$(4,4'- bipy)]×$4H_2O$, with H_3popha = 5-(4-carboxy-2-nitrophenoxy) isophthalic acid).[20] The criteria followed when choosing the structures were the following: for Bi we wanted to investigate which SBU type would be more fitting for the possible insertion of Ir, monomeric (BiPF-1) or rod-type that would potentially facilitate the sequencing of atoms, as seen in previous chapters (BiPF-3); InPF-18 was selected because it displays octahedral In atoms (compatible with the octahedral environments that Ir tends to display) coordinated to carboxylic groups and an additional linker with an N-containing group (4,4'-bipyridine) that would facilitate the coordination of the Ir atoms due to their affinity for N-donor linkers.[21]

As a general strategy, the solvothermal synthesis experiments were initially performed following the procedures optimized for the single metal MOFs, but using the combination of Bi or In with Ir in an 8:2 ratio. The 8:2 ratio was preferred over 9:1, as some

experiments require a slightly higher concentration of the metal to be inserted, and it would facilitate its quantification. The results of these experiments demonstrated that iridium could not be inserted into the target frameworks. Instead, the MOFs were obtained as single-metal phases, along with a black amorphous powder rich in Ir, according to the EDX analysis. At the view of these results, the approach was shifted towards the design of new MOFs with different coordination environments, for which a key point was to include a N-donor linker that would preferably coordinate to the Ir atoms[21] and reticulate them, and an additional linker with carboxylate groups that would further extend the framework.

For our experiments, we selected linkers that were previously used in our group to obtain Bi- and In-based MOFs as this ensured the compatibility with the metals, and the prospects of generating frameworks were higher. The chelating molecule 2,2'-bipyridine (bipy) was selected as an N-donor linker, and the tritopic molecule 1,3,5-tris(4-carboxyphenyl)benzene (H_3BTB) was selected as main carboxylate linker due to its versatility (Figure 6.1).

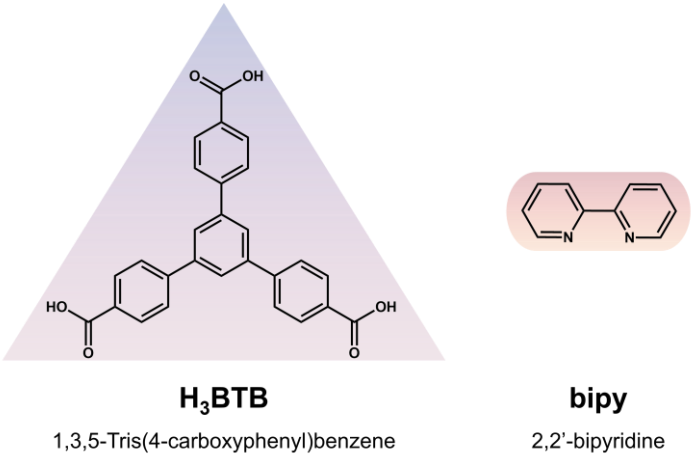

Figure 6.1. The linkers used in the synthesis of the MOFs of this chapter.

The hydrothermal synthesis experiments performed with the two linkers mentioned, and the combination of either Bi or In with Ir in an 8:2 ratio yielded a output similar to the previous case, where single-metal MOFs, where isolated, but not the multi-metal versions with iridium. Nevertheless, two new single-metal MOFs, one based on Bi (BiPF-11), and one based on In (InPF-32), were obtained, and they will be the main subjects of this chapter as they provide valuable information about how these atoms behave when acting as framework nodes, and help explore their chemistry as metal nodes for MOFs.

In addition, another novel bismuth MOF was obtained during my predoctoral stay at the Kyoto University iCeMS (Institute for Integrated Cell-Material Sciences) in the group of professor Shuhei Furukawa, and it is also included in this chapter. This structure was obtained during the investigation on the use of hydroxamic acid linkers to form metal-organic materials with bismuth, including MOFs and Metal-Organic Cages (MOCs),[22] as there are no reports of this type in the literature. These results fit well in this chapter as they complement the goal of achieving a deeper understanding of the behavior of bismuth cations in MOFs.

6.2. Bi-based MOF: BiPF-11

6.2.1. Synthesis of BiPF-11

The initial synthesis reaction included both H_3BTB and bipy linkers, following the above explained rationale for the obtaining of a multi-metal material. However, it was early found that only the H_3BTB linker coordinated to the Bi ions in the final structure, while the bipy molecules remain in the mother liquor. Therefore, the synthetic conditions were optimized by using just bismuth nitrate, H_3BTB and dimethylacetamide (DMA) at 90 ºC, which resulted in the formation of a crystalline product, BiPF-11. In particular, H_3BTB (0.1 mmol, 43.8 mg) and $Bi(NO_3)_3 \times 5H_2O$ (0.1 mmol, 48.5 mg) were dissolved in 5 mL of DMA, and sonicated to ensure the full homogenization of the solution. The mixture was placed in a 25 mL glass vial and heated for 24 hours (the crystals can be obtained in lower reaction times, 12-18 hours) on a heating plate at 90 °C. After cooling to room temperature, the white prism-shaped crystals (100-200 µm) were washed with DMA (3x10 mL). All reagents and solvents employed were commercially available and used as received without further purification: 1,3,5-tris(4-carboxyphenyl)benzene, H_3BTB (>98%, Strem); bismuth (III) nitrate pentahydrate, $Bi(NO_3)_3 \times 5H_2O$ (>98%, Fluka); DMA (Scharlau).

6.2.2. Characterization of BiPF-11

Single-crystal X-ray diffraction (SCXRD) analysis confirmed the formation of a new MOF, BiPF-11, which crystallizes in the monoclinic space group *C2/c* with cell parameters a = 32.217(8) Å, b = 11.312(3) Å, c = 27.649(7) Å, β = 117.519(7)° and cell volume 8926(4) $Å^3$ (full crystallographic parameters and refinement data are provided in Table 6.1).

Table 6.1. Crystallographic parameters and refinement data for BiPF-11.

Crystallographic parameters	BiPF-11
Empirical formula	$C_{70}H_{66}Bi_2N_4O_{16}$
Formula weight (g/mol)	1637.22
Crystal system	Monoclinic
Space group	*C2/c*
a (Å)	32.217(8)
b (Å)	11.312(3)
c (Å)	27.649(7)
α (º)	90
β (º)	117.519(7)
γ (º)	90
Volume (Å^3)	8926(4)
Z	4
Calculated density (g/cm^3)	1.217
Absorption coefficient (mm^{-1})	8.079
F(000)	3232.0
Radiation	CuKα (λ = 1.54178)
2θ range for data collection (º)	6.186 to 130.142
Index ranges	$-37 \leq h \leq 37$, $-13 \leq k \leq 13$, $-32 \leq l \leq 32$
Reflections collected	40859
Independent reflections	7532 [R_{int} = 0.0756, R_{sigma} = 0.0620]
Data/restraints/parameters	7532/0/421
Goodness-of-fit on F^2	1.061
Final R indexes [I>2σ (I)]	R_1 = 0.0650, wR_2 = 0.2061
Final R indexes [all data]	R_1 = 0.0843, wR_2 = 0.2333
Largest diff. peak/hole (e·Å^{-3})	1.94/-1.52

BiPF-11, with formula $[Bi(BTB)(DMA)_2]$, is a neutral, three-dimensional framework in which the inorganic SBU is comprised by distorted octa-coordinated Bi polyhedra (Figure 6.2). The asymmetric unit consists of one Bi atom, one BTB molecule and two DMA molecules (Figure 6.3). The Bi^{3+} atoms are coordinated to three chelating carboxylate groups from three different BTB linkers. Two DMA molecules complete the coordination sphere of Bi^{3+}, resulting in a SBU with the formula $[Bi(-CO_2)_3(DMA)_2]$, displayed in Figure 6.4. Given the distortion of the polyhedron, with bond distances between Bi and the atoms from its coordination sphere ranging from 2.263 to 2.775 Å, it is possible that the stereochemically active lone pair of electrons of Bi is directing the bonds towards a certain part of the coordination sphere, resulting in a hemidirected geometry.[23]

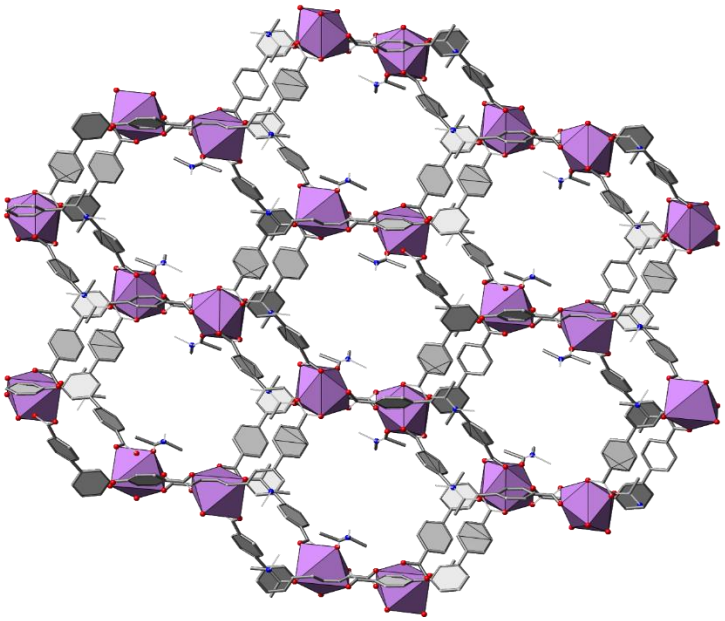

Figure 6.2. Structure of BiPF-11 viewed along the crystallographic *b* axis. Bi atoms are displayed in purple, O in red and N in blue. H atoms are omitted for clarity.

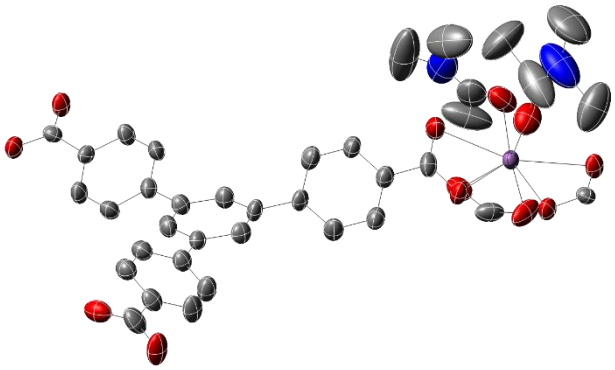

Figure 6.3. Thermal ellipsoid representation (50 % probability) of the asymmetric unit of BiPF-11. Bi atoms are displayed in purple, O in red and N in blue. H atoms are omitted for clarity.

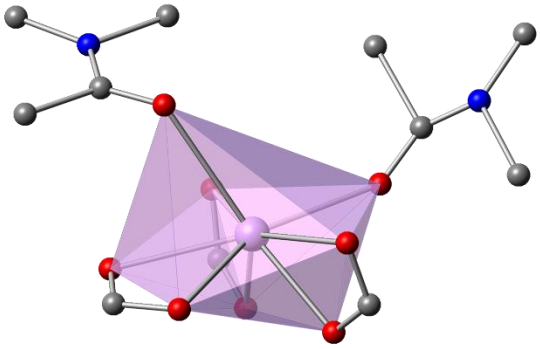

Figure 6.4. Monomeric eight-coordinated SBU of BiPF-11. Bi atoms are displayed in purple, O in red and N in blue. H atoms are omitted for clarity.

The structure of BiPF-11 consists of two interpenetrated networks (displayed in orange and blue in Figure 6.5) with **ths**-type topology,[24] where both the organic linker and the inorganic SBU act as three connected nodes.

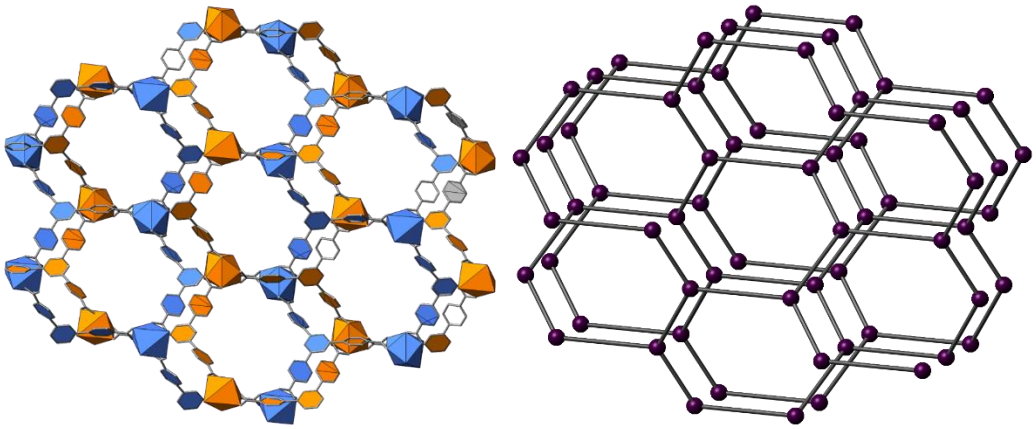

Figure 6.5. BiPF-11 displays a 2-fold interpenetrated structure (on the left, displayed in blue and orange) with a **ths**-type topology (on the right, represented in dark grey lines and purple spheres).

The PXRD pattern of the crystals of BiPF-11 is shown in Figure 6.6, compared to the simulated plot from the SCXRD data.

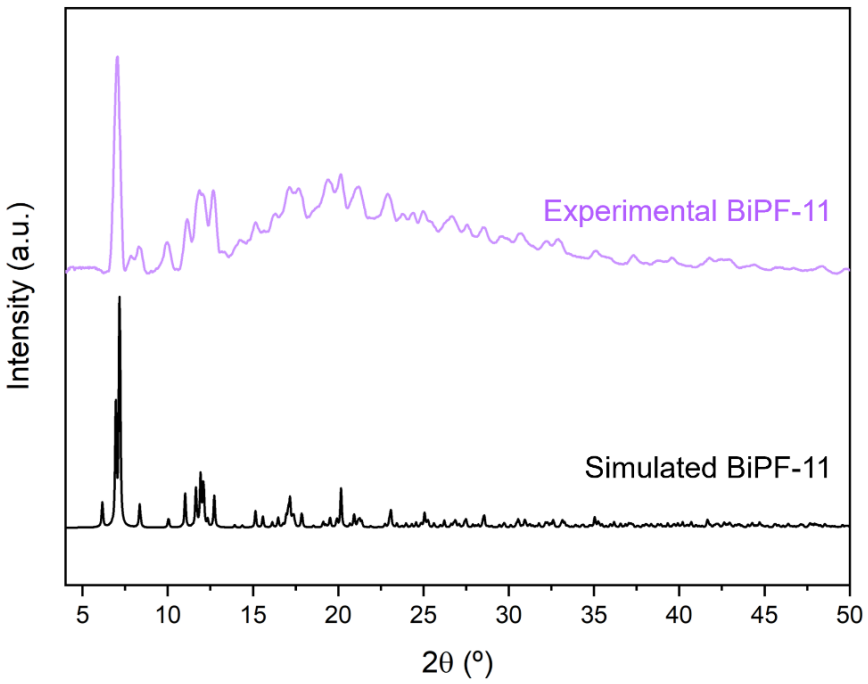

Figure 6.6. PXRD pattern of experimental BiPF-11 compared to the simulated data from the SCXRD experiment.

When checking the structural stability of BiPF-11 by submerging crystals in different solvents, a phase shift was observed, and as confirmed by PXRD, the framework does not collapse (Figure 6.7). Thus, BiPF-11 shifts to a new phase, A (PXRD plot displayed in orange) when submerged in ethanol or methanol, and the initial large prism-shaped crystals break down into small crystalline fragments. In addition, BiPF-11 shifts to another phase, B (PXRD plot displayed in teal) when left to dry in air or when submerged in water, and the initial crystals become a microcrystalline powder. This phase shift seems to point to a dynamic behavior of BiPF-11, where a crystalline phase is preserved during the process. However, the change involved the loss of its single-crystal character, which prevented the elucidation the structures of the transformed phases.

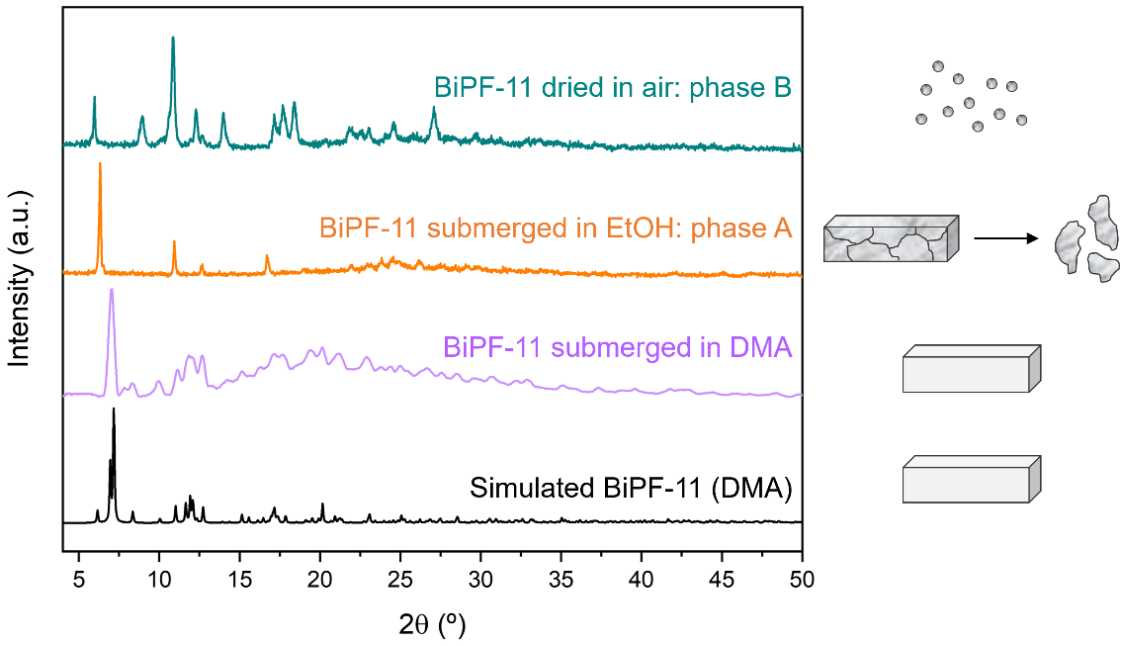

Figure 6.7. PXRD patterns of the SCXRD data simulated plot of BiPF-11 (black), experimental BiPF-11 after washing with DMA (purple), BiPF-11 submerged in EtOH or MeOH − phase A (orange) and BiPF-11 dried in air − phase B (teal). Representative images of the morphology of the crystals corresponding to each PXRD pattern are displayed on the right.

The results of the CHN elemental analysis of the activated sample are shown in Table 6.2. The calculated data displays slightly higher values than the percentages estimated from the formula of the MOF ($C_{70}H_{66}Bi_2N_4O_{16}$), and this difference can be due to the presence of DMA molecules enclosed in the pores of the MOF.

Table 6.2. EA results for BiPF-11.

BiPF-11	**Calculated CHN**			**Experimental CHN**		
	%C	%H	%N	%C	%H	%N
	51.349	4.071	3.426	50.478	4.886	4.439

The stability of the MOF was studied through thermogravimetric analysis (TG). The TG plot (Figure 6.8) displays three weight losses: 16.95% at 116 ºC, 8.40% at 149 ºC, 8.85% at 310 ºC, corresponding to the loss of solvent molecules enclosed in the pores of the MOF and the two coordinated DMA molecules. The total decomposition of the MOF occurs at 451 ºC, resulting in Bi (III) oxide (α-Bi_2O_3), as confirmed by PXRD (Figure 6.9).

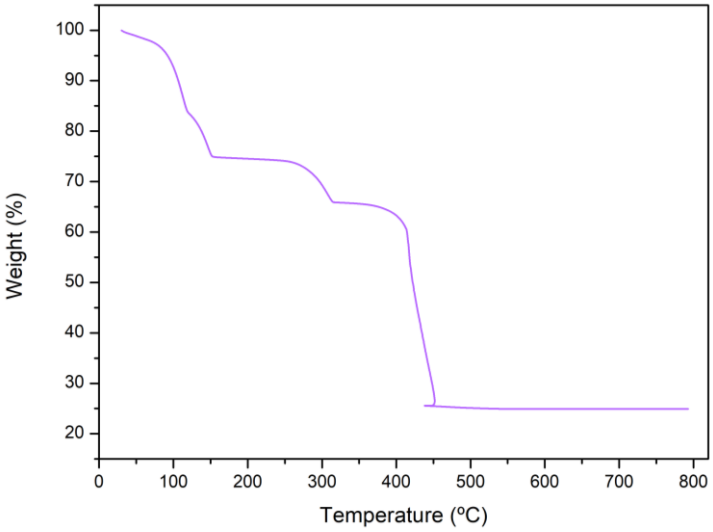

Figure 6.8. TGA plot for BiPF-11.

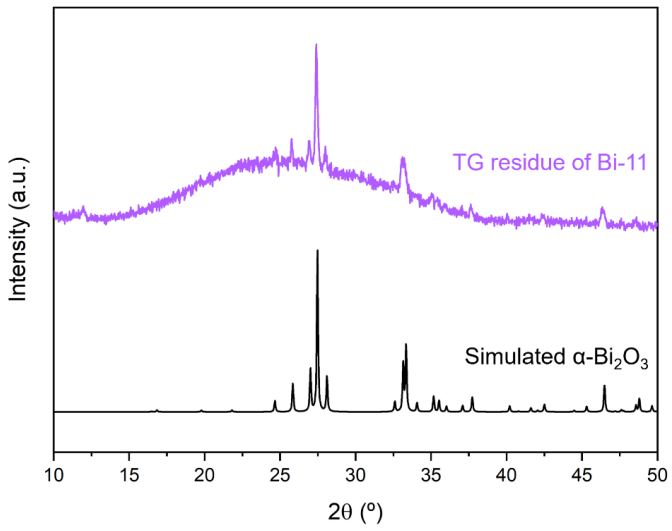

Figure 6.9. PXRD pattern of the TG residue of BiPF-11 (purple) compared to the simulated plot of α-Bi_2O_3 (black).

6.3. Bi-based MOF: KyU-13

During my PhD, a research internship was carried out at the Kyoto University iCeMS (Institute for Integrated Cell-Material Sciences) in the Furukawa group, with the purpose of investigating the use of linkers with different chemical functionalities in the synthesis of various classes of metal-organic materials with the use of bismuth as metal center. More particularly, the work was focused on the use of hydroxamic acid derivatives with different bite angles, ranging from 0 to 120º. After conducting a series of synthesis screening experiments, a crystalline product was obtained with the use of 1,4-benzo-dihydroxamic acid, H_4BDHA, (Figure 6.10). In the literature there are three MOFs based on this linker, namely ($[Zn_2(BDHA)_{0.5}(INA)_3]$),[25] ($[Co_2(BDHA)_{0.5}(INA)_3(DMF)]$)[25] (with INA=isonicotinic acid), MUV-11 ($[Ti_2(HBDHA)_{2.67}]$),[26] and one Ti-based metal-organic cage, cMUV-11 ($[Ti_8(p\text{-}H_2BDHA)_8(p\text{-}BDHA)_4]$)[27]; none of these structures match with the crystalline product obtained in the experiments, therefore the combination of Bi and H_4BDHA did not yield an isostructural framework with the already reported ones, but a new one, which will be referred to as KyU-13 (Kyoto University-13).

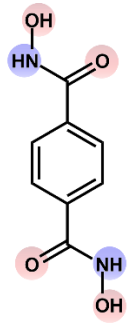

H_4BDHA

1,4-benzo-dihydroxamic acid

Figure 6.10. Representation of the linker H_4BDHA.

6.3.1. Synthesis of KyU-13

The H_4BDHA linker was synthesized following the protocol reported by Martí-Gastaldo *et. al*, but with a slight modification of the reaction temperature (the reaction was carried out at room temperature instead of at 40 ºC).[26]

A microcrystalline material (Figure 6.11) was obtained in the first few experiments, by using H_4BDHA (0.1 mmol, 19.6 mg), $Bi(NO_3)_3 \times 5H_2O$ (0.1 mmol, 48.5 mg) and 5 mL of DMF at 90 ºC. As this material was not suitable for carrying out a SCXRD experiment, the synthesis strategy needed to be optimized in order to obtain larger crystals. The first parameters that were modified were the temperature (80-120 °C), the reaction time (12-72 h), and the metal to linker ratio (0.5:1, 1:1, 1,5:1, 2:1 and vice versa). As slight changes in these parameters did not have any impact on the size of the crystals, we shifted towards changing the solvent. Trials with dimethylacetamide (DMA), dimethylsulfoxide (DMSO) and N-methyl-2-pyrrolidone (NMP) did not yield any crystals, and experiments carried out in ethanol, methanol or water yielded amorphous powders. Therefore, it was evident that the initial solvent choice was the most fitting for this reaction. Using an acidic modulator could help grow the initial crystals and lead to higher sizes, as it inhibits the linker deprotonation and overall slows down the metal-ligand complexation and thus the nucleation and subsequent growth processes would occur at slower rates.[28] Modulators are typically monotopic carboxylic acids or Brønsted bases, and we opted for the first option and used acetic, benzoic, and hydrochloric acid. This option seemed to render slightly bigger and less aggregated crystals, and after tweaking some of the reaction parameters (a smaller vial that would provide a higher pressure, less solvent, and an excess of the modulator), crystals of 100 µm were eventually obtained (Figure 6.11), and the optimized synthesis is the following: H_4BDHA (0.45 mmol, 88.2 mg), $Bi(NO_3)_3 \times 5H_2O$ (0.15 mmol, 73.5 mg) and benzoic acid (1.13 mmol, 138.0 mg) were dissolved in

3 mL of DMF, and sonicated to ensure the full homogenization of the solution. The mixture was placed in a 5 mL glass vial and heated for 24 hours (the crystals can be obtained in lower reaction times, 12-18 hours) in an oven at 100 °C. After cooling to room temperature, the white prism-shaped crystals (Figure 6.11) were washed with DMF (3x10 mL).

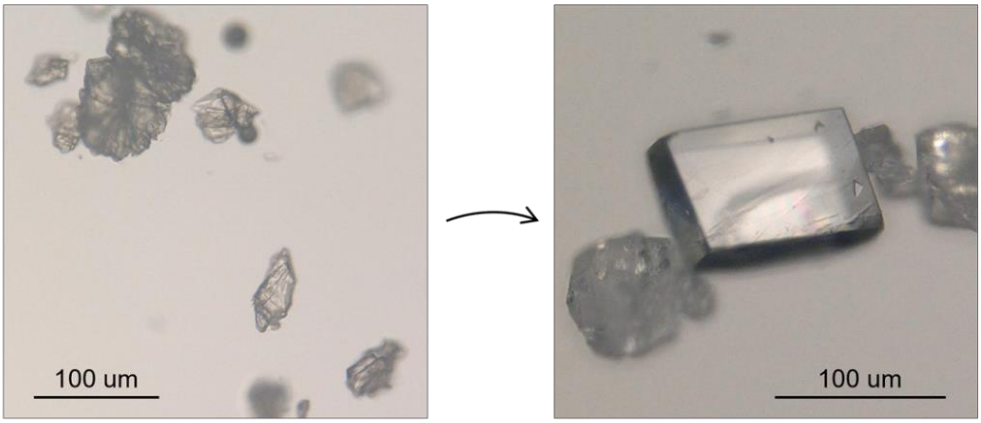

Figure 6.11. Optical microscope images of the size and morphology of the crystals of KyU-13 before **(left)** and after **(right)** the optimization of the synthesis.

6.3.2. Characterization of KyU-13

SCXRD analysis of the crystals of the sample revealed that the structure corresponds to a new MOF. This structure, called KyU-13, is a new Bi-based MOF with the linker H_4BDHA, and it crystallizes in the triclinic space group *P-1* with cell parameters a = 7.6171(5) Å, b = 10.3442(6) Å, c = 11.1366(6) Å, α = 109.397 (5)º, β = 100.363(5)º, γ = 105.585(5)º and cell volume 761.47(9) $Å^3$ (full crystallographic parameters and refinement data are provided in Table 6.3).

Table 6.3. Crystallographic parameters and refinement data for KyU-13.

Crystallographic parameters	KyU-13
Empirical formula	$C_{11}H_{11}BiN_3O_{8.4}$
Formula weight (g/mol)	544.912
Crystal system	Triclinic
Space group	*P-1*
a (Å)	7.6171(5)
b (Å)	10.3442(6)
c (Å)	11.1366(6)
α (°)	109.397(5)
β (°)	100.363(5)
γ (°)	105.585(5)
Volume (Å^3)	761.47(9)
Z	2
Calculated density (g/cm^3)	2.377
Absorption coefficient (mm^{-1})	11.756
F(000)	506.6
Radiation	Mo Kα (λ = 0.71073)
2θ range for data collection (°)	5.82 to 50.04
Index ranges	$-9 \le h \le 7$, $-12 \le k \le 12$, $-13 \le l \le 11$
Reflections collected	9228
Independent reflections	2672 [R_{int} = 0.0402, R_{sigma} = 0.0323]
Data/restraints/parameters	2672/0/229
Goodness-of-fit on F^2	1.103
Final R indexes [I>2σ (I)]	R_1 = 0.0429, wR_2 = 0.1093
Final R indexes [all data]	R_1 = 0.0457, wR_2 = 0.1104
Largest diff. peak/hole (e·Å^{-3})	4.84/-2.23

KyU-13, with formula [Bi(H_2BDHA)(DMF)], is a three-dimensional framework in which the SBU is comprised by distorted hepta-coordinated edge-linked Bi rods. Each rod is connected to four neighboring rods through the phenyl ring of the linker, resulting in 8 × 11 $Å^2$ channels along the *a* direction (Figure 6.12). The linkers display a chelating coordination mode by bonding to the metal cations through both oxygen atoms in the hydroxamate group. The formation of one-dimensional SBUs is enabled by virtue of the μ-bridging mode of the N-hydroxy functionality. (Figure 6.13). One DMF molecule completes the coordination sphere of the Bi atoms, resulting in a SBU with the formula [Bi(-CNO_2)$_2$(DMF)], displayed in Figure 6.15. At the view of this formula, it is clear that an additional negative charge is needed to ensure neutrality. While in other examples of hydroxamic acid-based reported MOFs the -NH group of the linker could be also deprotonated, the possible presence of counterions in the pores of KyU-13 cannot be fully ruled out. Indeed, during the analysis of the SCXRD data, a large electron density was present in the pores. Unfortunately, this electron density belongs to disordered guest species, and their exact chemical nature was not unambiguously confirmed.

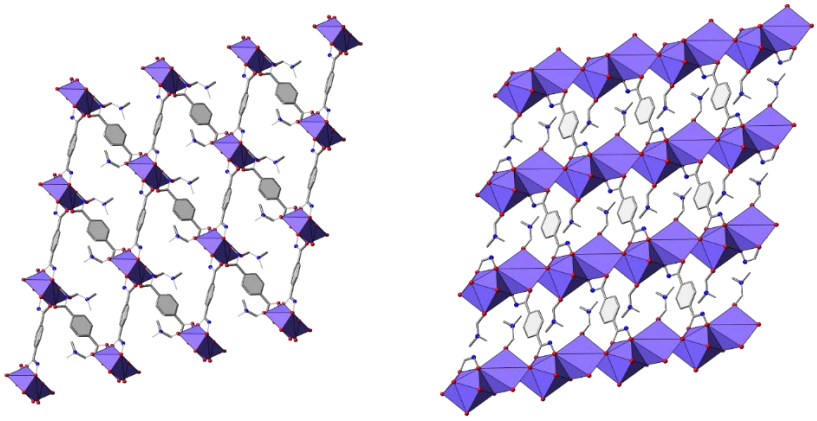

Figure 6.13. Structure of KyU-13 viewed along the crystallographic *a* **(left)** and **(right)** *c* axis. Bi atoms are displayed in purple, O in red and N in blue. H atoms are omitted for clarity.

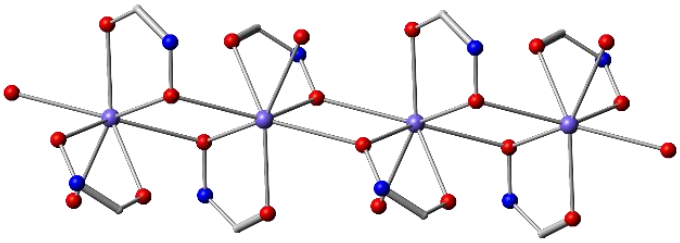

Figure 6.14. Ball and stick representation of the bonds of the rod-shaped SBUs of KyU-13. Bi atoms are displayed in purple, O in red and N in blue. H atoms are omitted for clarity.

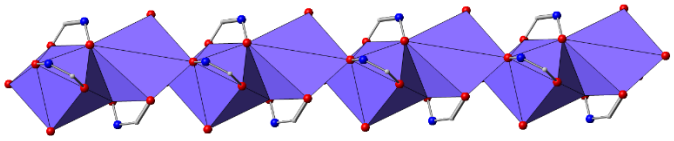

Figure 6.4. Rod-shaped hepta-coordinated edge-linked SBU of KyU-13. Bi atoms are displayed in purple, O in red and N in blue. H atoms are omitted for clarity.

The shape of the pores and the overall appearance of the structure are reminiscent of a wine-rack motif,[29] and point to a flexible or "breathing" behavior.[30,31] This was indeed evidenced by the PXRD analysis, where a slight difference in the patterns was observed (Figure 6.16) for dry and wet samples. Firstly, the as-synthesized sample was washed with DMF, so the structure would have coordinated DMF ligands (cDMF), and DMF solvent molecules (sDMF) enclosed in the pores. The presence of these molecules would create a steric hindrance and would force the pores of the structure to remain open. So, this phase would be the open-pore version (cDMF−sDMF). The SCXRD data was collected from a crystal synthesized in DMF, but washed with acetone; thus, the sDMF molecules were removed and this phase would be an intermediate version (cDMF−X, with X = absence of DMF). Extracting the coordinated DMF molecule would make the pores close even more, so the sample was vacuum-dried at 150 ºC, and this phase would be the closed-pore version (X−X).

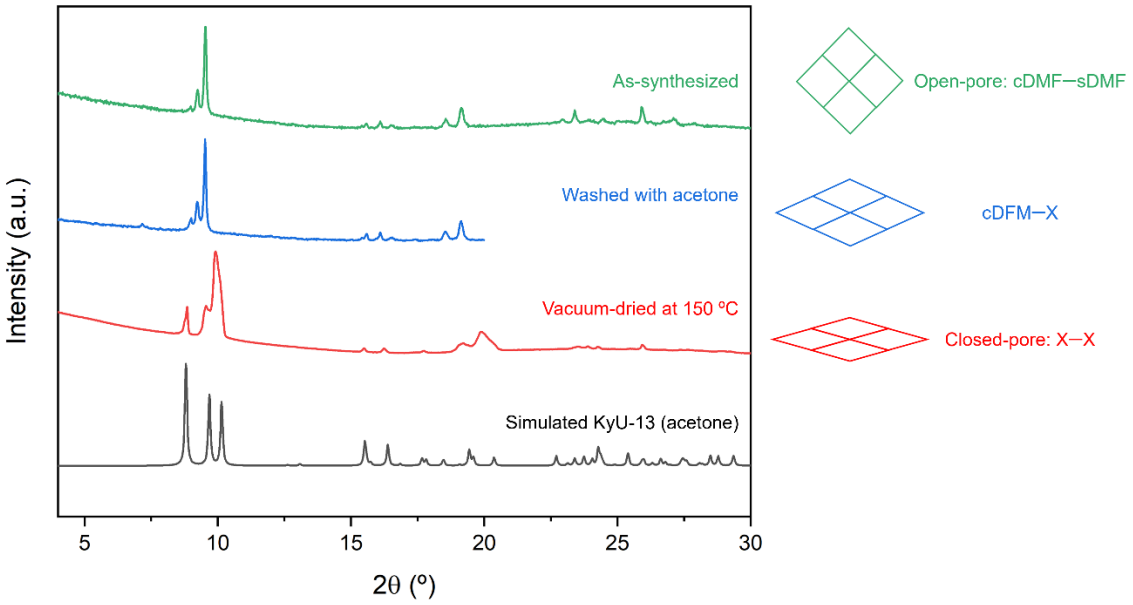

Figure 6.16. PXRD patterns and schematic representation of the structure and pore shape of the three phases of KyU-13. The simulated pattern from the SCXRD data (crystals washed with acetone) is displayed in black; the pattern of the as-synthesized (washed with DMF) sample is displayed in red; the pattern of the sample washed with acetone is displayed in blue; the plot of the vacuum-dried sample at 150 ºC is displayed in green. cDMF = coordinated DMF; sDMF = solvent DMF; X = absence of DMF.

Since the internship was completed during the final months of the PhD program, the full chemical and crystallographic characterization of this structure is currently being carried out at the Kyoto University iCeMS; however, these initial results and structural analysis further demonstrate the large versatility of bismuth for the formation of different MOFs with a flexible and an adaptative behavior. These features have been previously reported for other Bi-MOFs that display dimeric SBUs,[1,32] but this is the first example of a flexible structure with rod-shaped SBU.

6.4. In-based MOF: InPF-32

The hydrothermal reaction of indium acetate, H_3BTB and bipy in a mixture of water/ethanol at 170 ºC resulted in the formation of a crystalline product, InPF-32.

6.4.1. Synthesis of InPF-32

All reagents and solvents employed were commercially available and used as received without further purification: 1,3,5-tris(4-carboxyphenyl)benzene, H_3BTB (>98%, Strem); indium (III) acetate, $In(CH_3COO)_3$ (>99.99%, Alfa Aesar); ethanol (Scharlau).

H_3BTB (0.1 mmol, 48.5 mg), 2,2'-bipy (0.1 mmol, 15.7 mg) and $In(CH_3COO)_3$ (0.11 mmol, 31.7 mg) were dissolved in 5 mL of deionized water and 5 mL of ethanol. The mixture was placed in a 50 mL Teflon-lined steel autoclave and heated for 24 hours in an oven at 160 °C. After cooling to room temperature, the white plate-like crystals (50-100 µm) were washed with water (2x10 mL) and ethanol (2x10 mL).

6.4.2. Characterization of InPF-32

The single-crystal X-ray diffraction analysis of the sample show that InPF-32 crystallizes in the monoclinic space group *C2/c* with cell parameters a = 32.12(3) Å, b = 12.450(10) Å, c = 27.649(7) Å, β = 110.480(18)° and cell volume 6971(9) $Å^3$ (full crystallographic parameters and refinement data are provided in Table 6.4).

Table 6.4. Crystallographic parameters and refinement data for InPF-32.

Crystallographic parameters	InPF-32
Empirical formula	$C_{37}H_{23}InN_2O_6$
Formula weight (g/mol)	700.65
Crystal system	Monoclinic
Space group	*C2/c*
a (Å)	32.12(3)
b (Å)	12.450(10)
c (Å)	18.048(12)
α (º)	90
β (º)	110.480(18)
γ (º)	90
Volume (Å^3)	6971(9)
Z	8
Calculated density (g/cm^3)	1.335
Absorption coefficient (mm^{-1})	5.538
F(000)	2828.0
Radiation	CuKα (λ = 1.54178)
2θ range for data collection (º)	5.698 to 130.058
Index ranges	-38 ≤ h ≤ 38, -14 ≤ k ≤ 14, -21 ≤ l ≤ 20
Reflections collected	55636
Independent reflections	5898 [R_{int} = 0.0879, R_{sigma} = 0.0470]
Data/restraints/parameters	5898/0/415
Goodness-of-fit on F^2	1.071
Final R indexes [I>2σ (I)]	R_1 = 0.0422, wR_2 = 0.1253
Final R indexes [all data]	R_1 = 0.0494, wR_2 = 0.1319
Largest diff. peak/hole (e·Å^{-3})	0.70/-0.58

InPF-32, with formula [In(BTB)(bipy)], is a neutral, two-dimensional framework. The asymmetric unit consists of one In atom, one BTB molecule and bipy molecule, therefore one molecular formula per unit cell (Figure 6.17). The SBU is comprised by eight-coordinated In polyhedra (Figure 6.18). The In^{3+} atoms are coordinated in a μ-fashion to the carboxylate groups from three different H_3BTB linkers, and in a *N*-heterocyclic chelating fashion to one bipy molecule, resulting in the formula [In(-CO_2)$_3$(bipy)]. In this case, the distances between In and the atoms from its coordination sphere have more similar values, ranging between 2.279 and 2.371 Å. The growth and extension of the framework in the three dimensions is frustrated by the bipy linkers, which are interdigitated in adjacent layers, thus generating a two-dimensional framework (Figure 6.19). The structure consists of four stacked layers per unit cell, with Van der Waals interactions stabilizing them. Each layer is three-dimensional and self-entangled, and this generates a new type of topology (Figure 6.20).

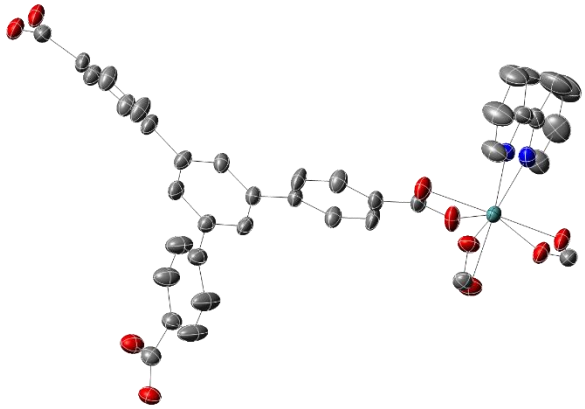

Figure 6.17. Thermal ellipsoid representation (50 % probability) of the asymmetric unit of InPF-32. In atoms are displayed in teal, O in red and N in blue. H atoms are omitted for clarity.

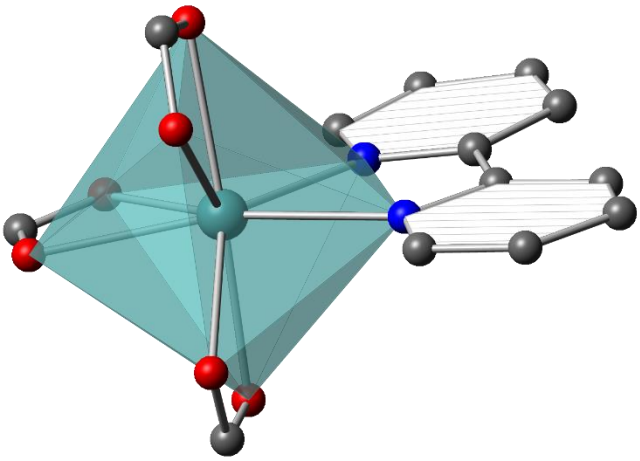

Figure 6.18. Monomeric eight-coordinated SBU of InPF-32. In atoms are displayed in teal, O in red and N in blue. H atoms are omitted for clarity.

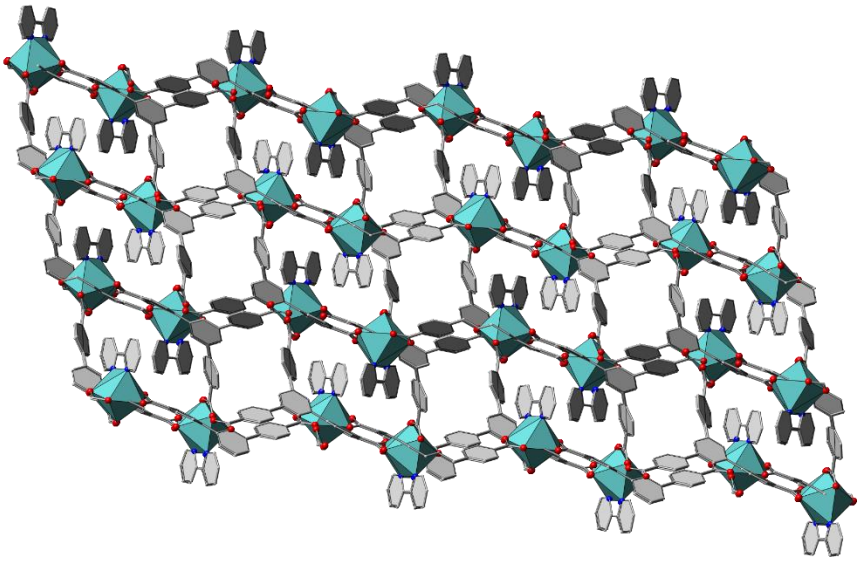

Figure 6.19. Structure of InPF-32 viewed along the crystallographic *b* axis. In atoms are displayed in teal, O in red and N in blue. H atoms are omitted for clarity.

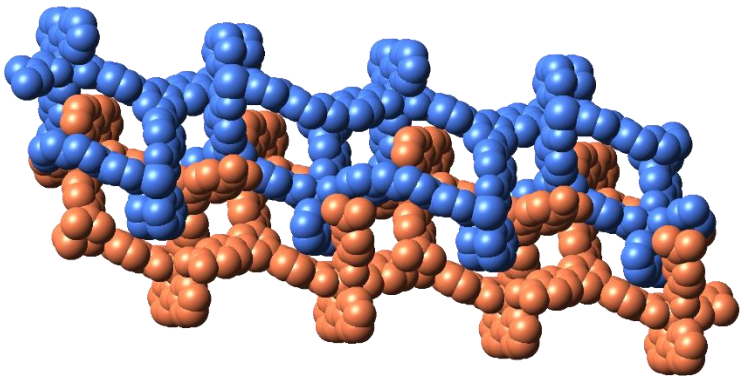

Figure 6.20. Space-filling representation of two stacked layers (one is displayed in blue, the other one in orange) of InPF-32 viewed along the crystallographic *b* axis.

The PXRD pattern of the experimental InPF-32 crystals matches the simulated plot from the SCXRD data collection (Figure 6.21), and this MOF was found to be stable in air.

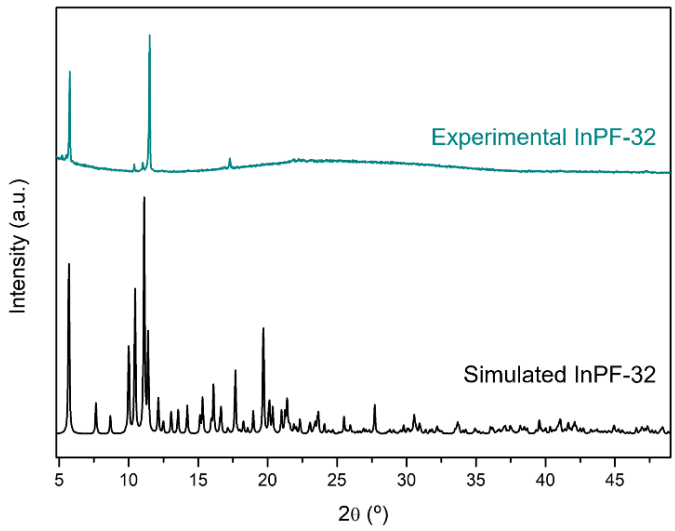

Figure 6.21. PXRD pattern of experimental InPF-32 compared to the simulated data from the SCXRD experiment.

The stability of the MOF (activated under vacuum overnight) was studied through thermogravimetric analysis. The TG plot (Figure 6.22) displays one weight loss of 13% at 250 ºC, corresponding to the loss of water molecules enclosed in the pores of the sample. The total degradation of the structure occurs at 462 ºC, resulting in In (III) oxide (In_2O_3), as confirmed by PXRD (Figure 6.23).

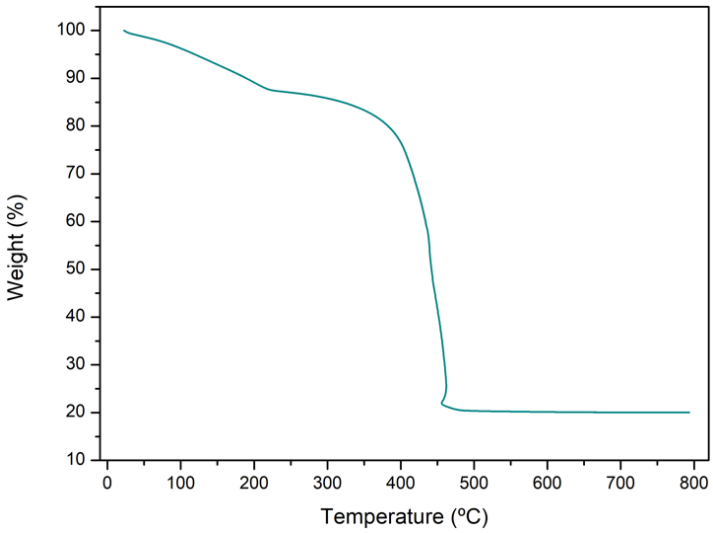

Figure 6.22. TG plot for InPF-32.

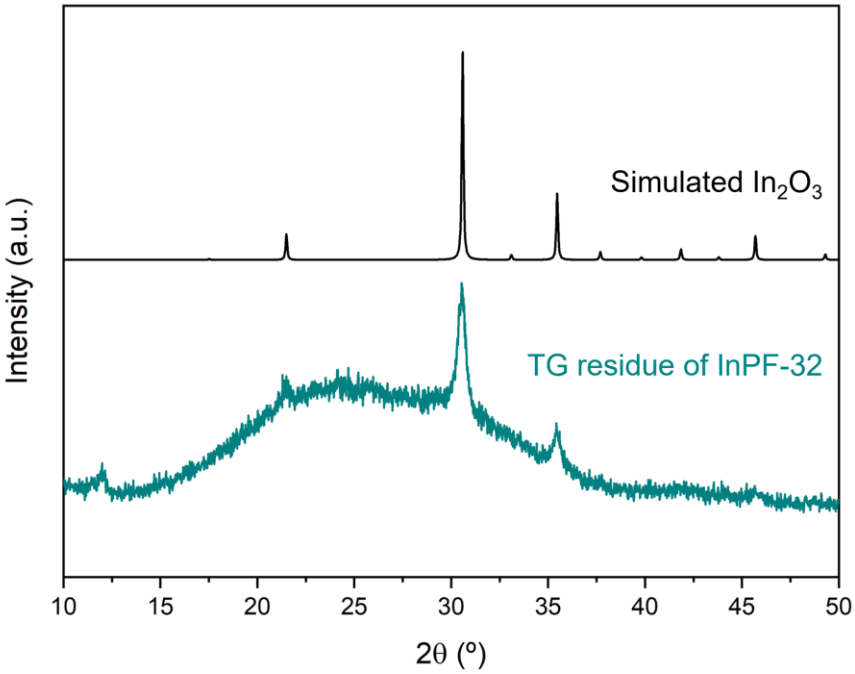

Figure 6.23. PXRD pattern of the TG residue of InPF-32 (teal) compared to the simulated plot of indium oxide, In_2O_3 (black).

6.5. Conclusions

To outline the main ideas from this chapter, we found that the insertion of iridium into selected Bi and In-based frameworks was not feasible, and this might be associated with a lack of compatibility between the metal combinations, or with a lack of affinity of Ir for the SBUs or for the overall structures. Nevertheless, the synthetic studies led to the discovery of two new Bi- and In-MOFs. Despite being very different metals, both bismuth and indium have generated similar SBUs, octa-coordinated polyhedral SBUs (slightly more distorted in the case of Bi), and the structures they generate crystallize in the same system but with different dimensionalities and characteristics. In the case of InPF-32, the chelating bipy molecules "lock" in place two of the eight coordination sites of In^{3+}, which provides extra rigidity to the structure and dictates the overall topology of the network. For BiPF-11, these positions are more flexible or "free" as they are occupied by two DMA molecules, and this contributes to the dynamic behavior of the system.

BiPF-11 is not the first Bi-MOF reported with the linker H_3BTB. The first example, CAU-7, dates back to 2012,[11] and also BiPF-1,[19] a MOF from my group already mentioned in this chapter, is also based on the same linker; however, the relevance of BiPF-11 lies in the fact that it provides information on how Bi behaves when mixed with the same linker but in different synthesis conditions, and the versatility of this combination.

Table 6.5. Comparison of MOFs based on Bi and H_3BTB.

MOF	Formula	c.i. Bi	SBU	Solvent	T (ºC)	t (h)
BiPF-1	$[Bi(BTB)DMF_2]$	8	$Bi(-CO_2)_3DMF_2$	DMF	90	144
BiPF-11	$[Bi(BTB)DMA_2]$	8	$Bi(-CO_2)_3DMA_2$	DMA	90	18-24
CAU-7	[Bi(BTB)]	9	$Bi(-CO_2)_3$ rods	MeOH	120	12

c.i. = coordination index; T = temperature (ºC); t = time (hours).

Among metals from group 13, In^{3+} is known to form monomeric SBUs and generate 2D layered materials.[18] In the literature there are three reports of In-MOFs obtained with the combination of H_3BTB and bipy.[33] These MOFs display 2D interpenetrated structures based on In^{3+} octahedral nodes, resulting in a 6,3-connected **hcb**-type topology. Even if InPF-32 is not the first MOF reported with that combination of building units, its structure stands out due to its unique stacking.

The results of this chapter have not yet been published because some pending experiments must be carried out; however, once this work is completed, two manuscripts (one based on BiPF-11 and InPF-32, and one centered on KyU-13) are expected to stem from the MOFs detailed in this chapter.

6.6. References

(1) Gómez-Oliveira, E. P.; Reinares-Fisac, D.; Aguirre-Díaz, L. M.; Esteban-Betegón, F.; Pintado-Sierra, M.; Gutiérrez-Puebla, E.; Iglesias, M.; Ángeles Monge, M.; Gándara, F. Framework Adaptability and Concerted Structural Response in a Bismuth Metal-Organic Framework Catalyst. *Angewandte Chemie - International Edition* **2022**, *61* (37), 1–7. https://doi.org/10.1002/anie.202209335.

(2) Reinares-Fisac, D.; Aguirre-Díaz, L. M.; Iglesias, M.; Snejko, N.; Gutiérrez-Puebla, E.; Monge, M. Á.; Gándara, F. A Mesoporous Indium Metal-Organic Framework: Remarkable Advances in Catalytic Activity for Strecker Reaction of Ketones. *J Am Chem Soc* **2016**, *138* (29), 9089–9092. https://doi.org/10.1021/jacs.6b05706.

(3) Aguirre-Díaz, L. M.; Gándara, F.; Iglesias, M.; Snejko, N.; Gutiérrez-Puebla, E.; Monge, M. Á. Tunable Catalytic Activity of Solid Solution Metal-Organic Frameworks in One-Pot Multicomponent Reactions. *J Am Chem Soc* **2015**, *137* (19), 6132–6135. https://doi.org/10.1021/jacs.5b02313.

(4) Briand, G. G.; Burford, N. Bismuth Compounds and Preparations with Biological or Medicinal Relevance. *Chem Rev* **1999**, *99* (9), 2601–2658. https://doi.org/10.1021/cr980425s.

(5) Grape, E. S.; Gabriel Flores, J.; Hidalgo, T.; Martínez-Ahumada, E.; Gutierrez-Alejandre, A.; Hautier, A.; Williams, D. R.; O'Keeffe, M.; Ohrström, L.; Willhammar, T.; Horcajada, P.; Ibarra, I. A.; Ken Inge, A. A Robust and Biocompatible Bismuth Ellagate MOF Synthesized under Green Ambient Conditions. *J Am Chem Soc* **2020**, *142* (39), 16795–16804. https://doi.org/10.1021/jacs.0c07525.

(6) Gómez-Oliveira, E. P.; Méndez, N.; Iglesias, M.; Gutiérrez-Puebla, E.; Aguirre-Díaz, L. M.; Monge, M. Á. Building a Green, Robust, and Efficient Bi-MOF Heterogeneous Catalyst for the Strecker Reaction of Ketones. *Inorg Chem* **2022**. https://doi.org/10.1021/acs.inorgchem.2c00628.

(7) Babaryk, A. A.; Contreras Almengor, O. R.; Cabrero-Antonino, M.; Navalón, S.; García, H.; Horcajada, P. A Semiconducting Bi2O2(C4O4) Coordination Polymer Showing a Photoelectric Response. *Inorg Chem* **2020**, *59* (6), 3406–3416. https://doi.org/10.1021/acs.inorgchem.9b03290.

(8) Kan, L.; Li, J.; Luo, X.; Li, G.; Liu, Y. Three Novel Bismuth-Based Coordination Polymers: Synthesis, Structure and Luminescent Properties. *Inorg Chem Commun* **2017**, *85*, 70–73. https://doi.org/10.1016/j.inoche.2017.06.018.

(9) Cordero, B.; Gómez, V.; Platero-Prats, A. E.; Revés, M.; Echeverría, J.; Cremades, E.; Barragán, F.; Alvarez, S. Covalent Radii Revisited. *Journal of the Chemical Society. Dalton Transactions* **2008**, No. 21, 2832–2838. https://doi.org/10.1039/b801115j.

(10) Wang, Z.; Zeng, Z.; Wang, H.; Zeng, G.; Xu, P.; Xiao, R.; Huang, D.; Chen, S.; He, Y.; Zhou, C.; Cheng, M.; Qin, H. Bismuth-Based Metal–Organic Frameworks and Their Derivatives: Opportunities and Challenges. *Coord Chem Rev* **2021**, *439*, 213902. https://doi.org/10.1016/j.ccr.2021.213902.

(11) Feyand, M.; Mugnaioli, E.; Vermoortele, F.; Bueken, B.; Dieterich, J. M.; Reimer, T.; Kolb, U.; De Vos, D.; Stock, N. Automated Diffraction Tomography for the Structure Elucidation of Twinned, Sub-Micrometer Crystals of a Highly Porous, Catalytically Active Bismuth Metal-Organic Framework. *Angewandte Chemie - International Edition* **2012**, *51* (41), 10373–10376. https://doi.org/10.1002/anie.201204963.

(12) García-Sánchez, A.; Gomez-Mendoza, M.; Barawi, M.; Villar-Garcia, I. J.; Liras, M.; Gándara, F.; De La Peña O'Shea, V. A. Fundamental Insights into Photoelectrocatalytic Hydrogen Production with a Hole-Transport Bismuth Metal-Organic Framework. *J Am Chem Soc* **2020**, *142* (1), 318–326. https://doi.org/10.1021/jacs.9b10261.

(13) Gomez, G. E.; D'Vries, R. F.; Lionello, D. F.; Aguirre-Díaz, L. M.; Spinosa, M.; Costa, C. S.; Fuertes, M. C.; Pizarro, R. A.; Kaczmarek, A. M.; Ellena, J.; Rozes, L.; Iglesias, M.; Van Deun, R.; Sanchez, C.; Monge, M. A.; Soler-Illia, G. J. A. A. Exploring Physical and Chemical Properties in New Multifunctional Indium-, Bismuth-, and Zinc-Based 1D and 2D Coordination Polymers. *Dalton Transactions* **2018**, *47* (6), 1808–1818. https://doi.org/10.1039/c7dt04287f.

(14) Peralta, R. A.; Huxley, M. T.; Lyu, P.; Díaz-Ramírez, M. L.; Park, S. H.; Obeso, J. L.; Leyva, C.; Heo, C. Y.; Jang, S.; Kwak, J. H.; Maurin, G.; Ibarra, I. A.; Jeong, N. C. Engineering Catalysis within a Saturated In(III)-Based MOF Possessing Dynamic Ligand-Metal Bonding. *ACS Appl Mater Interfaces* **2022**, No. Iii. https://doi.org/10.1021/acsami.2c19984.

(15) Lu, C.; Xiong, D.; Chen, C.; Wang, J.; Kong, Y.; Liu, T.; Ying, S.; Yi, F. Y. Indium-Based Metal-Organic Framework for Efficient Photocatalytic Hydrogen Evolution. *Inorg Chem* **2022**, *61* (5), 2587–2594. https://doi.org/10.1021/acs.inorgchem.1c03628.

(16) Zheng, S. T.; Bu, J. J.; Wu, T.; Chou, C.; Feng, P.; Bu, X. Porous Indium-Organic Frameworks and Systematization of Structural Building Blocks. *Angewandte Chemie - International Edition* **2011**, *50* (38), 8858–8862. https://doi.org/10.1002/anie.201101957.

(17) Gutie, E.; Iglesias, M.; Monge, M. A.; Snejko, N.; Ciencia, I. De; Madrid, D. M. De. Supramolecular 3D Framework with Catalytic Activity. *Framework* **2002**, *41* (9), 2429–2432.

(18) Aguirre-Díaz, L. M.; Reinares-Fisac, D.; Iglesias, M.; Gutiérrez-Puebla, E.; Gándara, F.; Snejko, N.; Monge, M. Á. Group 13th Metal-Organic Frameworks and Their Role in Heterogeneous Catalysis. *Coord Chem Rev* **2017**, *335*, 1–27. https://doi.org/10.1016/j.ccr.2016.12.003.

(19) Aguirre-Díaz, L. M.; Gutiérrez-Puebla, E.; Monge, M. Á. Unpublished Work, Manuscript in Preparation.

(20) Aguirre-Díaz, L. M.; Iglesias, M.; Snejko, N.; Gutiérrez-Puebla, E.; Monge, M. Á. Synchronizing Substrate Activation Rates in Multicomponent Reactions with Metal-Organic Framework Catalysts. *Chemistry - A European Journal* **2016**, *22* (19), 6654–6665. https://doi.org/10.1002/chem.201504576.

(21) Housecroft, C. E. Iridium: Inorganic & Coordination Chemistry. *Encyclopedia of Inorganic Chemistry* **2006**, *6*, 1–18. https://doi.org/10.1002/0470862106.ia101.

(22) Tateishi, T.; Yoshimura, M.; Tokuda, S.; Matsuda, F.; Fujita, D.; Furukawa, S. Coordination/Metal–Organic Cages inside Out. *Coord Chem Rev* **2022**, *467*. https://doi.org/10.1016/j.ccr.2022.214612.

(23) Shimoni-Livny, L.; Glusker, J. P.; Bock, C. W. Lone Pair Functionality in Divalent Lead Compounds. *Inorg Chem* **1998**, *37* (8), 1853–1867. https://doi.org/10.1021/ic970909r.

(24) Ths-Type Topology. Http://Rcsr.Net/Nets/Ths.

(25) Sugamata, K.; Takagi, C.; Awano, K.; Iihama, T.; Minoura, M. Structural Analysis of and Selective CO2adsorption in Mixed-Ligand Hydroxamate-Based Metal-Organic Frameworks. *Dalton Transactions* **2020**, *49* (29), 9948–9952. https://doi.org/10.1039/d0dt01105c.

(26) Padial, N. M.; Castells-Gil, J.; Almora-Barrios, N.; Romero-Angel, M.; Da Silva, I.; Barawi, M.; García-Sánchez, A.; De La Peña O'Shea, V. A.; Martí-Gastaldo, C. Hydroxamate Titanium-Organic Frameworks and the Effect of Siderophore-Type Linkers over Their Photocatalytic Activity. *J Am Chem Soc* **2019**, *141* (33), 13124–13133. https://doi.org/10.1021/jacs.9b04915.

(27) Lerma-Berlanga, B.; Castells-Gil, J.; Ganivet, C. R.; Almora-Barrios, N.; Gonzalez-Platas, J.; Fabelo, O.; Padial, N. M.; Marti-Gastaldo, C. Permanent Porosity in Hydroxamate Titanium-Organic Polyhedra. *J Am Chem Soc* **2021**, *143* (50), 21195–21199. https://doi.org/10.1021/jacs.1c09278.

(28) Marshall, C. R.; Staudhammer, S. A.; Brozek, C. K. Size Control over Metal-Organic Framework Porous Nanocrystals. *Chem Sci* **2019**, *10* (41), 9396–9408. https://doi.org/10.1039/c9sc03802g.

(29) Yan, Y.; O'Connor, A. E.; Kanthasamy, G.; Atkinson, G.; Allan, D. R.; Blake, A. J.; Schröder, M. Unusual and Tunable Negative Linear Compressibility in the Metal-Organic Framework MFM-133(M) (M = Zr, Hf). *J Am Chem Soc* **2018**, *140* (11), 3952–3958. https://doi.org/10.1021/jacs.7b11747.

(30) Chen, L.; Mowat, J. P. S.; Fairen-Jimenez, D.; Morrison, C. A.; Thompson, S. P.; Wright, P. A.; Düren, T. Elucidating the Breathing of the Metal-Organic Framework MIL-53(Sc) with Ab Initio Molecular Dynamics Simulations and in Situ X-Ray Powder Diffraction Experiments. *J Am Chem Soc* **2013**, *135* (42), 15763–15773. https://doi.org/10.1021/ja403453g.

(31) Loiseau, T.; Serre, C.; Huguenard, C.; Fink, G.; Taulelle, F.; Henry, M.; Bataille, T.; Férey, G. A Rationale for the Large Breathing of the Porous Aluminum Terephthalate (MIL-53)

Upon Hydration. *Chemistry - A European Journal* **2004**, *10* (6), 1373–1382. https://doi.org/10.1002/chem.200305413.

(32) Grape, E. S.; Xu, H.; Cheung, O.; Calmels, M.; Zhao, J.; Dejoie, C.; Proserpio, D. M.; Zou, X.; Inge, A. K. Breathing Metal-Organic Framework Based on Flexible Inorganic Building Units. *Cryst Growth Des* **2020**, *20* (1), 320–329. https://doi.org/10.1021/acs.cgd.9b01266.

(33) WANG, R.-M.; Ming-Hui, Z.; Wen, W.; Yu-Wen, X.; Zhi-Ying, W.; Fang-Na, D.; Liang-Liang, Z.; SUN, D.-F. Interpenetration of Three 2D In-MOFs With（6,3）Topology:Syntheses,Structures and Fluorescent Properties. *Chinese Journal of structural chemistry* **2016**, *11*, 1714–1722.

─ CHAPTER 7 ─

Reticulating Iridium: A New MOF Family, MIrPF-13 (M = In, Sc)

7.1. Introduction

Iridium is an element with very low earth abundance, but widely used in a breadth of applications, ranging from solar cells,[1] organic electronic devices[2] to biological applications[3] (anticancer agent,[4] biological probe,[5] biocompatible materials[6]). Although iridium is a transition metal, it is part of the ubiquitous noble metal family (Ag, Au, Pt, Rh, Ir, Pd, Ru and Os) which implies that it can be quite expensive. However, considering that its price is less than half that of rhodium, it seems that iridium is an interesting cost-effective alternative. Over the past decades, almost every metal element in the periodic table has been used to create MOFs, from alkali metals[7] to uranium,[8] with only a few exceptions, including iridium as one of the elements that has not yet been incorporated into the SBU of a MOF.[9,10] Although there are examples of iridium-containing MOFs used in catalytic applications such as water splitting,[11–17] CO_2 and O_2 reduction,[18] hydrogenation of CO_2 to formate,[19] Si-H bond functionalization,[20] aerobic alcohol oxidation,[21] or ethylene hydrogenation, [22–24] in all of these the iridium atoms are either incorporated into the structure as part of a metalloligand, or inserted post-synthetically and coordinated to anchoring groups of the linkers. These strategies are generally carried out in two-step processes, and the accessibility and tunability of the metal centers can be hindered and/or the porosity of the MOFs can be reduced due to the presence of bulky complexes. The direct use of iridium in MOF synthesis remains elusive, partly due to the distinctive coordination chemistry properties of iridium cations.

In the literature we can find reports of anchored molecular iridium compounds onto solid matrixes[25–27] used in heterogenous catalysis; however, incorporating Ir atoms into the structure of a porous solid, specifically a MOF, would provide more advantages: a simpler and more cost-effective synthesis of the catalyst, a molecularly and chemically tunable environment for the Ir atoms, and the possibility of recycling the catalyst.

Nowadays, catalysis is deemed to be the core of the development of modern science, as it has made molecular complexity accessible with high selectivity and efficiency. Not only does it make synthetic methodologies more cost-effective and less time-consuming, but it also allows for greener chemistry to be used and thus alleviate the strain we are putting on the environment, especially during the environmental crisis that has been steadily worsening in the last few decades. Transition metal catalysis plays a key role in the field of organic synthesis, as it allows carrying out novel or non-conventional transformations, not obtainable through traditional chemistry. Ir-based materials are widely used in the catalysis field due to their unique properties and unparalleled activity. Thus, iridium compounds are key catalysts for important chemical transformations, such as water splitting for which IrO_2 is a staple catalyst, as it can withstand harsh acidic conditions.[28–31] In addition, iridium molecular catalysts, such as pincer complexes[32] or *N*-heterocyclic carbenes complexes[33] are generally used in homogeneous phase.[34]

So, the key point of this chapter is the strategy used for reticulating iridium into a metal-organic framework, and testing the catalytic activity of the material. To achieve this goal, a strategy based on the combination of iridium with additional metal elements has been explored, for which various synthetic approaches were attempted. Following, the quest for the reticulation of iridium atoms in MOF building units is detailed.

7.2. First experiments: inserting Ir into already known MOFs

Our first approach to reticulate iridium was to insert it into the structure of already reported MOFs, in a simple one-pot synthetic pathway. This would direct the insertion of the Ir atoms into specific positions of the SBUs of the MOFs, and no other complexes or post-synthetical treatments would be required. As mentioned in the introduction (chapter 1) of this thesis, there are many precedents of additional metal elements being incorporated into already reported single-metal MOFs, which is accomplished through an array of routes depending on the compatibility of the target MOF with the additional metal element.[35] So, we decided to explore the insertion of Ir in known MOFs containing trivalent cations of different atomic radii and coordination environments. The chemistry of Ir-based compounds resembles that of its group 9 congener, rhodium,[36,37] and in the literature there are examples of multi-metal Rh-based MOFs with either other transition metals[38,39] or elements from group 13,[40] thus we assumed that iridium would also generate multi-metal systems.

7.2.1. Rare-earth based MOFs: RPF-4 and RE-1,4-NDC-fcu-MOF

The MOF family **RPF-4**, discussed in chapter 4 of this thesis, was chosen as the first candidate for the insertion of Ir. The reason behind this was that, after the exhaustive study carried out in chapter 4, we have knowledge about how the structure behaves when two cations are combined in the same building unit. Also, the rod-shaped SBUs of this MOF contain a high density of metal ions in close vicinity and accessible through the pores, which facilitate cation exchange in the SBU.

Following the synthetic procedure already detailed in chapter 4 and using $IrCl_3 \times nH_2O$ as an Ir^{3+} precursor, the one-pot synthesis (in a reaction time of 1 and 3 days) of La-Ir,

Nd-Ir and Yb-Ir was carried out, all of them in an 8:2 ratio. We chose La and Yb to check if the different crystallization mechanisms that the RPF-4 combinations based on these metals display would have any impact on the insertion of Ir, and Nd as an intermediate cation between the other two. The 8:2 ratio was preferred over 9:1, as some experiments require a slightly higher concentration of the metal to be inserted, and it would facilitate its quantification.

The PXRD patterns of the combinations confirm that RPF-4 was obtained as a pure phase (Figure 7.1). No presence of peaks corresponding to any Ir-containing compound, such as IrO_2 or $Ir(OH)_3$, was observed.

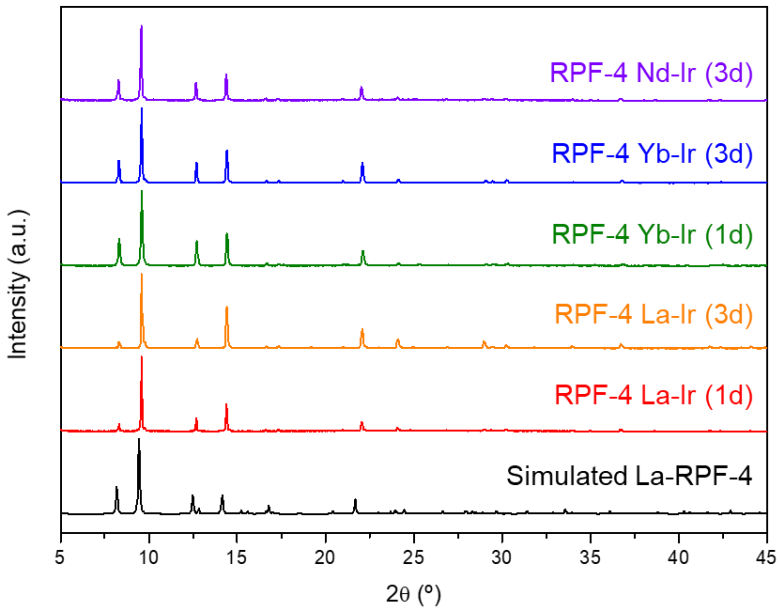

Figure 7.1. PXRD patterns of the M-Ir RPF-4 combinations (M = La, Nd, Yb).

The morphology and composition of the crystals of the samples was studied using SEM-EDX (Figure 7.2). Samples containing La displayed defective morphologies similar to those displayed by single-metal La-RPF-4 (in both 1 and 3 days), and the same applies to Yb-containing samples; Nd-based samples displayed crystals with smooth surfaces, similar to the case of Yb. EXD analysis revealed a 9:1 ratio (within experimental error)

for the La- and Yb-based combinations, and no presence of Ir in the case of the Nd-Ir combination. However, we also noticed the frequent presence of submicron particle aggregates in all the samples. It was not clear whether these particles were another compound that had generated during the synthesis, nuclei of RPF-4 that did not get to grow correctly, or pieces of broken crystals. As these particles were found generally on the surface of crystals, and due to their small size, it was not possible to get a clear analysis of their composition through EDX.

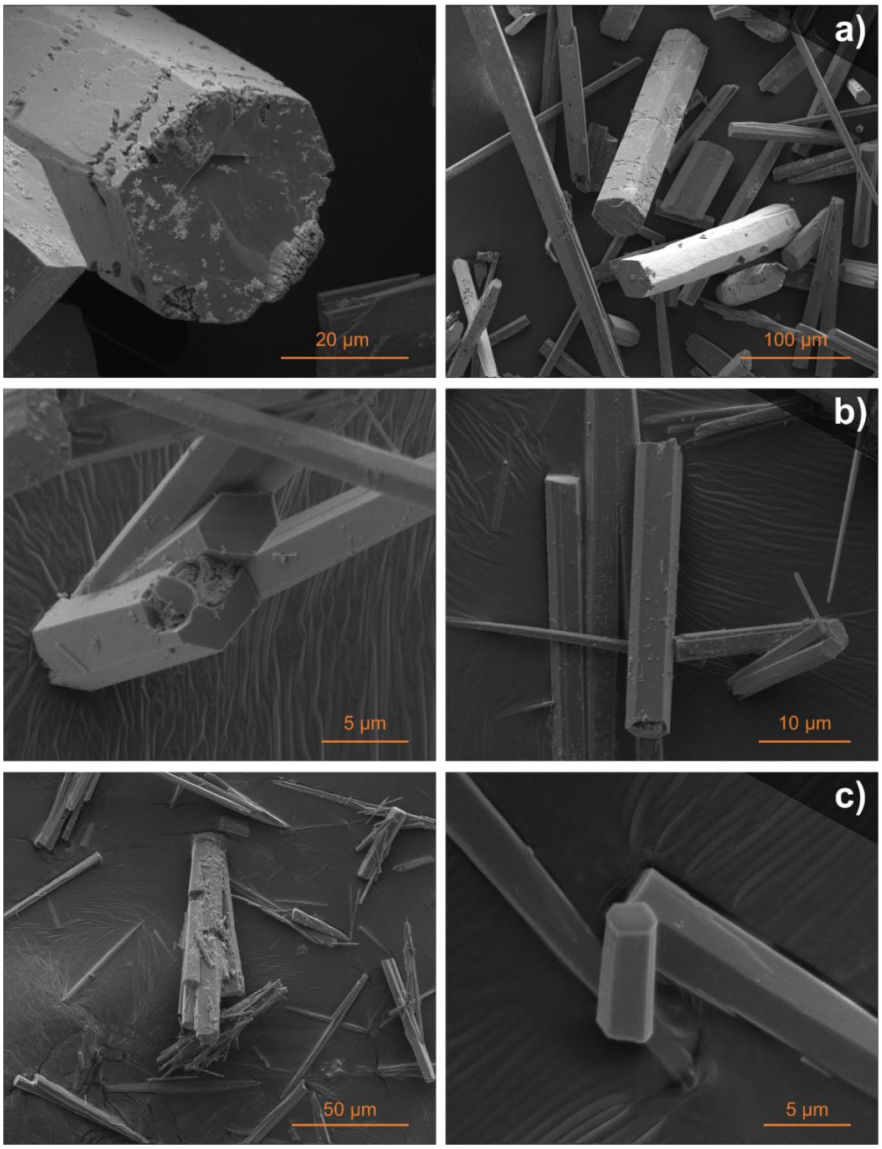

Figure 7.2. SEM images of the M-Ir RPF-4 combinations synthesized in 3 days (M = La, Nd, Yb). **a)** RPF-4 La-Ir, **b)** RPF-4 Nd-Ir, **c)** RPF-4 Yb-Ir.

The TXRF analysis of the La-Ir sample revealed an excess of Ir in the bulk (La-Ir 0.14:9.86), which does not match the ratio obtained by EDX (La-Ir 9:1 ratio), and implies that the particles observed in the SEM images were rich in Ir.

As the insertion of Ir into the RPF-4 system did not seem successful, we shifted to a MOF with a different type of trivalent rare-earth based SBU. The structure of **M-1,4-NDC-fcu-MOF** (1,4-NDC = 1,4-naphtalenedicarboxylic acid; M = Y, Tb) is generated by bridging hexanuclear clusters with formula $[M_6(\mu_3\text{-}OH)_8(O_2C^-)_{12}]$ (Figure 7.3). This cluster is similar to the archetypal Zr-based SBU of UiO-66,[41] which has been successfully doped with other metals,[42] so it would be an interesting candidate for the insertion of Ir. The synthesis of combinations of M-Ir of **M-1,4-NDC-fcu-MOF** was also carried out following the reported procedure, using $IrCl_3 \times nH_2O$ as an Ir^{3+} precursor.[43]

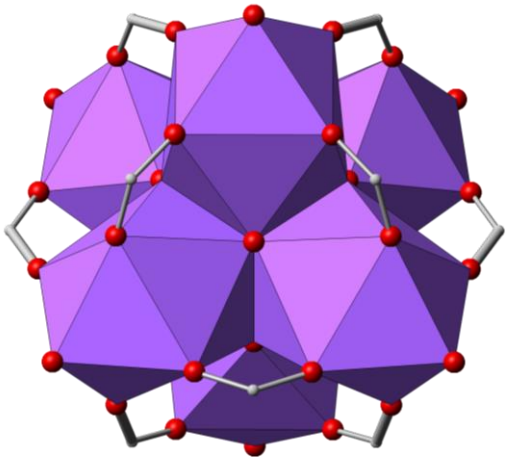

Figure 7.3. 12-connected cuboctahedron-shaped SBU of RE-1,4-NDC-fcu-MOF (RE = Y, Tb). RE atoms are displayed in purple, C in grey, O in red. H atoms are omitted for clarity.

The combinations that were synthesized were Y-Ir and Tb-Ir in an 8:2 ratio. While the Tb-based combination did not yield any solid, the Y-based MOF resulted in a phase mixture with an amorphous black powder, similar to the one obtained for RPF-4 (Figure 7.4), and again implying that iridium was not effectively incorporated in the SBU.

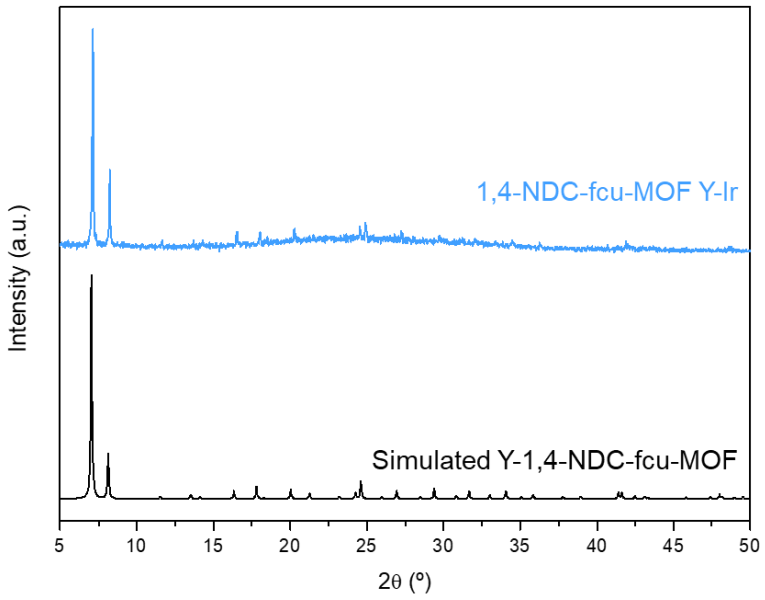

Figure 7.4. PXRD patterns of RE-1,4-NDC-fcu-MOF Y-Ir.

7.2.2. Bismuth- and Indium-based MOFs

Given that the insertion of Ir into rare-earth-based MOFs was not successful, we pondered whether Ir is not compatible with the selected lanthanide-based systems, and we shifted to our other MOFs based on In and Bi, discussed in chapter 6. In^{3+} generally display an octahedral coordination environment, similar to Ir^{3+}, and the presence of an additional linker with an N-containing group in the case of InPF-32 (2,2'-bipyridine) would facilitate the coordination of the Ir atoms due to their affinity for N-donor linkers.[36] BiPF-11 was also selected for these experiments due to its dynamic behavior which would potentially allow the framework to adapt to the insertion of the Ir cations, and also to explore the combination of iridium with elements with a higher number of electrons. We synthesized **BiPF-11** and **InPF-32** following the synthetic routes described in chapter 6, with a M:Ir (M = Bi, In) ratio of 8:2, and using $IrCl_3 \times nH_2O$ as an Ir^{3+} precursor. The PXRD patterns of the samples match the simulated ones from the SCXRD data from chapter 6 (Figure 7.5). In the case of InPF-32, the PXRD plot indicates low crystallinity of the sample, and the presence of additional peaks indicate that there is another phase forming along the MOF. The results from the EDX analysis point to a lack of iridium in both systems. Again, the SEM images (Figure 7.6) display the presence of particle aggregates on the surface of the crystals of the MOFs. Therefore, it seems that is was not possible to obtain multi-metal MTV-MOFs with these combination of metals in the studied conditions.

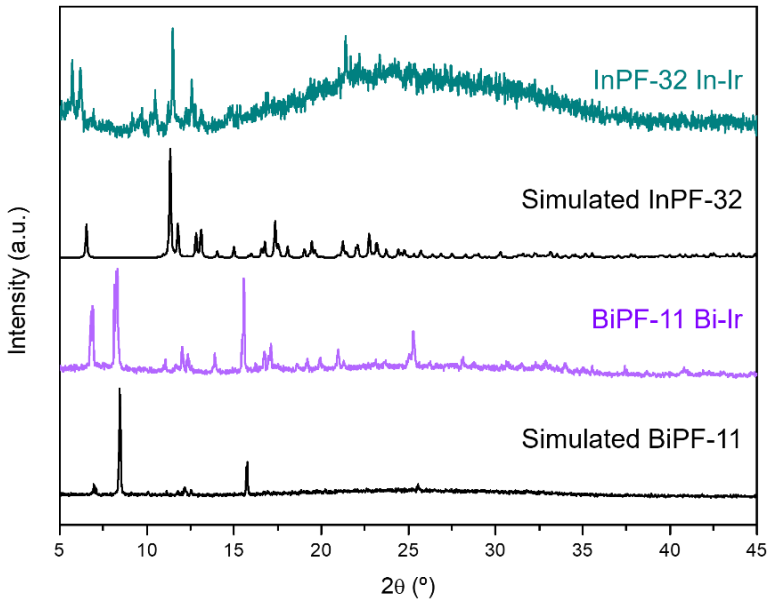

Figure 7.5. PXRD patterns of BiPF-11 and InPF-32.

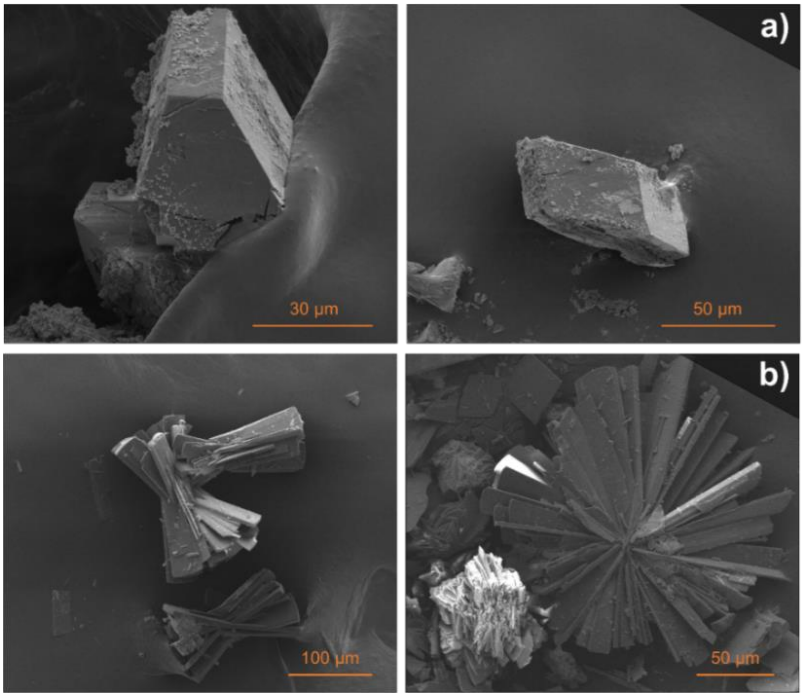

Figure 7.6. SEM images of **a)** BiPF-11 and **b)** InPF-32.

7.2.3. Aluminium-based MOFs

Again, since the insertion of Ir in our Bi- and In- based MOFs was also not successful, we thought of using a metal with a similar radius value (atomic radius of Ir = 1.35 Å). We chose aluminium. a cost-effective, green, abundant metal, with a radius of 1.25 Å. Generally, Al^{3+} displays an octahedral coordination environment, similar to that of Ir^{3+}. We considered a series of Al-based reported MOFs with different types of SBUs, as displayed in Figure 7.7: **MIL-53** (rods)[44], **Al(OH)ndc** (rods)[44], **MIL-100** (trimers)[45,46] and **MOF-520** (ring-shaped SBU)[47–49]. The synthesis of the materials was carried out following the corresponding reported route, with an 8:2 Al:Ir ratio, and using $IrCl_3 \times nH_2O$ as an Ir^{3+} precursor.

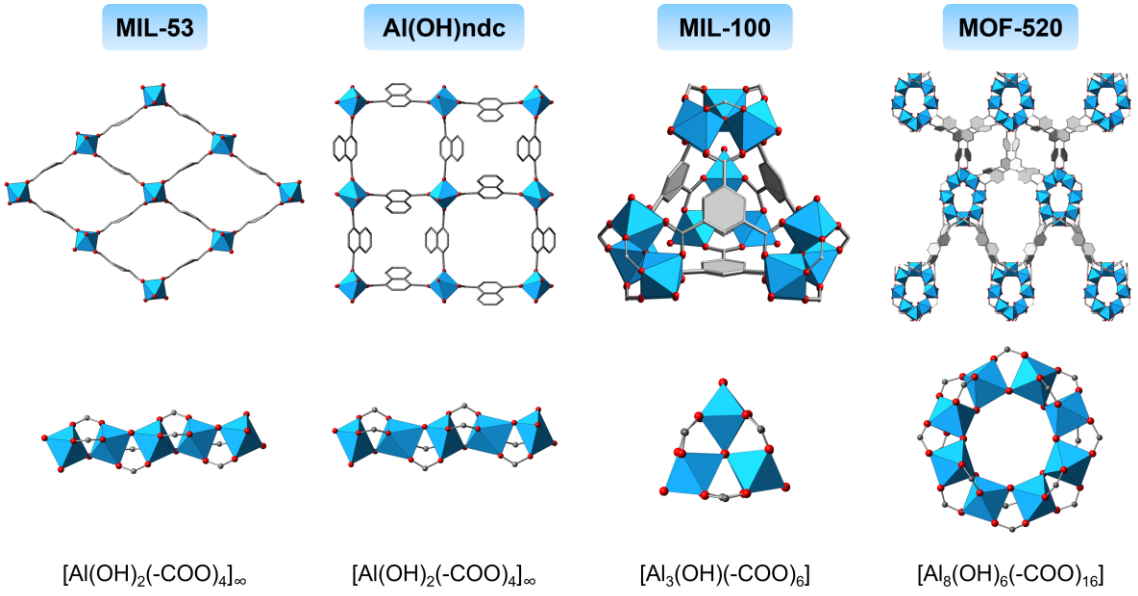

Figure 7.7. Al-based MOFs and their corresponding SBUs. Al atoms are displayed in blue, C in grey, O in red. H atoms are omitted for clarity.

In the case of Al-Ir **MIL-100**, the synthesis attempts resulted in the recrystallization of the linker, or in the formation of polymorphs of the linker H_3BTC, as confirmed by the PXRD analysis (Figure 7.8). SCXRD analysis of the unit cell parameters of a crystal of the sample further confirmed that the structure matched the polymorph with CSD code BTCOAC.

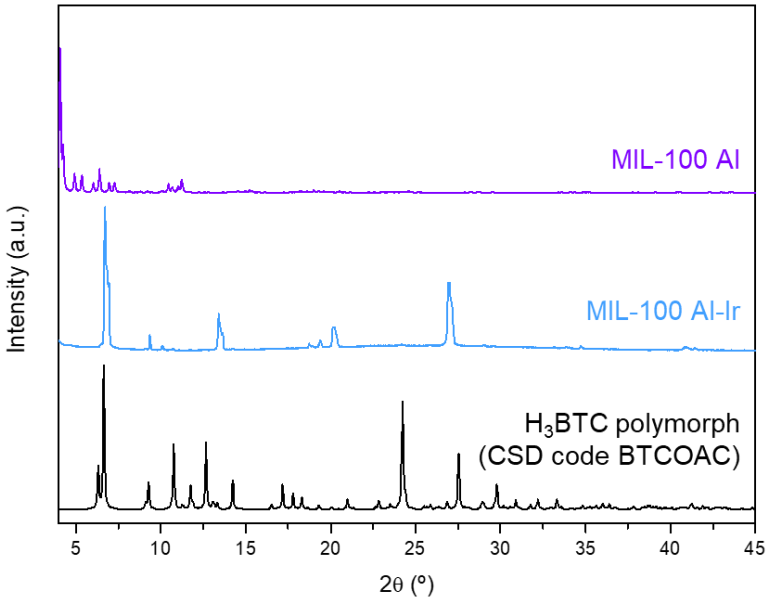

Figure 7.8. PXRD patterns of MIL-100 Al-Ir.

The synthesis of Al-Ir **MOF-520** yielded small white crystals mixed with a black amorphous powder (Figure 7.9). As the crystals were not of the size needed for the SCXRD analysis, and the presence of the black powder was indicative of phase segregation instead of insertion of Ir in the MOF, we assumed that the insertion experiment was not fruitful.

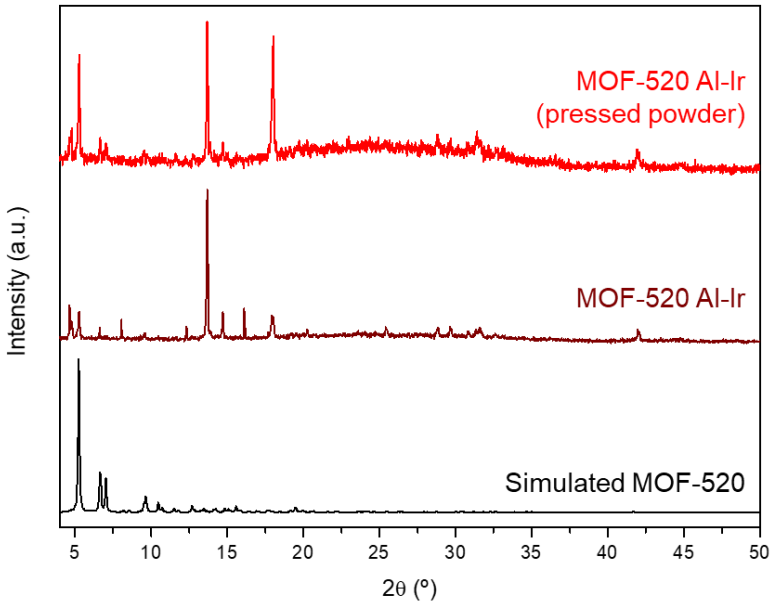

Figure 7.9. PXRD patterns of Al-Ir MOF-520.

For **Al(OH)ndc**, the synthesis yielded grey crystals, and the PXRD confirmed the purity of the sample (Figure 7.10). However, the SEM-EDX analysis revealed that the sample consisted of the prism-shaped crystals of Al(OH)ndc, and spherical particles and aggregates of uneven sizes. The presence of these particles leads to a charging effect that generates an anomalous contrast in the SEM images, even if the samples were previously coated with Au (Figure 7.11). Also because of this, the EDX microanalysis could not be performed in individual crystals, and the composition of the bulk reveals a high content of Ir (Al:Ir 3:1 and 2:1), and presence of a considerable amount of Cl (Al:Ir:Cl 8:4:1 and 9:3:1). These results led us to rule out this MOF option as it seems that the combination of Al-Ir is not compatible with this system.

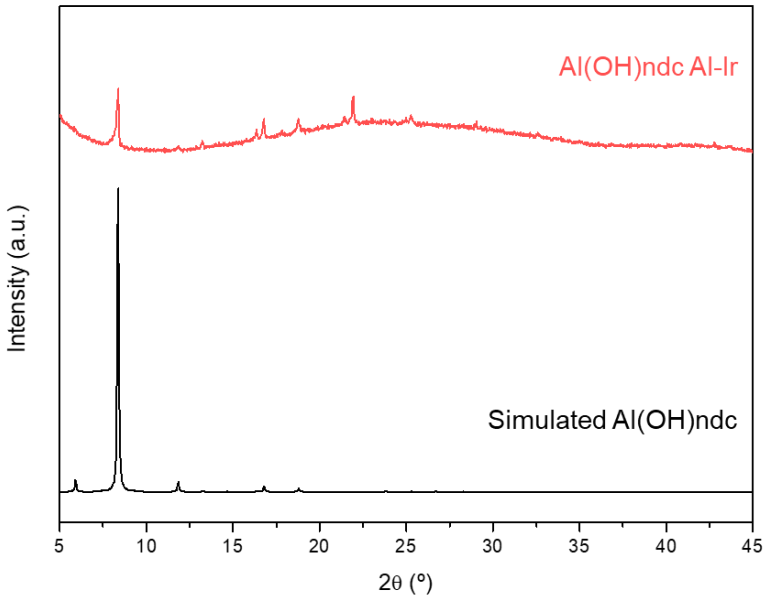

Figure 7.10. PXRD patterns of Al(OH)ndc Al-Ir.

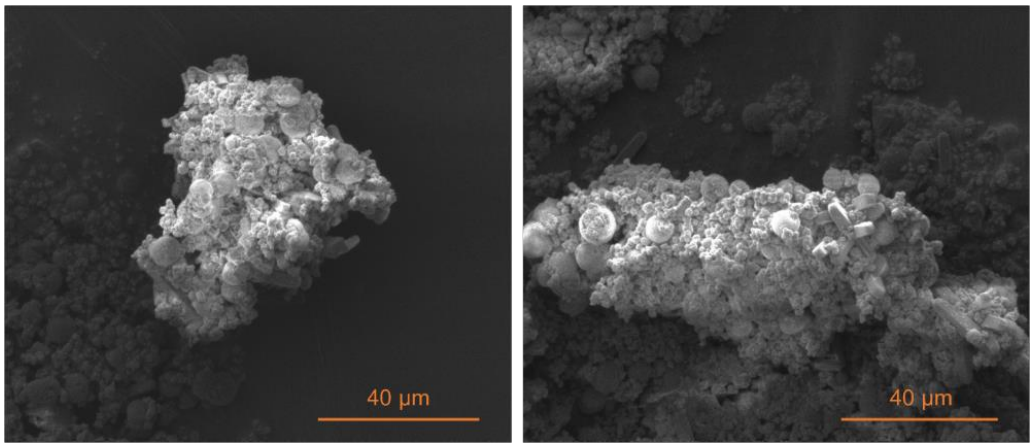

Figure 7.11. SEM images of Al-Ir Al(OH)ndc.

Regarding Al-Ir **MIL-53**, the synthesis yielded grey crystals, and the experimental PXRD pattern matches the reported one, but with significant differences in the relative intensity of multiple diffraction peaks. (Figure 7.12).

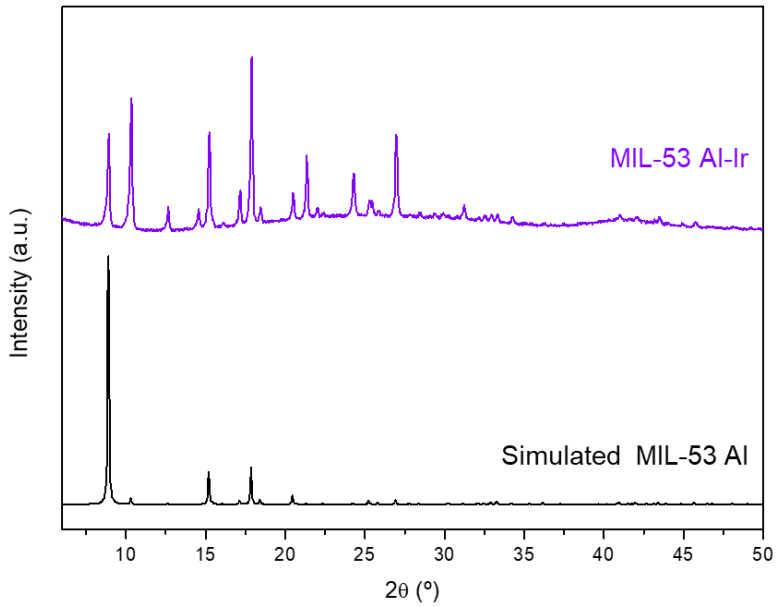

Figure 7.12. PXRD patterns of MIL-53 Al-Ir.

To ensure the purity of the sample, we used a Soxhlet method to carry out several cycles of washing (solid-liquid extraction) of the material and extract any possible contaminants or remaining linker. The solvent of choice was methanol because of its low boiling point (64.7 ºC), and the sample did not change color after this process.

The TGA plot of the MOF is shown in Figure 7.13, and it matches the reported behavior of conventional Al-MIL-53.[50] There is a weight loss of approximately 30% at around 250 ºC, and the total decomposition of the framework occurs between 500-600 ºC. The total degradation of the MOF resulted in iridium(IV) oxide (IrO_2), as evidenced by PXRD (Figure 7.14), demonstrating the presence of iridium in the bulk of the solid.

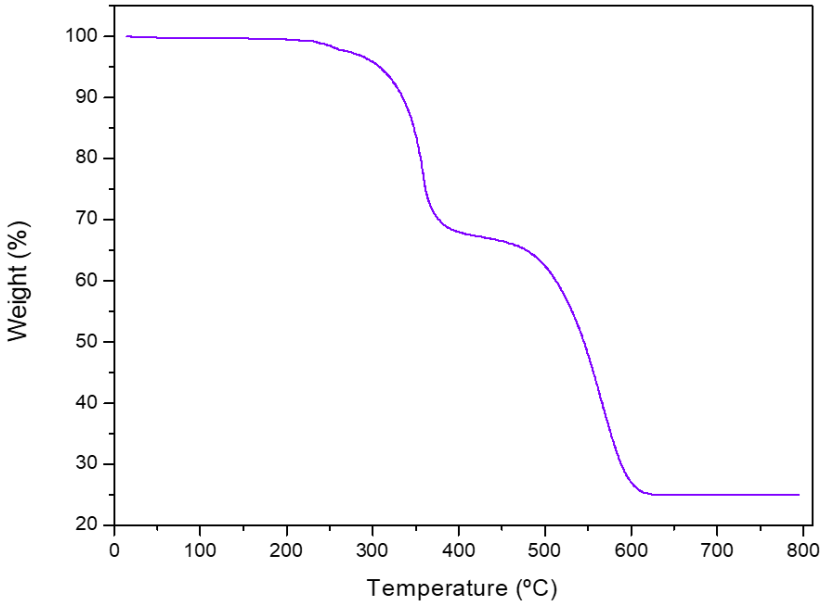

Figure 7.13. TG plot of Al-Ir MIL-53.

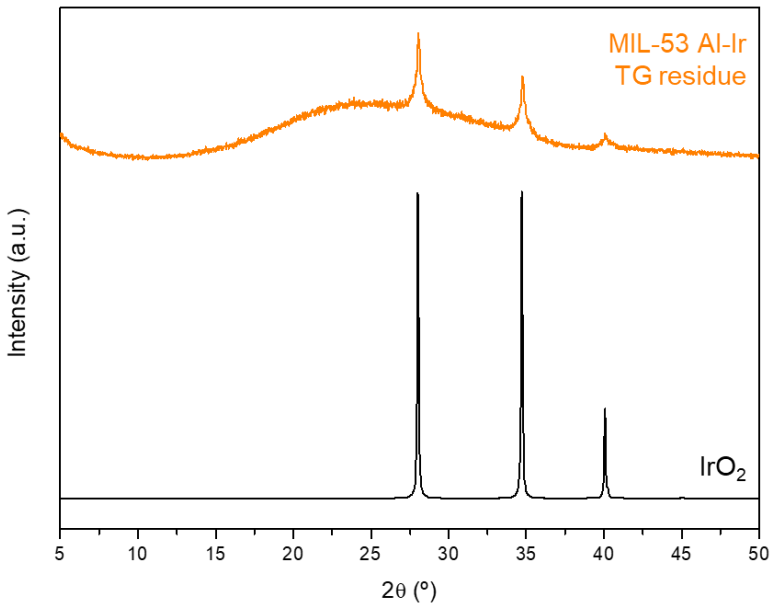

Figure 7.14. PXRD of the TG residue of Al-Ir MIL-53.

The TXRF analysis of the composition of the bulk of the sample resulted in an Al:Ir ratio of 8:2, matching the initial synthesis ratio. However, a closer look at the crystals of the sample through SEM and a EDX mapping analysis revealed that the Ir atoms were not evenly distributed throughout the MOF, but mostly located in spherical areas found on the surface of the crystals (Figure 7.15.). Since these areas were not washed out after the Soxhlet process, it could be possible that iridium atoms are preferentially incorporated in the external crystal faces during the synthesis, but also that a different phase is formed, and strongly attached to the surface of the MOF crystals.

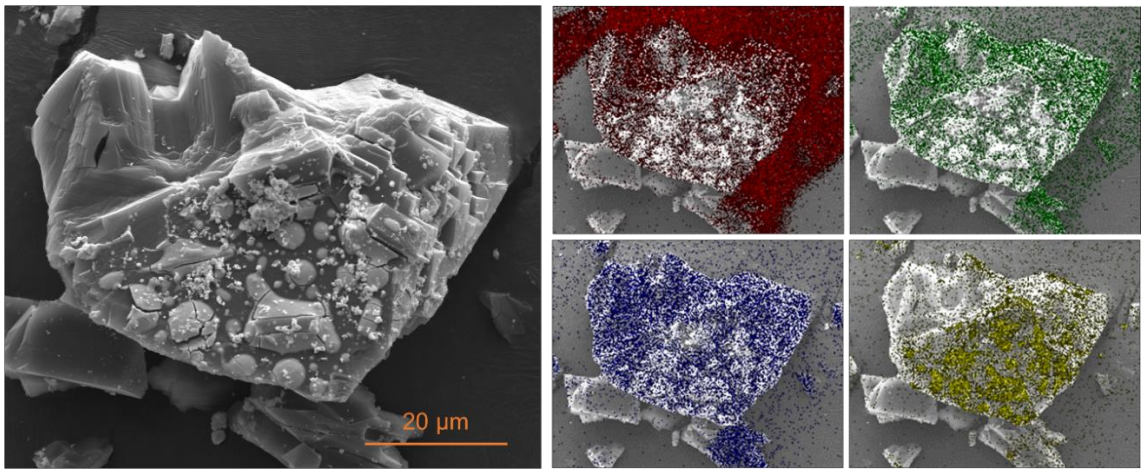

Figure 7.15. EDX mapping of a crystal of Al-Ir MIL-53. In the mapping, C is displayed in red, O in green, Al in blue and Ir in gold.

XPS analysis indicated a high O 1s signal, which can be ascribed to the functional groups of the linkers (the carboxylates groups) or to the metal-OH chains of the SBUs of the MOF; however, we cannot rule out the possibility of iridium oxide particles present in the bulk sample contributing to the high intensity of this XPS signal. Although the sample was not easy to analyze by SCXRD as the crystals displayed a morphology similar to thin plates or needles, we were able to record the data of one crystal, and the refinements point to an absence of Ir in the structure. In view of these results, we conclude that Al-based MOFs are not the most fitting candidates for the insertion of Ir.

We hypothesize that, in all the cases previously described, during the one-pot synthesis reactions, the iridium atoms are not actually being inserted in the framework of the MOFs, but rather forming iridium or iridium oxide nanoparticles (1-5 nm) or particles with small domains, and because of the size of these particles, they are not distinguishable nor detectable with X-ray diffraction techniques or SEM.

7.3. Reticulating Iridium: a new heterometallic MOF family, MIrPF-13 (M = In, Sc)

At this stage and in view of the fact that we were unable to achieve the insertion of Ir in already reported MOFs, we considered designing a new multi-metal Ir-based MOF. As opposed to the previous experiments where the formation of a multi-metal MTV-MOF was pursued, in the present approach we sought to create a structure where different metal cations would occupy specific sites. In this way, the additional metal element could facilitate the formation of an extended iridium-based framework and also provide the resulting MOF with additional properties resulting from the combination of multiple metal elements. To implement this strategy, we envisioned the use of a linker with two coordination modes to facilitate the insertion of each metal into specific locations, while avoiding the formation of single-metal phases. We had in mind organic linkers with dual functionalities as Ir seems to have a higher affinity for nitrogen rather than carboxylate groups.[36] Having considered an array of linkers, we settled on a *N*,*O*-donor linker with three different substitutions (Figure 7.16): 2,4-pyridinedicarboxilic acid (2,4-H_2PDC); 2,5-pyridinedicarboxilic acid (2,5-H_2PDC); 2,6-pyridinedicarboxilic acid (2,6-H_2PDC). In the literature we found examples of Ir complexes with 2,6-H_2PDC,[51,52] and different pyridinecarboxylic moieties,[53] in which the Ir atoms coordinate to both the pyridinic nitrogen and the carboxylic oxygen atoms, and in the case of the linkers we selected, this would leave the carboxylate groups at the 4-, 5- and 6-position of the ring available to coordinate to the second metal atom, thus facilitating the extension and growth of a framework.

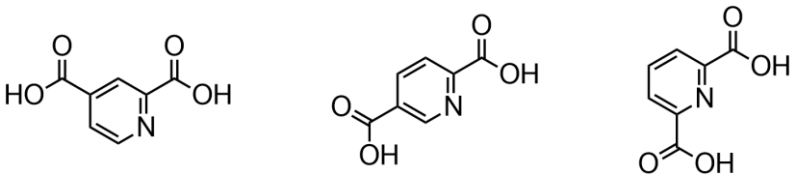

Figure 7.16. Pyridinedicarboxilic acids used in this section of the chapter.

7.3.1. InIrPF-13

The first metal that was chosen to be combined with Ir was In. Indium is a cost-effective, low-toxicity, group 13 metal that displays different coordination capabilities, resulting in a rich structural diversity,[54] and a strong Lewis acid character that makes it widely used in the field of catalysis.[55–59] Generally, In-based MOFs display high stability in air or in a humid environment, and good catalytical performance.[63] In systems with six-coordinate In atoms, the stability of the structure is the result of an electron-rich hypervalent bonding pattern, which has a direct impact on the general features of the material, making it generally more thermodynamically stable and more reactive from a kinetics point-of-view.[64]

This synthetic strategy yielded one new heterometallic In-Ir MOF only with the 2,5-H_2PDC linker: InIrPF-13. The combinations of In-Ir and the other two linkers resulted in the formation amorphous solids, or recrystallized linker.

7.3.1.1. Synthesis of InIrPF-13

All reagents and solvents employed were commercially available and used as received without further purification: 2,5-pyridinedicarboxilic acid, 2,5-H_2PDC (>98%, TCI); iridium(III) chloride hydrate, $IrCl_3 \times nH_2O$ (99.8%, Alfa Aesar); indium(III) acetate, $In(CH_3COO)_3$ (99.99%, Alfa Aesar); indium(III) nitrate hexahydrate, $In(NO_3)_3 \times 5H_2O$ (99.99%, Alfa Aesar); indium(III) chloride tetrahydrate, $InCl_3 \times 4H_2O$ (99.99%, Strem);

indium(III) fluoride hydrate, $IrF_3 \times nH_2O$ (99%, abcr); indium(III) acetylacetonate, $In(acac)_3$ (≥99%, Sigma Aldrich).

2,5-PDC (0.32 mmol, 54.6 mg), $In(CH_3COO)_3$ (0.08 mmol, 23.4 mg), and $IrCl_3 \times nH_2O$ (0.08 mmol, 24.0 mg) were dissolved in 13 mL of deionized water. The ratio between the linker, $In(CH_3COO)_3$ and $IrCl_3 \times nH_2O$ is 4:1:1. The mixture was placed in a 50 mL Teflon-lined steel autoclave and heated during 24 hours in an oven at 170 °C. After cooling to room temperature, the yellow crystals were washed with water (3x10 mL).

This synthetic pathway yielded the new heterometallic In-Ir MOF, InIrPF-13. However, during the synthesis reaction, another already reported single-metal indium-based structure[61] forms along, and in the range of conditions we tested (Table 7.1 and 7.2), it was not possible to obtain InIrPF-13 as a pure phase. This will be discussed more in depth in the following section of this chapter.

Table 7.1. Synthetic conditions tested in the attempt to obtain pure InIrPF-13.

Entry	mmol 2,5-PDC	mmol Indium salt	Indium salt	mmol $IrCl_3xnH_2O$	Temp. (ºC)	Time (h)	Solvent	mL	Modulator
1	0.24	0.12	A	0.08	170	24	H_2O	13	-
2	0.24	0.10	A	0.06	150	24	H_2O	13	-
3	0.20	0.21	A	0.13	150	24	H_2O	13	-
4	0.20	0.16	A	0.12	150	24	H_2O	13	-
5	0.20	0.16	A	0.10	150	24	H_2O	13	-
6	0.20	0.16	A	0.08	150	24	H_2O	13	-
7	0.20	0.16	A	0.06	150	24	H_2O	13	-
8	0.20	0.16	A	0.04	170	24	H_2O	13	-
9	0.20	0.16	A	0.04	170	24	DMSO	14	-
10	0.20	0.16	A	0.04	150	24	H_2O	13	-
11	0.20	0.12	A	0.04	150	24	H_2O	13	-
12	0.20	0.10	A	0.06	170	24	H_2O	13	-
13	0.20	0.10	A	0.06	150	144	H_2O	13	-
14	0.20	0.10	A	0.06	150	72	H_2O	13	-
15	0.20	0.10	A	0.06	150	24	H_2O	13	-
16	0.20	0.10	A	0.06	150	24	DMF	13	-
17	0.20	0.10	A	0.06	150	24	EtOH	13	-
18	0.20	0.10	N	0.06	150	24	H_2O	13	-
19	0.20	0.10	C	0.06	150	24	H_2O	13	-
20	0.20	0.10	A	0.06	150	24	H_2O	10	-
21	0.20	0.10	A	0.06	150	24	H_2O	8	-
22	0.20	0.10	A	0.06	150	24	H_2O	5	-
23	0.20	0.10	A	0.06	150	24	H_2O+EtOH	8+5	-
24	0.20	0.10	A	0.06	150	24	H_2O+EtOH	6.5+6.5	-
25	0.20	0.10	A	0.06	150	5	H_2O	13	-
26	0.20	0.10	A	0.06	150	3	H_2O	13	-
27	0.20	0.10	A	0.06	130	24	H_2O	13	-
28	0.20	0.10	A	0.04	150	24	H_2O	13	-
29	0.20	0.08	A	0.04	150	24	H_2O	13	-
30	0.20	0.06	A	0.04	150	24	H_2O	13	-
31	0.20	0.04	A	0.04	150	24	H_2O	13	-
32	0.20	0.02	A	0.04	150	24	H_2O	13	-
33	0.16	0.16	A	0.04	170	168	H_2O	13	-
34	0.16	0.16	A	0.04	170	72	H_2O	13	-
35	0.16	0.16	A	0.04	170	48	H_2O	13	-
36	0.16	0.16	A	0.04	170	24	H_2O	13	-
37	0.16	0.16	A	0.04	170	Aging+24	H_2O	13	-
38	0.16	0.16	A	0.04	150	24	H_2O	13	-
39	0.16	0.12	A	0.08	170	72	H_2O	13	-
40	0.16	0.12	A	0.04	150	24	H_2O	13	-
41	0.16	0.10	A	0.06	150	24	H_2O	13	-
42	0.16	0.08	A	0.12	170	72	H_2O	13	-
43	0.16	0.08	A	0.04	170	24	H_2O	13	-
44	0.16	0.08	A	0.04	150	24	H_2O	13	-
45	0.16	0.06	A	0.04	150	24	H_2O	13	-
46	0.16	0.04	A	0.08	170	24	H_2O	13	-

47	0.16	0.04	A	0.04	170	168	H_2O	13	-
48	0.16	0.04	A	0.04	170	48	H_2O	13	-
49	0.16	0.04	A	0.04	170	Aging+24	H_2O	13	-
50	0.16	0.04	A	0.04	170	24	H_2O	13	-
51	0.16	0.04	A	0.04	150	24	H_2O	13	-
52	0.12	0.16	A	0.04	150	24	H_2O	13	-
53	0.12	0.12	A	0.08	170	24	H_2O	13	-
54	0.12	0.12	A	0.04	150	24	H_2O	13	-
55	0.12	0.08	A	0.04	150	24	H_2O	13	-
56	0.12	0.06	A	0.04	150	24	H_2O	13	-
57	0.12	0.04	A	0.08	170	24	H_2O	13	-
58	0.12	0.04	A	0.04	150	24	H_2O	13	-
59	0.08	0.16	A	0.04	150	24	H_2O	13	-
60	0.08	0.12	A	0.04	150	24	H_2O	13	-
61	0.08	0.08	A	0.04	150	24	H_2O	13	-
62	0.08	0.06	A	0.04	150	24	H_2O	13	-
63	0.08	0.04	A	0.04	150	24	H_2O	13	-
64	0.06	0.16	A	0.04	150	24	H_2O	13	-
65	0.06	0.12	A	0.04	150	24	H_2O	13	-
66	0.06	0.08	A	0.04	150	24	H_2O	13	-
67	0.06	0.06	A	0.04	150	24	H_2O	13	-
68	0.06	0.04	A	0.04	150	24	H_2O	13	-
69	0.2	0.17	A	0.04	150	24	H_2O	13	0.05 mL Et_3N
70	0.2	0.10	A	0.06	150	24	H_2O	13	500 µL HNO_3 cc
71	0.2	0.10	A	0.06	150	24	H_2O	13	300 µL HNO_3 cc
72	0.2	0.10	A	0.06	150	24	H_2O	13	100 µL HNO_3 cc
73	0.2	0.10	A	0.06	150	24	H_2O	13	50 µL HNO_3 cc
74	0.2	0.10	A	0.06	150	24	H_2O	13	500 µL AcOH cc
75	0.2	0.10	A	0.06	150	24	H_2O	13	300 µL AcOH cc
76	0.2	0.10	A	0.06	150	24	H_2O	13	100 µL AcOH cc
77	0.2	0.10	A	0.06	150	24	H_2O	13	50 µL AcOH cc
78	0.2	0.10	A	0.06	150	24	H_2O	13	500 µL NaOH 1M
79	0.2	0.10	A	0.06	150	24	H_2O	13	300 µL NaOH 1M
80	0.2	0.10	A	0.06	150	24	H_2O	13	100 µL NaOH 1M
81	0.2	0.10	A	0.06	150	24	H_2O	13	50 µL NaOH 1M
82	0.2	0.06	A	0.06	150	24	H_2O	13	100 µL HNO_3 cc
83	0.2	0.06	A	0.06	150	24	H_2O	13	10 µL HNO_3 cc
84	0.2	0.06	A	0.06	150	24	H_2O	13	0.2 mmol Oxalic acid
85	0.2	0.04	A	0.04	190	24	H_2O	13	100 µL AcOH cc
86	0.2	0.04	A	0.04	180	24	H_2O	13	100 µL AcOH cc
87	0.2	0.04	A	0.04	170	24	H_2O	13	100 µL AcOH cc

A = indium (III) acetate; N = indium (III) nitrate hexahydrate ; C = indium (III) chloride tetrahydrate; F = indium (III) fluoride; AC = indium (III) acetylacetonate; AcOH = acetic acid; Aging = The linker and the iridium salt were left stirring in water at room temperature for 24 hours; the indium salt was added afterwards, and the solution was heated up to the specified temperature for each case.

Table 7.2. Synthetic conditions tested in the attempt to obtain pure InIrPF-13, using stock solutions of the linker as a precursor.

Entry	Stock solution	mmol 2,5-PDC	mmol Indium salt	Indium salt	mmol $IrCl_3xnH_2O$	Temp. (ºC)	Time (h)	Modulator
1	12.5 mL EtOH	0.1	0.08	A	0.02	150	72	-
2	12.5 mL EtOH	0.1	0.08	A	0.02	150	24	-
3	12.5 mL H_2O	0.05	0.06	A	0.01	170	24	-
4	12.5 mL H_2O	0.05	0.05	A	0.01	150	24	-
5	12.5 mL H_2O	0.05	0.045	A	0.01	150	24	-
6	12.5 mL H_2O	0.05	0.04	A	0.02	170	24	-
7	12.5 mL H_2O	0.05	0.04	A	0.01	180	24	-
8	12.5 mL H_2O	0.05	0.04	A	0.01	180	Aging+24	-
9	12.5 mL H_2O	0.05	0.04	A	0.01	170	72	-
10	12.5 mL H_2O	0.05	0.04	A	0.01	170	Aging+72	-
11	12.5 mL H_2O	0.05	0.04	A	0.01	170	48	-
12	12.5 mL H_2O	0.05	0.04	A	0.01	170	24	-
13	12.5 mL H_2O	0.05	0.04	A	0.01	170	Aging+24	-
14	12.5 mL H_2O	0.05	0.04	A	0.01	150	72	-
15	12.5 mL H_2O	0.05	0.04	A	0.01	150	24	-
16	12.5 mL H_2O	0.05	0.04	N	0.01	150	24	-
17	12.5 mL H_2O	0.05	0.04	C	0.01	150	24	-
18	12.5 mL H_2O	0.05	0.04	F	0.01	150	24	-
19	12.5 mL H_2O	0.05	0.04	AC	0.01	150	24	-
20	12.5 mL H_2O	0.05	0.04	A	0.01	150	5	-
21	12.5 mL H_2O	0.05	0.04	A	0.01	150	3	-
22	12.5 mL H_2O	0.05	0.037	A	0.01	170	48	-
23	12.5 mL H_2O	0.05	0.035	A	0.01	150	24	-
24	12.5 mL H_2O	0.05	0.031	A	0.01	170	48	-
25	12.5 mL H_2O	0.05	0.03	A	0.01	150	24	-
26	12.5 mL H_2O	0.05	0.27	A	0.01	170	48	-
27	12.5 mL H_2O	0.05	0.25	A	0.01	150	24	-
28	12.5 mL H_2O	0.05	0.21	A	0.01	170	48	-
29	12.5 mL H_2O	0.05	0.20	A	0.01	190	24	-
30	12.5 mL H_2O	0.05	0.20	A	0.01	180	24	-
31	12.5 mL H_2O	0.05	0.20	A	0.01	170	72	-
32	12.5 mL H_2O	0.05	0.20	A	0.01	170	24	-
33	12.5 mL H_2O	0.05	0.16	A	0.01	170	48	-
34	12.5 mL H_2O	0.05	0.11	A	0.01	170	48	-
35	12.5 mL H_2O	0.05	0.01	A	0.01	170	48	-
36	12.5 mL H_2O	0.05	0.01	N	0.01	170	48	-
37	12.5 mL H_2O	0.05	0.01	C	0.01	170	48	-
38	12.5 mL H_2O	0.05	0.01	F	0.01	170	48	-
39	12.5 mL H_2O	0.05	0.01	AC	0.01	170	48	-
40	12.5 mL H_2O	0.05	0.05	A	0.01	170	24	100 µL AcOH cc
41	12.5 mL H_2O	0.05	0.04	A	0.01	170	24	50 µL AcOH cc
42	12.5 mL H_2O	0.05	0.04	A	0.01	150	24	300 µL AcOH 6M
43	12.5 mL H_2O	0.05	0.04	A	0.01	150	24	100 µL AcOH 6M
44	12.5 mL H_2O	0.05	0.04	A	0.01	150	24	50 µL AcOH 6M
45	12.5 mL H_2O	0.05	0.04	A	0.01	150	24	10 µL AcOH 6M
46	12.5 mL H_2O	0.05	0.02	A	0.01	170	24	300 µL HNO_3 cc

47	12.5 mL H_2O	0.05	0.02	A	0.01	170	24	100 µL HNO_3 cc
48	12.5 mL H_2O	0.05	0.02	A	0.01	170	24	50 µL HNO_3 cc
49	12.5 mL H_2O	0.05	0.02	A	0.01	170	24	300 µL AcOH cc
50	12.5 mL H_2O	0.05	0.02	A	0.01	170	24	100 µL AcOH cc
51	12.5 mL H_2O	0.05	0.02	A	0.01	170	24	50 µL AcOH cc

Stock solutions of the linkers were prepared in the following concentrations: 0.0042 M for H_2O; 0.0085 M for EtOH. A = indium (III) acetate; N = indium (III) nitrate hexahydrate ; C = indium (III) chloride tetrahydrate; F = indium (III) fluoride; AC = indium (III) acetylacetonate; AcOH = acetic acid; Aging = the linker and the iridium salt were left stirring in water at room temperature for 24 hours; the indium salt was added afterwards, and the solution was heated up to the specified temperature for each case.

7.3.1.2. Characterization of InIrPF-13

As already mentioned before, the hydrothermal reaction of iridium chloride, indium acetate and 2,5-H_2PDC at 170 ºC resulted in the formation of a crystalline product, InIrPF-13.

Single-crystal X-ray diffraction (SCXRD) analysis confirmed the formation of an extended framework through the coordination of both indium and iridium atoms to the 2,5-H_2PDC linkers. The new MOF, InIrPF-13, crystallizes in the orthorhombic space group *Cmc2₁* with cell parameters a = 25.6795(12) Å, b = 23.9298(11), c = 9.8205(5), and cell volume 6034.6(5) $Å^3$ (full crystallographic parameters and refinement data are provided in Table 7.3).

Table 7.3. Crystallographic parameters and refinement data for InIrPF-13.

Crystallographic parameters	InIrPF-13
Empirical formula	$C_{42}H_{18}Cl_{0.5}In_{2.21}Ir_2N_6O_{28.21}$
Formula weight (g/mol)	1713.86
Crystal system	Orthorhombic
Space group	*Cmc*2$_1$
a (Å)	25.6795(12)
b (Å)	23.9298(11)
c (Å)	9.8202(5)
α (º)	90
β (º)	90
γ (º)	90
Volume (Å^3)	6034.6(5)
Z	4
Calculated density (g/cm^3)	1.886
Absorption coefficient (mm^{-1})	15.959
F(000)	3234.0
Radiation	CuKα (λ = 1.54178)
2θ range for data collection (º)	5.048 to 130.204
Index ranges	-30 ≤ h ≤ 27, -25 ≤ k ≤ 28, -11 ≤ l ≤ 11
Reflections collected	27820
Independent reflections	5197 [Rint = 0.0309, Rsigma = 0.0218]
Data/restraints/parameters	5197/0/406
Goodness-of-fit on F^2	1.056
Final R indexes [I>2σ (I)]	R1 = 0.0300, wR2 = 0.0798
Final R indexes [all data]	R1 = 0.0310, wR2 = 0.0808
Largest diff. peak/hole (e·Å^{-3})	0.7/-0.66
Flack parameter	0.368(17)

In this structure, the metals generate two independent SBUs with different geometry. On one hand, the iridium atoms form an inorganic SBU with formula $[IrN_3(\text{-}COO)_3]$ by bonding via N- and O-heterochelation to three linker molecules in an octahedral geometry (Figure 7.17). On the other hand, the indium atoms generate trimers with formula $[In_3(OH)_2(\text{-}COO_2)_6]_\infty$ that are formed by μ-O vertex-sharing indium octahedra (Figure 7.17). These trimers are further bridged by carboxylic groups, forming zig-zag chains. A careful analysis of the X-ray diffraction data reveals that only the central indium atom (labeled as In2 in Figure 7.17) is fully occupied; the other two atoms (In1 and In3) are partially occupied, and the free refinement of their occupancy factor resulted in a significant improvement of the residual values, with final occupancy values of 72% for In1 and 48% for In3. This occupational disorder of the metal atoms is also accompanied by positional disorder of the carboxylic oxygen atoms involved in their coordination. Despite the intrinsically defective nature of the structure, as at least one indium atom is always present in the trimer, the formation of an extended framework is ensured. In addition, a chlorine atom was identified near this trimer, also with partial occupancy (50%), as well as water molecules. The combination of both SBUs and the organic linker leads to a heterometallic layered coordination framework (Figure 7.18). The layers are stacked forming hydrogen bonds, generating oval-shaped channels filled with water molecules. The formula obtained from the single-crystal X-ray data analysis is $Ir_2In_{2.2}(2,5\text{-}PDC)_6Cl_{0.5}(H_2O)_{4.2}$.

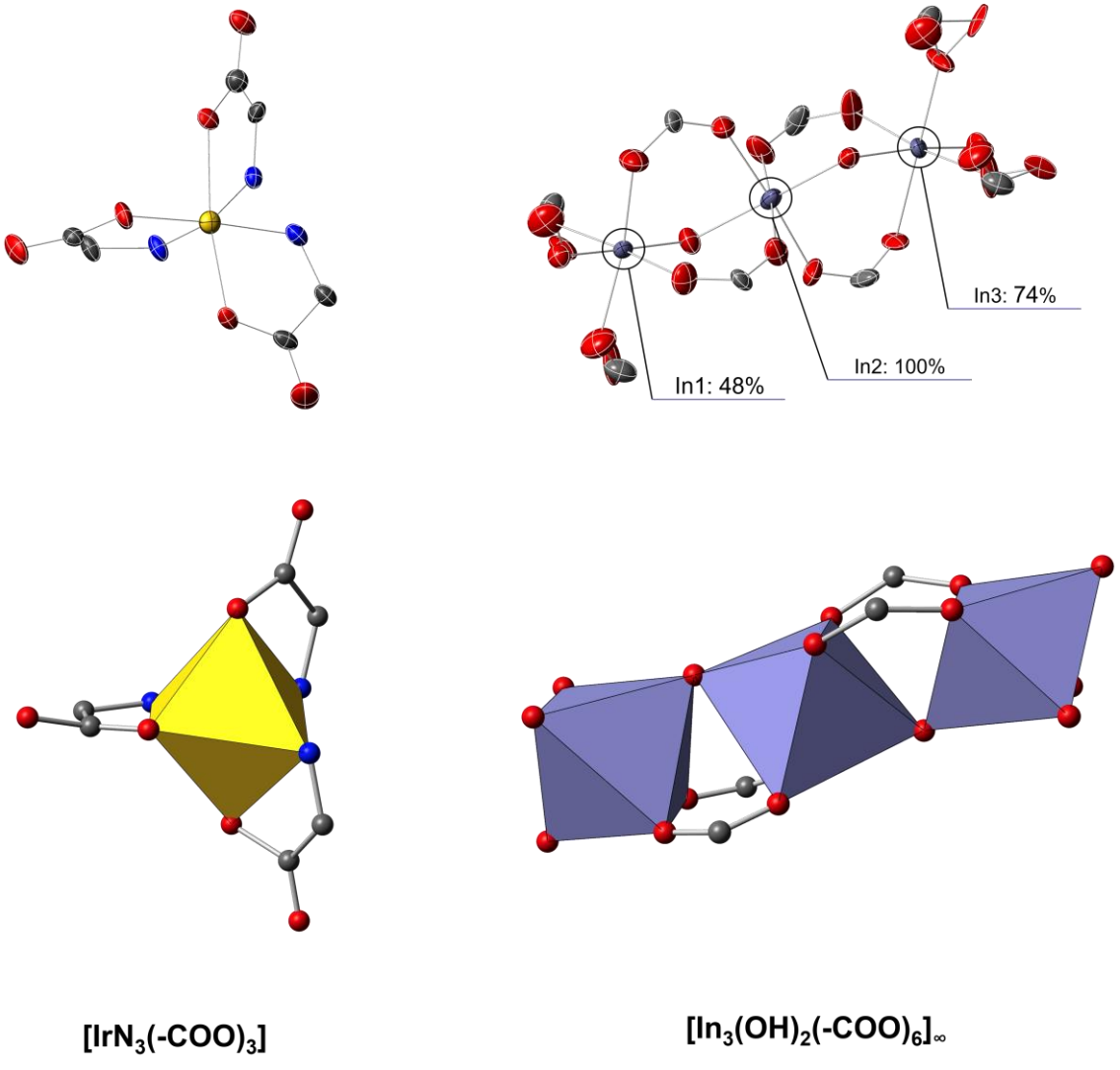

Figure 7.17. Ir- and In-based SBUs of InIrPF-13. Ir atoms are displayed in gold, In in purple, O in red, C in grey, N in blue. H atoms were omitted for clarity.

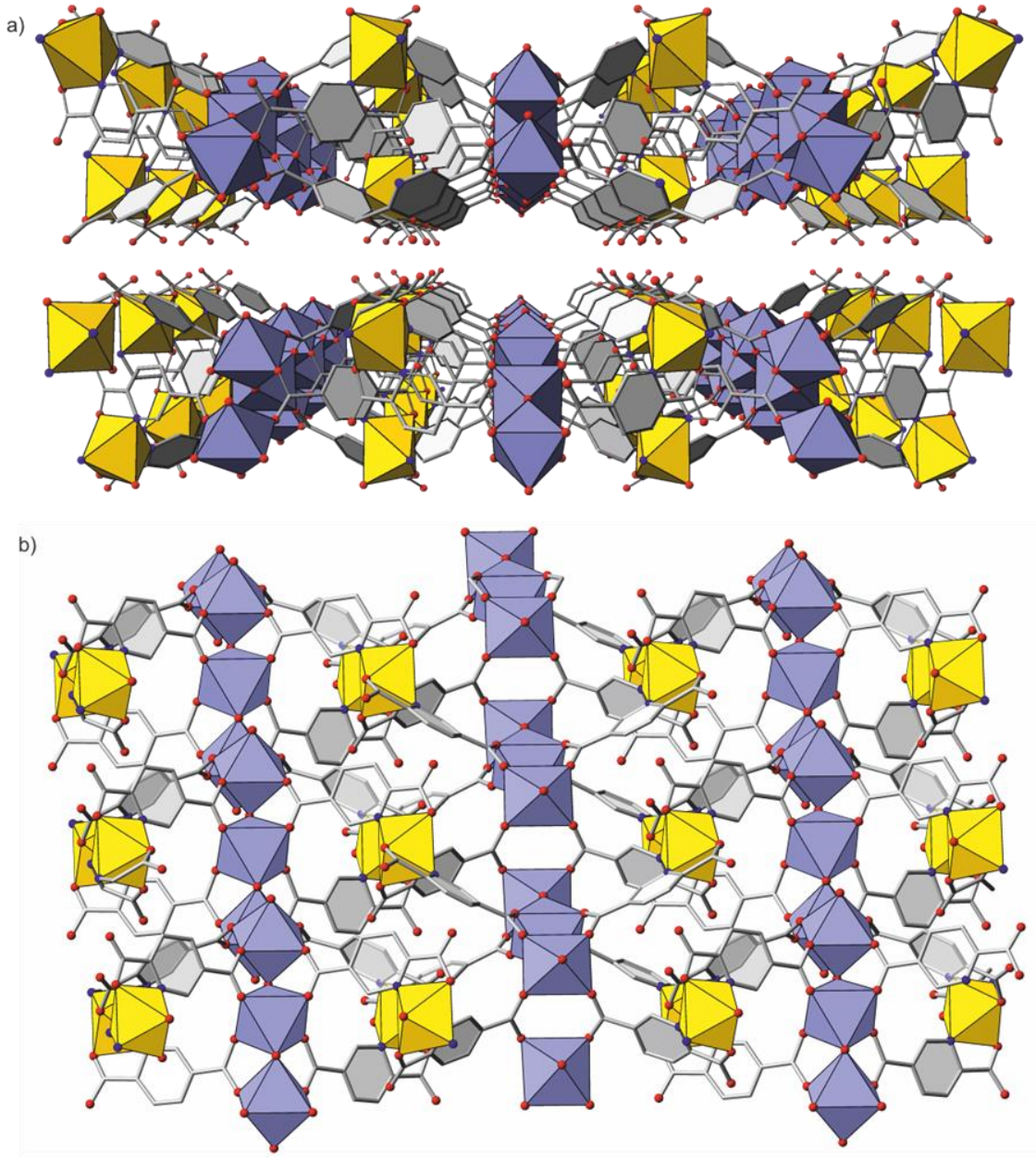

Figure 7.18. Polyhedral representation of the crystal structure of InIrPF-13. Gold and violet polyhedra represent Ir and In atoms, respectively; O and N atoms are red and blue spheres, respectively; C atoms are shown as grey sticks. H atoms were omitted for clarity. **a)** View of the structure along the *c* axis showing the two-dimensional structure, and the oval shaped channels formed in the interlayer space. Occluded water molecules are omitted for clarity **b)** Top view of one of the layers, showing the connection between the two types of SBUs.

A SEM-EDX analysis was carried out to check the ratios between the metals. A total of 27 analyses were performed on individual crystals of 9 different samples, finding In:Ir ratios between 1.5 and 1.0, with an average of 1.2, being this value also the most frequently recorded in all the samples. A non-defective structure would have a 1.5 ratio. This variability in the indium content is another evidence of the intrinsically defective nature of the In SBU in the MOF.

As mentioned in the previous section of this chapter, it was not possible to isolate this MOF as pure phase, given that a competing phase always appeared in the bulk of the samples. The experimental PXRD pattern of InIrPF-13 matches the simulated pattern from the SCXRD data (Figure 7.19); however, it displays some additional peaks that can be assigned to another competing phase, in this case, an already reported In-MOF based on the same organic linker, $[In(OH)(2,5\text{-}PDC)]_n$ (CCDC number 659856).[61] Further confirmation of the presence of this In-based MOF in the bulk of the samples was obtained through SEM-EDX: there is a coexistence of elliptical prism-shaped crystals corresponding to InIrPF-13 with presence of both metals, and spherical aggregates of $[In(OH)(2,5\text{-}PDC)]_n$ that contain only indium (Figure 7.20).

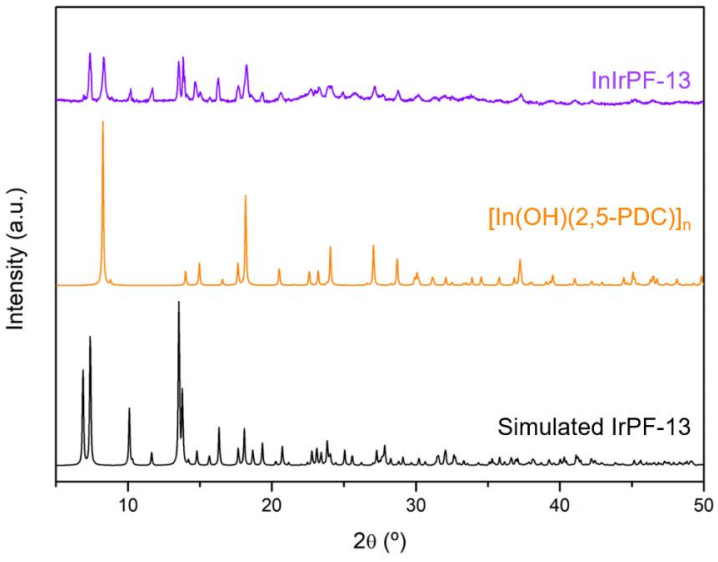

Figure 7.19. PXRD patterns of InIrPF-13 (purple) and $[In(OH)(2,5\text{-}PDC)]_n$ (orange).

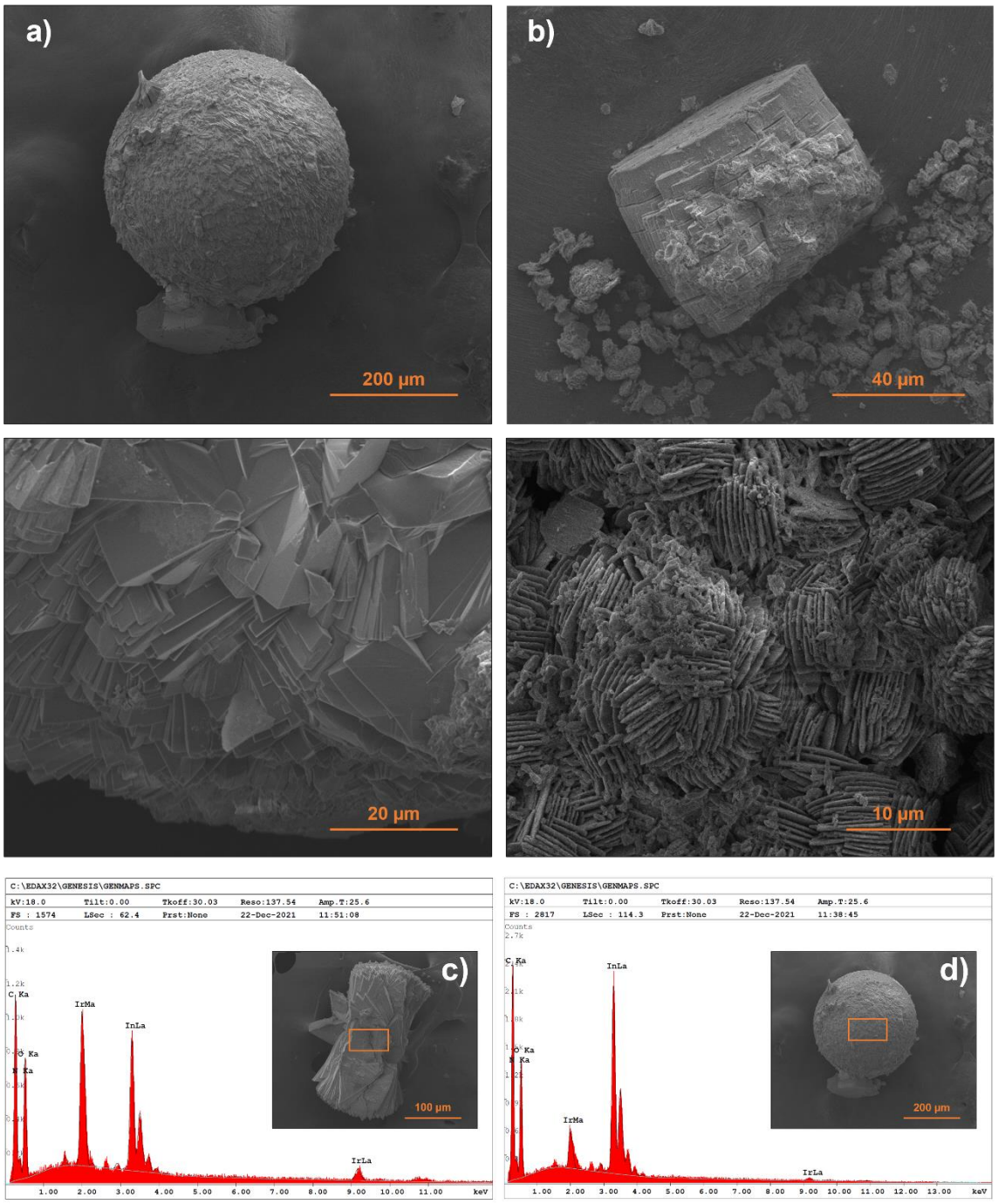

Figure 7.20. SEM images of **a)** a spherical aggregate and a close-up of crystals of $[In(OH)(2,5\text{-}PDC)]_n$, **b)** an individual crystal of InIrPF-13 covered in aggregates of small particles of $[In(OH)(2,5\text{-}PDC)]_n$ and a close-up of the particles. EDX spectrum of **c)** an individual crystal of InIrPF-13 and **d)** $[In(OH)(2,5\text{-}PDC)]_n$, both present in the bulk of the same sample. For InIrPF-13, the ratio between In and Ir is 1.5.

We tried to optimize the synthesis of the MOF in order to avoid the formation of the In-based phase (screening of conditions displayed in Tables 1-2). The first parameters that were modified were the temperature, the reaction time, and the In:Ir:linker ratio, but slight changes in these parameters did not yield pure InIrPF-13. Changes in the solvent or in the In precursor also generated a phase mixture. To test whether a much shorter reaction time would prevent the other phase from forming, a synthesis experiment was performed with only 3 hours of heating. The PXRD of the sample shows the formation of a mixture of $In(OH)_3$ and low crystallinity $[In(OH)(2,5\text{-}PDC)]_n$, suggesting that it is a kinetically favored phase (Figure 7.21). Using an acidic modulator, specifically acetic and nitric acid, to shift the dissociation equilibrium of the indium precursor also yielded a phase mixture of InIrPF-13 and $[In(OH)(2,5\text{-}PDC)]_n$. We also carried out aging experiments by first mixing the Ir salt with the linker for one day, and after that adding the In salt and heating up the reaction mixture. We hoped that this would avoid the competition between In and Ir as it would favor the coordination of the Ir atoms to the linker; however, this was not the case as the result of the experiment was a phase mixture. The 2,5-PDC linker does not display a high solubility in water, so we gravitated towards using stock solutions of each element of the synthesis in order to assure a homogeneous starting solution, and also to prevent the In atoms from reacting with the linker faster than the Ir ones. This strategy was not fruitful as it also yielded a phase mixture.

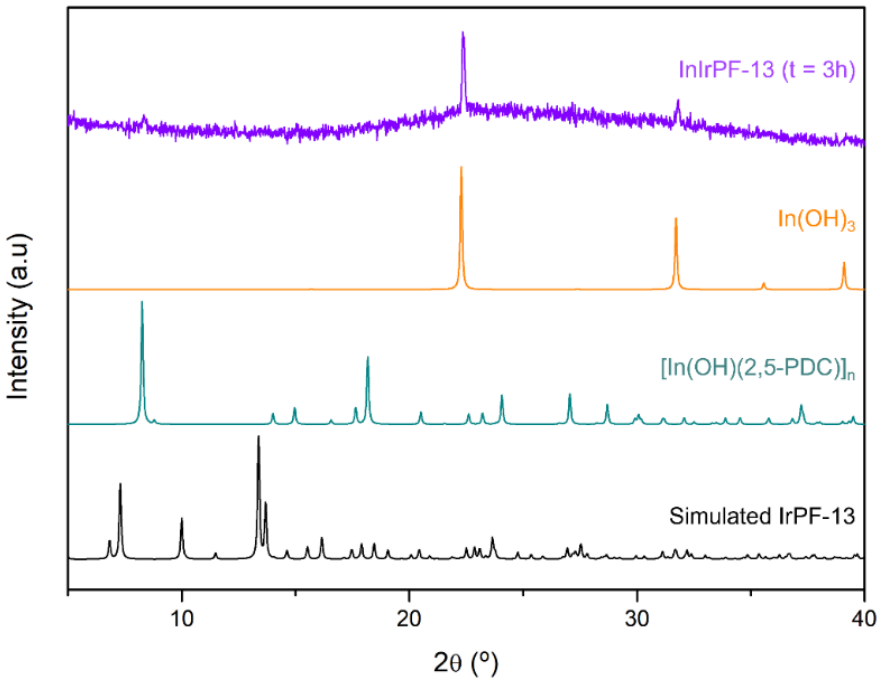

Figure 7.21. PXRD patterns of InIrPF-13 synthesized in 3h (purple), $In(OH)_3$ (orange) and $[In(OH)(2,5\text{-}PDC)]_n$ (teal).

7.3.2. ScIrPF-13

Given that Ir was already reticulated into a new framework and the only inconvenience was the phase competition with the other In-based MOF, the most straightforward approach was to shift towards other trivalent metals that would substitute the indium ions in the framework, and a feasible candidate was scandium. It is the smallest and least basic rare-earth element, with a strong oxyphilic character for Sc^{3+}, as it tends to coordinate to hard donor atoms like O atoms from carboxylate groups. In a similar way to indium, it usually generates highly robust and stable frameworks.[65] Moreover, there are examples of isostructural MOFs reported with indium or scandium,[55,66] as well as MOFs with SBUs comprised of scandium trimers and chains.[67,68] Bearing this in mind, the strategy of using scandium instead of indium was successful, and the combination of iridium chloride, scandium nitrate and 2,5-H_2PDC in water lead to the formation of a compound isostructural to InIrPF-13.

7.3.2.1. Synthesis of ScIrPF-13

All reagents and solvents employed were commercially available and used as received without further purification: 2,5-pyridinedicarboxilic acid, 2,5-H_2PDC (>98%, TCI); iridium(III) chloride hydrate, $IrCl_3 \times nH_2O$ (99.8%, Alfa Aesar); scandium nitrate pentahydrate, $Sc(NO_3)_3 \times 5H_2O$ (99.9%, Strem Chemicals).

2,5-PDC (0.32 mmol, 54.6 mg), $Sc(NO_3)_3 \times 5H_2O$ (0.08 mmol, 25.7 mg), and $IrCl_3 \times nH_2O$ (0.08 mmol, 24.0 mg) were dissolved in 13 mL of deionized water. The ratio between the linker, $Sc(NO_3)_3 \times 5H_2O$ and $IrCl_3 \times nH_2O$ is 4:1:1. The mixture was placed in a 50 mL Teflon-lined steel autoclave and heated during 24 hours in an oven at 170 °C. After cooling to room temperature, the yellow crystals were washed with water (3x10 mL).

7.3.2.2. Characterization of ScIrPF-13

Single-crystal X-ray diffraction (SCXRD) analysis confirmed the formation of an isostructural framework to InIrPF-13, with cell parameters a = 25.4624(5) Å, b = 24.3673(5), c = 9.7884(2), and cell volume 6073.2(2) $Å^3$. The full crystallographic parameters and the refinement data are displayed in Table 7.4. The refinement of the occupancies factors of the Sc atoms in the trimers resulted in a similar situation to that of the In trimers; however, in this case, the Sc SBUs are mostly fully occupied for the analyzed crystal, as the best residual values were obtained for occupancy factors of 89% and 91% for Sc1 and Sc3, respectively (Figure 7.22). This structure did not show presence of chlorine atoms; therefore, hydroxyl groups must be present to compensate the charges and assure charge neutrality. The exact positions of the corresponding hydrogen atoms could not be determined from the difference in the electron density maps, but it seems reasonable to assume that these are located near the two bridging O atoms, as well as near

the terminal O with a partial occupancy. The formula derived from the SCXRD refinement is $Ir_2Sc_{2.8}(2,5\text{-PDC})_6(OH)_{2.4}(H_2O)_{4.4}$.

Table 7.4. Crystallographic parameters and refinement data for ScIrPF-13.

Crystallographic parameters	ScIrPF-13
Empirical formula	$C_{42}H_{18}Sc_{2.8}Ir_2N_6O_{28.8}$
Formula weight (g/mol)	1577.56
Crystal system	Orthorhombic
Space group	*Cmc*2$_1$
a (Å)	25.4624(5)
b (Å)	24.3673(5)
c (Å)	9.7884(2)
α (º)	90
β (º)	90
γ (º)	90
Volume (Å^3)	6073.2(2)
Z	4
Calculated density (g/cm^3)	1.725
Absorption coefficient (mm^{-1})	11.602
F(000)	3021.0
Radiation	CuKα (λ = 1.54178)
2θ range for data collection (º)	5.02 to 130.224
Index ranges	$-29 \leq h \leq 29$, $-28 \leq k \leq 26$, $-11 \leq l \leq 11$
Reflections collected	17162
Independent reflections	5003 [R_{int} = 0.0304, R_{sigma} = 0.0273]
Data/restraints/parameters	5003/97/388
Goodness-of-fit on F^2	1.087
Final R indexes [I>2σ (I)]	R_1 = 0.0327, wR_2 = 0.0761
Final R indexes [all data]	R_1 = 0.0369, wR_2 = 0.0784
Largest diff. peak/hole (e·Å^{-3})	1.29/-0.86
Flack parameter	0.47(2)

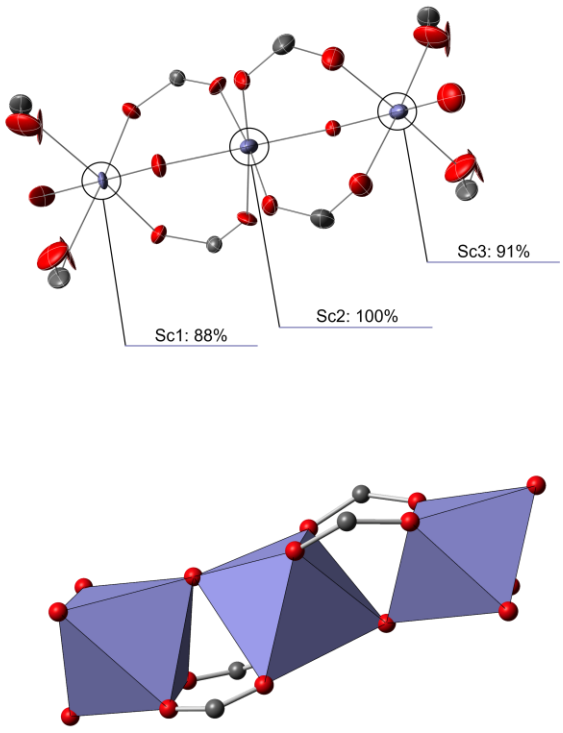

Figure 7.22. Sc-based SBU of ScIrPF-13. Ir atoms are displayed in gold, Sc in purple, O in red, C in grey, N in blue. H atoms were omitted for clarity.

A SEM-EDX study was conducted to confirm the ratio between the metals and to check the purity of the sample. Only elliptical prism-shaped crystals corresponding to ScIrPF-13 were observed in the sample (Figure 7.23). From a total of 14 analyses, the average Sc:Ir ratio was determined to be 1.2. This confirms the presence of metal-site vacancies in this inherently defective SBU also when using scandium.

The experimental PXRD pattern of the sample was recorded as a complementary validation of its purity. The data is displayed in Figure 7.24, and it shows no presence of any other crystalline compound.

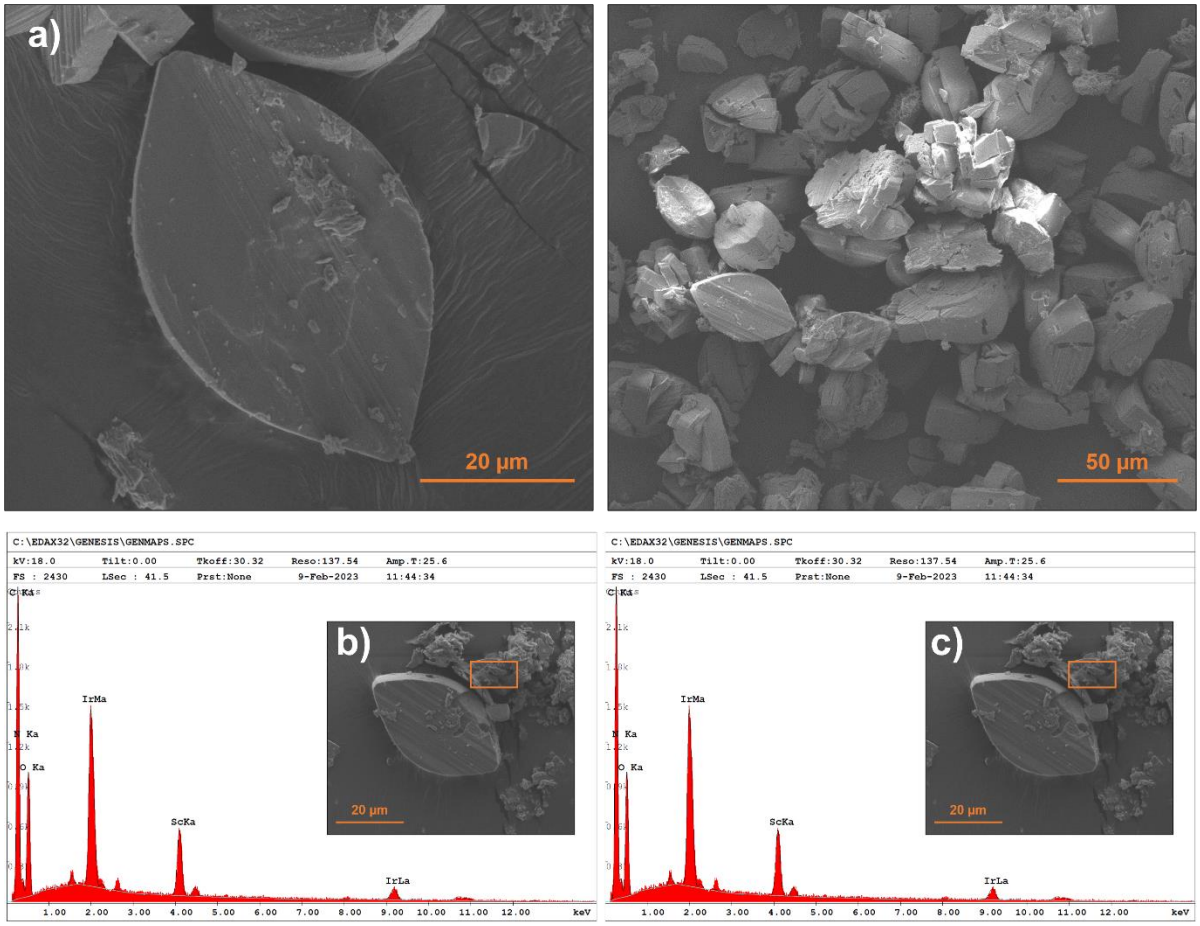

Figure 7.23. SEM images of **a)** an individual crystal of ScIr-PF-13 of the bulk of the sample. EDX spectrum of **b)** an individual crystal and **c)** an aggregate of particles of ScIrPF-13. In both cases, the ratio between Sc and Ir is 1.3, therefore in this sample there is no phase coexistence.

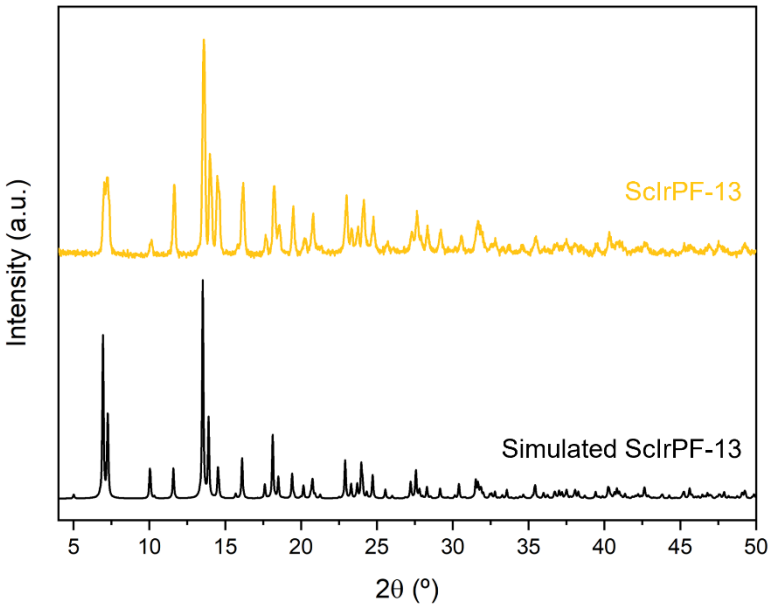

Figure 7.24. PXRD pattern of experimental ScIrPF-13 (gold) compared to the simulated pattern from the SCXRD data (black).

As this MOF was obtained as a pure phase, we carried out its complete bulk chemical characterization. Firstly, the results of the CHN elemental analysis are shown in Table 7.5. The experimental data matches the CHN percentages estimated from the formula of the MOF derived from the SCXRD data ($Ir_2Sc_{2.8}$(2,5-PDC)$_6(OH)_{2.4}(H_2O)_{4.4}$).

Table 7.5. EA results for ScIrPF-13.

	Calculated CHN			Experimental CHN		
ScIrPF-13	%C	%H	%N	%C	%H	%N
	31.742	1.856	5.290	33.167	1.765	5.768

The stability of the MOF (activated under vacuum overnight) was studied through thermogravimetric analysis (TGA). The TGA plot (Figure 7.25) displays one weight loss of 11.42% at around 60-100 ºC, corresponding to the loss of water molecules adsorbed in the pores of the MOF, and the total decomposition of the framework occurs at 440 ºC in only one step, which is equivalent to a 56.34% weight loss. The total degradation of the

MOF resulted in a mixture of scandium(III) oxide (Sc_2O_3) and iridium(IV) oxide (IrO_2), as evidenced by PXRD (Figure 7.26).

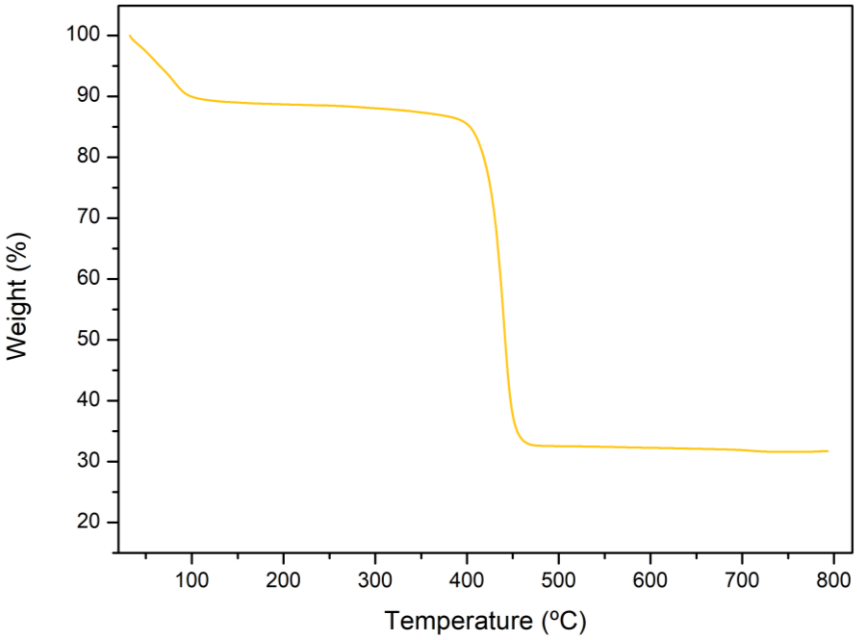

Figure 7.25. TGA plot of ScIrPF-13.

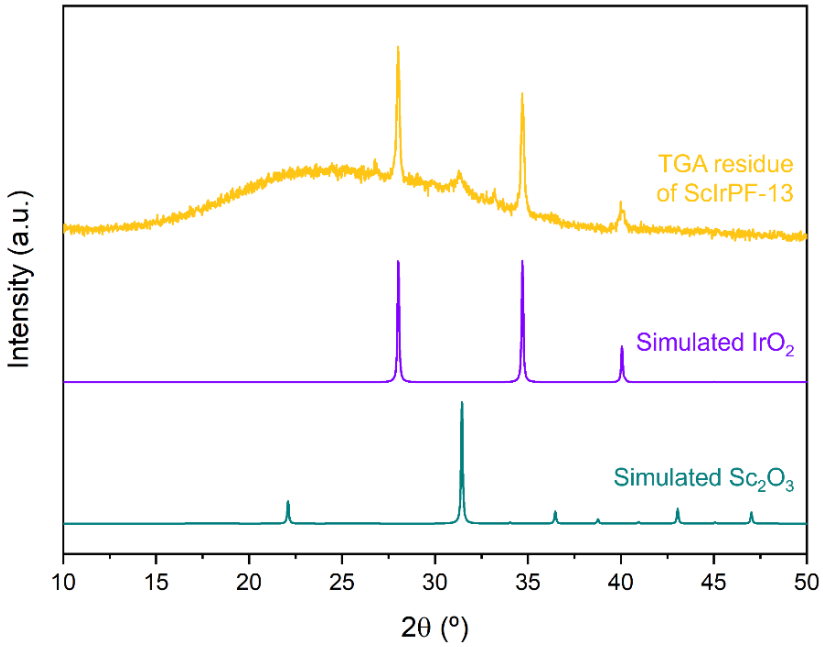

Figure 7.26. PXRD patterns of the residue from the TG analysis of ScIrPF-13 (gold), simulated IrO_2 (purple) and simulated Sc_2O_3 (teal).

Regarding the UV-Visible spectrum, ScIrPF-13 display a wide absorption range (200-500 nm^{-1}), which implies that this MOF is more suited for photocatalysis (Figure 7.27).

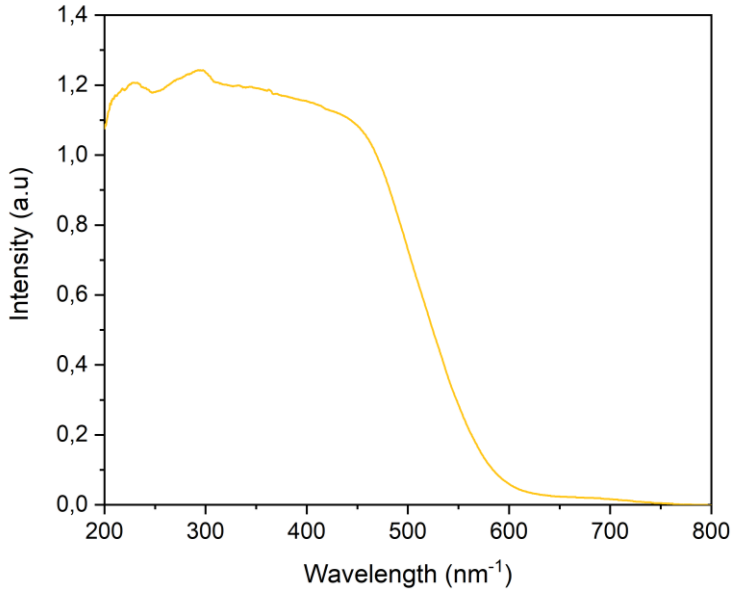

Figure 7.27. UV-Vis absorbance spectrum of ScIrPF-13.

The textural properties of ScIrPF-13 were evaluated through N_2 sorption at 77K. The activation of the material prior to the measurement was completed by heating it under vacuum at 100 ºC overnight. The resulting isotherm is shown in Figure 7.28, and it displays a profile characteristic of layered materials with intercalated molecules.[69] The accessible surface area was calculated using the Brunauer–Emmett–Teller (BET) model, yielding a value of 24 m^2/g.[69]

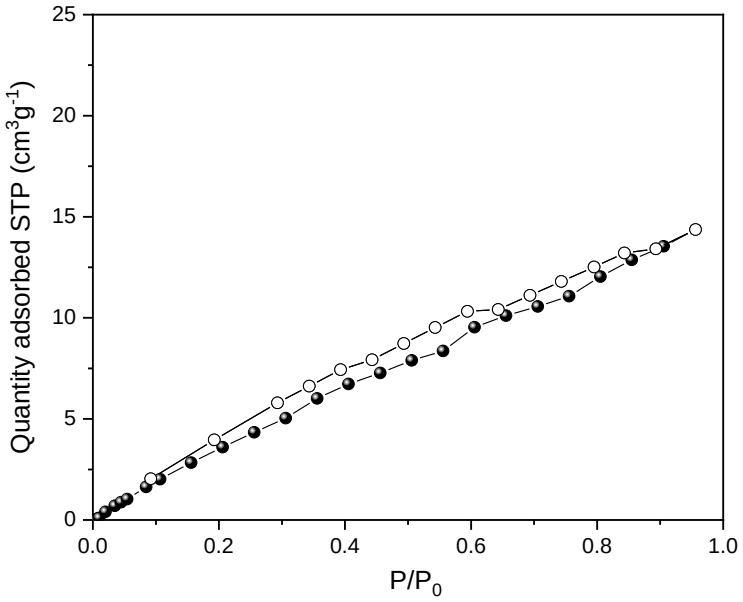

Figure 7.28. Adsorption-desorption isotherm of ScIrPF-13. Filled and hollow circles represent adsorption and desorption points, respectively.

7.3.2.3. Catalytic performance of ScIrPF-13

Upon successfully obtaining the novel iridium MOF, ScIrPF-13, we moved towards proving that this material is a feasible candidate to be used as a heterogeneous catalyst, and thus evidencing the activity of the reticulated iridium sites. We decided to investigate the photocatalytic activity of the ScIrPF-13 under irradiation with visible light. Iridium(III) complexes are receiving increasing attention as sensitizers in numerous light-induced photoredox catalytic transformations due to the broad range of potentials that they might exhibit through linker modification.[70–72] As a demonstration of the suitability of ScIrPF-13 as a photoredox heterogeneous catalyst, we investigated its use in the photooxidation of sulfides. Thus, in presence of 2 mol% of the catalyst (based on Ir), the model substrate methylphenylsulfide was quantitatively and selectively oxidized to the

corresponding sulfoxide under irradiation with blue light, at room temperature, after 20 hours and in a O_2 atmosphere (Table 7.6). Remarkably, the catalyst was easily recovered and could be reused in up to 6 consecutive cycles with no significant loss of activity nor selectivity. Moreover, the PXRD pattern of the recovered catalyst (Figure 7.29) demonstrates that the structure is preserved after the catalysis cycles. The photocatalytic activity of the MOF was further evaluated with other substituted sulfides. Thus, p-tolylmethylsulfide and 4-chlorophenylmethylsulfide were also fully oxidized to their corresponding sulfoxides, after reaction times of 28 and 36 hours, respectively. We also tested the ability of ScIrP-13 to photooxidize the toxic sulfur mustard simulant 2-(chloroethyl)ethylsulfide,[73] again obtaining quantitatively less toxic sulfoxide in a reaction time of 20 hours.

To investigate the nature of the reactive oxygen species (ROS) involved in the photooxidation process, a series of experiments were carried out in presence of different scavenger species. In particular, when in presence of *p*-benzoquinone (BQ), more than 75% conversion was achieved, while when 1,4-diazabicyclo[2.2.2]octane (DABCO) was present, the conversion drastically dropped to less than 5%, clearly indicating that $^1O_2$ is the most important ROS generated.[74] Moreover, the presence of electron and hole scavengers, namely copper sulfate and potassium iodide, respectively, also resulted in a drastic inhibition of the reaction (< 5% conversion) indicating the critical role of the charge separation process initiated by ScIrP-13 in the photooxidation process.

Table 7.6. Photooxidation of sulfides with ScIrPF-13[a]

Sulfide	Time (h)	Conversion (%)	Selectivity to sulfoxide (%)
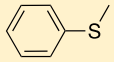	20	> 99	100
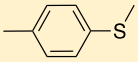	28	> 99	100
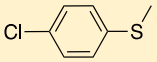	36	> 99	100
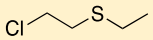	20	> 99	100
Scavenger tests[b]			
$CuSO_4$	20	2	
KI	20	2	
BQ	20	76	
DABCO	20	3	
Cyclability tests[b]			
Cycle 1	20	100	99
Cycle 2	20	97	99
Cycle 3	20	96	99
Cycle 4	20	95	99
Cycle 5	20	95	99
Cycle 6	20	94	99

[a]Photooxidation conditions: sulfide (0.135 mmol), catalyst (2 mol% Ir), acetonitrile (0.5 mL), irradiated with blue LED light (2x30W) at RT in a O_2 (balloon) atmosphere.

[b]Carried out with methylphenylsulfide.

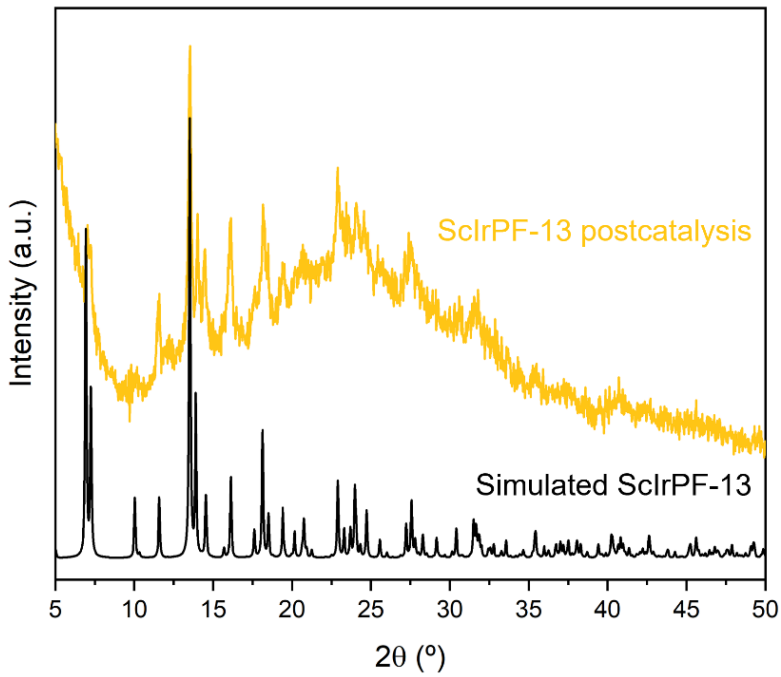

Figure 7.29. PXRD pattern of ScIrPF-13 postcatalysis (gold), compared to the simulated plot from the SCXRD data (black).

7.4. Conclusions

In summary, we here demonstrated, for the first time, the feasibility of synthesizing metal-organic frameworks with iridium as a structural chemical building component. Our multi-metal-based approach paves the way to extend the field of reticular chemistry to previously unexplored metal elements, incorporating new active metal sites and expanding the range of reactivity achievable with MOFs. We anticipate that this approach will be instrumental in obtaining other frameworks with diverse chemical and pore environments, specifically tailored to exploit the activity of these high-value metal elements in the future.

The results of this chapter have been summarized in a manuscript, which has been already submitted for publication and it is currently under revision. A preprint of the paper can be accessed at: 10.26434/chemrxiv-2023-cbm9z.

7.5. References

(1) Li, Y.; Huang, B.; Zhang, X.; Ding, J.; Zhang, Y.; Xiao, L.; Wang, B.; Cheng, Q.; Huang, G.; Zhang, H.; Yang, Y.; Qi, X.; Zheng, Q.; Zhang, Y.; Qiu, X.; Liang, M.; Zhou, H. Lifetime over 10000 Hours for Organic Solar Cells with Ir/IrOx Electron-Transporting Layer. *Nat Commun* **2023**, *14* (1), 1241. https://doi.org/10.1038/s41467-023-36937-8.

(2) Ma, D.; Tsuboi, T.; Qiu, Y.; Duan, L. Recent Progress in Ionic Iridium(III) Complexes for Organic Electronic Devices. *Advanced Materials* **2017**, *29* (3). https://doi.org/10.1002/adma.201603253.

(3) Ma, D. L.; Wu, C.; Tang, W.; Gupta, A. R.; Lee, F. W.; Li, G.; Leung, C. H. Recent Advances in Iridium(III) Complex-Assisted Nanomaterials for Biological Applications. *J Mater Chem B* **2018**, *6* (4), 537–544. https://doi.org/10.1039/c7tb02859h.

(4) Gou, Y.; Huang, G. J.; Li, J.; Yang, F.; Liang, H. Versatile Delivery Systems for Non-Platinum Metal-Based Anticancer Therapeutic Agents. *Coord Chem Rev* **2021**, *441*, 213975. https://doi.org/10.1016/j.ccr.2021.213975.

(5) Shi, H.; Wang, Y.; Lin, S.; Lou, J.; Zhang, Q. Recent Development and Application of Cyclometalated Iridium(Iii) Complexes as Chemical and Biological Probes. *Dalton Transactions* **2021**, *50* (19), 6410–6417. https://doi.org/10.1039/d1dt00592h.

(6) Brown, A. L.; Winter, H.; Goforth, A. M.; Sahay, G.; Sun, C. Facile Synthesis of Ligand-Free Iridium Nanoparticles and Their In Vitro Biocompatibility. *Nanoscale Res Lett* **2018**, *13*. https://doi.org/10.1186/s11671-018-2621-3.

(7) Platero Prats, A. E.; de la Peña-O'Shea, V. A.; Iglesias, M.; Snejko, N.; Monge, Á.; Gutiérrez-Puebla, E. Heterogeneous Catalysis with Alkaline-Earth Metal-Based MOFs:

A Green Calcium Catalyst. *ChemCatChem* **2010**, *2* (2), 147–149. https://doi.org/10.1002/cctc.200900228.

(8) Li, P.; Vermeulen, N. A.; Malliakas, C. D.; Gómez-Gualdrón, D. A.; Howarth, A. J.; Mehdi, B. L.; Dohnalkova, A.; Browning, N. D.; O'Keeffe, M.; Farha, O. K. Bottom-up Construction of a Superstructure in a Porous Uranium-Organic Crystal. *Science* **2017**, *356* (6338), 624–627. https://doi.org/10.1126/science.aam7851.

(9) Kalmutzki, M. J.; Hanikel, N.; Yaghi, O. M. Secondary Building Units as the Turning Point in the Development of the Reticular Chemistry of MOFs. *Sci Adv* **2018**, *4* (10). https://doi.org/10.1126/sciadv.aat9180.

(10) Yusuf, V. F.; Malek, N. I.; Kailasa, S. K. Review on Metal-Organic Framework Classification, Synthetic Approaches, and Influencing Factors: Applications in Energy, Drug Delivery, and Wastewater Treatment. *ACS Omega* **2022**, *7* (49), 44507–44531. https://doi.org/10.1021/acsomega.2c05310.

(11) Wang, C.; Xie, Z.; Dekrafft, K. E.; Lin, W. Doping Metal-Organic Frameworks for Water Oxidation, Carbon Dioxide Reduction, and Organic Photocatalysis. *J Am Chem Soc* **2011**, *133* (34), 13445–13454. https://doi.org/10.1021/ja203564w.

(12) Jiang, Q.; Xu, J.; Li, Z.; Zhou, C.; Chen, X.; Meng, H.; Han, Y.; Shi, X.; Zhan, C.; Zhang, Y.; Zhang, Q.; Jia, X.; Zhang, R. Two-Dimensional Metal-Organic Framework Nanosheet Supported Noble Metal Nanocrystals for High-Efficiency Water Oxidation. *Adv Mater Interfaces* **2021**, *8* (5), 1–10. https://doi.org/10.1002/admi.202002034.

(13) Chang, T. E.; Chuang, C. H.; Chen, Y. H.; Wang, Y. C.; Gu, Y. J.; Kung, C. W. Iridium-Functionalized Metal-Organic Framework Nanocrystals Interconnected by Carbon Nanotubes Competent for Electrocatalytic Water Oxidation. *ChemCatChem* **2022**, *14* (15). https://doi.org/10.1002/cctc.202200199.

(14) Liao, C. H.; Fan, K.; Bao, S. S.; Fan, H.; Wang, X. Z.; Hu, Z.; Kurmoo, M.; Zheng, L. M. From a Layered Iridium(Iii)-Cobalt(Ii) Organophosphonate to an Efficient Oxygen-Evolution-Reaction Electrocatalyst. *Chemical Communications* **2019**, *55* (92), 13920–13923. https://doi.org/10.1039/c9cc06164a.

(15) Perumal, S.; Lim, T.; Seenivasan, S.; Seo, J. Electrocatalytic Oxygen Evolution Reaction at IrOx Supported by Ni/Co-ZIF-67: Controlled Ratio of Metallic Ir and Ir3+ States. *Appl Surf Sci* **2022**, *604* (August), 154553. https://doi.org/10.1016/j.apsusc.2022.154553.

(16) Zhao, Y.; Zhang, S.; Wang, M.; Han, J.; Wang, H.; Li, Z.; Liu, X. Engineering Iridium-Based Metal Organic Frameworks towards Electrocatalytic Water Oxidation. *Dalton Transactions* **2018**, *47* (13), 4646–4652. https://doi.org/10.1039/c8dt00485d.

(17) Mo, Q.; Zhang, L.; Li, S.; Song, H.; Fan, Y.; Su, C. Y. Engineering Single-Atom Sites into Pore-Confined Nanospaces of Porphyrinic Metal-Organic Frameworks for the Highly Efficient Photocatalytic Hydrogen Evolution Reaction. *J Am Chem Soc* **2022**, *144* (49), 22747–22758. https://doi.org/10.1021/jacs.2c10801.

(18) Hao, Y. C.; Chen, L. W.; Li, J.; Guo, Y.; Su, X.; Shu, M.; Zhang, Q.; Gao, W. Y.; Li, S.; Yu, Z. L.; Gu, L.; Feng, X.; Yin, A. X.; Si, R.; Zhang, Y. W.; Wang, B.; Yan, C. H. Metal-Organic Framework Membranes with Single-Atomic Centers for Photocatalytic CO2 and O2 Reduction. *Nat Commun* **2021**, *12* (1), 1–11. https://doi.org/10.1038/s41467-021-22991-7.

(19) Gumbo, M.; Makhubela, B. C. E.; Mehlana, G. Two Novel Metal-Organic Frameworks Functionalised with Pentamethylcyclopentadienyl Iridium(Iii) Chloride for Catalytic Conversion of Carbon Dioxide to Formate. *Dalton Transactions* **2023**, 6501–6514. https://doi.org/10.1039/d3dt00635b.

(20) Chen, C.; Mo, Q.; Fu, J.; Yang, Q.; Zhang, L.; Su, C. Y. PtCu@Ir-PCN-222: Synergistic Catalysis of Bimetallic PtCu Nanowires in Hydrosilane-Concentrated Interspaces of an Iridium(III)-Porphyrin-Based Metal-Organic Framework. *ACS Catal* **2022**, No. Iii, 3604–3614. https://doi.org/10.1021/acscatal.1c05922.

(21) Abednatanzi, S.; Derakhshandeh, P. G.; Abbasi, A.; Van Der Voort, P.; Leus, K. Direct Synthesis of an Iridium(III) Bipyridine Metal–Organic Framework as a Heterogeneous Catalyst for Aerobic Alcohol Oxidation. *ChemCatChem* **2016**, *8* (23), 3672–3679. https://doi.org/10.1002/cctc.201600985.

(22) Babucci, M.; Conley, E. T.; Hoffman, A. S.; Bare, S. R.; Gates, B. C. Iridium Pair Sites Anchored to Zr6O8 Nodes of the Metal–Organic Framework UiO-66 Catalyze Ethylene Hydrogenation. *J Catal* **2022**, *411*, 177–186. https://doi.org/10.1016/j.jcat.2022.04.003.

(23) Yang, D.; Gaggioli, C. A.; Conley, E.; Babucci, M.; Gagliardi, L.; Gates, B. C. Synthesis and Characterization of Tetrairidium Clusters in the Metal Organic Framework UiO-67: Catalyst for Ethylene Hydrogenation. *J Catal* **2020**, *382*, 165–172. https://doi.org/10.1016/j.jcat.2019.11.031.

(24) Perlata, R. A.; Huxley, M. T.; Shi, Z.; Zhang, Y. B.; Sumby, C. J.; Doonan, C. J. A Metal-Organic Framework Supported Iridium Catalyst for the Gas Phase Hydrogenation of Ethylene. *Chemical Communications* **2020**, *56* (97), 15313–15316. https://doi.org/10.1039/d0cc06058e.

(25) Rojas-Luna, R.; Castillo-Rodríguez, M.; Ruiz, J. R.; Jiménez-Sanchidrián, C.; Esquivel, D.; Romero-Salguero, F. J. Ru- and Ir-Complex Decorated Periodic Mesoporous Organosilicas as Sensitizers for Artificial Photosynthesis. *Dalton Transactions* **2022**, *51* (48), 18708–18721. https://doi.org/10.1039/d2dt03147g.

(26) Staples, O.; Ferrandon, M. S.; Laurent, G. P.; Kanbur, U.; Kropf, A. J.; Gau, M. R.; Carroll, P. J.; McCullough, K.; Sorsche, D.; Perras, F. A.; Delferro, M.; Kaphan, D. M.; Mindiola, D. J. Silica Supported Organometallic IrI Complexes Enable Efficient Catalytic Methane Borylation. *J Am Chem Soc* **2023**, *145* (14), 7992–8000. https://doi.org/10.1021/jacs.2c13612.

(27) Lu, J.; Serna, P.; Gates, B. C. Zeolite- and MgO-Supported Molecular Iridium Complexes: Support and Ligand Effects in Catalysis of Ethene Hydrogenation and H-D Exchange in the Conversion of H2 + D2. *ACS Catal* **2011**, *1* (11), 1549–1561. https://doi.org/10.1021/cs200397r.

(28) Jun, S. E.; Kim, Y. H.; Kim, J.; Cheon, W. S.; Choi, S.; Yang, J.; Park, H.; Lee, H.; Park, S. H.; Kwon, K. C.; Moon, J.; Kim, S. H.; Jang, H. W. Atomically Dispersed Iridium Catalysts on Silicon Photoanode for Efficient Photoelectrochemical Water Splitting. *Nat Commun* **2023**, *14* (1). https://doi.org/10.1038/s41467-023-36335-0.

(29) Liao, F.; Yin, K.; Ji, Y.; Zhu, W.; Fan, Z.; Li, Y.; Zhong, J.; Shao, M.; Kang, Z.; Shao, Q. Iridium Oxide Nanoribbons with Metastable Monoclinic Phase for Highly Efficient Electrocatalytic Oxygen Evolution. *Nat Commun* **2023**, *14* (1). https://doi.org/10.1038/s41467-023-36833-1.

(30) Torrero, J.; Morawietz, T.; García Sanchez, D.; Galyamin, D.; Retuerto, M.; Martin-Diaconescu, V.; Rojas, S.; Alonso, J. A.; Gago, A. S.; Friedrich, K. A. High Performance and Durable Anode with 10-Fold Reduction of Iridium Loading for Proton Exchange Membrane Water Electrolysis. *Adv Energy Mater* **2023**, *2204169*, 1–13. https://doi.org/10.1002/aenm.202204169.

(31) Retuerto, M.; Pascual, L.; Torrero, J.; Salam, M. A.; Tolosana-Moranchel, Á.; Gianolio, D.; Ferrer, P.; Kayser, P.; Wilke, V.; Stiber, S.; Celorrio, V.; Mokthar, M.; Sanchez, D. G.;

Gago, A. S.; Friedrich, K. A.; Peña, M. A.; Alonso, J. A.; Rojas, S. Highly Active and Stable OER Electrocatalysts Derived from Sr2MIrO6 for Proton Exchange Membrane Water Electrolyzers. *Nat Commun* **2022**, *13* (1). https://doi.org/10.1038/s41467-022-35631-5.

(32) Choi, J.; MacArthur, A. H. R.; Brookhart, M.; Goldman, A. S. Dehydrogenation and Related Reactions Catalyzed by Iridium Pincer Complexes. *Chem Rev* **2011**, *111* (3), 1761–1779. https://doi.org/10.1021/cr1003503.

(33) Bhaskararao, B.; Rotella, M. E.; Kim, D. Y.; Kee, J. M.; Kim, K. S.; Kozlowski, M. C. Ir and NHC Dual Chiral Synergetic Catalysis: Mechanism and Stereoselectivity in γ-Butyrolactone Formation. *J Am Chem Soc* **2022**, *144* (35), 16171–16183. https://doi.org/10.1021/jacs.2c07376.

(34) Yin, C.; Jiang, Y. F.; Huang, F.; Xu, C. Q.; Pan, Y.; Gao, S.; Chen, G. Q.; Ding, X.; Bai, S. T.; Lang, Q.; Li, J.; Zhang, X. A 13-Million Turnover-Number Anionic Ir-Catalyst for a Selective Industrial Route to Chiral Nicotine. *Nat Commun* **2023**, *14* (1), 3718. https://doi.org/10.1038/s41467-023-39375-8.

(35) Castillo-Blas, C.; Gándara, F. Metal-Organic Frameworks Incorporating Multiple Metal Elements. *Isr J Chem* **2018**, *58* (9), 1036–1043. https://doi.org/10.1002/ijch.201800085.

(36) Housecroft, C. E. Iridium: Inorganic & Coordination Chemistry. *Encyclopedia of Inorganic Chemistry* **2006**, *6*, 1–18. https://doi.org/10.1002/0470862106.ia101.

(37) Jardine, F. H. Rhodium: Inorganic & Coordination Chemistry. *Encyclopedia of Inorganic and Bioinorganic Chemistry* **2011**. https://doi.org/10.1002/9781119951438.eibc0190.

(38) Ejegbavwo, O. A.; Berseneva, A. A.; Martin, C. R.; Leith, G. A.; Pandey, S.; Brandt, A. J.; Park, K. C.; Mathur, A.; Farzandh, S.; Klepov, V. V.; Heiser, B. J.; Chandrashekhar,

M.; Karakalos, S. G.; Smith, M. D.; Phillpot, S. R.; Garashchuk, S.; Chen, D. A.; Shustova, N. B. Heterometallic Multinuclear Nodes Directing MOF Electronic Behavior. *Chem Sci* **2020**, *11* (28), 7379–7389. https://doi.org/10.1039/d0sc03053h.

(39) Shakya, D. M.; Ejegbavwo, O. A.; Rajeshkumar, T.; Senanayake, S. D.; Brandt, A. J.; Farzandh, S.; Acharya, N.; Ebrahim, A. M.; Frenkel, A. I.; Rui, N.; Tate, G. L.; Monnier, J. R.; Vogiatzis, K. D.; Shustova, N. B.; Chen, D. A. Selective Catalytic Chemistry at Rhodium(II) Nodes in Bimetallic Metal–Organic Frameworks. *Angewandte Chemie - International Edition* **2019**, *58* (46), 16533–16537. https://doi.org/10.1002/anie.201908761.

(40) Desai, S. P.; Ye, J.; Zheng, J.; Ferrandon, M. S.; Webber, T. E.; Platero-Prats, A. E.; Duan, J.; Garcia-Holley, P.; Camaioni, D. M.; Chapman, K. W.; Delferro, M.; Farha, O. K.; Fulton, J. L.; Gagliardi, L.; Lercher, J. A.; Penn, R. L.; Stein, A.; Lu, C. C. Well-Defined Rhodium-Gallium Catalytic Sites in a Metal-Organic Framework: Promoter-Controlled Selectivity in Alkyne Semihydrogenation to E-Alkenes. *J Am Chem Soc* **2018**, *140* (45), 15309–15318. https://doi.org/10.1021/jacs.8b08550.

(41) Winarta, J.; Shan, B.; McIntyre, S. M.; Ye, L.; Wang, C.; Liu, J.; Mu, B. A Decade of UiO-66 Research: A Historic Review of Dynamic Structure, Synthesis Mechanisms, and Characterization Techniques of an Archetypal Metal-Organic Framework. *Cryst Growth Des* **2020**, *20* (2), 1347–1362. https://doi.org/10.1021/acs.cgd.9b00955.

(42) Lomachenko, K. A.; Jacobsen, J.; Bugaev, A. L.; Atzori, C.; Bonino, F.; Bordiga, S.; Stock, N.; Lamberti, C. Exact Stoichiometry of Ce x Zr 6-x Cornerstones in Mixed-Metal UiO-66 Metal-Organic Frameworks Revealed by Extended X-Ray Absorption Fine Structure Spectroscopy. *J Am Chem Soc* **2018**, *140* (50), 17379–17383. https://doi.org/10.1021/jacs.8b10343.

(43) Xue, D. X.; Belmabkhout, Y.; Shekhah, O.; Jiang, H.; Adil, K.; Cairns, A. J.; Eddaoudi, M. Tunable Rare Earth Fcu-MOF Platform: Access to Adsorption Kinetics Driven Gas/Vapor Separations via Pore Size Contraction. *J Am Chem Soc* **2015**, *137* (15), 5034–5040. https://doi.org/10.1021/ja5131403.

(44) Canossa, S.; Gonzalez-Nelson, A.; Shupletsov, L.; del Carmen Martin, M.; Van der Veen, M. A. Overcoming Crystallinity Limitations of Aluminium Metal-Organic Frameworks by Oxalic Acid Modulated Synthesis. *Chemistry - A European Journal* **2020**, *26* (16), 3564–3570. https://doi.org/10.1002/chem.201904798.

(45) Volkringer, C.; Popov, D.; Loiseau, T.; Férey, G.; Burghammer, M.; Riekel, C.; Haouas, M.; Taulelle, F. Synthesis, Single-Crystal X-Ray Microdiffraction, and NMR Characterizations of the Giant Pore Metal-Organic Framework Aluminum Trimesate MIL-100. *Chemistry of Materials* **2009**, *21* (24), 5695–5697. https://doi.org/10.1021/cm901983a.

(46) Mali, G.; Mazaj, M.; Arčon, I.; Hanžel, D.; Arčon, D.; Jagličić, Z. Unraveling the Arrangement of Al and Fe within the Framework Explains the Magnetism of Mixed-Metal MIL-100(Al,Fe). *Journal of Physical Chemistry Letters* **2019**, *10* (7), 1464–1470. https://doi.org/10.1021/acs.jpclett.9b00341.

(47) Lee, S.; Kapustin, E. A.; Yaghi, O. M. Coordinative Alignment of Molecules in Chiral Metal-Organic Frameworks. *Science* **2016**, *353* (6301), 808–811. https://doi.org/10.1126/science.aaf9135.

(48) Pei, X.; Bürgi, H. B.; Kapustin, E. A.; Liu, Y.; Yaghi, O. M. Coordinative Alignment in the Pores of MOFs for the Structural Determination of N-, S-, and P-Containing Organic Compounds Including Complex Chiral Molecules. *J Am Chem Soc* **2019**, *141* (47), 18862–18869. https://doi.org/10.1021/jacs.9b10501.

(49) Gándara, F.; Furukawa, H.; Lee, S.; Yaghi, O. M. High Methane Storage Capacity in Aluminum Metal-Organic Frameworks. *J Am Chem Soc* **2014**, *136* (14), 5271–5274. https://doi.org/10.1021/ja501606h.

(50) Sánchez-Sánchez, M.; Getachew, N.; Díaz, K.; Díaz-García, M.; Chebude, Y.; Díaz, I. Synthesis of Metal-Organic Frameworks in Water at Room Temperature: Salts as Linker Sources. *Green Chemistry* **2015**, *17* (3), 1500–1509. https://doi.org/10.1039/c4gc01861c.

(51) Nguyen, D. H.; Greger, I.; Pérez-Torrente, J. J.; Jiménez, M. V.; Modrego, F. J.; Lahoz, F. J.; Oro, L. A. ONO Dianionic Pincer-Type Ligand Precursors for the Synthesis of σ,π-Cyclooctenyl Iridium(III) Complexes: Formation Mechanism and Coordination Chemistry. *Organometallics* **2013**, *32* (23), 6903–6917. https://doi.org/10.1021/om400767d.

(52) Bucci, A.; Savini, A.; Rocchigiani, L.; Zuccaccia, C.; Rizzato, S.; Albinati, A.; Llobet, A.; MacChioni, A. Organometallic Iridium Catalysts Based on Pyridinecarboxylate Ligands for the Oxidative Splitting of Water. *Organometallics* **2012**, *31* (23), 8071–8074. https://doi.org/10.1021/om301024s.

(53) Gonçalves, M. R.; Frin, K. P. M. Synthesis, Electrochemical and Photochemical Properties of Neutral Ir(III) Complex Based on 3-Iodopyridine-2-Carboxylate Ligand. *J Mol Struct* **2021**, *1224*. https://doi.org/10.1016/j.molstruc.2020.129312.

(54) Aguirre-Díaz, L. M.; Reinares-Fisac, D.; Iglesias, M.; Gutiérrez-Puebla, E.; Gándara, F.; Snejko, N.; Monge, M. Á. Group 13th Metal-Organic Frameworks and Their Role in Heterogeneous Catalysis. *Coord Chem Rev* **2017**, *335*, 1–27. https://doi.org/10.1016/j.ccr.2016.12.003.

(55) Reinares-Fisac, D.; Aguirre-Díaz, L. M.; Iglesias, M.; Snejko, N.; Gutiérrez-Puebla, E.; Monge, M. Á.; Gándara, F. A Mesoporous Indium Metal-Organic Framework:

Remarkable Advances in Catalytic Activity for Strecker Reaction of Ketones. *J Am Chem Soc* **2016**, *138* (29), 9089–9092. https://doi.org/10.1021/jacs.6b05706.

(56) Aguirre-Díaz, L. M.; Gándara, F.; Iglesias, M.; Snejko, N.; Gutiérrez-Puebla, E.; Monge, M. Á. Tunable Catalytic Activity of Solid Solution Metal-Organic Frameworks in One-Pot Multicomponent Reactions. *J Am Chem Soc* **2015**, *137* (19), 6132–6135. https://doi.org/10.1021/jacs.5b02313.

(57) Tian, X. R.; Shi, Y.; Hou, S. L.; Ma, Y.; Zhao, B. Efficient Cycloaddition of CO2and Aziridines Activated by a Quadruple-Interpenetrated Indium-Organic Framework as a Recyclable Catalyst. *Inorg Chem* **2021**, *60* (20), 15383–15389. https://doi.org/10.1021/acs.inorgchem.1c02034.

(58) Lu, C.; Xiong, D.; Chen, C.; Wang, J.; Kong, Y.; Liu, T.; Ying, S.; Yi, F. Y. Indium-Based Metal-Organic Framework for Efficient Photocatalytic Hydrogen Evolution. *Inorg Chem* **2022**, *61* (5), 2587–2594. https://doi.org/10.1021/acs.inorgchem.1c03628.

(59) Zhang, B.; Guo, P. Y.; Ma, L. N.; Liu, B.; Hou, L.; Wang, Y. Y. Two Robust In(III)-Based Metal-Organic Frameworks with Higher Gas Separation, Efficient Carbon Dioxide Conversion, and Rapid Detection of Antibiotics. *Inorg Chem* **2020**, *59* (7), 5231–5239. https://doi.org/10.1021/acs.inorgchem.0c00539.

(60) He, Y. C.; Kan, W. Q.; Guo, J.; Yang, Y.; Du, P.; Liu, Y. Y.; Ma, J. F. Iodine-Templated Assembly of an In(Iii) Complex with a Single-Crystal-to- Single-Crystal Transition. *CrystEngComm* **2013**, *15* (37), 7406–7409. https://doi.org/10.1039/c3ce41337c.

(61) Guo, Z.; Li, Y.; Yuan, W.; Zhu, X.; Li, X.; Cao, R. Syntheses, Structures, and Characterizations of Two New Indium(III) Compounds from 1D ···In-OH-In-OH··· Chains and Pyridinedicarboxylic Ligands. *Eur J Inorg Chem* **2008**, No. 8, 1326–1331. https://doi.org/10.1002/ejic.200701060.

(62) Liu, Y.; Kravtsov, V. C.; Beauchamp, D. A.; Eubank, J. F.; Eddaoudi, M. 4-Connected Metal-Organic Assemblies Mediated via Heterochelation and Bridging of Single Metal Ions: Kagomé Lattice and the M6L 12 Octahedron. *J Am Chem Soc* **2005**, *127* (20), 7266–7267. https://doi.org/10.1021/ja051259q.

(63) Zhang, B.; Wang, W.; Liu, B.; Hou, L. Indium Metal-Organic Frameworks Based on Pyridylcarboxylate Ligands and Their Potential Applications. *Dalton Transactions* **2021**, *50* (17), 5713–5723. https://doi.org/10.1039/d1dt00504a.

(64) Goesten, M. G.; Fonseca Guerra, C.; Kapteijn, F.; Gascon, J.; Bickelhaupt, F. M. Six-Coordinate Group 13 Complexes: The Role of d Orbitals and Electron-Rich Multi-Center Bonding. *Angewandte Chemie - International Edition* **2015**, *54* (41), 12034–12038. https://doi.org/10.1002/anie.201504864.

(65) Gupta, N. K.; Osorio-Toribio, G.; Hernández, M.; Percástegui, E. G.; Lima, E.; Ibarra, I. A. Sc(Iii)-Based Metal-Organic Frameworks. *Chemical Communications* **2022**, *58* (26), 4116–4131. https://doi.org/10.1039/d1cc05768e.

(66) Ibarra, I. A.; Lin, X.; Yang, S.; Blake, A. J.; Walker, G. S.; Barnett, S. A.; Allan, D. R.; Champness, N. R.; Hubberstey, P.; Schröder, M. Structures and H2 Adsorption Properties of Porous Scandium Metal-Organic Frameworks. *Chemistry - A European Journal* **2010**, *16* (46), 13671–13679. https://doi.org/10.1002/chem.201000926.

(67) Perles, J.; Snejko, N.; Iglesias, M.; Monge, M. Á. 3D Scandium and Yttrium Arenedisulfonate MOF Materials as Highly Thermally Stable Bifunctional Heterogeneous Catalysts. *J Mater Chem* **2009**, *19* (36), 6504–6511. https://doi.org/10.1039/b902954k.

(68) Lv, H. J.; Fan, S. C.; Jiang, Y. C.; Li, S. N.; Zhai, Q. G. Design of a Robust Rod-Packing Scandium-Organic Framework for C2Hx/CO2 Separation, CO2 Storage, and Catalytic

CO2 Cycloaddition. *Inorg Chem Front* **2023**, 3015–3024. https://doi.org/10.1039/d3qi00314k.

(69) Panda, A. K.; Mishra, B. G.; Mishra, D. K.; Singh, R. K. Effect of Sulphuric Acid Treatment on the Physico-Chemical Characteristics of Kaolin Clay. *Colloids Surf A Physicochem Eng Asp* **2010**, *363* (1–3), 98–104. https://doi.org/10.1016/j.colsurfa.2010.04.022.

(70) Twilton, J.; Le, C. C.; Zhang, P.; Shaw, M. H.; Evans, R. W.; MacMillan, D. W. C. The Merger of Transition Metal and Photocatalysis. *Nat Rev Chem* **2017**, *1*. https://doi.org/10.1038/s41570-017-0052.

(71) Takizawa, S. Y.; Okuyama, T.; Yamazaki, S.; Sato, K. I.; Masai, H.; Iwai, T.; Murata, S.; Terao, J. Ion Pairing of Cationic and Anionic Ir(III) Photosensitizers for Photocatalytic CO2 Reduction at Lipid-Membrane Surfaces. *J Am Chem Soc* **2023**, *145* (28), 15049–15053. https://doi.org/10.1021/jacs.3c03625.

(72) Bevernaegie, R.; Wehlin, S. A. M.; Elias, B.; Troian-Gautier, L. A Roadmap Towards Visible Light Mediated Electron Transfer Chemistry with Iridium(III) Complexes. *ChemPhotoChem* **2021**, *5* (3), 217–234. https://doi.org/10.1002/cptc.202000255.

(73) Padial, N. M.; Quartapelle Procopio, E.; Montoro, C.; López, E.; Oltra, J. E.; Colombo, V.; Maspero, A.; Masciocchi, N.; Galli, S.; Senkovska, I.; Kaskel, S.; Barea, E.; Navarro, J. A. R. Highly Hydrophobic Isoreticular Porous Metal–Organic Frameworks for the Capture of Harmful Volatile Organic Compounds. *Angewandte Chemie International Edition* **2013**, *52* (32), 8290–8294. https://doi.org/10.1002/anie.201303484.

(74) Li, L.-P.; Ye, B.-H. Efficient Generation of Singlet Oxygen and Photooxidation of Sulfide into Sulfoxide via Tuning the Ancillary of Bicyclometalated Iridium(III) Complexes. *Inorg Chem* **2019**, *58* (12), 7775–7784. https://doi.org/10.1021/acs.inorgchem.9b00220.

─ CHAPTER 8 ─

Concluding Remarks

The key point of this Doctoral Thesis was to explore the feasibility of generating multi-metal MOFs with specific metal combinations, and to determine which are the crucial factors that impact the outcome of the reactions.

One of the main objectives of this investigation was to use the MOF family RPF-4 as a platform to evaluate if it is possible to obtain MTV-MOFs with specific binary combinations of rare-earth atoms, and to determine which parameter would determine the outcome of the reactions. The results of the experimental work that was carried out for Chapter 4 made it possible to determine the sequencing scenarios within the SBUs of the RPF-4, and also which combinations resulted in a MTV-MOF with the desired metal ratio and atomic distribution. The results of the research highlighted the relevance of the synthesis and crystallization mechanism of a MOF, which for RPF-4 were proven to be determinant for the incorporation of different metal ions into the SBUs. Another crucial point was that, while the compositional analysis of the bulk of lanthanum-based RPF-4 samples indicated a homogeneous distribution of the metal ions, a more thorough analysis of the composition of individual crystals revealed the presence of a compositional segregation, even for combination of metals for which the MOF can be obtain in the single-metal form. So, this emphasizes the importance of understanding the MOF system and also carrying out an exhaustive analysis of the samples. Upon understanding that the composition of different metal combinations of MTV-RPF-4 was determined by a complex interplay between thermodynamic and kinetic crystallization factors, it was possible to tune the composition of any binary combination of this MOF family to suit any application. Bearing this in mind, and in view of the initial goal of translating specific metal sequences to other materials, MOF-derived oxides were obtained by calcining RPF-4 samples with specific compositions, and these materials displayed an enhanced catalytic performance compared to traditional oxides.

Additionally, as established in the initial main goals, other metal combinations including noble metals, specifically iridium (III), have been explored throughout this Doctoral Thesis. As discussed in Chapter 6 and 7, it was not possible to insert iridium into already reported MOFs through a one-pot approach, and this led to designing an alternative strategy. Following a one-step multi-metal approach, iridium (III) building units were reticulated into a framework, generating the new MOF family, MIrPF-13 (M = Sc, In). This new multi-metal material was a suitable heterogeneous catalyst for photocatalysis, as the iridium building units are responsible for the enhanced catalytic performance.

The one-step multi-metal strategy showcased in Chapter 7 paves the way for extending the field of reticular chemistry to other unexplored metal elements and broaden the range of reactivity and chemical versatility that can be achieved in MOFs.

As a final remark, I would like to mention that, considering the initial objectives and the conclusions, the research work carried out in my Doctoral Thesis is expected to be broadly beneficial for the field of reticular chemistry, especially for the emerging sequence-oriented development of multi-metal MOFs, as it helps to overcome some of its main challenges through the fundamental comprehension of their synthetic process.